

# Optical and Electrical Characterisation of $\alpha$ -Ga<sub>2</sub>O<sub>3</sub> thin films

David Nicol

A thesis presented for the degree of  
Doctor of Philosophy



Department of Physics  
University of Strathclyde  
Date May 9, 2025

*For Harper*

This thesis is the result of the author's original research. It has been composed by the author and has not been previously submitted for examination which has led to the award of a degree.

The copyright of this thesis belongs to the author under the terms of the United Kingdom Copyright Acts as qualified by University of Strathclyde Regulation 3.50. Due acknowledgement must always be made of the use of any material contained in or derived from this thesis.

# Abstract

$\text{Ga}_2\text{O}_3$  is an emerging ultra-wide bandgap semiconductor for next-generation power electronics, deep ultraviolet photodetectors, and high-temperature optoelectronic devices. However, the performance of  $\text{Ga}_2\text{O}_3$  devices is often limited by the presence of defects.  $\text{Ga}_2\text{O}_3$  is a polymorphic compound, with the  $\alpha$  phase offering several advantages over the other phases such as it exhibits the widest bandgap and demonstrates the ability for bandgap engineering through isomorphic compounds. To improve the efficiency and reliability, it is crucial to understand the influence of defects on the electrical and optical properties of the material. This thesis aims to generate new knowledge on the metastable  $\alpha$   $\text{Ga}_2\text{O}_3$  that will aid the future development of  $\alpha$   $\text{Ga}_2\text{O}_3$  devices. Through temperature-dependent photoluminescence spectroscopy, a previously unreported emission line at 3.8 eV was observed at temperatures below 90 K and was attributed to donor-acceptor pair recombination between H decorated  $V_{Ga}$ , and  $H_O$  or  $H_I$  serving as the acceptor and donor, respectively. Low temperature cathodoluminescence mapping further revealed a spatial dependence, indicating a nonuniform distribution of Hydrogen decorated gallium vacancies. To investigate the photoelectric properties of  $\alpha$ - $\text{Ga}_2\text{O}_3$ , a custom-built photoelectrical characterisation setup was developed with capabilities for time-resolved and power-dependent measurements. Using this setup, we evaluated the performance of  $\alpha$ - $\text{Ga}_2\text{O}_3$  photodetectors and found that commonly reported metrics such as responsivity and response time are strongly influenced by experimental conditions and device architecture. These findings highlight the need for careful consideration when comparing detector performance across different studies. We propose that photoconductance serves as a more reliable parameter for such comparisons

and emphasise the importance of conducting optical power-dependent measurements when benchmarking photodetectors in the literature. Further work on the photoelectrical properties presents the first application of the constant photocurrent method to  $\alpha$ -Ga<sub>2</sub>O<sub>3</sub>, enabling the determination of sub-bandgap absorption coefficients of  $1 \times 10^5 \text{ cm}^{-1}$  at the band edge (5.3 eV) to  $0.8 \text{ cm}^{-1}$  close to the midgap (2.7 eV). Variations in the absorption edge slope indicated the presence of an exponentially distributed defect-related states below the Fermi level. Complementary thermally stimulated current measurements allowed for the identification of traps above the Fermi level, identifying three traps at approximately 138 K, 220 K, and 235 K, which correspond to trap activation energies of 0.28 eV, 0.47 eV, and 0.51 eV, respectively. Tentatively, we assign trap E1 (0.28 eV) to be related to O related divancies such as  $\text{O}_{\text{Ga}}\text{-V}_{\text{Ga}}$ , where the Sn related complexes also demand attention. Trap E2(0.47 eV) and E3 (0.51 eV) were tentatively assigned to  $\text{Si}_{\text{Ga}}\text{-H}$ , together providing a near full bandgap mapping of defect states. Finally, we make use the broad absorption spectrum of our samples, introduced by native defects identified in previous chapters, as proof-of-concept study to demonstrate the capability of  $\alpha$ -Ga<sub>2</sub>O<sub>3</sub>-based photodetectors to monitor water quality contamination. Photocurrent measurements reveal 3 distinct regions that match key water contaminant absorption characteristics. Region (i) (200-250 nm) corresponds to band-to-band transitions and is ideal for nitrate detection, region (ii) (250-350 nm) is related to band tail transitions and fits the absorption peak of DOC, and finally, region (iii) (350-470 nm) addresses SSC detection using defect-mediated transitions. For the wavelengths selected for the contamination test, strong correlations ( $R^2 > 90$ ) were observed between the concentration of the contaminant and the photocurrent. The  $R^2$  correlations strongly depended on the selected illumination wavelength, which demonstrates good selectivity of the photodetectors. This work opens the door to a more sensitive, compact, and energy-efficient system to monitor water quality.

# Acknowledgements

If someone told me 8 years ago when I walked into the first-year mechanics class that 8 years later, I would complete a PhD... I probably would have turned right back out the door. However, here I am and I couldn't be more grateful for the experience. Whether it be travelling to Japan for my first international conference, spending months in Lyon learning about life in a clean room, finally seeing an experiment go to plan, or even the first set of comments from the dreaded *Reviewer No.2*- I will remember it all for the rest of my life.

None of this would have been possible without the support and guidance of my supervisor, **Dr Fabien Massabuau**. Fabien's patience and constant stream of encouragement inspired me to continually improve as a researcher, and without him I would have had a very different PhD experience. I also would like to give special thanks to **Dr Stephen Reynolds**, who acted as a 2nd supervisor and taught me everything I needed to know about the topic of photoconductivity and our regular football chats to break up the science.

Over the years, I was trained on how to use scanning electron microscopes and here I would like to give a special thanks to **Dr Paul Edwards** for his patience and happy-to-help attitude. He was always there to help out, no matter how many times I asked. A shout out here also goes to **Dr Douglas Cameron** who also shared his tips and tricks for imaging and cathodoluminescence on the Scanning Electron Microscopes, as well as gathering the Atomic Force Microscopy data used in Chapter 3.

I would also like to thank my collaborators for supplying me with the samples required for the experimental work in this thesis. **Dr Yuichi Oshima**, **Dr Joseph**

## Chapter 0. Acknowledgements

**Roberts**, and **Dr Paul Chalker**. In chapter 6, we got to use  $\alpha\text{-Ga}_2\text{O}_3$  for water quality monitoring applications thanks to the preparation of the water samples by **Dr Nuria Martinez-Carreras**

I would like to say a special thanks everyone in the semiconductor spectroscopy and devices student office for always supplying the laughs and distractions during the working day. In particular, my close friend **Dr Kris Barr** who was always there to talk to during my weekly breakdowns. Kris's hard work and determination inspired me to do more, even training me on how to use labVIEW when I needed it most. Thank you mate.

It goes without saying, but I couldn't have done this without the support from my **mum and dad**. They have always believed in me, and without them I wouldn't have had the courage to go and study Physics in the first place.

Finally, **Kirsten** . I can't put into words the volume of love and support Kirsten has given me over the years, and believing in me even when I didn't believe in myself. I would not have reached this stage in my life without her by my side. I cannot thank her enough.

# List Of Publications

## Published

1. **D. Nicol**, F. Hadizadeh, S. Douglas, S. Reynolds, F. Massabuau, *Consistent reporting of performances in Ga<sub>2</sub>O<sub>3</sub> UV-C photodetectors*, APL Electronic Devices, Vol. 1 (2025)
2. **D. Nicol**, S. Reynolds, K. Barr, J.W Roberts, J.J. Jarman, P.R. Chalker, F. C-P. Massabuau, *Constant Photocurrent Method to probe the sub-bandgap Absorption in Wide Bandgap Semiconductor Films: The case of  $\alpha$ -Ga<sub>2</sub>O<sub>3</sub>*, Physica Status Solidi (b), Vol. 261 (2024)
3. **D. Nicol**, Y. Oshima, J.W. Roberts, L. Penman, D. Cameron, P.R. Chalker, R.W. Martin, F.C-P. Massabuau, *Hydrogen-related 3.8 eV luminescence in  $\alpha$ -Ga<sub>2</sub>O<sub>3</sub>*, Applied Physics Letters, Vol. 122 (2023)
4. F. C-P. Massabuau, F. Adams, **D. Nicol**, J.C. Jarman, M. Fentrup, J.W. Roberts, T.J. O'Hanlon, A. Kovacs, P.R. Chalker, R. Oliver, *Ni/Au Contacts to corundum  $\alpha$ -Ga<sub>2</sub>O<sub>3</sub>*, Japanese Journal of Applied Physics, Vol. 62 (2023)
5. F.C-P. Massabuau, **D. Nicol**, F. Adams, J.J. Jarman, J.W. Roberts, A. Kovacs, P.R. Chalker, R. Oliver, *Study of Ti Contacts to corundum  $\alpha$ -Ga<sub>2</sub>O<sub>3</sub>*, Journal of Physics D: Applied Physics, Vol. 54 (2021)
6. F.C-P. Massabuau, J.W. Roberts, **D. Nicol**, P.R. Edwards, M. McLelland, G.L. Dallas, D.A. Hunter, E.A Nicholson, J.C. Jarman, A. Kovacs, R.W. Martin, R.

## Chapter 0. List Of Publications

Oliver, P.R. Chalker, *Progress in atomic layer deposited  $\alpha$ -Ga<sub>2</sub>O<sub>3</sub> materials and solar-blind detectors*, Proceedings SPIE, Vol. 11687 (2021)

7. **D. Nicol**, S. Reynolds, F. Massabuau, *Impact of experimental conditions on the properties of  $\alpha$ -Ga<sub>2</sub>O<sub>3</sub> photodetectors*

### **In preparation**

8. **D. Nicol**, J. Gracie, A. Uras, J. W. Roberts, N. Lidgi-Guigui, W. Peveler, N. Martinez-Carreras, F. Massabuau, *Novel Approach for water quality monitoring using  $\alpha$ -Ga<sub>2</sub>O<sub>3</sub> based photodetectors*

# Acronyms/Abbreviations

<b>AFM</b>	Atomic force microscopy
<b>CCD</b>	Charged coupled device
<b>CL</b>	Cathodoluminescence
<b>CPM</b>	Constant Photocurrent Method
<b>DAP</b>	Donor acceptor pair
<b>DFT</b>	Density functional theory
<b>DLTS</b>	Deep level transient spectroscopy
<b>DOC</b>	Disolved organic carbon
<b>DOS</b>	Density of states
<b>HSI</b>	Hyperspectral imaging
<b>HVPE</b>	Halide vapor phase epitaxy
<b>ND</b>	Neutral density
<b>NPLC</b>	Number of power line cycles
<b>ODLTS</b>	Optical deep level transient spectroscopy
<b>PEALD</b>	Plasma enhanced atomic layer deposition
<b>PL</b>	Photoluminescence
<b>SE</b>	Secondary electron
<b>SEM</b>	Secondary electron microscope
<b>SSC</b>	Suspended solids concentration
<b>STH</b>	Self trapped hole
<b>TSC</b>	Thermally stimulated current
<b>XRD</b>	X-ray diffraction

# List of Figures

1.1	Relationship between bandgap and breakdown electric field value. Image taken from [1] . . . . .	3
1.2	Crystal structure of (a) $\alpha$ -Ga <sub>2</sub> O <sub>3</sub> (b) $\beta$ -Ga <sub>2</sub> O <sub>3</sub> modelled using VESTA. . . . .	5
1.3	A comparison of the band structure of (a) $\alpha$ - Ga <sub>2</sub> O <sub>3</sub> and (b) $\beta$ Ga <sub>2</sub> O <sub>3</sub> based on DFT hybrid functional calculations. [2,3] . . . . .	6
1.4	Schematic representation of a distribution of atoms in a lattice. (a) perfect lattice. (b) Lattice containing a vacancy. (c) Lattice containing an interstitial. . . . .	8
1.5	Representation of the fermi level at (a) T= 0 K. (b) T > 0 K. The dashed region represents the probability of finding an electron. At T=0 the probabilty of finding an electron below the Fermi level is 1, whereas above the Fermi level the probabilty is 0. At elevated temperatures, there is some probabilty of finding the electron above the Fermi level . . . . .	9
1.6	Formation energy of various defects in $\alpha$ -Ga <sub>2</sub> O <sub>3</sub> in (left) Ga-rich and (right) O-rich conditions using a Generalised Gradient Approximation. Image taken from [4] . . . . .	10
1.7	Formation energy H decorated V <sub>Ga</sub> in $\alpha$ -Ga <sub>2</sub> O <sub>3</sub> in (left) Ga-rich, and (right) O-rich conditions. Image taken from [5] . . . . .	13
1.8	Optical Absorption measurements obtained from UV-Vis spectrophotometry of $\alpha$ -Ga <sub>2</sub> O <sub>3</sub> showing the absorption coefficient versus energy . . . . .	14
1.9	Optical Absorption measurements obtained from PDS of $\beta$ -Ga <sub>2</sub> O <sub>3</sub> showing the absorption coefficient versus energy. Image taken from [6] . . . . .	15

List of Figures

1.10	Schematic of luminescence processes in $\text{Ga}_2\text{O}_3$ : (a) Band to band recombination where the energy of the emitted photon will equal to the bandgap energy, (b) recombination of electron and STH at trapped site, (c) recombination of electron from a donor site and hole in the valence band (d) donor acceptor pair recombination. . . . .	17
1.11	Configuration coordinate diagram illustrating the absorption and emission process in $\text{Ga}_2\text{O}_3$ . Excitation with photons with energy greater than the bandgap creates electron-hole pairs. Due to lattice distortion from the STH, the emission energy is lowered reflected in a large stokes shift in the emission . . . . .	18
1.12	Illustration of the various processes after a material being illuminated by above-bandgap light. (a) Light absorption process where an electron can be excited from the valence band, or from filled defect states into the conduction band directly. (b) Carrier transport where the electron moves in the conduction band, generating the measured photocurrent. (c) Carrier trapping in which the electrons are intermittently trapped before being re-excited back into the conduction band. (d) Carrier recombination were the electron will recombine with a hole at a recombination center, or the valence band. . . . .	20
1.13	Schematic of metal-semiconductor-metal photodetector with contacts in interdigitated configuration . . . . .	23
1.14	Schematic of HVPE growth process of $\alpha\text{-Ga}_2\text{O}_3$ . . . . .	26
1.15	Schematic of PEALD growth process of $\alpha\text{-Ga}_2\text{O}_3$ in 2 stages. Left shows the precursor stage with the precursor gas represented in blue. Right shows the plasma gas inlet, represented in purple. . . . .	27

List of Figures

2.1	Schematic of PL set up for data acquired in Chapter 3. The 224 nm pulsed laser illuminates the sample where the emitted light is collimated and focused to the entrance slit of the monochromator. At the entrance slit, a 280 nm filter was used to reject laser lines from the emission spectrum. The diffraction grating resolves the emitted light and collected by the Andor DV-420-0E camera . . . . .	30
2.2	PL spectrum of HVPE grown $\alpha$ -Ga <sub>2</sub> O <sub>3</sub> measured at 290 K with the intensity scale (y) converted in terms of (left) counts/nm, and (right) counts/eV. . . . .	31
2.3	SEM electron-matter interactions and resulting radiations. Image taken from [7]. . . . .	33
2.4	Monte-Carlo simulation of electron-matter interactions in Ga <sub>2</sub> O <sub>3</sub> with an accelerating voltage of (top) 1 keV, and (bottom) 7 keV. The tilted interaction volume derives from the sample being tilted at 45° relative to the electron beam. . . . .	34
2.5	Schematic of the SEM used for SE imaging and CL measurements. . . . .	35
2.6	Hyperspectral imaging where the electron beam is rastered across the sample surface, and a CL spectrum is acquired at each pixel. . . . .	36
2.7	Typical data obtained for SEM acquisitions: (left) SE image, (middle) Panchromatic HSI obtained over the square region marked by the dashed lines in the SE image, and (right) CL spectra obtained at two regions in HSI map. . . . .	37
2.8	Monochromatic CL images obtained from SE image in the (middle) 3.2-3.4 eV ,and (right) 3.7-3.9 eV spectral regions. . . . .	38
2.9	Example of centroid analysis feature: (a) Monochromatic CL image between 3.2-3.4 eV and (b) corresponding centroid analysis; and (c) monochromatic CL image between 3.7-3.9 eV with (d) corresponding centroid analysis. . . . .	39

List of Figures

2.10	Representation of the PL system response accounting for the efficiency of (a) diffraction grating (b) CCD camera (c) Lens. The convolution of the effect of the optical elements is shown in (d)	41
2.11	Quantum efficiencies of a variety of Andor CCD cameras. In the experimental PL setup an ANDOR DV420-OE was used to generate the emitted spectrum.	42
2.12	Blackbody emission spectrum using the Planck's equation at temperatures of 2500 - 4000 K	44
2.13	PL system response: (left) Theoretical and Experimental emission from the blackbody source, and (right) attempt at corrected PL system response.	45
2.14	CL System Response	46
2.15	Comparison of the CL spectrum before correction for system response (red) and after correction (black). Here we see a removal of the spike feature around 2.5 eV	46
2.16	Schematic of the core photoconductivity experimental setup consisting of a light source to provide excitation, monochromator to resolve the light, Keithley source-measure unit. Optical power was measured via a secondary optic fiber from the monochromator	48
2.17	Deuterium Light source emission spectrum. Here we see a dominant broad emission between 200-300 nm. The sharp feature around 650 nm is the characteristic emission line of the Balmer series	50
2.18	Spot size estimation a illuminated spot using a 635 nm LED	52
2.19	Wavelength-dependent transmission curves for NDfilters used during photoconduction experiments	54
2.20	Comparison of the photoconductivity spectrum of an $\alpha$ Ga <sub>2</sub> O <sub>3</sub> sample versus wavelength measured using (a) LEDs (b) Deuterium light source.	55
2.21	Photocurrent measurements from deuterium light source measured without filter (black circles), with 280 nm longpass filter (blue squares), and with 400 nm long pass filter (red triangles).	56

## List of Figures

2.22	Schematic of the photoconduction setup adapted for CPM measurements. Here ND filters were added for coarse attenuation of the optical power, while fine adjustments were made by varying the LED driving current . . . . .	58
2.23	Experimental setup used for power-dependent photocurrent measurements. A resistance box was added to stabilise the LED driving current at low operating voltages. . . . .	59
2.24	Schematic of the experimental setup used for high optical power measurements required for water quality measurements in Chapter 6. Attenuation from the setup was decreased by removing the monochromator. . . . .	61
2.25	Schematic of the Thermally Stimulated Current spectroscopy experimental setup at the University of Dundee. . . . .	62
2.26	Experimental setup used for transient photocurrent measurements when illuminated via Deuterium light source. The monochromator was removed for LED excitation to avoid additional attenuation for high power measurements . . . . .	64
2.27	Transient decay modelled by (a) Exponential Decay (b) Power-law decay (c) Stretched Exponential . . . . .	64
2.28	Schematic of contact of contact architecture on 130 nm $\alpha$ -Ga <sub>2</sub> O <sub>3</sub> . . . . .	67
2.29	UV-VIS spectrophotometry setup. A broadband light source is spectrally resolved and illuminates the sample. The light source is spectrally resolved between 200-700 nm. Transmitted light is collected in an integrating sphere. . . . .	70
2.30	Optical Transmittance spectrum of $> \mu\text{m}$ thick sample $\alpha$ Ga <sub>2</sub> O <sub>3</sub> used in chapters 3 . . . . .	71
2.31	Optical Transmission Measurements of 250 nm thick samples $\alpha$ -Ga <sub>2</sub> O <sub>3</sub> used in chapters 4,5 and 6 . . . . .	72
3.1	PL measurements on 250 nm thick PEALD samples obtained at (left) 290 K (right) 9 K. The Intensity axis is plotted in log scale due to the relative low intensity peak centered around 3.8 eV . . . . .	76

List of Figures

3.2	290 K PL spectrum of sample C where the H concentration ( $[H] = 1.5 \times 10^{17} \text{ cm}^{-3}$ ). Inset shows the PL spectrum of sample C measured at 290 K in log scale highlighting the presence of the 3.8 eV peak (b) 290 K PL spectrum of sample C ( $[H] = 1.5 \times 10^{17} \text{ cm}^{-3}$ ) with 280 nm filter (black) and 470 nm filter (red) . . . . .	78
3.3	PL spectra of samples A, B, C and D measured at (a) 290 K (b) 9 K. (c) Illustrates the correlation between the integrated intensity of the 3.8 eV luminescence line and H concentrations of the samples . . . . .	81
3.4	Topography maps obtained from AFM of (a) sample A, (b) sample B, (c) Sample C, and (d) sample D . . . . .	84
3.5	XRD diffractograms of samples B,C, and D showing a sharp characteristic $\alpha\text{-Ga}_2\text{O}_3$ reflection around $40.25^\circ$ . . . . .	85
3.6	Temperature-dependent luminescence of sample C measured between 9 K and 110 K . . . . .	86
3.7	Arrhenius plot to obtain the activation energy of the 3.8 eV luminescence line . . . . .	87
3.8	Model for the 3.8 eV luminescence recombination mechanism. The purple dashed line represents donor acceptor pair recombination when $T < 110 \text{ K}$ . . . . .	90
3.9	SEM information obtained from sample C with $[H]=1.5 \times 10^{17} \text{ cm}^{-3}$ (a) SEM image (b) panchromatic CL image (c) System corrected CL spectra measured at 290 K (d) Horizontal line scan showing variations in CL peak intensity . . . . .	91
3.10	(top)CL temperature dependence measured between between 90 190 K (bottom) Activation energy obtained via Arrhenius equation revealing an activation energy of 5.6 meV . . . . .	93

List of Figures

3.11	CL measurements obtained from sample C at 80 K. HSI measurements are shown in (a) Panchromatic between 3- 4.2 eV (b) Monochromatic 3.1 - 3.2 eV (c) Monochromatic (3.79-3.81 eV). Mean CL spectra measured (d) entire HSI region (e) mean spectra over region 1 marked by the red circle in image b (c) mean spectra over region 2 marked by the green circle shown in images b and c . . . . .	95
4.1	photocurrent transient using (left) deuterium light source (right) 250 nm LED, where the led is around 2 orders of magnitude higher in light intensity . . . . .	101
4.2	(a) Responsivity measured as a function of illumination intensity using 250 nm Thorlabs LED. Inset shows the response speed as a function of illumination intensity measured under a 10 V applied bias (b) Responsivity versus wavelength under 250 nm excitation (c) Responsivity as a function of excitation wavelength under a 4 V bias . . . . .	103
4.3	(left) Photocurrent rise after illumination with light measured at 4 different illumination intensities (right) Photocurrent decreasing as a function of time after initial saturation while the optical power remains constant	107
4.4	Photoconductance measured as a function of light intensity. Here we compare our detector performance with others in the field, converted to a standard parameter of photoconductance. Here we use an excitation wavelength 250 nm . . . . .	109
5.1	Schematic of accessible states available from CPM and TSC measurements. CPM works as a tool for probing defect states below the dark Fermi level (black dashed line) whilst TSC serves as a tool for probing defect states above the dark Fermi level. . . . .	116

List of Figures

5.2 Transmitted light intensity (incident from the left) versus depth in a 130 nm thick film, described by the Beer-Lambert law: i)  $\alpha d \gg 1$ : incident light is strongly absorbed at the surface of the film; ii)  $\alpha d = 1$ . 67 % of the light is absorbed non-uniformly within the film; and iii)  $\alpha d \ll 1$ : light absorption is small and uniform throughout the film, giving a constant generation rate and carrier lifetime . . . . . 117

5.3 Workflow diagram for obtaining CPM spectrum. Green box represents an action where the gold diamond shows a decision . . . . . 123

5.4 TSC band diagram schematic showing experimental process (a) sample cooled to low-temperature illuminated with light and allowed to reach steady-state (b) temperature increases and the quasi-Fermi level drops below trap level, resulting in an increase in the measured TSC signal. The TSC signal decreases due to trap depopulation (c) Temperature increased again and a second trap becomes thermally activated resulting in a second peak in the observed TSC spectrum (d) Temperature increased further to reveal 3rd trap and quasi-Fermi level brought back down to the dark Fermi level observed after thermal annealing . . . . . 124

5.5 Dark current activation energy of PEALD grown  $\alpha$  Ga<sub>2</sub>O<sub>3</sub> measured between 350 - 400 K, revealing an activation energy of around 1 eV . . . 126

5.6 TSC spectrum obtained from TSC measurements between 110 - 400 K revealing 3 distinct peaks labelled E1-E3. E4 appears at a discontinuity therefore disregarded. Onset of the dark current is observed from around 350 K . . . . . 127

5.7 Absorption coefficient spectra of  $\alpha$ -Ga<sub>2</sub>O<sub>3</sub> obtained via CPM using different CPM reference currents (8 pA [green squares], 40 pA [white circles], and 177 pA [black triangles]) and optical transmission methods [gold]. The black line indicates how the absorption coefficient should scale in a direct bandgap semiconductor for a perfect crystal [8] . . . . . 132

5.8 (a) Absorption coefficient obtained using CPM (b) Band diagram illustrating electron transitions from deep lying states below the Fermi Level 134

## List of Figures

5.9	Schematic of defect states identified using a combination of TSC and CPM137	
6.1	(a) Schematic of the cross section of the Ga <sub>2</sub> O <sub>3</sub> -based photodetector. (b) SEM image of the contact structure, with inset showing a magnified image of the interdigitated finger area. (c) XRD diffractogram revealing reflections from Al <sub>2</sub> O <sub>3</sub> , Ga <sub>2</sub> O <sub>3</sub> , and Au. (d) Transmission electron microscope image of device cross section (e) Photodetector responsivity and (f) contrast versus wavelength . . . . .	143
6.2	Absorption Coefficient measured between 3.4 and 6 eV for (a) PEALD grown sample 250 nm (b) HVPE grown sample. The red dashed line represents how the absorption coefficient scales with in energy in perfect direct bandgap semiconductor . . . . .	145
6.3	Defect diagram indicating the various electronic pathways to the conduction band to enable water quality monitoring for (i) Nitrates (ii) DOC (iii) SSC . . . . .	146
6.4	Photocurrent measurements versus concentration of (a) nitrates using 225 nm optical excitation (b) DOC using 260 nm optical excitation (c) SSC using 465 nm optical excitation. The data point marked in red signifies the photocurrent response to the cuvette filled with deionised water. . . . .	147
6.5	Absorbance measurements of (left) DOC (right) Nitrates . . . . .	148
6.6	Effect of excitation wavelength on (a) contrast (b) goodness of fit values for water quality monitoring . . . . .	150

# List of Tables

2.1	Details of LEDs used, supplied from Thorlabs . . . . .	51
2.2	Slit width and corresponding wavelength resolutions using ML44 monochromator. . . . .	51
2.3	Range of NDfilters used to attenuate light from 50% to 0.01%. . . . .	53
3.1	Summary of the growth conditions for H series of HVPE grown samples	75
4.1	Comparison of photodetector performance parameters of several Ga <sub>2</sub> O <sub>3</sub> based devices . . . . .	99
4.2	Measured photocurrents and corresponding photoconductance transformations with 4 pairs of electrodes with a length $\approx 500 \mu\text{m}$ spaced $100\mu\text{m}$ apart. . . . .	110
5.1	Trap activation energies obtained from TSC measurement using the T4 approximation . . . . .	128

# Contents

<b>Abstract</b>	<b>iii</b>
<b>Acknowledgements</b>	<b>v</b>
<b>List Of Publications</b>	<b>vii</b>
<b>Acronyms/Abbreviations</b>	<b>ix</b>
<b>List of Figures</b>	<b>ix</b>
<b>List of Tables</b>	<b>xviii</b>
<b>1 Introduction</b>	<b>1</b>
1.1 Background . . . . .	1
1.2 Crystal Structure . . . . .	4
1.3 Electronic Properties . . . . .	6
1.3.1 Band Structure . . . . .	6
1.4 Defects in Ga <sub>2</sub> O <sub>3</sub> . . . . .	7
1.4.1 Doping . . . . .	11
1.5 Optical Properties . . . . .	13
1.5.1 Absorption properties . . . . .	13
1.5.2 Emission properties . . . . .	16
1.6 Photoconductivity . . . . .	19
1.7 Photodetectors . . . . .	22
1.7.1 Working Principal of Photodetectors . . . . .	23

## Contents

1.7.2	Fundamental Parameters of Photodetectors . . . . .	24
1.8	Sample Growth . . . . .	25
1.8.1	Halide Vapour Phase Epitaxy . . . . .	26
1.8.2	Plasma Enhanced Atomic Layer Deposition . . . . .	27
<b>2</b>	<b>Experimental Methods</b>	<b>28</b>
2.1	Luminescence . . . . .	28
2.1.1	Photoluminescence Spectroscopy . . . . .	28
2.1.2	Cathodoluminescence Spectroscopy . . . . .	32
2.1.3	System Response . . . . .	40
2.2	Photoconduction . . . . .	47
2.2.1	Setup construction considerations . . . . .	47
2.2.2	Wavelength-Dependent Photoconductivity . . . . .	55
2.2.3	Constant Photocurrent Method . . . . .	57
2.2.4	Power-Dependent Photoconductivity . . . . .	58
2.2.5	High Optical Power Measurements . . . . .	60
2.2.6	Thermally Stimulated Current spectroscopy . . . . .	62
2.2.7	Transient Photoconductivity . . . . .	63
2.2.8	Unit conversions for photoconductivity measurements . . . . .	67
2.3	UV-VIS . . . . .	68
2.3.1	Background . . . . .	68
2.3.2	Experimental set up . . . . .	69
2.3.3	The Transmission Spectrum . . . . .	71
<b>3</b>	<b>Hydrogen Related Luminescence in <math>\alpha</math>-Ga<sub>2</sub>O<sub>3</sub></b>	<b>73</b>
3.1	Background . . . . .	73
3.2	Experimental method . . . . .	74
3.2.1	Sample Details . . . . .	74
3.3	PL Results . . . . .	76
3.4	CL Results . . . . .	91
3.5	Conclusions and future work . . . . .	96

<b>4</b>	<b>Impact of Experimental Conditions on the Behavior of <math>\alpha</math>-Ga<sub>2</sub>O<sub>3</sub> Photodetectors</b>	<b>98</b>
4.1	Background . . . . .	98
4.2	Method . . . . .	100
4.3	Results and Discussion . . . . .	101
4.3.1	Effect of illumination intensity . . . . .	101
4.3.2	Effect of illumination wavelength . . . . .	105
4.3.3	Effect of applied voltage . . . . .	106
4.3.4	Photocurrent overshoot . . . . .	107
4.4	Proposing a new metric . . . . .	108
4.4.1	Photoconductance . . . . .	108
4.4.2	Comparing to the literature . . . . .	110
4.5	Conclusion . . . . .	111
<b>5</b>	<b>Advanced Photoconduction Techniques to Probe Defect states in <math>\alpha</math>-Ga<sub>2</sub>O<sub>3</sub> Thin Films</b>	<b>113</b>
5.1	Background . . . . .	113
5.2	Theoretical Background . . . . .	115
5.3	Method . . . . .	121
5.3.1	Constant Photocurrent Method . . . . .	121
5.3.2	Thermally Stimulated Current Spectroscopy . . . . .	124
5.4	Results . . . . .	126
5.4.1	TSC for above Fermi level measurements . . . . .	126
5.4.2	CPM for below Fermi level measurements . . . . .	132
5.5	Summary and Future work . . . . .	137
<b>6</b>	<b>A Novel Approach to Water Quality Monitoring using <math>\alpha</math>-Ga<sub>2</sub>O<sub>3</sub> photodetectors</b>	<b>139</b>
6.1	Background . . . . .	139
6.2	Methods . . . . .	141
6.3	Results and Discussion . . . . .	142

Contents

6.4	Summary and Future Work . . . . .	151
<b>7</b>	<b>Conclusions and Further Work</b>	<b>153</b>
7.1	Conclusions . . . . .	153
7.2	Further Work . . . . .	155

# Chapter 1

## Introduction

### 1.1 Background

It is difficult to imagine in 1833 when Michael Faraday first described the concept of a semiconductor [9], that even he could have foreseen the impact the material would have in shaping future generations. Fast forward 40 years and Smith discovered the phenomenon of photoconductivity when he observed a decrease in the resistance of Selenium when illuminated by light [10]. Semiconductors are a critical component in modern society with applications in power electronics and renewable energy systems in the form of solar cells. The first class of semiconductors was those such as Si, Ge, and GaAs and have had a significant impact on society. However, with a limited bandgap of 1.1, 0.74, and 1.52 eV [11] an advancement in the field was required to keep up with the growing demands of the technological revolution. The development of semiconductors with larger bandgaps leads to a shorter emission wavelength and a larger electric field breakdown value, and comes in the form of wide bandgap semiconductors, characterised by exhibiting a bandgap between 2.3-3.4 eV . Wide-bandgap materials such as GaN and SiC, with bandgaps of 3.3 and 3.4 eV respectively [12, 13], are the most mature in the field. GaN has attracted much attention for its applications in solid-state lighting through LEDs (Light Emitting Diodes), where the bandgap can be tuned by alloying with Indium to achieve emission over the visible wavelength region. On the other hand, SiC has been largely developed for its applications in high-power

## Chapter 1. Introduction

electronics for devices such as Schottky barrier diodes and metal oxide semiconductor field-effect transistors [14–16]. In terms of power electronics, the materials bandgap places a physical limitation on its application due to its relationship with so called electric field breakdown value [17, 18].

With applications in power electronics and UV detection systems,  $\text{Ga}_2\text{O}_3$  has attracted much attention because of its advantages over SiC, GaN, and Si devices currently being used. In a world with an ever-growing demand for power consumption, knowing how we manage that power within the grid is crucial. For example, the conversion of any generated power from DC to AC requires transformers with electrical circuits involving a series of transistors and diodes.

Ultrawide-bandgap semiconductors, classified by a bandgap  $> 3.4$  eV, offer an alternative material to the current materials, with the wider bandgap meaning the material can handle a higher voltage with lower losses. This key parameter is termed the electric field breakdown value, which describes the maximum electric field the material can withstand before the chemical bonds begin to break down. This breakdown field value is directly correlated with the material bandgap ( $E_g$ ) [1], shown below in Figure 1.1

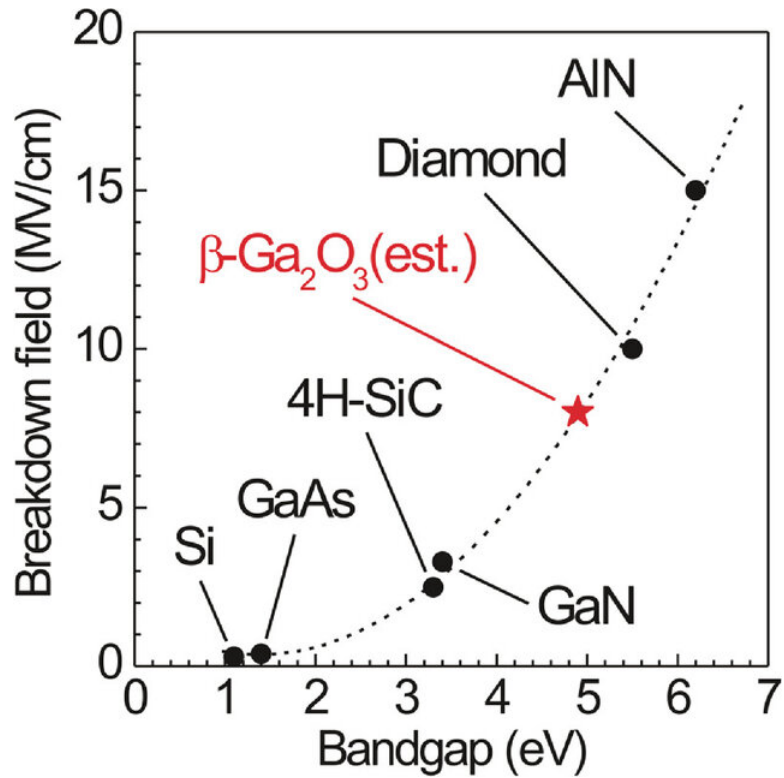


Figure 1.1: Relationship between bandgap and breakdown electric field value. Image taken from [1]

Therefore, Ga<sub>2</sub>O<sub>3</sub> with a band gap between 4.7-5.3 eV offers significant advantages over Si, SiC, and GaN with  $E_g$  values of 1.1, 3.3, and 3.4 eV, respectively [11, 19].

In addition to the substantial benefits in the power industry, the ultrawide bandgap of Ga<sub>2</sub>O<sub>3</sub> is ideally suited for photodetectors designed for UV detection. The ultraviolet (UV) spectrum spans wavelengths from 10 to 400 nm and is typically divided into four categories: UV-A (320–400 nm), UV-B (280–320 nm), UV-C (100–280 nm), and extreme UV (10–120 nm). The Earth's atmosphere effectively absorbs UV-C radiation, while extreme UV is absorbed primarily by molecular oxygen. As a result of this atmospheric absorption, UV light with wavelengths shorter than 280 nm does not reach the Earth's surface. This phenomenon is referred to as "solar blind," meaning that detectors sensitive to these wavelengths can operate without interference from solar radiation. Monitoring solar-blind radiation offers a wide range of environmental, civil, and military applications, such as flame detection [20], UV monitoring to track

ozone depletion or biochemical sensing [21,22]– in this, we will pay particular attention to UV photodetectors for water quality.

$\text{Ga}_2\text{O}_3$  is a polymorphic material that exists as five different phases, also referred to as polymorphs. Each of the 5 phases exhibits its own unique crystal structure depending on the temperature and pressure during the growth process. The five crystal structures are known as  $\alpha$ ,  $\beta$ ,  $\gamma$ ,  $\delta$ , and  $\epsilon$  which in turn influences the electronic properties of the material [23–26]. Much of the attention has been dedicated to the thermodynamic stable monoclinic  $\beta$ - $\text{Ga}_2\text{O}_3$ . However The rhombohedral  $\alpha$ -phase of  $\text{Ga}_2\text{O}_3$  exhibits many advantages over the other phases of  $\text{Ga}_2\text{O}_3$ . Notably, it exhibits the highest bandgap (*ca* 5.1–5.3 eV) among all phases [27–30], which should result in a higher breakdown electric field value of 9.5 MV/cm compared to 8 MV/cm for  $\beta$ - $\text{Ga}_2\text{O}_3$  [31,32] and offers interesting prospects for bandgap engineering through alloying with several isomorphic sesquioxides, such as  $\text{Al}_2\text{O}_3$  [33],  $\text{In}_2\text{O}_3$  [34],  $\text{Fe}_2\text{O}_3$  [35], or  $\text{Ti}_2\text{O}_3$  [36]. Thus far, most of the attention of  $\alpha$ - $\text{Ga}_2\text{O}_3$  research has been focused on material growth due to the thermodynamic metastability of the phase, leaving a gap in the knowledge of the properties of defects in the material.

To improve the efficiency and reliability of  $\text{Ga}_2\text{O}_3$  based devices, it is crucial to understand the influence of defects on the electrical and optical properties of the material. This thesis aims to generate new knowledge on the metastable  $\alpha$ - $\text{Ga}_2\text{O}_3$  that will aid the future development of the  $\alpha$ - $\text{Ga}_2\text{O}_3$  devices.

## 1.2 Crystal Structure

With the thermodynamically stable  $\beta$  attracting the most research, we compare the crystal structures of  $\alpha$  and  $\beta$ - $\text{Ga}_2\text{O}_3$  .

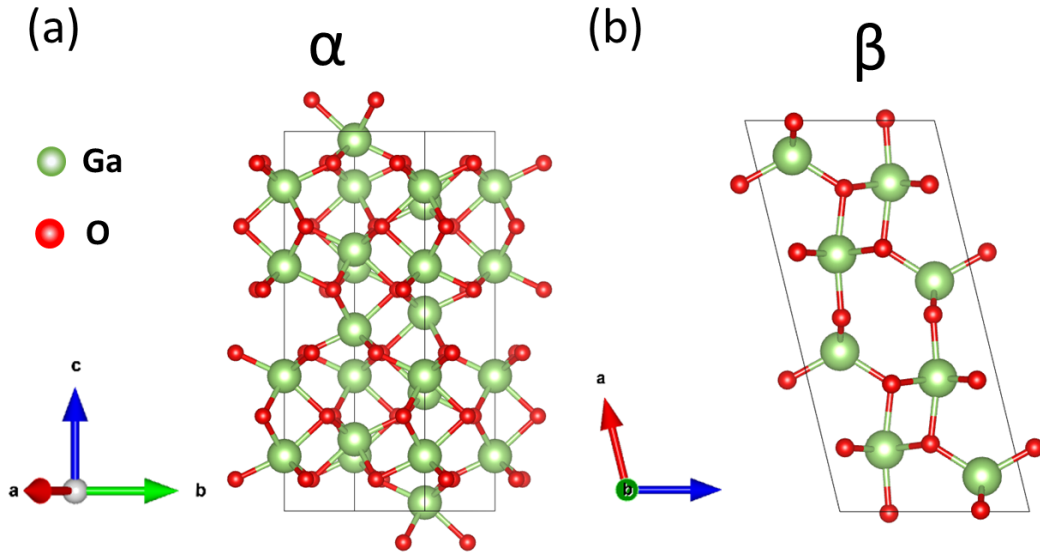


Figure 1.2: Crystal structure of (a)  $\alpha$ - $\text{Ga}_2\text{O}_3$  (b)  $\beta$ - $\text{Ga}_2\text{O}_3$  modelled using VESTA.

$\alpha$ - $\text{Ga}_2\text{O}_3$  (Figure 1.2(a)) exhibits a corundum crystal structure that belongs to the  $R\bar{3}c$  space group with lattice constants  $a = b = 4.983 \text{ \AA}$ ,  $c = 13.433 \text{ \AA}$  [24,37]. The unit cell consists of one O site and one Ga site. The O atoms are approximately hexagonal closed packed, and the Ga atoms occupy two-thirds of the octahedral sites. Each of the Ga atoms shares a face and three edges with three other octahedra. The primitive cell consists of 10 atoms and exhibits a volume between  $285$ - $305 \text{ \AA}^3$  [24, 38, 39].

Figure 1.2(b) illustrates the monoclinic crystal structure  $\beta$ - $\text{Ga}_2\text{O}_3$ , belonging to the  $C2/m$  space group with lattice constants of  $a = 12.2 \text{ \AA}$ ,  $b = 3 \text{ \AA}$ ,  $c = 58 \text{ \AA}$  [24,25,40]. Unlike  $\alpha$ - $\text{Ga}_2\text{O}_3$ ,  $\beta$ - $\text{Ga}_2\text{O}_3$  has three O and two distinct Ga sites, referred to as Ga(1) and Ga(2), which are coordinated tetrahedrally and octahedrally, respectively [41]. The O atoms are positioned at 3 sites, where O(1) and O(2) are three-fold coordinated while O(3) is four-fold coordinated [42].

## 1.3 Electronic Properties

### 1.3.1 Band Structure

The electronic properties of semiconductors can be understood through density functional theory (DFT) calculations of the band structure to reveal the energy-momentum (E-K) diagram [24, 43–46]. Figure 1.3 illustrates a comparison of the band structure of  $\alpha$  and  $\beta$   $\text{Ga}_2\text{O}_3$

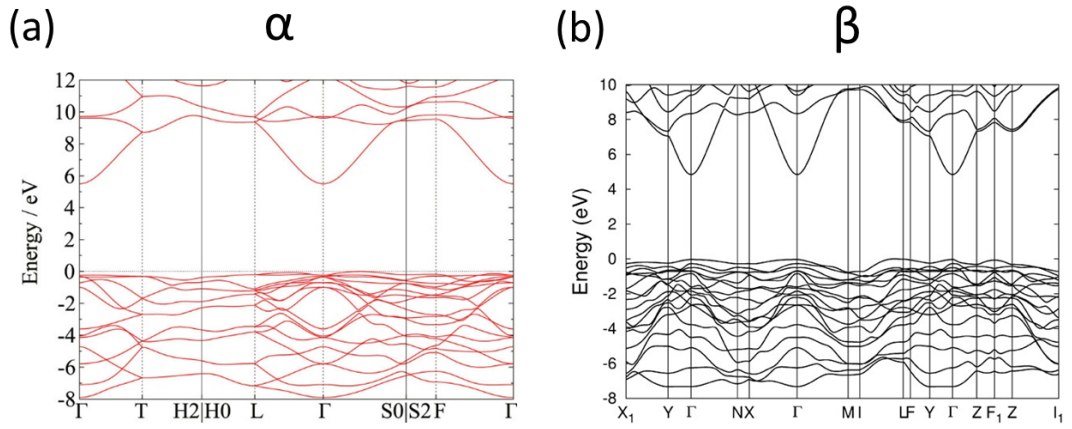


Figure 1.3: A comparison of the band structure of (a)  $\alpha$ -  $\text{Ga}_2\text{O}_3$  and (b)  $\beta$   $\text{Ga}_2\text{O}_3$  based on DFT hybrid functional calculations. [2, 3]

The calculated band structure of  $\alpha$ - $\text{Ga}_2\text{O}_3$  from DFT calculations is shown in Figure 1.3(a), with a bandgap of 5.73 eV and 5.49 eV occurring at the point  $\Gamma$  for the direct and indirect bandgaps, respectively [2]. The calculated bandgap in the literature has been shown to vary, with Sharma *et al.* reporting a direct and indirect bandgap of 5.29 eV and 5.24 eV [45]. Despite the variation in the calculated bandgaps, there is a general consensus that the conduction band minimum is situated at the  $\Gamma$  point in the k-space diagrams, indicated in Figure 1.3.

The conduction band is mainly comprised of hybridised Ga 4s orbitals, where the shape of the conduction band will determine the effective mass of the electrons with

reports in the literature suggesting an effective electron mass of *ca.* 0.26-0.30 $m_0$  [47,48] with an electron mobility ( $\mu_n$ ) of around 220  $\text{cm}^2\text{V}^{-1}\text{cm}^{-1}$  at room-temperature.

The valence band consists mainly of O 2p orbitals [47,48] with minor contributions from the Ga 3d and O 2s orbitals that make up the lower regions of the valence band. Like other wide-bandgap oxides, the flat nature of the valence band leads to small dispersion amongst the band, resulting in large hole effective mass, indicating low hole mobility [49]. This feature of low hole mobility is critical for the analysis used in Chapter 5. The holes with a large effective mass become self-trapped because of large electron-phonon coupling, and the hole induces a local distortion in the lattice, forming a self-trapped hole (STH). The rearrangement of the atoms in the lattice induces an electrostatic potential that traps the holes [50]. Theoretical studies by Varley *et al.* show that these holes become trapped at O 2p orbitals [42].

To compare with  $\alpha\text{-Ga}_2\text{O}_3$ , the band structure of  $\beta\text{-Ga}_2\text{O}_3$  is shown in Figure 1.3(b). DFT calculations show that the electronic structure of the phases shares the characteristic of a relatively flat valence band and conduction band minimum situated at the  $\Gamma$  point in the k-space diagram. The dispersion in the valence band again results in the STH formation in  $\beta\text{-Ga}_2\text{O}_3$ . DFT calculations theoretically predict a bandgap of  $\approx 4.8$  eV, with a 50 meV separation of the direct and indirect bands.

## 1.4 Defects in $\text{Ga}_2\text{O}_3$

Defects refer to imperfections in a crystal lattice, where these defects introduce additional energy states into the material's bandgap. Point defects refer to localised atomic-scale imperfections in the lattice, for example atoms not being at their designated lattice site. Point defects will significantly impact the electrical and optical properties of the material, potentially acting as scattering centres and reducing electron mobility in the material [51].

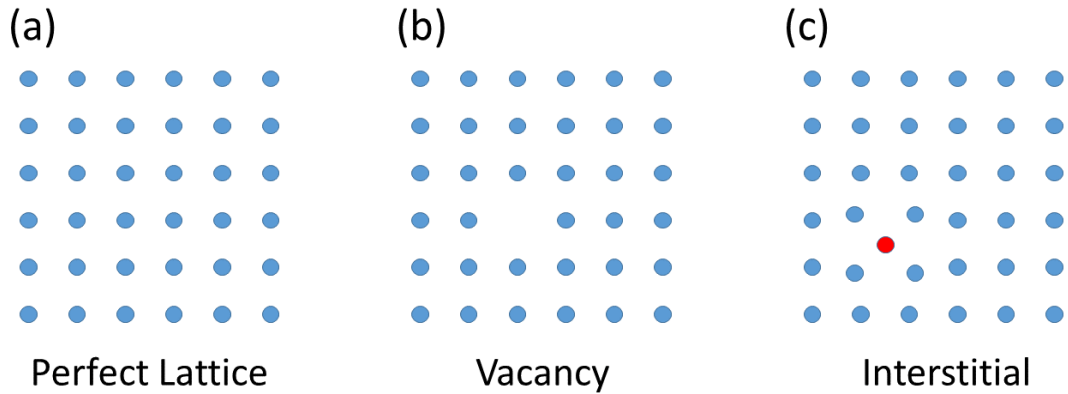


Figure 1.4: Schematic representation of a distribution of atoms in a lattice. (a) perfect lattice. (b) Lattice containing a vacancy. (c) Lattice containing an interstitial.

In an ideal crystal lattice, the atoms are positioned in a perfectly periodic arrangement. However, in realistic materials, there is always some disruption in this periodic order, leading to imperfections known as defects. One such defect pertinent to this study is the vacancy. A vacancy occurs when an atom is missing from its lattice site. In the context of  $\text{Ga}_2\text{O}_3$ , this refers to a Ga vacancy ( $V_{\text{Ga}}$ ) and an O vacancy ( $V_{\text{O}}$ ). Figure 1.4(b) schematically represents this type of defect. Another type of defect involves an atom occupying a position between lattice sites, termed an interstitial highlighted in Figure 1.4 (c). In the  $\text{Ga}_2\text{O}_3$  crystal, the interstitial can be in the form of a Ga interstitial ( $\text{Ga}_i$ ) or an O interstitial ( $\text{O}_i$ ).

The influence of defects on the electronic properties of semiconductors is often examined through computational modelling utilising DFT, hybrid functionals, and first-principles methods. A key aspect of such modelling is the defect formation energy, which measures the energy required for introducing a defect into the crystal lattice. Different defects exhibit distinct formation energies that are heavily influenced by the Fermi level within the material.

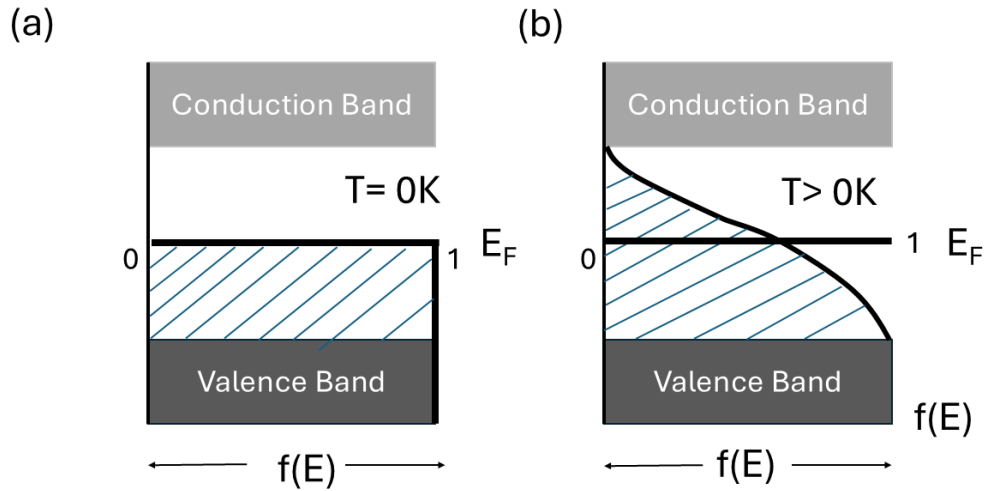


Figure 1.5: Representation of the Fermi level at (a)  $T = 0\text{ K}$ . (b)  $T > 0\text{ K}$ . The dashed region represents the probability of finding an electron. At  $T = 0$  the probability of finding an electron below the Fermi level is 1, whereas above the Fermi level the probability is 0. At elevated temperatures, there is some probability of finding the electron above the Fermi level

The Fermi level is a statistical description of electron occupancy from Fermi-Dirac statistics and defines a level in the bandgap where electrons are confined to. At  $0\text{ K}$  in an undoped semiconductor, the Fermi level lies at mid bandgap level where no electrons are allowed above the Fermi level, shown in (a) on Figure 1.5. Here we see the electron occupancy, represented by the dashed region. At elevated temperatures, the Fermi Dirac distribution broadens and the probability of finding an electron above the Fermi level is non zero, with the magnitude depending on the temperature.

### Oxygen Vacancies

$V_{\text{O}}$  corresponds to a missing O atom from the crystal lattice. The defect formation energy as a function of the position of the Fermi level is shown in Figure 1.6, where the defect formation energy is shown when the sample is under O- or Ga-rich conditions. The growth process or annealing condition will dictate the O-rich or Ga-rich conditions, where Ga-rich refers to a sample grown under vacuum, H, or exposed to Ga where the

O content is low. Here  $E_F = 0$  eV corresponds to a Fermi level positioned at the valence band maximum. Until now, most computational defect studies have focused on  $\beta$ - $\text{Ga}_2\text{O}_3$  [44, 52]. Jewel *et al.* gave the first insight into a comparison of the defect formation energies in  $\alpha$ - $\text{Ga}_2\text{O}_3$ .

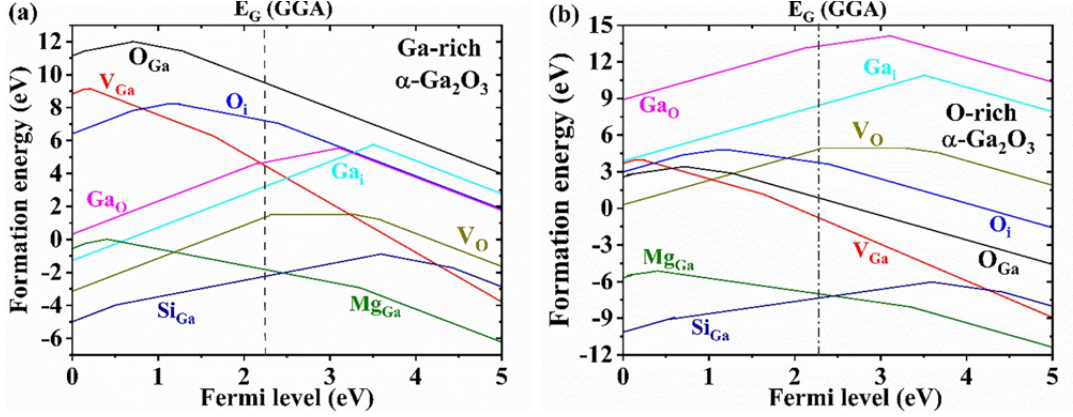


Figure 1.6: Formation energy of various defects in  $\alpha$ - $\text{Ga}_2\text{O}_3$  in (left) Ga-rich and (right) O-rich conditions using a Generalised Gradient Approximation. Image taken from [4]

Figure 1.6 shows that  $V_O$  has a lower formation energy under Ga-rich conditions compared to O-rich conditions, indicating that the concentration of  $V_O$  will be (expectedly) higher in O-poor environments. Furthermore, the transition level, indicated by the inflection point in the formation energy diagram, is located around 1 eV below the conduction band minimum, classifying  $V_O$  as a deep level donor. This finding aligns with the theoretical study by Varley *et al.* on  $\beta$ - $\text{Ga}_2\text{O}_3$  [41].

### Gallium Vacancies

Focusing on  $V_{\text{Ga}}$ , we observe that the transition levels appear in the lower half of the bandgap, suggesting that  $V_{\text{Ga}}$  serves as an acceptor defect in the material, independent of growth conditions. As shown in Figure 1.6,  $V_{\text{Ga}}$  is more energetically favourable under O-rich conditions compared to O-poor conditions, and it remains the predominant defect regardless of the position of the Fermi level under O-rich conditions. The acceptor nature of  $V_{\text{Ga}}$  is observed between  $\alpha$ ,  $\beta$ , and  $\kappa$  phases of the  $\text{Ga}_2\text{O}_3$  family [5, 53, 54], with variations of the formation energy resulting from different computational ap-

proaches. However, in the first instance, the structure of the defects is shared between all polymorphs. Therefore, it seems acceptable to use the literature of  $\beta$ -Ga<sub>2</sub>O<sub>3</sub> to explore some of the more exotic defects in the material.

### “Exotic” defects

When the atom is removed from its lattice site to create a vacancy, the removed atom can become mobile and migrate through the crystal, which in turn is a different type of defect known as an interstitial. First, consider the host atom of O, we can see from Figure 1.6 that O<sub>i</sub> acts as an acceptor defects in Ga<sub>2</sub>O<sub>3</sub> and the formation energy is reduced as the Fermi level is moved towards the conduction band minimum. In  $\beta$ -Ga<sub>2</sub>O<sub>3</sub>, Ingebrigsten *et al* showed that O<sub>i</sub> exhibits a low migration barrier and therefore is highly mobile, leading to interactions with other defects [55]. The interaction between defects will be expanded upon later in this section. Given the formation energy, Ga<sub>i</sub> acts as a deep level donor and exhibits low formation energies in Ga-rich conditions. Due to the low atomic weight of Ga, the low mobility and low migration [56] lends itself to the generation of an interesting type of defect in which Ga<sub>i</sub> migrates and resides at an interstitial site and becomes complexed with the V<sub>Ga</sub> denoted as V<sub>Ga</sub>-Ga<sub>i</sub>. These split type vacancies have been shown in the  $\beta$ -Ga<sub>2</sub>O<sub>3</sub> literature to be more energetically favourable to form relative to isolated V<sub>Ga</sub>, due to low energy barriers to formation [54, 55].

#### 1.4.1 Doping

Additional energy levels are created within the bandgap due to foreign atoms added to the lattice where the atom can act as a donor by adding additional electrons to the conduction band, or as an acceptor where the added atom can take an electron from the valence band without generating electrons in the conduction band [57]. The donor levels are between the conduction band and the Fermi level, and the acceptor levels are between the valence band and the Fermi level. The donor and acceptor levels are typically subcategorised into shallow levels, which are close to the edge of the band such that ionisation of the atoms can occur by thermal effects, or deep levels, categorised

as being further away from the bands [58]. The occurrence of STH has a detrimental effect on shallow acceptor doping in  $\alpha$ -Ga<sub>2</sub>O<sub>3</sub>, where the holes generated by acceptors become trapped at the STH site with poor mobilities theoretically predicted to be around  $10^{-6}\text{cm}^2\text{V}^{-1}\text{s}^{-1}$  [59]. Deep acceptor levels typically have intrinsic origins of  $V_{\text{Ga}}$ ,  $V_{\text{Ga}} - n\text{H}$  complexes, and  $V_{\text{O}}-V_{\text{Ga}}$  split vacancies [60–62].

Shallow donor levels are almost exclusively related to dopant atoms such as Sn [63], Silicon (Si) [64], Germanium (Ge) [31], and Hydrogen (H) [42]. Islam *et al.* also suggested that  $V_{\text{Ga}}-4\text{H}$  can serve as a shallow donor level [65]. Deep level donors are encompassed by a host of intrinsic and extrinsic impurities.

### H in Ga<sub>2</sub>O<sub>3</sub>

An important chapter of this thesis explores the impact of H on the emission characteristics of Ga<sub>2</sub>O<sub>3</sub>. It is necessary to discuss how H behaves within this material. Although H is a common but hard to detect impurity in Ga<sub>2</sub>O<sub>3</sub>, few studies have indicated that it can significantly influence the properties of the material, such as regulating n- and p-type conductivity in  $\beta$ -Ga<sub>2</sub>O<sub>3</sub> [41], and negatively affecting the photocurrent [66].

H is predicted to act as a shallow donor, occupying interstitial ( $\text{H}_i$ ) or substitutional sites ( $\text{H}_\text{O}$ ), and the low formation energy in both configurations suggests that it will be easily incorporated into the crystal lattice [54, 67]. Furthermore, the low migration barrier means that we can expect H to diffuse in the lattice and interact with other defects such as  $V_{\text{Ga}}$ , where the vacancy has 6 dangling bonds [5] that can easily accept H and form  $V_{\text{Ga}}-n\text{H}$  complexes, where n is the number of H atoms in the complex [54]. The theory predicts that the formation of  $V_{\text{Ga}}-n\text{H}$  complexes in  $\beta$ -Ga<sub>2</sub>O<sub>3</sub> is indeed more energetically favourable than that of isolated  $V_{\text{Ga}}$  [5]. Recent computational studies by Varley *et al.* revealed the formation energy  $V_{\text{Ga}}-n\text{H}$  in  $\alpha$ -Ga<sub>2</sub>O<sub>3</sub>, revealing low formation energies particularly under O-rich conditions. Unlike the  $\beta$  phase, the study reveals that the complex can accommodate up to 5 H atoms. The formation energy diagram of  $V_{\text{Ga}}$  is shown below in Figure 1.7

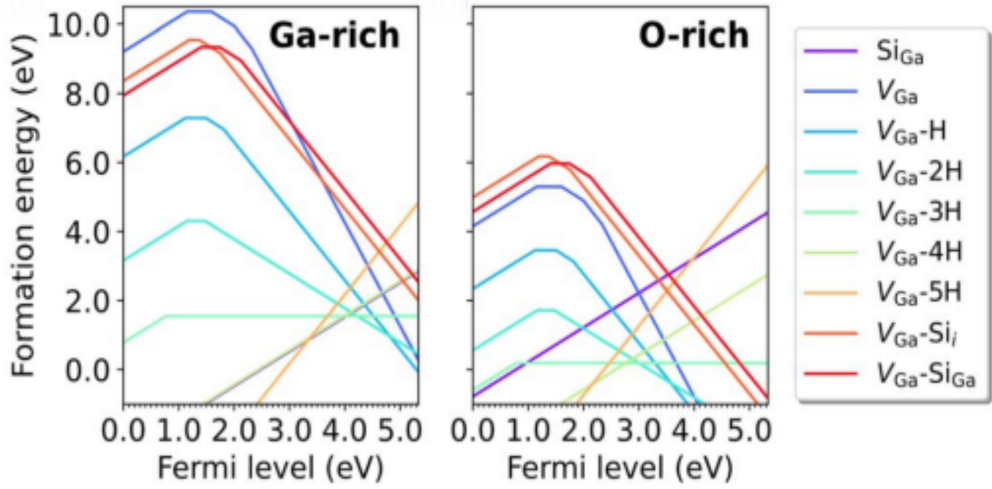


Figure 1.7: Formation energy H decorated  $V_{\text{Ga}}$  in  $\alpha\text{-Ga}_2\text{O}_3$  in (left) Ga-rich, and (right) O-rich conditions. Image taken from [5]

The state of the art suggests that H in  $V_{\text{Ga-nH}}$  is strongly bound, so much so that work by Wei *et al.* theoretically predicted that temperatures in excess of 1000 K are required to dissociate the complex [67].

The influence of  $V_{\text{Ga-nH}}$  on the electrical properties of  $\beta\text{Ga}_2\text{O}_3$  has been studied by Islam *et al.* who demonstrated that by controlling the incorporation of H in the crystal, the conductivity of the material changed from n-type ( $V_{\text{Ga-4H}}$ ) to p-type ( $n=1, 2, 3$ ) [65]. From the computational study conducted by Okumura *et al.*,  $V_{\text{Ga-5H}}$  will also serve as a donor in  $\alpha\text{-Ga}_2\text{O}_3$  [5].

## 1.5 Optical Properties

### 1.5.1 Absorption properties

Given the ultrawide bandgap of  $\alpha\text{-Ga}_2\text{O}_3$ , the material is transparent down to the UV region of around 250 nm (*ca* 5 eV) [68–71]. UV-Vis spectrophotometry is the standard method for measuring the optical absorption in semiconductors where the absorption edge is clearly defined. A typical measurement of the absorption coefficient of  $\alpha\text{-Ga}_2\text{O}_3$  is shown in Figure 1.8.

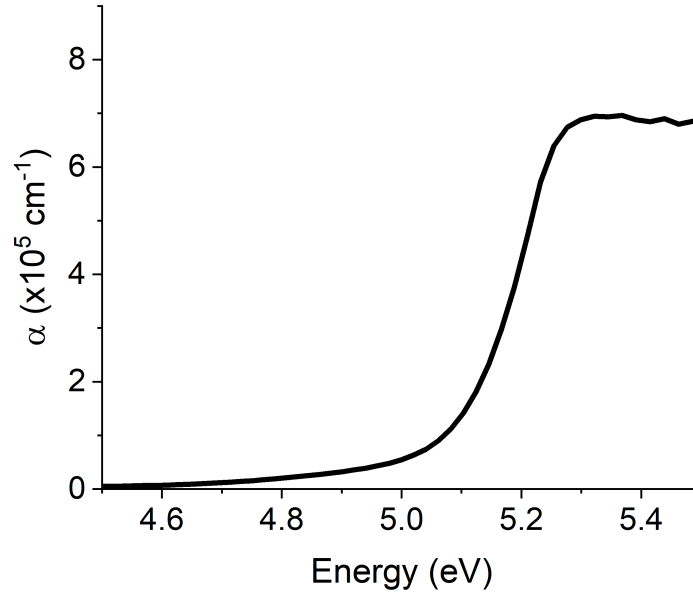


Figure 1.8: Optical Absorption measurements obtained from UV-Vis spectrophotometry of  $\alpha$ -Ga<sub>2</sub>O<sub>3</sub> showing the absorption coefficient versus energy

From measurements of the absorption coefficient, the optical bandgap can be estimated [72, 73], revealing a bandgap between 5.1 - 5.3 eV [27–30]. Although optical absorption measurements from UV-Vis is excellent for revealing the absorption properties at energy values close to the bandgap, the measurement technique loses its effectiveness at measuring absorption at sub-bandgap energies. The introduction of defects into the crystal will create a distribution of energetic states within the bandgap, at which the carrier may reside, acting as additional absorption pathways. Therefore, measuring changes in the absorption coefficient at sub-bandgap energies may indicate the defect energy levels within the bandgap.

The standard technique for sub-bandgap absorption measurements in semiconductors is photothermal deflection spectroscopy [74], where a sample is placed in a medium with a known refractive index. As the sample is illuminated with spectrally resolved light, the absorption of light by the semiconductor results in the heating of the semiconductor, which in turn changes the refractive index of the medium, giving a measurement of the absorption coefficient of the semiconductor. Hao *et al.* [6] measured the

sub-bandgap absorption coefficient in  $\beta\text{-Ga}_2\text{O}_3$ , with spectrum shown in Figure 1.9.

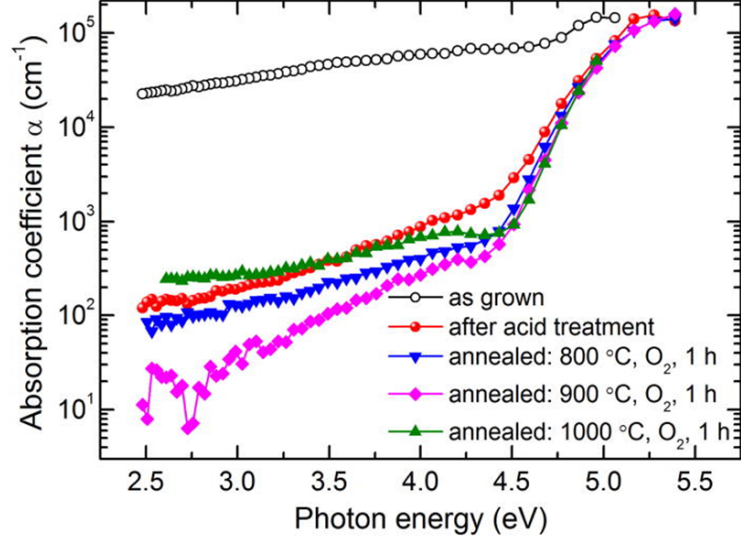


Figure 1.9: Optical Absorption measurements obtained from PDS of  $\beta\text{-Ga}_2\text{O}_3$  showing the absorption coefficient versus energy. Image taken from [6]

Here we see an extension of the measurable absorption coefficient down to around 2.5 eV, equating to around half of the bandgap energy whereas in optical transmission measurements the measured absorption coefficient becomes dominated by noise at 4.5 eV.

An alternative approach to measuring the absorption coefficient in the sub-bandgap range is the constant photocurrent method (CPM) [75]. This photoconductive technique involves continually adjusting the photon flux incident on the material to maintain a constant photocurrent across the energy spectrum. Under such conditions, the reciprocal of the photon flux is proportional to the absorption coefficient [76]. The value of the absorption coefficient is determined by the sum of all the allowed transitions. Therefore, there is a relationship between the absorption coefficient and the density of states (DOS) of the material. Therefore, CPM can be used as a DOS spectroscopy technique to map states across the bandgap [77]. Thus far, CPM has never been applied to wide-bandgap materials, and in Chapter 4 we present a revival of the technique with

a novel approach to tailor the experimental setup to wide-bandgap materials.

### 1.5.2 Emission properties

Luminescence describes the process in which light is emitted from a material following excitation, either from photons, described as photoluminescence (PL), or by electrons termed cathodoluminescence (CL). Upon excitation, for example, from photons with  $h\nu > E_g$ , electron-hole pairs are generated. A thermalisation process will then occur where the electrons and holes are transferred to the conduction band minimum and valence band maximum, where they will be able to recombine. When in the excited state, there are several recombination pathways where the recombination of the electron and hole results in the emission of a photon (radiative recombination) or generation of phonons (non-radiative recombination), illustrated in Figure 1.10. Studying the resulting emission spectrum can reveal a host of information about the internal mechanisms of the material. Typically,  $\beta$ -Ga<sub>2</sub>O<sub>3</sub> exhibits luminescence in UV spectral regions (3.2 to 3.6 eV) [78–80], blue (2.8 to 3.0 eV) [78,81], and green (2.5 eV) [82] spectral regions, with luminescence in red (1.7 to 1.9 eV) also reported [83–85].

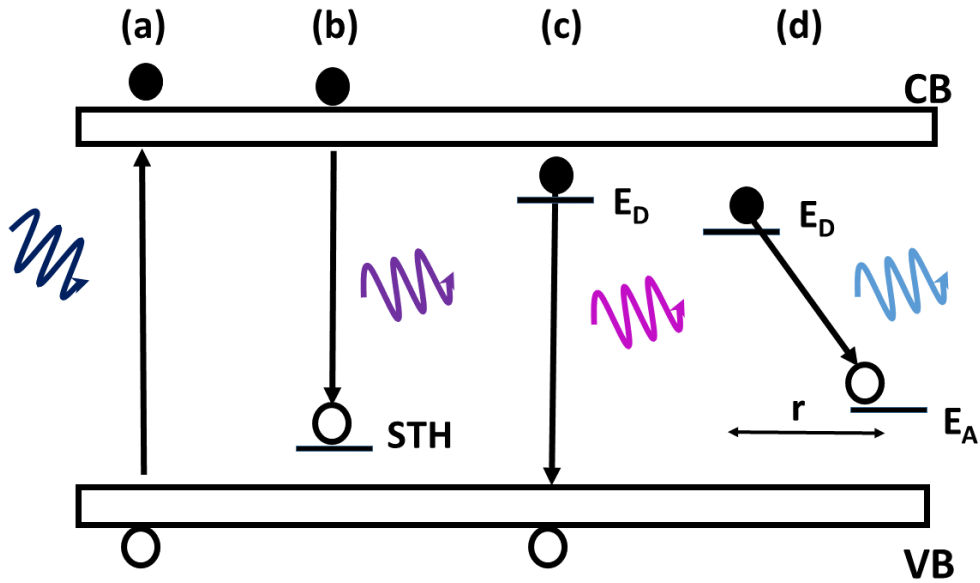


Figure 1.10: Schematic of luminescence processes in  $\text{Ga}_2\text{O}_3$ : (a) Band to band recombination where the energy of the emitted photon will equal to the bandgap energy, (b) recombination of electron and STH at trapped site, (c) recombination of electron from a donor site and hole in the valence band (d) donor acceptor pair recombination.

In a perfect semiconductor with no energy states within the bandgap, excitation with energy greater than the bandgap, the only recombination pathway that exists is between the valence band and the conduction band, where the recombination would result in the emission of a photon with energy equal to the bandgap. This process is referred to as band-to-band recombination, as represented by process (a) in Figure 1.10. The general consensus within the  $\text{Ga}_2\text{O}_3$  community is that band to band recombination in  $\text{Ga}_2\text{O}_3$  is prohibited due to the presence of STHs. When the holes become trapped, emission energies below the bandgap value are observed [42].

### Emission from STH

When the holes become trapped, emission energies below the bandgap value are observed [42]. The optical signatures of STH luminescence are broad bands with a large characteristic Stokes shift [42, 86]. Illustrated by the configuration coordinate diagram recreated from the work of Varley *et al.* [42].

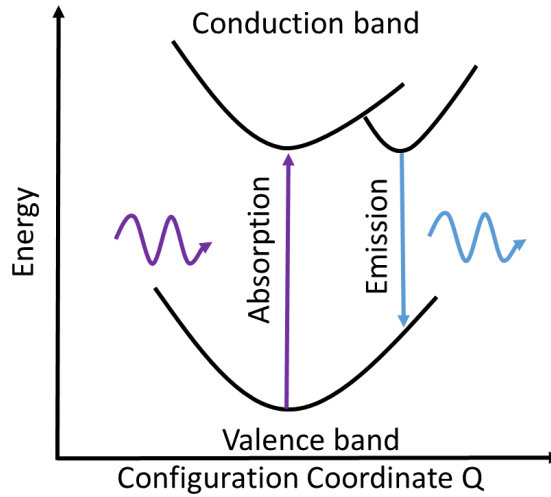


Figure 1.11: Configuration coordinate diagram illustrating the absorption and emission process in  $\text{Ga}_2\text{O}_3$ . Excitation with photons with energy greater than the bandgap creates electron-hole pairs. Due to lattice distortion from the STH, the emission energy is lowered reflected in a large Stokes shift in the emission

Varley *et al.* modelled the STH recombination based on the configuration diagram shown in Figure 1.11 using the Heyd-Scuseria-Ernzerof hybrid functional [42, 87]. The self-trapping effect on the luminescence is represented by process (b) in Figure 1.10. Two UV lines have been assigned intrinsic origins, and experimental and theoretical calculations attribute the luminescence to the recombination of free electrons with STH [42, 79]. However, Onuma *et al.* suggested that the UV luminescence was composed of not only the recombination of STH and free electrons but also had a contribution from donor acceptor pair (DAP) recombination involving Si as a shallow donor with potential acceptors being  $V_{\text{Ga}}$ ,  $\text{Mg}_{\text{Ga}}$ ,  $\text{N}_{\text{O}}$ , and O-Ga split vacancies ( $V_{\text{O}}-V_{\text{Ga}}$ ) [78].

### Defect related emission

The addition of donor and acceptor levels results in recombination pathways within the bandgap where the electron at a donor level can recombine with a hole in the valence band, shown by the process (c) in Figure 1.10. Rather than recombine with a hole in the valence band, the electron can recombine with a hole at the acceptor level within the bandgap, where this well-established process is termed DAP recombination. The energy of the photon emitted after a DAP recombination is given by [88–90]

$$hv(DAP) = E_g - (E_A + E_D) + \frac{e^2}{4\pi\epsilon r} \quad (1.1)$$

where  $E_g$  is the bandgap energy,  $E_A$  is the acceptor energy level,  $E_D$  is the donor energy level,  $\epsilon$  is the dielectric constant and  $r$  is the separation distance. DAP recombination is typically associated with the blue, green and red spectral regions in  $\text{Ga}_2\text{O}_3$  [78, 80, 81, 83, 91–95].

The blue luminescence is typically associated with DAP recombination involving a host of intrinsic defects with  $V_O$ ,  $V_{\text{Ga}}$ ,  $V_O-V_{\text{Ga}}$ ,  $\text{Mg}_{\text{Ga}}$ ,  $\text{Ga}_i$  suggested as possible donors and acceptors. The green luminescence line has been less studied and so far the attribution is to DAP recombination involving a range of defects including  $\text{O}_i$  and  $V_{\text{Ga}}$  [80, 83] Finally, red luminescence has been linked to H or N impurities [84, 96] as well as reported sharp red luminescence lines attributed to the incorporation of  $\text{Cr}^{3+}$  ions [85].

Therefore, studying the luminescence spectra can reveal important information about the electronic structure of the material. In Chapter 2, we give a description of the experimental setup used for both systems.

## 1.6 Photoconductivity

Photoconductivity in semiconductors refers to the increase in conductivity when a sample is illuminated with light, described by equation 1.2

$$\Delta\sigma = q(\Delta n\mu_n + \Delta p\mu_p) \quad (1.2)$$

where  $q$  is the charge of the carrier,  $\Delta n$  ( $\Delta p$ ) is the excess free electron density (hole) generated by incident photons, and  $\mu_n$  ( $\mu_p$ ) is the mobility of electrons (hole) [97].

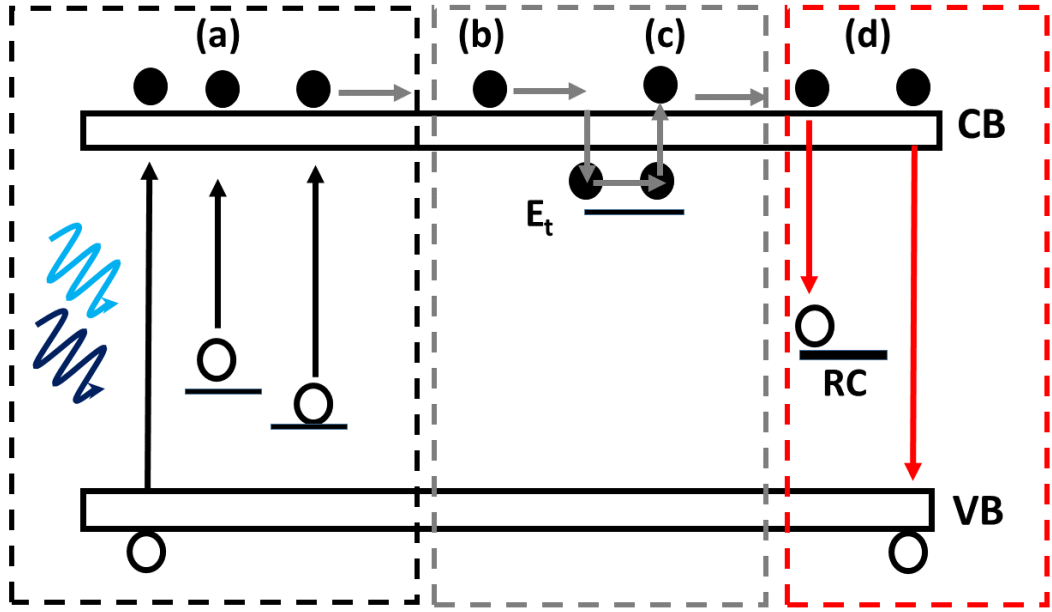


Figure 1.12: Illustration of the various processes after a material being illuminated by above-bandgap light. (a) Light absorption process where an electron can be excited from the valence band, or from filled defect states into the conduction band directly. (b) Carrier transport where the electron moves in the conduction band, generating the measured photocurrent. (c) Carrier trapping in which the electrons are intermittently trapped before being re-excited back into the conduction band. (d) Carrier recombination where the electron will recombine with a hole at a recombination center, or the valence band.

Figure 1.12 illustrates the fundamental processes that govern the photoconduction cycle are (a) optical absorption, (b-c) carrier transport, and (d) carrier recombination. Generally speaking, electrons are excited from the valence band to the conduction band when illuminated with light greater than the bandgap. Here, we will refer to this as intrinsic optical absorption. Due to defects in the material, additional energy levels are created within the bandgap. Extensive studies of deep level transient spectroscopy (DLTS) and optical deep level transient spectroscopy (ODLTS) have shown a vast distribution of sub-bandgap energies in  $\alpha$ - $\text{Ga}_2\text{O}_3$ , indicating extrinsic optical absorption will contribute to the measured conductivity [62, 98, 99]. The intrinsic and extrinsic optical absorption process is represented by (a) in Figure 1.12 where the absorption process is classified quantitatively by the absorption coefficient. Later in this work, we will show how we measured the absorption coefficient at sub-bandgap energy levels by

adapting the constant photocurrent technique for its first application to wide-bandgap semiconductors.

In the conduction band, two transport mechanisms allow the electrons to move: diffusion and drift currents. The drift currents describe the movement of carriers in the mobility bands under the influence of an electric field where the equation of motion ( $F = m^*e a = -eE$ ) where  $e$  is the elementary charge,  $a$  is the acceleration, and  $E$  is the electric field. Here we see that if the electric field is constant, we would expect the velocity to increase linearly with time. However, this is never the case, where the defects discussed earlier in chapter 2 become charged and can act as scattering centres for the electrons, which will alter the velocity and, thus, the magnitude of the current. The second mechanism for current generation in semiconductors is the diffusion current, which describes the movement of charge caused by a charge density gradient. This process is mediated by the diffusion coefficient given by  $J_{nx} |_{diff} = eD_n \frac{dn}{dx}$ , where  $D_n$  is the diffusion coefficient of electrons. In this work, we assume that the drift component dominates the transport process as we have unintentionally doped samples (UID). Therefore, the density gradient will be relatively small. In Chapters 4,5, and 6 an electric field value of *ca.* 1000 V/cm was applied to the samples. Therefore, the drift mechanism is proposed to dominate. This process is shown in (b) of Figure 1.12.

Without defects in the material, the electron would be free to move in the conduction band before recombining, deemed the free carrier lifetime  $\tau$ . The additional energy levels brought by defects can act as traps, where the defect can capture an electron before being re-excited by the conduction band. This process is known as carrier trapping and is illustrated in Figure 1.12 (c). The trapping process will have three significant effects on semiconductor parameters. The rise and decay times are longer due to the additional time-dependent processes associated with the filling and emptying of the traps [100,101]. A second implication of the traps is the effect on drift mobility. In the absence of traps, carriers are free to move and the drift mobility is the same as the conductivity mobility. In the presence of traps, the mobility of the carrier will be affected by the average time to escape the trap [100,102].

The final aspect to consider in the photoconduction process is the recombination

process (Figure 1.12(d)). The recombination process acts as a photoconduction loss mechanism. When light excitation is stopped, the photocurrent will decay until it reaches the dark current values. In the absence of traps, the decay will follow a simple exponential

$$I(t) = I(0)\exp(-t/\tau) \quad (1.3)$$

where  $\tau$  is the lifetime,  $I(0)$  is the steady-state photocurrent, and  $t$  is the time. In the presence of traps, the photocurrent decay will no longer be in the form of a simple exponential due to multiple retrapping prior to recombination, increasing  $\tau$ .

In the previous section, we looked at how studying the luminescence spectrum will reveal information about the radiative recombination mechanisms at play from which we can deduce information regarding the electronic structure of the material. The same reasoning can be applied to studying the photoconduction process, in which the conductivity varies with photon energy, illumination intensity, temperature, and time, which can reveal detailed information regarding several key material parameters such as the absorption coefficient [103, 104], carrier mobility [105], Fermi level position via dark current measurements [106] defect distributions.

## 1.7 Photodetectors

As previously mentioned, the wide-bandgap of  $\alpha$ -Ga<sub>2</sub>O<sub>3</sub> makes this material well suited for solar-blind photodetector applications. In this section, we clarify the term “solar-blind” and explain the operation principles of a specific type of photodetector known as metal-semiconductor-metal detectors, which will be employed in Chapters 4, 5, and 6.

It is known that UV radiation ranges from approximately 10 nm to 400 nm, and the UV spectrum is divided into several regions, including UV-A (400-320 nm), UV-B (320-280 nm), UV-C (280-200 nm), and vacuum UV (200-10 nm). Given the bandgap of 5.1-5.3 eV (230-245 nm),  $\alpha$ -Ga<sub>2</sub>O<sub>3</sub> is not affected by solar radiation due to the strong absorption of vacuum UV by the Earth’s atmosphere and the sub-bandgap nature of

UV-A and UV-B. Hence, the material is considered to be “solar-blind”. However, as will be illustrated in Chapters 4, 5, and 6, the term ‘solar-blind’ should be taken cautiously, as defect-induced sub-bandgap energy levels promotes absorption at sub-bandgap energies, i.e. in the UB-B, UV-A or even visible region.

### 1.7.1 Working Principal of Photodetectors

Photodetectors come in various types, including photoconductors, p-n diodes [107], and schottky photodiodes [108].

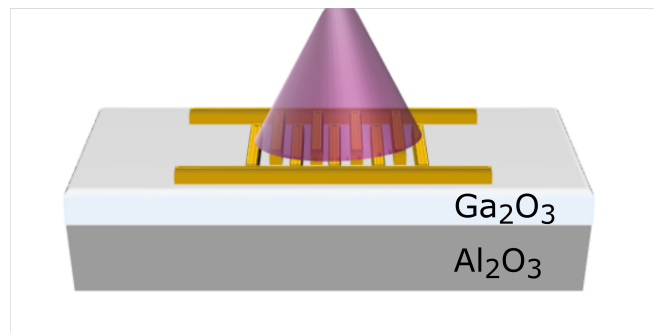


Figure 1.13: Schematic of metal-semiconductor-metal photodetector with contacts in interdigitated configuration

Figure 1.13 illustrates the design of a typical metal-semiconductor-metal photodetector used in this study. The primary objective of a photodetector is to absorb the energy from the incident light and transform it into an electric current. Incident light generates free carriers in the material, specifically electrons in the case of Ga<sub>2</sub>O<sub>3</sub> due to the self-trapping nature of the holes, and the excited electrons are transported through the material conduction band and collected through electrical contacts.

Photodetectors come in various types, including photoconductors, p-n diodes [107], and schottky photodiodes [108]. The device used in this research features a coplanar structure, as described previously. In the photodetector literature, it is common to find electrodes arranged as interdigitated fingers, enhancing the effective electric field applied to the material at lower operating voltages. The metal choice for the electrodes predominantly determines whether the device exhibits ohmic or rectifying behaviour [109,110]. According to the schottky-mott model, ohmic contact forms at the metal-

semiconductor interface if the electron affinity of the material surpasses the metal work function, and vice versa [57]. However, in Ga<sub>2</sub>O<sub>3</sub>, interfacial reactions at the metal-semiconductor surface add complexity to the process. This work used Ti contacts coated with Au as ohmic contacts. Massabuau *et al.* studied electrical contacts based on annealing temperatures and discovered that Ti/Au forms an ohmic contact on  $\alpha$ -Ga<sub>2</sub>O<sub>3</sub> regardless of the annealing temperature. However, an annealing temperature of 450 °C yielded the highest material conductivity due to the formation of a thin Ti<sub>x</sub>O<sub>y</sub> layer [111].

### 1.7.2 Fundamental Parameters of Photodetectors

The performance of photodetectors is often characterised by several parameters, here we will define performance factors used for device characterisation [112].

1. Responsivity: Defined as the ratio of the generated photocurrent per incident optical power, measured in AW<sup>-1</sup> determined by

$$R = \frac{I_{ph} - I_d}{P} \quad (1.4)$$

where  $I_{ph}$  is the photocurrent,  $I_d$  is the dark current and P is the incident optical power.

2. Response Time: The response time describes the change in conductivity of the material due to the changes in illumination conditions. This is usually measured as a rise time and a fall time. The rise time accounts for the time taken to rise from dark current values to a steady-state photocurrent, where the rise time can be taken as the time taken to rise from 10 % to 90% of the steady-state photocurrent value and vice versa for the fall time. Alternatively, a fitting function can be used to model the photocurrent rise and decay time, where in the Ga<sub>2</sub>O<sub>3</sub> the bi-exponential fit appears to be commonly used [69, 113, 114]. In chapter 2, we will review different models for fitting the photocurrent transients and argue on their validity.

3. Detectivity: A measurement of how well a weak signal can be detected relative to the noise measurements. This value is given by

$$D = \sqrt{\frac{A}{2eI_{dark}}} R \quad (1.5)$$

where  $A$  is the illuminated area,  $e$  is the charge of an electron,  $I_{dark}$  is the dark current and  $R$  is the responsivity. In our measurements presented in Chapter 4, the illuminated area was fixed, and the dark current was held constant for power-dependent measurements. Therefore, a linear relationship is maintained between responsivity and detectivity. Thus, responsivity was used as a measurand for the work included in this thesis.

These parameters are often used in the literature to report on devices claiming “record high” responsivity [115] or “ultra-fast” response times [116]. However, in chapter 4 we nuance these claims and show that the experimental conditions have a huge influence on the responsivity and response times in the material, so pragmatism must be shown when comparing photodetectors across the field.

## 1.8 Sample Growth

The samples in this work were grown by external collaborators, and an introduction to the growth techniques will be detailed here. Specific growth conditions relevant to the work will be detailed in the relevant chapters.

### 1.8.1 Halide Vapour Phase Epitaxy

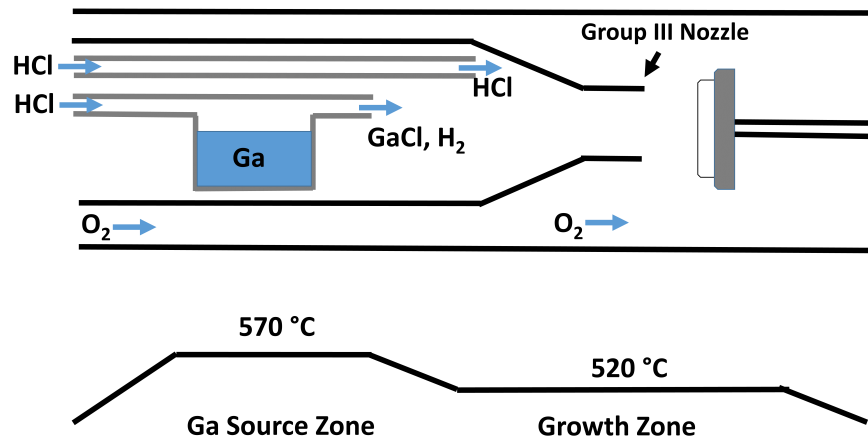


Figure 1.14: Schematic of HVPE growth process of  $\alpha\text{-Ga}_2\text{O}_3$ .

Halide Vapour Phase Epitaxy (HVPE) is a technique widely used in the semiconductor industry, characterised by its fast growth rate and superior ability to grow  $> \mu\text{m}$  thick epitaxial layers compared to other methods [117]. In this growth method,  $\text{O}_2$  and  $\text{GaCl}$  are used as the precursor.  $\text{HCl}$  gas is introduced into the chamber to generate a chemical reaction with  $\text{Ga}$ , resulting in a chemical reaction that produces  $\text{GaCl} + \text{H}_2$  gas in the  $\text{Ga}$  source zone. The  $\text{GaCl}$  gas is transported by the carrier gas to the lower temperature growth zone.  $\text{O}_2$  gas is injected into the growth zone, resulting in the deposition of a crystalline layer of  $\text{Ga}_2\text{O}_3$  onto the substrate [118].

## 1.8.2 Plasma Enhanced Atomic Layer Deposition

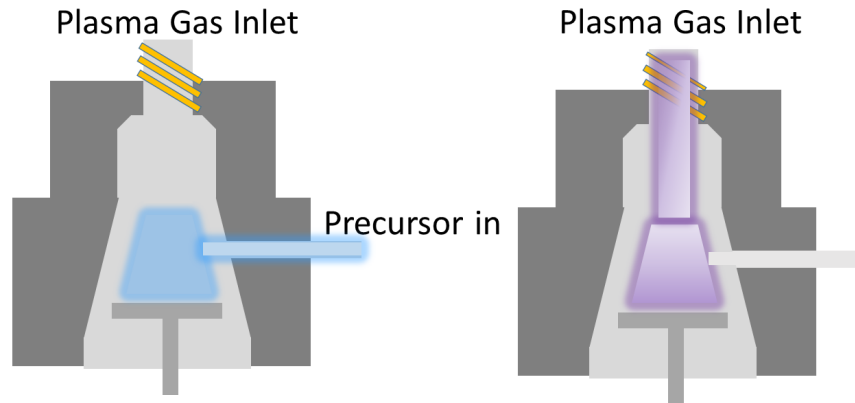


Figure 1.15: Schematic of PEALD growth process of  $\alpha$ -Ga<sub>2</sub>O<sub>3</sub> in 2 stages. Left shows the precursor stage with the precursor gas represented in blue. Right shows the plasma gas inlet, represented in purple.

Given the metastable nature of  $\alpha$ -Ga<sub>2</sub>O<sub>3</sub>, there was interest in growing the material at low-temperature. This was achieved by the work of Roberts *et al.* who successfully synthesised the material at 200 °C. The growth temperature had a significant impact on the different phases achieved [29].

The Plasma Enhanced Atomic Layer Deposition (PEALD) process involves introducing a Ga precursor gas (e.g. Triethylgallium (TEGa)) into the growth chamber. Following the precursor pulse, a purge gas, typically inert (e.g. Ar), is introduced to remove any unreacted elements from the precursor gas. The next step in the process is the addition of an O<sub>2</sub> plasma aspect of the traditional atomic layer deposition process. The process is completed with a further Ar purge. The cycle is repeated until the desired film thickness is achieved.

## Chapter 2

# Experimental Methods

### 2.1 Luminescence

#### 2.1.1 Photoluminescence Spectroscopy

PL corresponds to the emission of light from a material due illumination of light. A major advantage of PL compared over CL is the control of the excitation wavelength, meaning the user can carry out above-bandgap or below-bandgap measurements. In this work, a 224 nm (5.53 eV) Helium-Silver gas laser was used to provide above-bandgap excitation.

#### Penetration Depth

In the PL technique, the penetration depth of the photons is based on the chosen excitation wavelength. This process is generalised by the Beer-Lambert law given by equation 2.1.

$$\left(\frac{I}{I_0}\right) = \exp(-\alpha d) \quad (2.1)$$

where  $\alpha$  is the absorption coefficient and  $d$  is the depth,  $I_0$  is the light intensity at the surface of the material ( $d=0$ ), and  $I$  is the light intensity at a given depth of the material. Equation 2.1 illustrates that the absorbed light decays exponentially as a function of depth, where the rate of decay is governed by the absorption coefficient. In

practice, reflections from both the surface of the  $\text{Ga}_2\text{O}_3$  and the underlying substrate, as well as anisotropy of the crystal structure will lead to deviations of the transmitted light through the sample. The experimental approach to measuring the absorption coefficient will be expanded later in this work. When  $\hbar\omega > E_g$ , the absorption coefficient can be accurately determined by optical transmission measurements where we observe a value in the order of  $10^5\text{cm}^{-1}$  [29, 119]. From Equation 2.1 it is possible to estimate how deep the photons at a given energy can penetrate the material, also known as the penetration depth. The penetration depth can be estimated as the reciprocal of the absorption coefficient [120]

$$d(\alpha) = \frac{1}{\alpha} \quad (2.2)$$

Equation 2.2 expresses the depth in the material at which the intensity of light drops to  $1/e$  of the incident intensity at the surface. Therefore, for  $\alpha\text{-Ga}_2\text{O}_3$  excited by a 224 nm light source ( $\alpha \text{ ca } 10^5\text{cm}^{-1}$ ), the penetration depth will be *ca.* 100 nm. The penetration depth effect is an important consideration when studying thin films because of the possibility for photons to penetrate deep enough to interact with the underlying substrate, leading to an erroneous interpretation of the luminescence spectrum.

## Experimental Setup

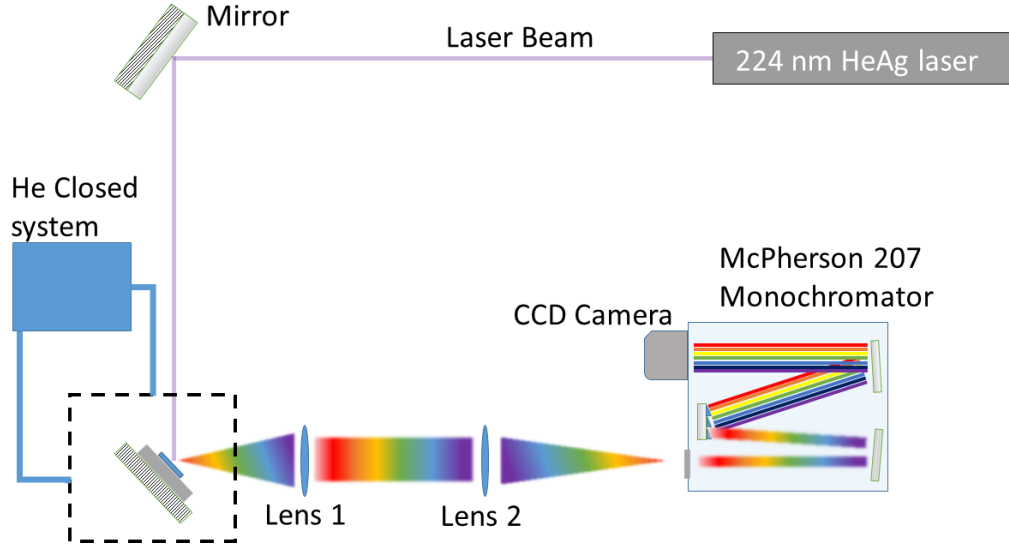


Figure 2.1: Schematic of PL set up for data acquired in Chapter 3. The 224 nm pulsed laser illuminates the sample where the emitted light is collimated and focused to the entrance slit of the monochromator. At the entrance slit, a 280 nm filter was used to reject laser lines from the emission spectrum. The diffraction grating resolves the emitted light and collected by the Andor DV-420-0E camera

*Excitation Source:* Here we used a 224 nm (5.53 eV) Helium-Silver pulsed laser to generate photons  $\hbar\omega > E_g$ .

*Cryogenic System:* The samples were enclosed in a closed-cycle Helium cryostat. The PL measurements were carried out under vacuum with the sample stage coupled with a heater and the cold finger of the cryostat to allow temperature-dependent measurements between 10 and 300 K.

*McPherson monochromator:* The light emitted from the sample was collected in a McPherson 207 monochromator consisting of two mirrors reflecting the light onto a diffraction grating consisting of 300 l/mm. External software controlled the grating position, allowing grating rotation to move the spectral window to higher or lower wavelengths.

*Charged Coupled Device:* A Charged Coupled Device (CCD) is a highly sensitive

camera, typically composed of Si detectors subdivided into an array of pixels to convert photons into electrons. The number of electrons collected at each pixel is directly proportional to the number of incident photons. Here, the diffraction grating enclosed within the McPherson 207 monochromator spectrally resolves the light emitted from the material enclosed within the sample holder in Figure 2.1 and the light is diffracted to an array of pixels within the camera. Before measurements were performed, the camera was calibrated to the emission spectrum of a mercury lamp with well-defined emission lines.

### Emitted Spectrum

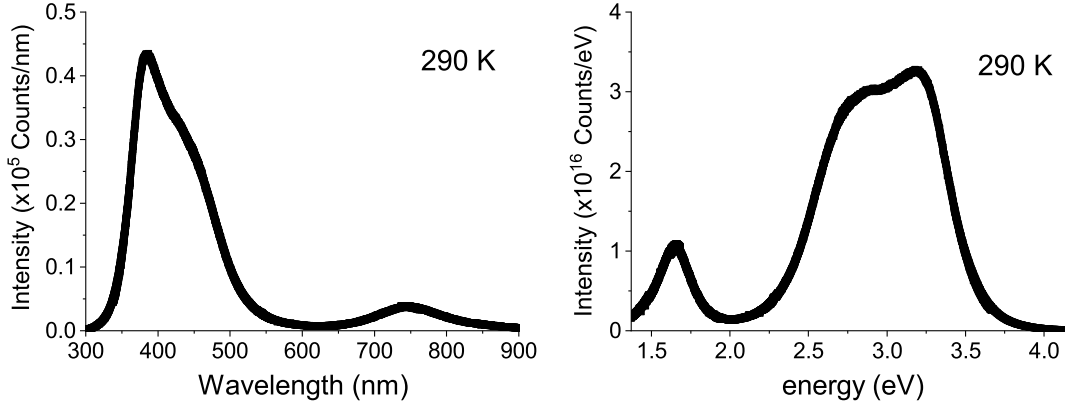


Figure 2.2: PL spectrum of HVPE grown  $\alpha$ -Ga<sub>2</sub>O<sub>3</sub> measured at 290 K with the intensity scale (y) converted in terms of (left) counts/nm, and (right) counts/eV.

Figure 2.2 shows a typical PL spectrum of  $\alpha$ -Ga<sub>2</sub>O<sub>2</sub> measured at room-temperature. In our experimental setup, the intensity of the emitted light is given in terms of counts per nm. However, spectroscopic data in terms of energy should be presented to gain a qualitative understanding of the internal mechanisms of the material [121]. This requires a conversion of the wavelength and intensity axes through a Jacobian transformation. The wavelength to energy conversion is expressed in equation 2.3

$$E = \left( \frac{hc}{\lambda} \right) \quad (2.3)$$

where  $E$  is energy,  $h$  is Planck's constant,  $c$  is the speed of light and  $\lambda$  is the wavelength.

However, given that the CCD camera measures the intensity of light in terms of counts/nm at each bin, the inverse relationship between wavelength and energy requires one to perform a conversion of the intensity to those in terms of counts/eV. This process is required to ensure that the intensity in each bin is uniform. To correct the y-axis from a wavelength-dependent to an energy-dependent intensity, a correction factor must be applied. In terms of differentials, this can be shown as

$$I_{\lambda}d\lambda = I_E dE \quad (2.4)$$

Where  $I_{\lambda}$  is the intensity in terms of wavelength,  $d\lambda$  is the wavelength interval,  $I_E$  is the energy-dependent intensity and  $dE$  is the energy interval. Combining equations 2.3 and 2.4, the conversion factor applied to the intensity scale is given as

$$I_E = I_{\lambda} * \left( \frac{\lambda^2}{hc} \right) \quad (2.5)$$

Failure to carry out this process of converting the intensity scale will result in an inaccurate representation of the relative intensities of the luminescence bands of the spectrum. The conversion from a wavelength scale to an energy-dependent intensity scale is particularly important for  $\text{Ga}_2\text{O}_3$ , where the luminescence spans a wide spectral range. Therefore, conversion can strongly affect the spectrum shape. This effect can be seen in Figure 2.2 where we see the red luminescence amplified, while the UV emission is dimmed relative to the wavelength spectrum.

### 2.1.2 Cathodoluminescence Spectroscopy

CL is the emission of light from a sample due to a high-energy electron beam generated by an FEG electron gun in a scanning electron microscope (SEM). The high-energy incident electrons undergo a series of inelastic collisions, generating electron-hole pairs.

The subsequent recombination of these electrons and holes releases photons that form the CL spectrum.

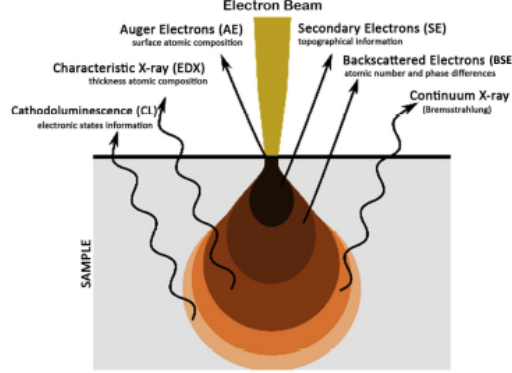


Figure 2.3: SEM electron-matter interactions and resulting radiations. Image taken from [7].

Unlike in PL, where the penetration depth is determined by the energy of the incident light and the absorption coefficient of the material, the depth at which electrons interact with matter within the sample is described by the interaction volume represented schematically in Figure 2.3. The interaction volume is determined primarily by the atomic weight of the species in the sample, the density of the material, the atomic number, and the incident beam energy. A mathematical description of the size of the interaction volume is given by the Kanya and Okayama range,  $R_{KO}$  [122]

$$R_{KO} = \left( \frac{27.6A}{\rho Z^{\frac{8}{9}}} \right) E_0^{\frac{5}{3}} \quad (2.6)$$

where  $A$  is the atomic weight,  $\rho$  is the density,  $Z$  is the atomic number, and  $E_0$  is the incident beam energy. Equation 1.6 shows that besides material parameters, the interaction volume is driven by beam energy. A visual representation of the interaction volume is obtained via simulations using CASINO, which is an estimation of The interaction volume by means of a Monte Carlo simulation. For this project, CASINO software was used to generate simulations of the volume of interaction at various incident beam energies [123], illustrated in the Figure 2.4.

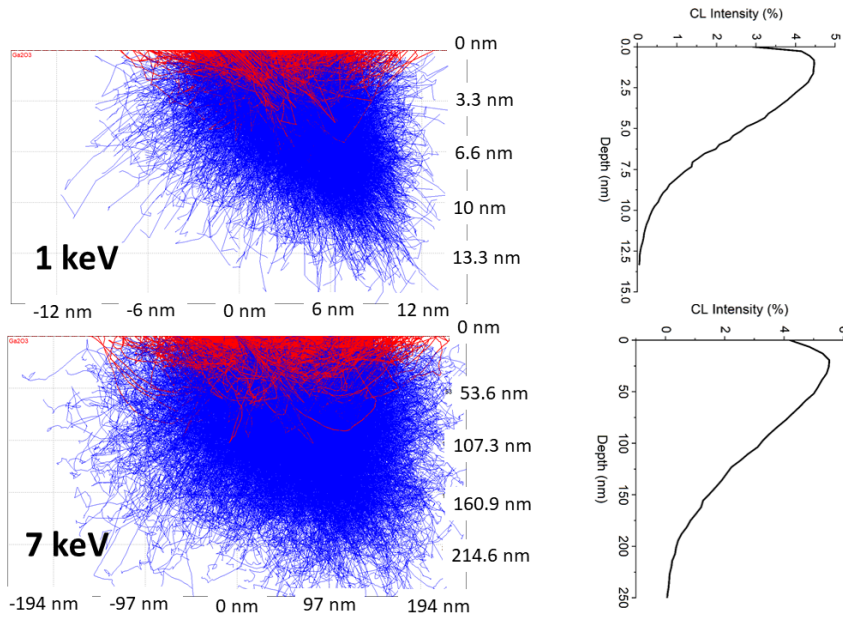


Figure 2.4: Monte-Carlo simulation of electron-matter interactions in  $\text{Ga}_2\text{O}_3$  with an accelerating voltage of (top) 1 keV, and (bottom) 7 keV. The tilted interaction volume derives from the sample being tilted at  $45^\circ$  relative to the electron beam.

From 2.4, we can see that there is a significant increase in the interaction volume by increasing the accelerating voltage from 1 keV to 7 keV. When considering CL, the primary consideration must be selecting an accelerating voltage such that the interaction volume does not extend to the substrate. Hence, any luminescence generated is exclusively from the  $\text{Ga}_2\text{O}_3$  film. After selecting an incident beam energy that will not excite the underlying substrate, the user may select accelerating voltages to suit the measurement requirements. The lower the accelerating voltage, the smaller the interaction volume, leading to an increased spatial resolution. However, lower accelerating voltages will produce a weaker CL signal, and thus a balance must be made between the strength of the signal and the resolution. Here, we must note that the beam current can also be varied, which acts as another method of varying the power of the electron beam without affecting the interaction. However, an increase in beam current will lead to a reduction in the spatial resolution of the measurements due to e-e interactions in the beam.

The electron-matter interactions generate different signals from within the interac-

tion volume, which can be interpreted for various types of experimental techniques. In this thesis we will focus on secondary electrons (SE) and CL signals.

**Secondary Electrons :** When the high-energy electrons interact with the sample, inelastic collisions are responsible for the removal of electrons from the outer shell of the atoms (Valence band of the atom), exhibiting a significantly lower energy than the incident electron. Given the low energy, only electrons generated near the sample surface will have enough energy to be ejected from the material and detected by the SE detector [124,125].

### Scanning Electron Microscope

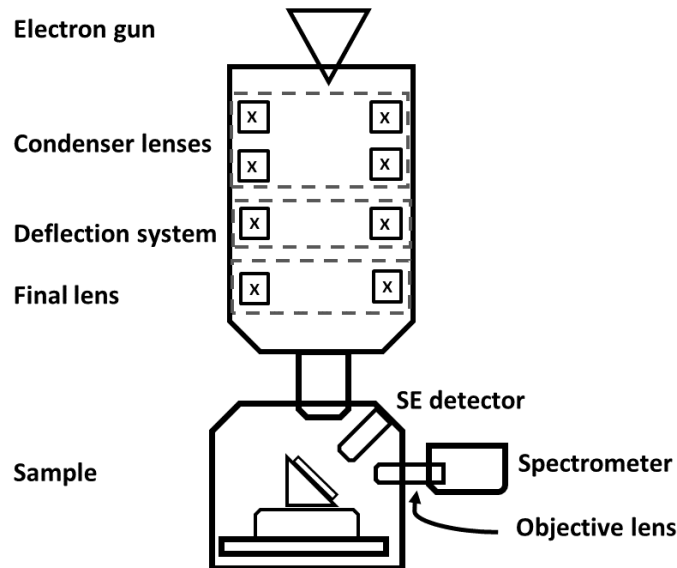


Figure 2.5: Schematic of the SEM used for SE imaging and CL measurements.

The SEM used for all electron microscopy measurements in this thesis was a Quanta FEG electron microscope capable of producing accelerating voltages ranging from 1 to 30 keV.

When electrons are emitted from the SEM electron gun, the electrons enter a lens system composed of a series of electromagnetic lenses to reduce the beam spot to a size of the order of nanometers on the sample surface [126]. The condenser lenses collect

the electrons emitted from the gun and creates a demagnified image at a given distance from the lens. The final lens is used for further demagnification to produce a final spot size on the sample surface. The deflection system consists of a pair of coils to raster the beam across the sample surface [127].

### Hyperspectral Imaging

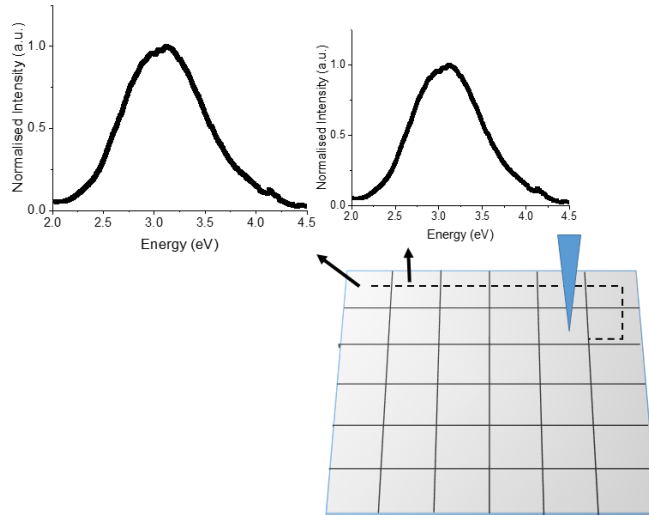


Figure 2.6: Hyperspectral imaging where the electron beam is rastered across the sample surface, and a CL spectrum is acquired at each pixel.

Hyperspectral imaging (HSI) allows the acquisition of an image that contains spatial and spectral information stored at each pixel in an image [128, 129]. In the CL setup described above, the electron beam is scanned across the sample, and the sample is projected into an array of pixels, where each pixel contains a CL spectrum. Therefore, the emission spectrum can be obtained over the sample's surface, yielding the material's spatially resolved luminescence characteristics. An example of an HSI acquisition is shown in Figure 2.7. The image on the left shows the SE image with the mapped region indicated by the dashed line, the centre image shows the CL image intensity of the dashed region and on the right we have the obtained CL spectrum at pixels indicated 1 and 2 on the map.

Selecting the correct operating parameters is crucial for generating a HSI with good resolution. One key influence of the resolution will be the interaction volume, which the accelerating voltage of the electrons can control. Ideally, one wants a small interaction volume by using a low accelerating voltage for the electrons. However, this must be compensated by using a high enough accelerating voltage to generate enough SE to generate a high-quality SE image to use as a reference for the CL map. The spot size will also have a significant effect on the resolution of the measurements. Using a larger spot size will result in a higher CL generation from the sample, however, it will lead to a decrease the resolution of the measurements. A final consideration that will influence the resolution is the carrier diffusion in the material. When the electron-hole pairs are generated within the material, they will naturally diffuse before recombining and effectively broaden the resolution [130].

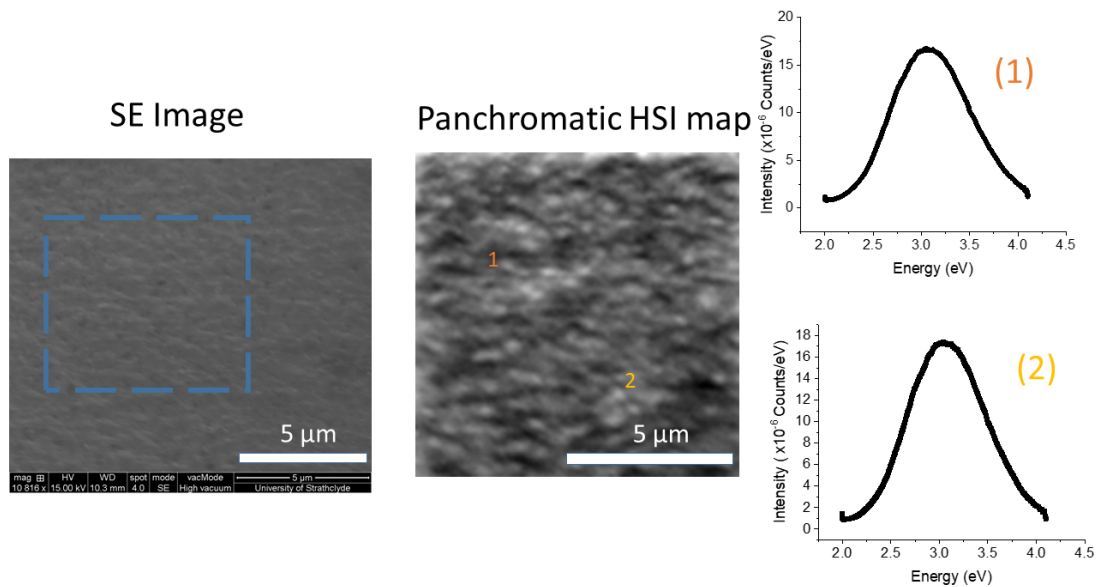


Figure 2.7: Typical data obtained for SEM acquisitions: (left) SE image, (middle) Panchromatic HSI obtained over the square region marked by the dashed lines in the SE image, and (right) CL spectra obtained at two regions in HSI map.

In Figure 2.7, the HSI map was presented as a panchromatic CL image, which means that the CL intensity is averaged over the full spectral range (2.4 -4.2 eV) where the contrast is determined by variations in radiative recombination rate between each

pixels. For monochromatic CL images, we can select a narrow range of spectral energies to image as shown in Figure 2.8.

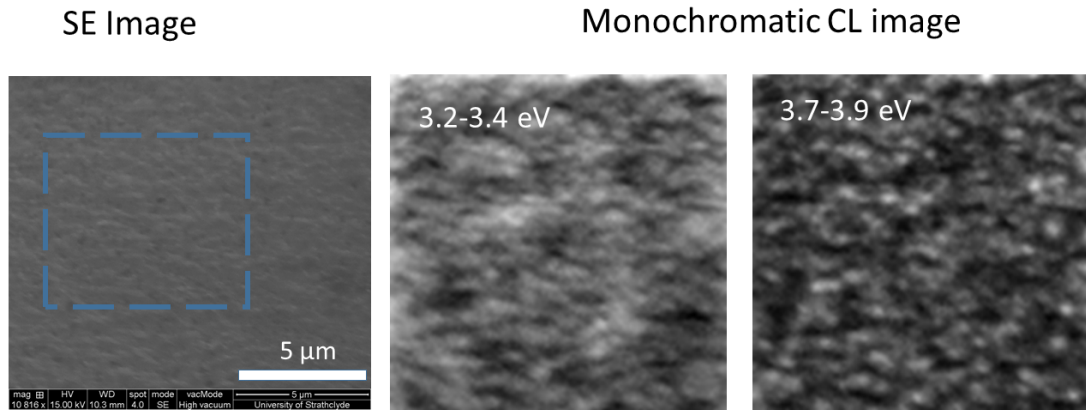


Figure 2.8: Monochromatic CL images obtained from SE image in the (middle) 3.2-3.4 eV ,and (right) 3.7-3.9 eV spectral regions.

SEM images and monochromatic CL images are shown in Figure 2.8 in the spectral regions of 3.2-3.4 eV (middle) and 3.7-3.9 eV (right). Here we can see that, while there are some small variations in the intensity between 3.2-3.4 eV, the overall intensity distribution appears fairly homogeneous. If we compare with the CL image at 3.7-3.9 eV, we see a larger contrast between the light and dark regions, indicating some localisation of the recombination centres responsible for this emission.

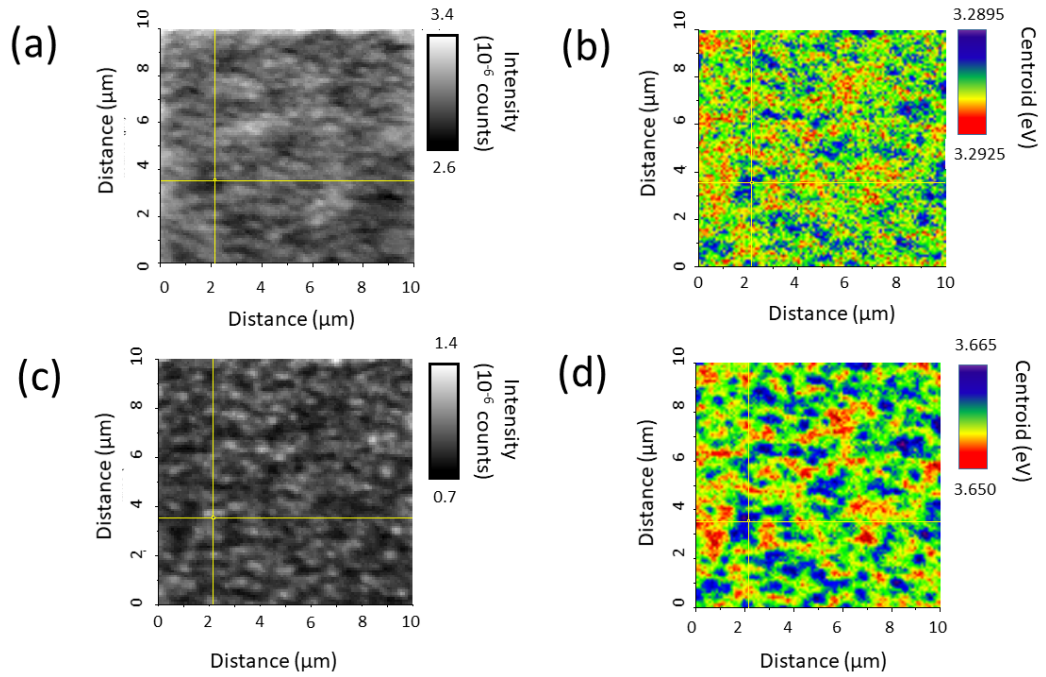


Figure 2.9: Example of centroid analysis feature: (a) Monochromatic CL image between 3.2-3.4 eV and (b) corresponding centroid analysis; and (c) monochromatic CL image between 3.7-3.9 eV with (d) corresponding centroid analysis.

The collected data from a HSI can be analysed in a number of ways thanks to the software CHIMP written by Dr Paul Edwards. The HSI can be viewed in terms of average intensity, such as in Figure 2.8, peak intensity, etc., but a relevant tool for this study is to view the map in terms of the centroid position. The centroid position calculates the mean energy within the spectral range. With sharp emissions, this process can show effective wavelength shifts of the peak position. However, in a broad emission generated from materials such as  $\text{Ga}_2\text{O}_3$ , the idea here is to use the centroid position to show variations in peaks contained in the broad emission. The centroid HSI data is shown in Figure 2.9. Figures 2.9 (a) and (b) show the CL image measured between 3.2-3.4 eV in terms of average intensity and centroid position, respectively. Although we can see some shift in the centroid position, it is reasonably well distributed across the mapped area. (c) and (d) show the CL image measured between 3.7-3.9 eV in terms of average intensity and centroid position, respectively. Here we observe some stronger shifts in the centroid position shown by the variation

of colour in (d). With just the average intensity CL image, we observe bright spots indicating an increase in the overall intensity of the CL emission. However, the shift in the centroid position indicates that at those bright spots, the overall centre position of the emission is blue-shifted, indicating that at those points there is a stronger influence of a higher energy band.

Additional capabilities of the software include peak fitting, however, at the time of this work the software wasn't adapted to carry out the peak fitting process for system corrected data.

Within the software, the user has control over parameters related to the hyperspectral scan, notably the scan size and acquisition speed. In theory, a fast scan rate over a large scan area would yield the best results. In practice, this isn't possible. The scan rate will dictate the generated CL signal and the size of the scan, i.e., how many pixels will be limited by the charging effects of the sample. With the ultrawide-bandgap of  $\text{Ga}_2\text{O}_3$ , sample charging presents a significant challenge. This can be somewhat mitigated by using silver paint around the edges of the sample which creates a conductive path for the built-up charge to flow [131]. Alternatively, the microscope can be operated in low-pressure mode which introduced a vapour into the chamber. However, operating in low-pressure mode is limited to room-temperature measurements.

### 2.1.3 System Response

#### General approach

In  $\text{Ga}_2\text{O}_3$ , where the luminescence spans a wide spectral range, the response of the system must be taken into account. The true spectrum emitted by the sample will differ from the luminescence spectrum acquired by the detector, due to the varying optical efficiency of the components in the system such as the lens, diffraction grating and CCD camera. This effect is particularly significant for luminescence measurements of  $\text{Ga}_2\text{O}_3$  due to the emitted light spanning a broad range from UV to the visible wavelength region where the optical efficiency of the components is non-linear across the range. In the field of spectroscopy, this effect is referred to as the system response. A simplistic illustration is shown in Figure 2.10 where we simulate a uniform photon intensity be-

tween 310 and 700 nm and assess the impact of the optical elements contributing the the system response.

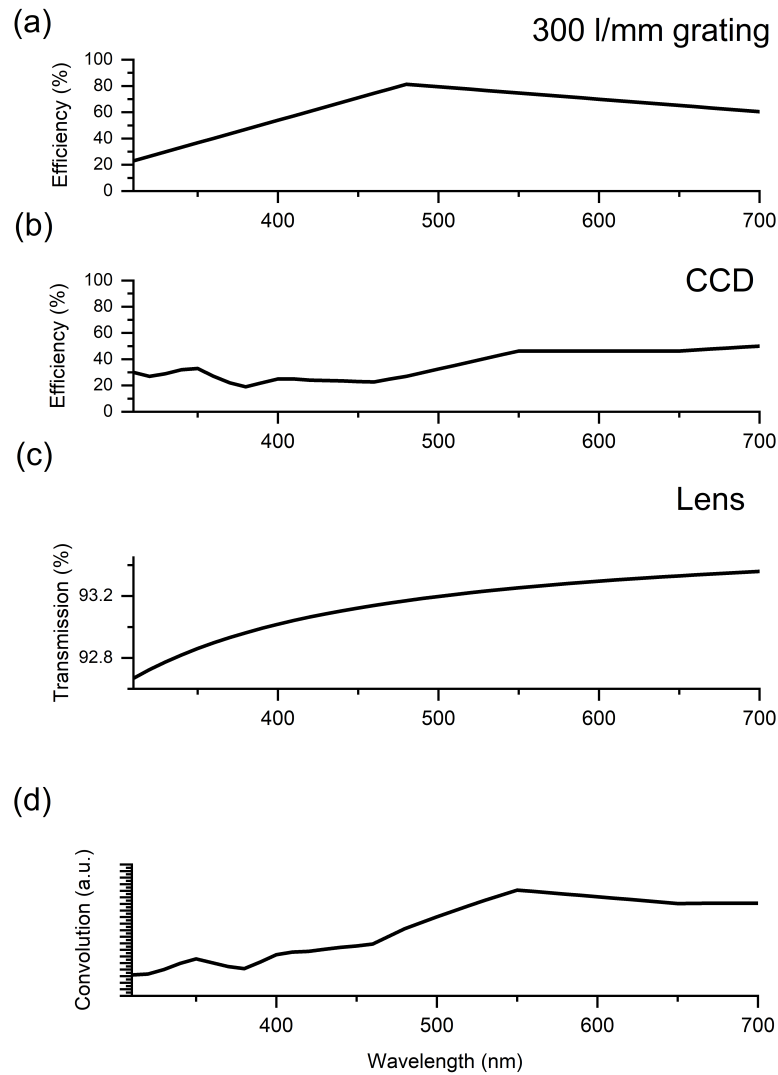


Figure 2.10: Representation of the PL system response accounting for the efficiency of (a) diffraction grating (b) CCD camera (c) Lens. The convolution of the effect of the optical elements is shown in (d)

In the experimental PL setup shown in Figure 2.1, the emitted light passes through 2 lenses, a diffraction grating, and a CCD camera. The impact of each of the elements on the system response is shown in Figure 2.10

In an ideal setup, every photon of each energy of light that is emitted by the sample will be converted into an electrical signal by the detector. However, this is not the case

and it is shown in Figure 2.11 that there is a significant wavelength dependence on the efficiency of the detector which can have a dramatic effect on the shape of the output spectrum. Figure 2.11 shows the quantum efficiencies of Andor 420 CCD cameras with different detection capabilities. Let us consider the extreme case of Andor BV(550 nm). We can see that the detectors quantum efficiency at 550 nm is approximately 9 times greater than at detecting photons at 300 nm. This in turn means that if an incident light contained an equal intensity of photons at 300 nm and 500 nm, 9 times more electrons would be created at the pixel detecting 500 nm photons, and in turn the spectrum would appear 9 times more intense relative to 300 nm even though the photon intensity is the same. Therefore, the detector's efficiency and optical components must be considered when obtaining a luminescence spectrum, particularly for any accurate quantitative analysis.

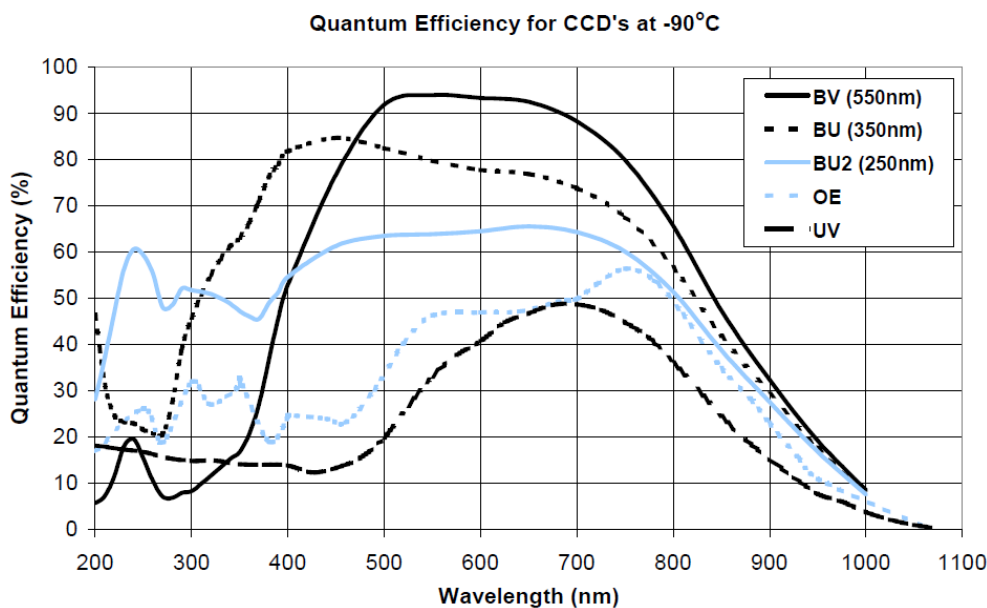


Figure 2.11: Quantum efficiencies of a variety of Andor CCD cameras. In the experimental PL setup an ANDOR DV420-OE was used to generate the emitted spectrum.

Not only does the CCD have a wavelength-dependent efficiency, the diffraction grating will also significantly affect the measured luminescence spectrum, where the efficiency versus wavelength is shown in panel (a) of Figure 2.10. The mirror and

lens also show a wavelength dependence on the reflectance and transmission, respectively. The convolution of these wavelength-dependent losses will significantly alter the apparent luminescence spectrum, resulting in an erroneous spectrum analysis, where additional peaks caused by fluctuations in the system response could be misinterpreted as luminescence from the sample.

### **System response in PL**

To obtain the system response in PL measurements, the emission spectrum of a black-body light source such as tungsten is commonly used with an emission spectrum given by Planck's black-body radiation equation [132].

$$Intensity(\lambda) = \left( \frac{2hv^3}{c^2 \exp\left(\frac{hv}{k_B T}\right) - 1} \right) \quad (2.7)$$

where  $h$  is the Planck's constant,  $\nu$  is the photon frequency,  $c$  is the speed of light,  $k_B$  is Boltzmann's constant and  $T$  is the temperature. As we can see from equation 2.7 there is a temperature dependence on the shape of the intensity distribution.

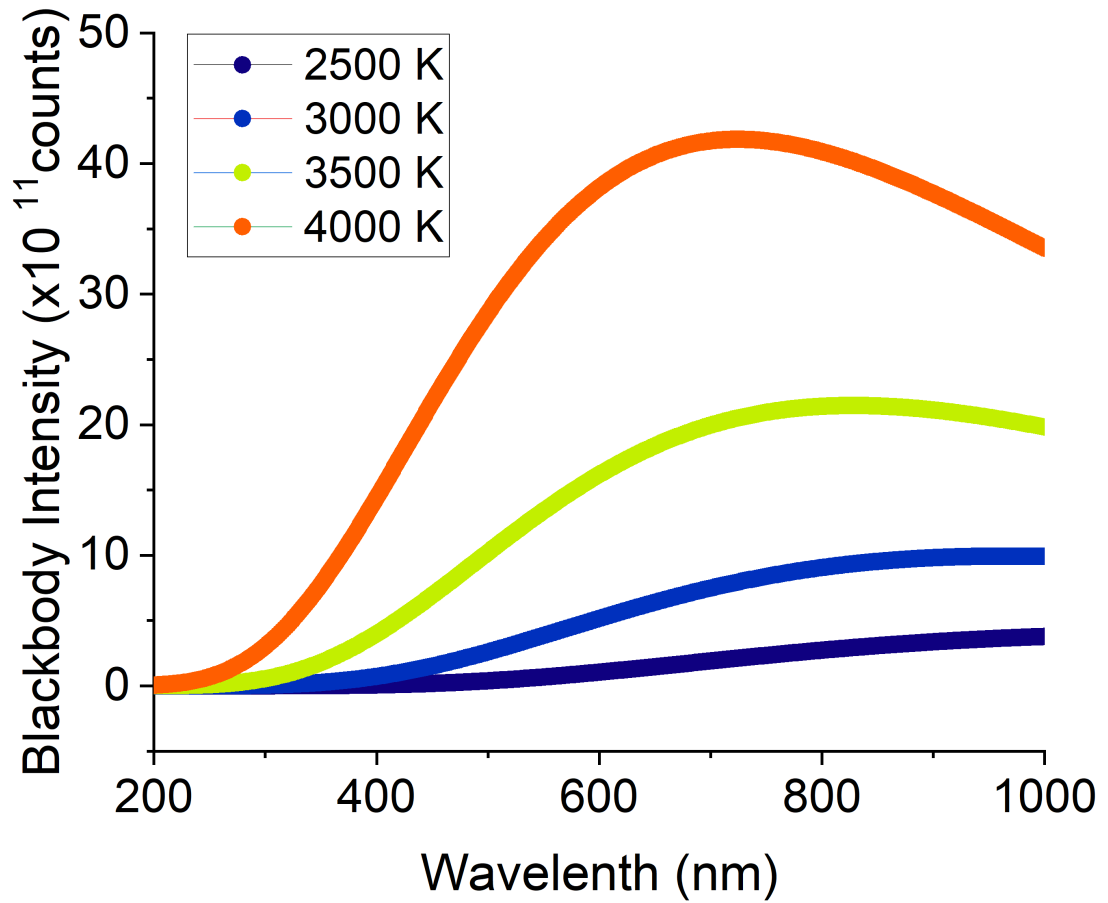


Figure 2.12: Blackbody emission spectrum using the Planck's equation at temperatures of 2500 - 4000 K

Figure 2.12 shows the blackbody radiation spectrum at different temperatures of 2500, 3000, 3500, and 4000 K. Figure 2.12 illustrates that as the temperature increases, the radiation spectrum broadens and shifts to the UV region according to Wein's displacement law [133]. As shown in Figure 2.2,  $\text{Ga}_2\text{O}_3$  is dominated by strong emission in the UV region around 400 nm. Therefore, we deduce that we want a blackbody operated at a high temperature to extend into the UV. However, here we are limited by the availability of a blackbody emitter with a high enough temperature rating to emit enough light below 400 nm.

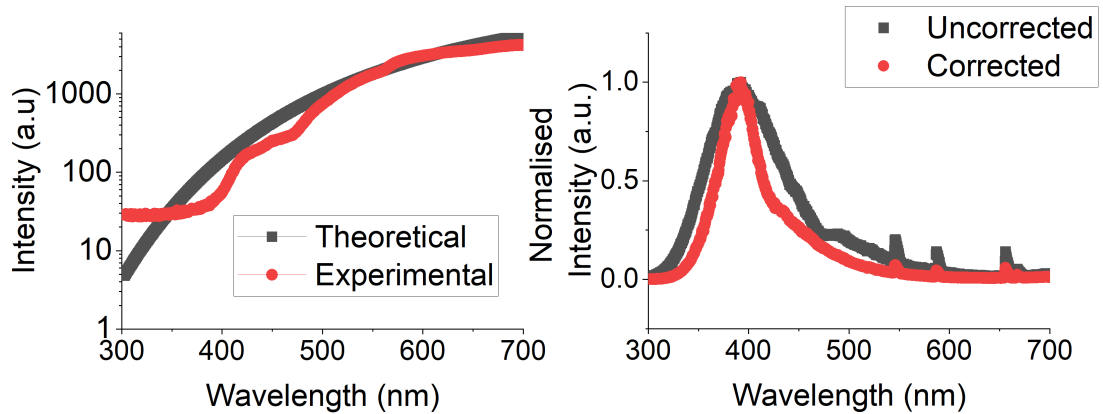


Figure 2.13: PL system response: (left) Theoretical and Experimental emission from the blackbody source, and (right) attempt at corrected PL system response.

An attempt was made to correct for the response of the system using a tungsten light source with a temperature rating of 2200 K, shown in Figure 2.13. Here, the sample was removed from the mounting position and the light source aligned to be in the same position. Placing the light source at the original sample position ensured that the light output from the lamp followed the same optical path to the CCD camera as the emission from the sample. We can see from Figure 2.13 that after correction for the system response, the step-like feature around 500 nm is removed. Due to the lack of corrected data below 400 nm, the correction for system response was not applied to the PL measurements. The justification for not accounting for the system response lies in the fact that the PL measurements in this thesis were used as a comparative measurement between the sample sets, where each sample was measured using the same PL system. Therefore, each of the samples experienced the same effect of the system response.

### System response in CL

To correct for the system response of the SEM and CL collection system, the CL spectrum was corrected using pure Aluminium transition radiation [134].

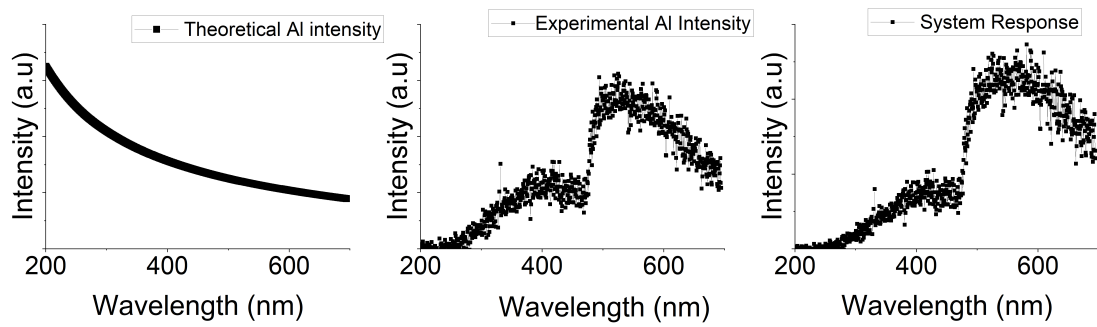


Figure 2.14: CL System Response

As shown in Figure 2.14, the system response is again primarily dominated by the CCD camera. Having extracted the system response of the CL measurement system, we can make a comparison between the corrected and uncorrected spectra, shown in Figure 2.15. Here we see the clear effect of the system response on the sample, and given the broad nature of the emission spectrum, perhaps surprisingly there does not seem to be much of an effect besides the kink centered around 2.5 eV ( 500 nm).

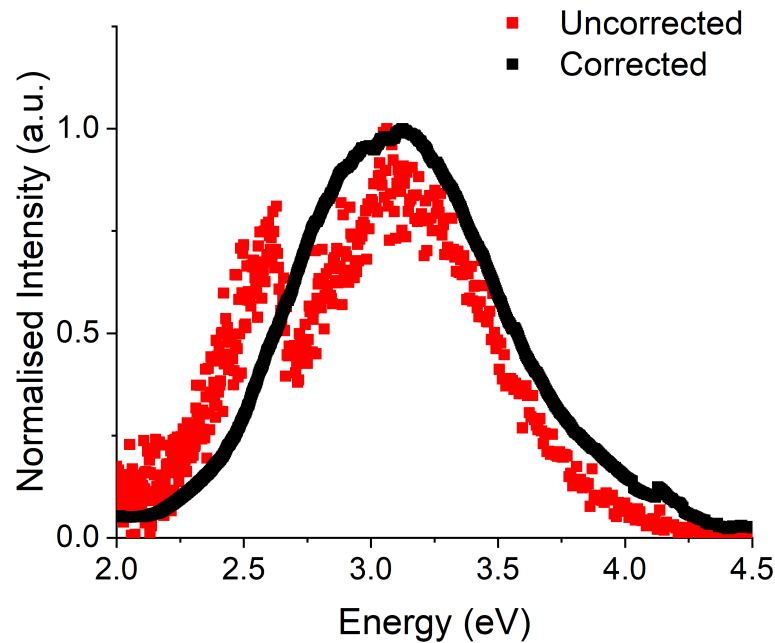


Figure 2.15: Comparison of the CL spectrum before correction for system response (red) and after correction (black). Here we see a removal of the spike feature around 2.5 eV

## 2.2 Photoconduction

In the previous section, we looked at how studying the luminescence spectrum will reveal information about the radiative recombination mechanisms at play from which we can deduce information regarding the electronic structure of the material. The same reasoning can be applied to studying the photoconduction process, whereby studying how the conductivity varies under illumination with different photon energy, illumination intensity, temperature, and time, which can reveal detailed information regarding several key material parameters such as the absorption coefficient [103, 104], carrier mobility [105], Fermi level position [106] defect distributions.

In this thesis, a photoconduction setup was built from scratch in order to acquire information regarding the carrier generation and transport properties of the material. In the remainder of this chapter, we will discuss the general experimental setup for photoconduction work and how the basic setup was adapted for each specific study.

### 2.2.1 Setup construction considerations

With the overall objective of the photoconductivity setup being to investigate the electrical response of  $\text{Ga}_2\text{O}_3$  to light, the lab design was broken down into the following considerations. Listed below are the primary considerations, and the extra experimental additions required for specific experiments will be discussed in the proceeding sections: (i) Appropriate voltage source and current measuring system; (ii) Light source capable of generating above-bandgap excitation of  $\alpha$   $\text{Ga}_2\text{O}_3$ ; (iii) Ability to resolve the light output.

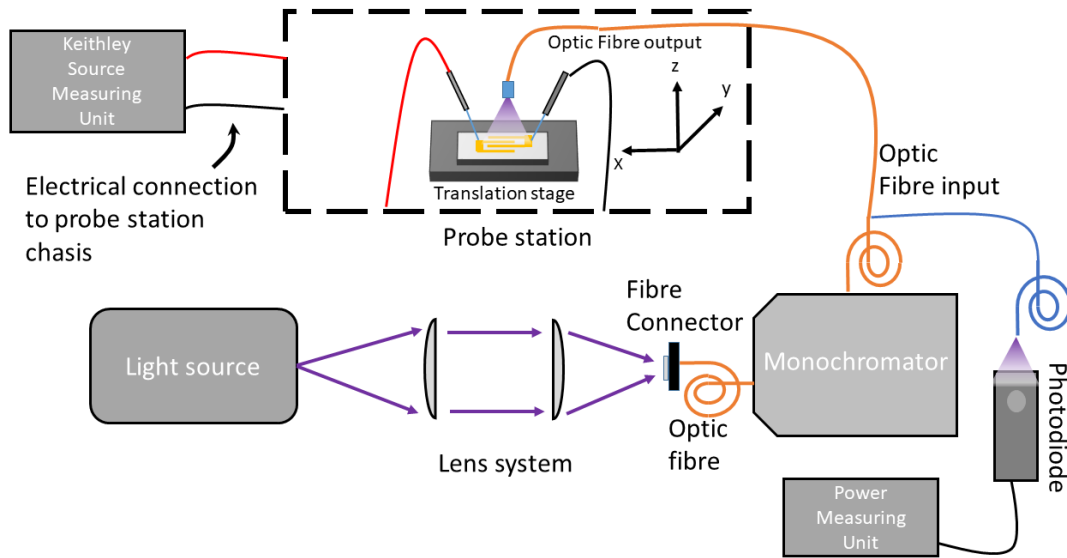


Figure 2.16: Schematic of the core photoconductivity experimental setup consisting of a light source to provide excitation, monochromator to resolve the light, Keithley source-measure unit. Optical power was measured via a secondary optic fiber from the monochromator

### Voltage and current measurement unit

A Keithley 6487 picoammeter was selected as the source measuring unit due to its excellent sensitivity and ability to measure current down at the fA range, ideally suited for low current measurements. Literature of  $\text{Ga}_2\text{O}_3$  detectors report dark currents ranging from nA to fA at room-temperature [135–138]. In practice, the range of fA was impossible to reach because of many contributions of electrical noise. Using the voltage source of the unit while simultaneously measuring current introduced additional noise into the system. Secondly, the accuracy of the measurements was strongly related to the acquisition rate of the device, which is expressed in terms of natural power line cycles (NPLC). The NPLC settings were adjusted depending on the measurement requirement. For high-accuracy measurements, NPLC was set to 5, resulting in approximately 10 data points per second. High-speed measurements were desirable for transient measurements with NPLC set to 1, resulting in around 50 data points per second. However, additional noise is incorporated into the measurement process. An

improvement on the experimental setup for future experiments would be to separate the voltage source and current measurement system by using an oscilloscope for the current measurements.

### **Excitation Source**

Due to the ultrawide band-gap between 5.1 -5.3 eV [23, 29], band-to-band excitation of the carriers required a UV light with strong emission from around 230 nm. In this thesis, we used two different sources to photoexcite our materials: a deuterium light source, and a series of light emitting diodes.

#### *Deuterium light source*

Broadband excitation was achieved using a Thorlabs SLS204 deuterium light source that emits light between 200-700 nm, with the measured excitation spectrum of Thorlabs shown in Figure 2.17. Here we see excellent UV emission properties because of the deuterium gas's ionisation by the bulb's arc within the light source. The strong UV emission is ideally suited for photoconduction measurements around the bandgap value. In the UV region around the peak at 250 nm, the optical output measured  $< 100$  nW. We observe a significant drop off in intensity in the visible region to around  $200\text{-}300$   $\mu\text{W}$ . For studying  $\alpha\text{-Ga}_2\text{O}_3$ , this source has the advantages of strong UV emission that is well suited to the band gap of the material, but it has shortcomings in terms of transferable power to the visible wavelength region, where the absorption in the material is low and therefore a high power is required to generate a photocurrent. Furthermore, to perform wavelength-dependent measurements, additional optical elements such as monochromators and lenses are required that will attenuate the optical signal, particularly in the UV region. To overcome this challenge, a higher power light source in the visible region could have been used. However, lack of control of the output power in the visible region and potential parasitic second order diffraction effects resulted to use a series of light-emitting diodes with overlapping bandwidths to generate a pseudo broadband light source.

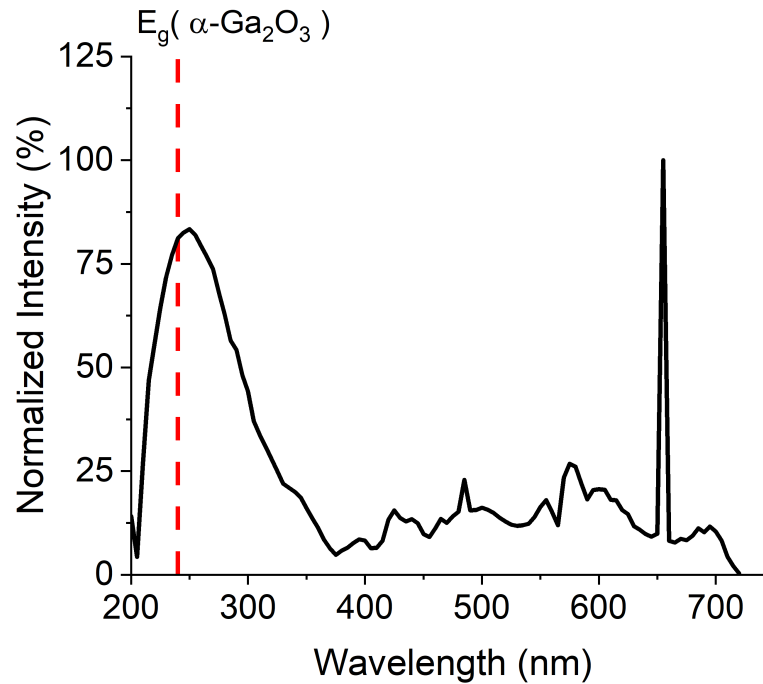


Figure 2.17: Deuterium Light source emission spectrum. Here we see a dominant broad emission between 200-300 nm. The sharp feature around 650 nm is the characteristic emission line of the Balmer series

### *LEDs*

An alternative approach to overcoming the power limitations of the deuterium light source was to use a series of LEDs, highlighted in Table 2.1. The LEDs open an excitation power space that is orders of magnitude larger than what can be achieved by the deuterium light source. This property is critical in order to study the impact of defects on the photoconduction process in  $\text{Ga}_2\text{O}_3$  where the samples in this thesis are unintentionally doped, therefore, highly resistive. The availability of higher power allowed for power-dependent photocurrent measurements, where the optical power could be attenuated over 3 orders of magnitude using a series of neutral density (ND) filters allowing a study carrier transport mechanisms in the material.

Part No.	Wavelength (nm)	Nominal Power (mW)	Bandwidth (nm)	Viewing half angle (°)
LED 250J	250	1	12	7.5
LED 275J	275	1.6	11	7.5
LED 325W2	325	1.7	11	114
LED 375L	375	1	10	20
LED 405E	405	8.4	15	5
LED 430L	430	8	20	22
LED 450L	450	7	20	20
LED 465E	465	20	25	8

Table 2.1: Details of LEDs used, supplied from Thorlabs

### Resolving the light emission

A Solar Laser Systems ML44 compact monochromator was used to resolve the excitation from the deuterium light source, as well as refine the emission spectrum of the LEDs. The ML44 has an operating range between 190-1200 nm. The broad range is achieved by using two gratings housed on a turret where a 1200 lines/mm grating with a blazing wavelength of 270 nm is used for the 190-600 nm spectral range, and 600 lines/mm blazed at 700 nm for the 500-1200 nm range. The entrance and exit slits on the monochromator are adjustable and mounted on two six-position rotation plates. The available slit widths and corresponding resolution are shown in Table 2.2.

Slit width ( $\mu\text{m}$ )	1200 l/mm (nm)	600 lines/mm (nm)
20	0.35	0.7
50	0.9	1.8
100	1.8	3.5
250	4.5	8.9
500	9.0	17.7
1000	18.0	35.5

Table 2.2: Slit width and corresponding wavelength resolutions using ML44 monochromator.

### Power measurement

As will be discussed later in this work, the energy of the optical excitation will impact not only the photoconductance, but the incident intensity of the optical excitation itself will also significantly impact the carrier generation process. To measure optical excitation power, a Thorlabs S130VC Si UV-extended photodiode was used, with a measuring

## Chapter 2. Experimental Methods

range between 200 and 1100 nm. To facilitate measurements, a second optical fiber (identified by the blue fiber in the setup shown in Figure 2.16) was connected at the exit of the monochromator and switched as needed between sample illumination and power measurement. The detection capabilities of the photodiode range from 500 pW to 0.5 mW, with the additional option to use a filter to measure up to 50 mW. Thorlabs calibrates the photodiode using a NIST-traceable calibration procedure. A PM100A power meter console converts the generated signals from the photodiode into readable output power. To convert the measured optical power to illumination intensity and flux, an estimation of the spot size incident on the device was required.

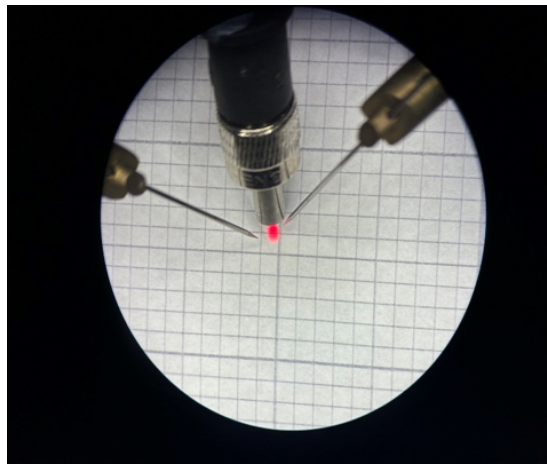


Figure 2.18: Spot size estimation a illuminated spot using a 635 nm LED .

A 2 mm x 2 mm grid sheet of paper was placed on the sample stage of the probe station at the height of the sample during measurement. The 2 mm x2 mm grid was used as a reference measurement to calibrate the pixel count to a length measurement. The calibration process was carried out using imageJ to correlate the 2mm grid size to a number of pixels. Here, the length of the box measured 72 pixels. The spot diameter was then measured as 45 pixels, indicating a spot diameter of 1.25 mm. The corresponding spot size area is then calculated as  $(1.1 \pm 0.4 \times 10^{-2}) \text{ cm}^2$ . Given the spot area has been calculated as above, the illumination intensity ( $\text{W}/\text{cm}^2$ ) was calculated by dividing the measured optical power by the spot size. Here this assumes the illumination intensity profile is uniformly distributed across the spot. In practice,

the intensity distribution will be non-uniform and exhibit a Gaussian profile. Ideally, the spot size would be much larger than the detector ensuring that the top of the Gaussian profile  $\gg$  detector resulting in an improved uniformity. However, this was experimentally impractical as a result of the light not being focused therefore as distance between sample and exit of the optic fiber increases, the measured optical power at the detector area decreases.

The optical flux then considers the energy of the photons that illuminate the sample. This was given by dividing the illumination intensity by the photon's energy in Joules, where the flux is measured in photons/s/cm.

### Neutral Density filters

The ND filters are designed using UV fused silica substrates with nickel coating on the reflective side to flatten the response curve. The ND attenuation specifications are given as numbers ranging from 0.1 to 5.0, where the corresponding transmission can be expressed as

$$T = 10^{-ND} \quad (2.8)$$

The ND filters used in this work are listed in Table 2.3, allowing us to adjust the illumination power by 3 orders of magnitude.

Part Number	ND	T (%)
NDUV0.3B	0.3	50
NDUV0.6B	0.6	25
NDUV1.0B	1.0	10
NDUV2.0B	2.0	1
NDUV3.0B	3.0	0.1
NDUV4.0B	4.0	0.01

Table 2.3: Range of NDfilters used to attenuate light from 50% to 0.01%.

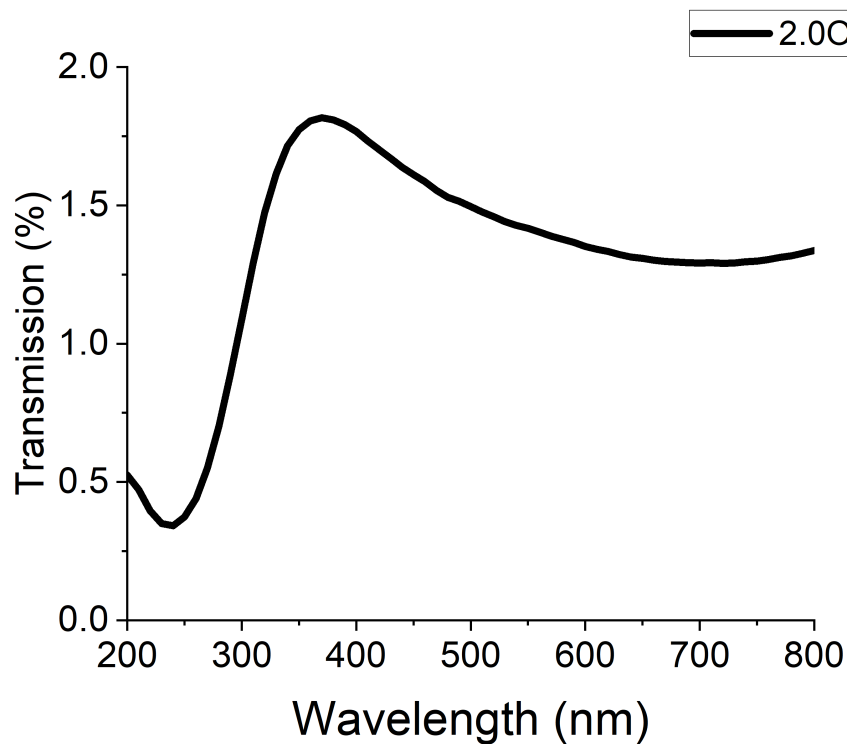


Figure 2.19: Wavelength-dependent transmission curves for ND filters used during photoconduction experiments

As evident in Figure 2.19, we see a wavelength-dependent transmission of the ND filters used during photoconduction investigations. The importance in accounting for wavelength transmission becomes clear in Chapter 4 where optical power estimations were made as incident optical powers were below the detection limit of the Si photodiode.

### Probe Station

Photoelectric characterisation in this work was carried out on  $\alpha$ -Ga<sub>2</sub>O<sub>3</sub> samples with photodetector architectures on a micron scale. The probe station consisted of two screw-driven mechanical probes with control in the x,y, and z directions and a translation stage in the x, y and z directions. An optical microscope was used to observe the sample to allow final adjustments to probe positions.

To ensure repeatability of the measurements, if possible, the sample was locked in position and not disturbed over the course of the measurement process. If the sample

moved, or the lens positions were adjusted to optimise photocurrent measurements at other wavelengths, a reference measurement was required to return the sample and optics back to the reference position. Here we used an LED and recorded the operating current, optical power, and photocurrent, and the micrometer readings on the screw gauge of the mechanical probes and translation stage.

### 2.2.2 Wavelength-Dependent Photoconductivity

A standard test for photodetector characterisation is to demonstrate wavelength selectivity. Furthermore, measuring the photocurrent in response to excitation wavelength can reveal information regarding sub-bandgap transitions in a material. At below-bandgap excitation, carriers do not have enough energy to be excited from the valence band to the conduction band. However, suppose that incident light has energy greater than the difference in energy between the defect energy level and the conduction band. In that case, electrons may be excited from the respective defect energy state to the conduction band. Thus, wavelength-dependent photocurrent measurements may yield information that describes the defect distribution within the bandgap.

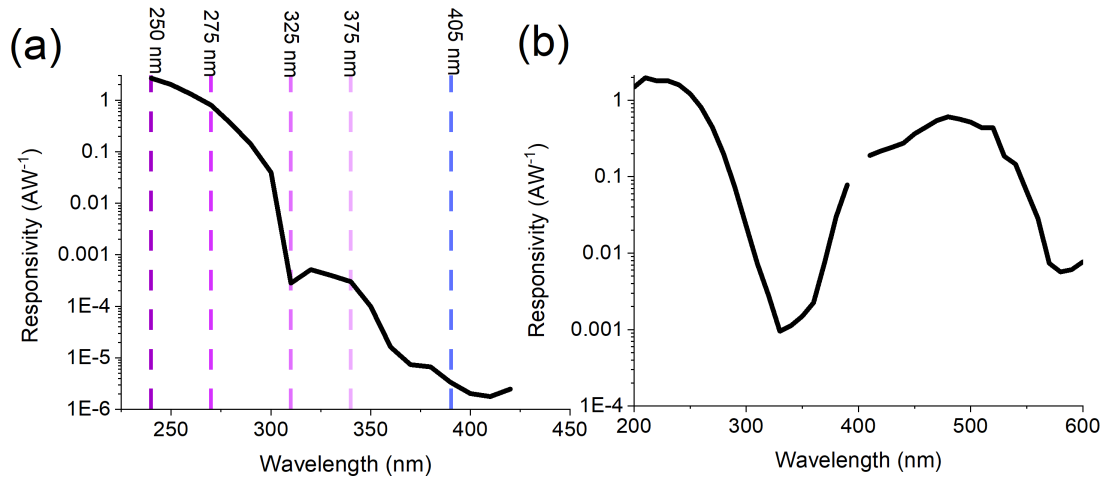


Figure 2.20: Comparison of the photoconductivity spectrum of an  $\alpha$   $\text{Ga}_2\text{O}_3$  sample versus wavelength measured using (a) LEDs (b) Deuterium light source.

Figure 2.20 shows the measured responsivity versus wavelength using the LEDs and deuterium light source. Due to the relative intensity and wavelength of the second

observed peak in the spectrum obtained via the deuterium light source, the impact of second order diffraction was checked using a range of longpass optical filters. With no filter, we observe a broad peak between 400 - 600 nm. Due to the relative intensity with the peak in the UV, and the wavelength position being around double the UV, we tested the possibility of second-order diffraction in the monochromator by inserting a 280 nm filter in the optical path resulting in a partial removal of the broad peak between 400 - 600 nm, shown in Figure 2.21. A further 400 nm filter was used showing a complete removal of the broad peak between 400 - 600 nm.

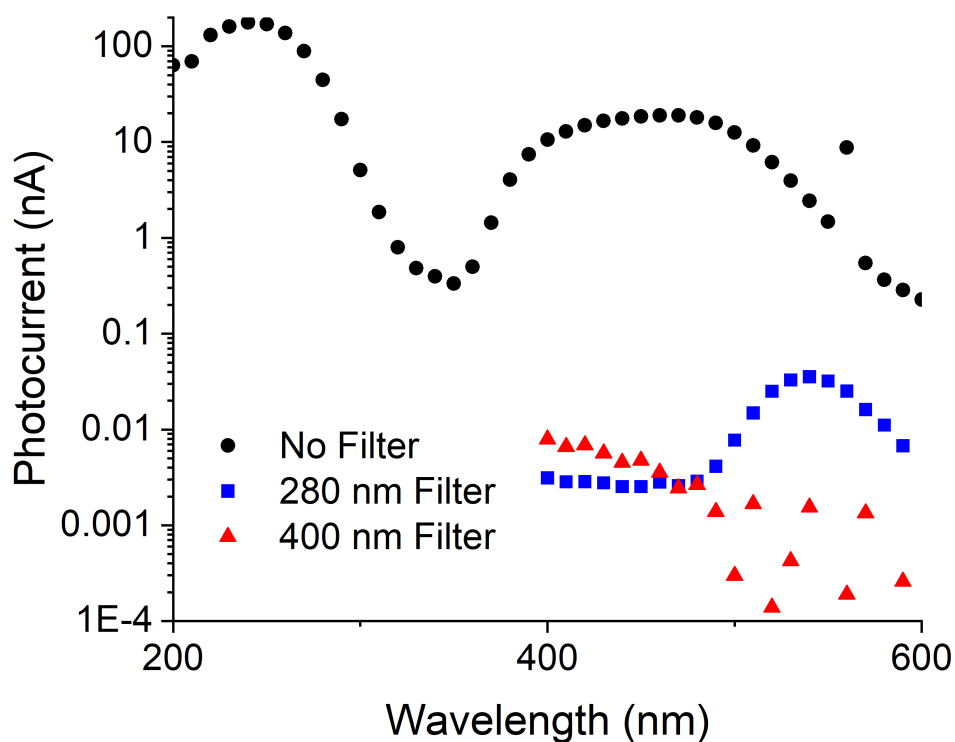


Figure 2.21: Photocurrent measurements from deuterium light source measured without filter (black circles), with 280 nm longpass filter (blue squares), and with 400 nm long pass filter (red triangles).

### 2.2.3 Constant Photocurrent Method

Because of the inherent relationship between photocurrent and the absorption coefficient of the material, one may think that the wavelength-dependent photocurrent measurements described above could give an indirect measurement of the absorption coefficient. This, in fact, holds true, but only for a very specific set of conditions in which the carrier lifetime remains constant with changes in carrier density [100]. The literature on power-dependent photocurrent measurements shows a non-linearity between light intensity and photocurrent, indicating intensity dependent carrier lifetime [28, 139, 140]. To overcome the variation in carrier lifetime with illumination intensity, a technique named CPM was developed in the 1960s, typically applied to hydrogenated amorphous Si, where the carrier lifetime was maintained constant by adjusting the illumination intensity to maintain a fixed photocurrent, in turn reflecting a fixed quasi-Fermi level position [141]

For optical excitation, LEDs were used to generate high optical power from 230 nm - 470 nm. Whilst considered monochromatic, the emission spectrum of LEDs can be relatively broad and shift with temperature and operating current. To select a narrower wavelength range and prevent a variation in peak position, the output of the LED was spectrally resolved using the ML44 monochromator. As the grating is automatically selected for the wavelength range under measurement, the control we had was the selection of the entrance and exit slits of the monochromator, with the grating options shown in Table 2.2. Using wider slits results in a greater light intensity illuminating the sample, but lower resolution and vice versa. A trade-off between these factors was required. Ideally, as CPM is essentially a spectroscopic measurement, the highest resolution is desirable.

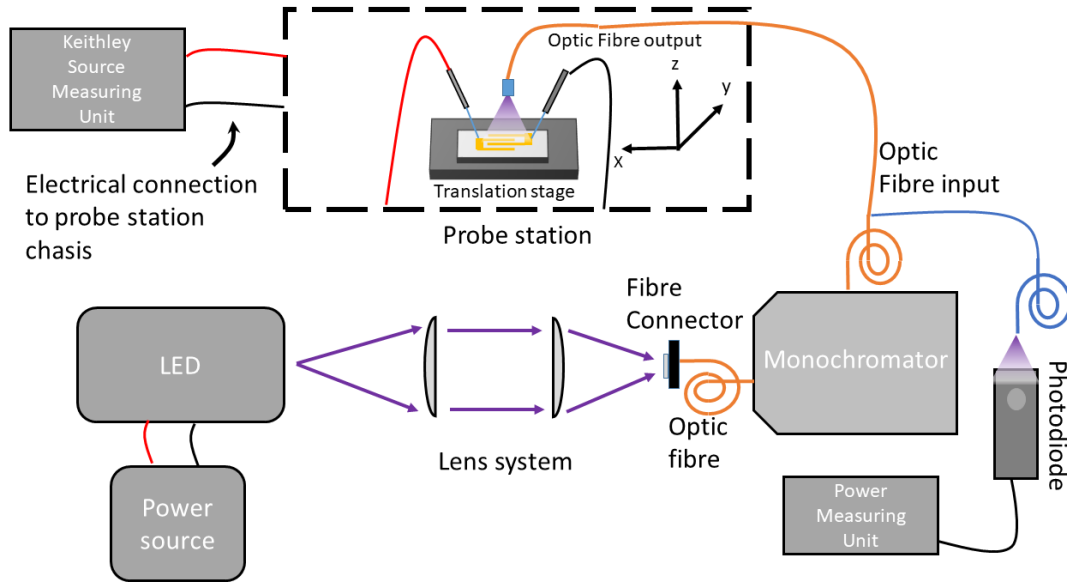


Figure 2.22: Schematic of the photoconduction setup adapted for CPM measurements. Here ND filters were added for coarse attenuation of the optical power, while fine adjustments were made by varying the LED driving current

#### 2.2.4 Power-Dependent Photoconductivity

When photons generate electron-hole pairs in semiconductor, the increase in photocurrent follows a power dependency on the illumination power, given by  $I_{PH} = P^\gamma$ , where  $\gamma$  can reveal information regarding carrier generation, trapping, and recombination processes [142–144]. Measurements of  $\gamma$  essentially describe the effect of illumination intensity on carrier lifetime [100]:

1. A linear relationship ( $\gamma = 1$ ) suggests an increase carrier density with a constant lifetime
2. A sub-linear behaviour ( $\gamma < 1$ ) suggests that the carrier lifetime decreases as carrier density increases.
3. A super linear behaviour ( $\gamma > 1$ ) indicated that the carrier lifetime increases with carrier density.

To carry out power-dependent photocurrent measurements, we adapted the exper-

perimental setup used for the wavelength-dependent measurements. The experimental setup is shown in Figure 2.23.

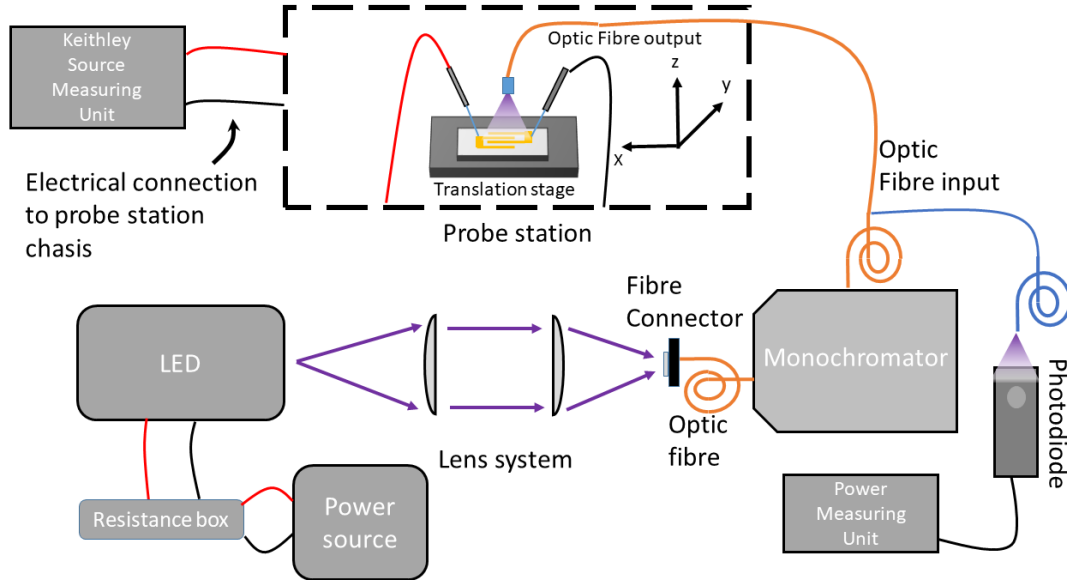


Figure 2.23: Experimental setup used for power-dependent photocurrent measurements. A resistance box was added to stabilise the LED driving current at low operating voltages.

For these measurements, LEDs were selected as the excitation source because of their high excitation power and wavelength-selection options. Here we have a range of LEDs listed in Table 2.1. For LED excitation, the experimental setup was adapted as shown in figure 2.23. To control the optical power, there was an option to either regulate the LED driving current or use a series of ND filters. Controlling the LED current allowed fine adjustments of the output optical power. However, this would shift the emitted light's centroid position. The wavelength shift can be corrected by using the monochromator but will result in an attenuation of the optical power, resulting in a limitation over the range of power-dependent measurements that can be recorded. Moreover, at low operating currents, the LED is particularly susceptible to heating effects. The use of ND filters allowed the LED to be operated at a fixed stable driving current, hence mitigated the effect of the shifting of the peak position of the output wavelength. One drawback of using the ND filters was that there was a limitation on

the number of data points. A series of ND filters was used to maximise the number of acquired data points allowing us to span from the nW to mW range.

For power-dependent photocurrent measurements, the rise time to steady-state was prolonged, and will be presented in chapter 4, particularly at low illumination intensity. To improve the acquisition process, measurements at high illumination were recorded first, and then a series of ND filters were used to attenuate the illumination intensity. The photocurrent was left to reach steady-state before attenuating further with the following ND filters.

The LED was powered by a Thurlby 30V-1A power supply connected in series with a Keithley 2001 multimeter to monitor the LED driving current. A resistive box containing a 100 $\Omega$ , 1k $\Omega$ , and 10k $\Omega$  resistor was used to stabilise the LED driving current. The 100 $\Omega$  resistor was used when operating at low operating currents (below 2 mA), the 1k $\Omega$  resistor was used for intermediate currents (typically 2 - 8 mA), and the 10k $\Omega$  resistor was used for all other LED driving currents.

After the photocurrent has reached steady-state, the optical fiber is switched to the photodiode for measuring the optical power. To remove any background light, the photodiode was enclosed in blackout material and noise levels were measured when ambient light was on.

### 2.2.5 High Optical Power Measurements

While spectral resolution was essential for wavelength-dependent photocurrent measurements, the addition of the monochromator was a large source of attenuation of the optical signal.

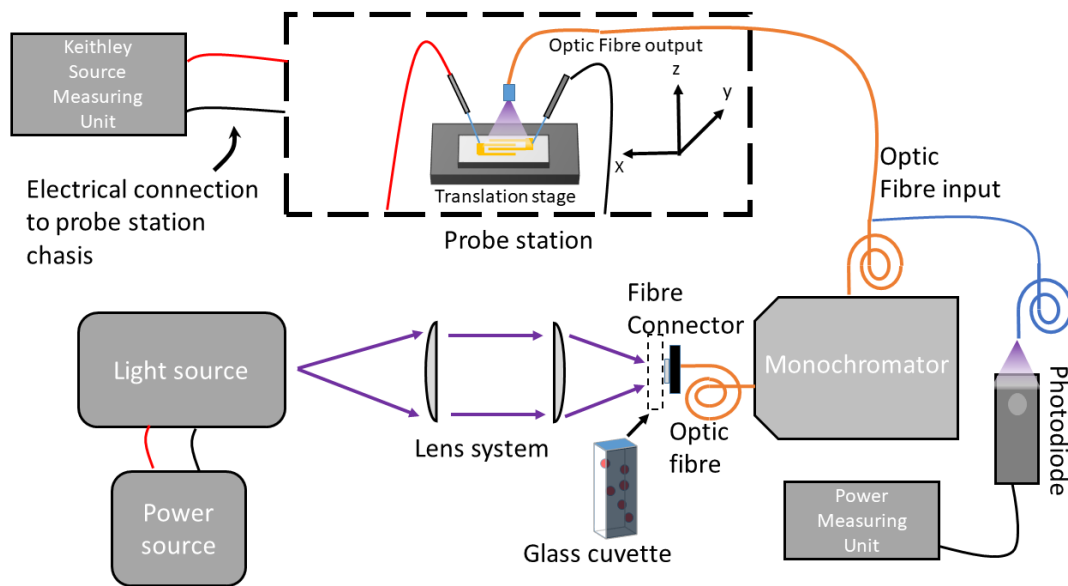


Figure 2.24: Schematic of the experimental setup used for high optical power measurements required for water quality measurements in Chapter 6. Attenuation from the setup was decreased by removing the monochromator.

In Chapter 6, we use a photoconduction approach to monitor water quality. For this purpose, high optical power was considered the key requirement, given that the spectral range can be covered by the LEDs listed in Table 2.1. Initial photocurrent measurements were recorded using a glass cuvette filled with deionised water to act as a reference. Subsequent photocurrent measurements were obtained with the cuvette filled with varying concentrations of contaminated water with different absorption profiles. The theory here being that as the concentration of the contaminant increases, more of the incident light is absorbed by the contaminants rather than being transmitted through the optic fiber. Hence, a decrease in photocurrent would be observed.

### 2.2.6 Thermally Stimulated Current spectroscopy

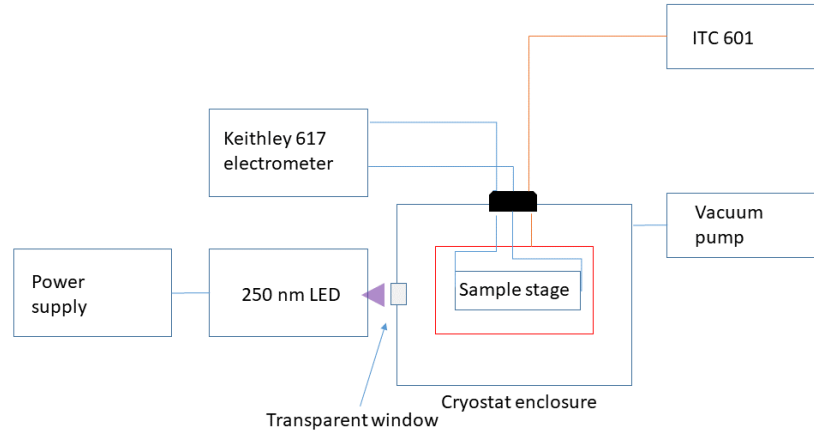


Figure 2.25: Schematic of the Thermally Stimulated Current spectroscopy experimental setup at the University of Dundee.

Thermally stimulated current (TSC) spectroscopy is a photoconduction technique used to probe electrically active defects in semiconductors to reveal information regarding energy levels, defect density, and capture coefficients [145]. Here, the sample is typically cooled down to low-temperatures and exposed to above-bandgap light to fill all the available energy levels. At low-temperatures, carriers do not have enough thermal energy to escape traps and contribute to the measured photoconductivity. The temperature is then increased; at some point the thermal energy will correspond to a trap depth resulting in thermal excitation to the mobility band. Thus, measuring the TSC signal as a function of temperature will reveal information about the trap depths in the material.

The TSC measurements in this work were carried out in collaboration with Dr. Stephen Reynolds at the University of Dundee, where the setup shown in Figure 2.25 allowed temperature control from 140 to 400 K. Optical excitation was generated from an LED with near-bandgap energy. The setup consisted of a Keithley 617 electrometer

that applied a bias of 10 V to the sample enclosed in a cryogenic enclosure which was pumped to vacuum. Before TSC measurements are performed, the dark current activation energy can be obtained by measuring the dark current as a function of temperature. In order to remove any charge trapped at deep levels, the temperature in the chamber was ramped to 400 K with temperature control achieved by an ITC 602 temperature controller and annealed for a period of 20 minutes to allow for current saturation to be reached. Liquid Nitrogen is then added to the chamber to bring the internal temperature of the chamber down to 110 K. The temperature was then ramped to 400 K at a rate of 2 K per minute. The dark current activation energy is given by

$$I_D = \exp\left(\frac{E_a}{KT}\right) \quad (2.9)$$

where  $E_a$  is the activation energy,  $K$  is the Boltzmann constant, and  $T$  is the temperature. The activation energy can then be extracted using an Arrhenius equation. Here we note the dark current was below the detection limit of the Keithley 617 at 300 K, meaning the dark current at room-temperature is sub-fA.

The 250 nm LED was placed at a distance of 1 cm from the sample and operated at a driving current of 20 mA, corresponding to an illumination power of 74  $\mu$ W. The sample was illuminated with 250 nm light for 10 minutes to allow all traps below the Fermi level to fill. The light is then terminated and carriers that don't have enough thermal energy to escape the traps are effectively frozen. The temperature ramp of 2K per minute is applied and the current is measured as a function of temperature.

### 2.2.7 Transient Photoconductivity

Measurement of the photocurrent response to switching on and off illumination can give details of the recombination and generation processes in a semiconductor. This is one of most widely discussed criteria when assessing photodetector performance. This is typically classified by the rise and decay time. The rise time describes the process at which illumination is initiated, and the photocurrent builds up from dark current level to near steady-state. The decay time refers to the instance at which illumination

is terminated and the generated photocurrent rapidly decays.

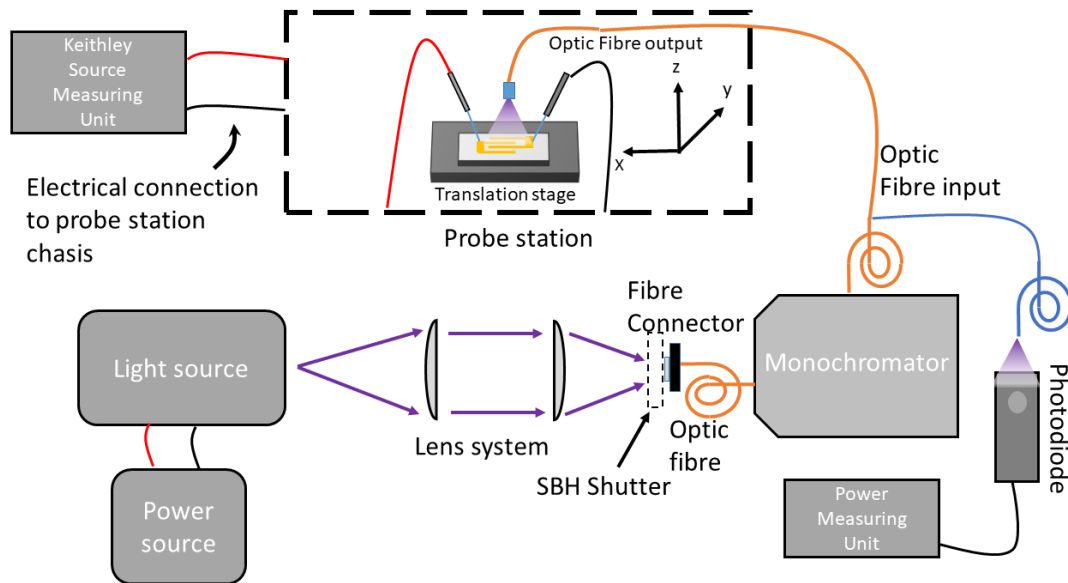


Figure 2.26: Experimental setup used for transient photocurrent measurements when illuminated via Deuterium light source. The monochromator was removed for LED excitation to avoid additional attenuation for high power measurements

In the literature, the rise and decay times appear to be quantified by various methods. Classically, the rise time is measured at the time taken to go from 10 % to 90 % of the steady-state value, and vice versa for the decay time. An alternative approach is to use a fitting method using a series of equations. Let us consider some of the most common fit equations.

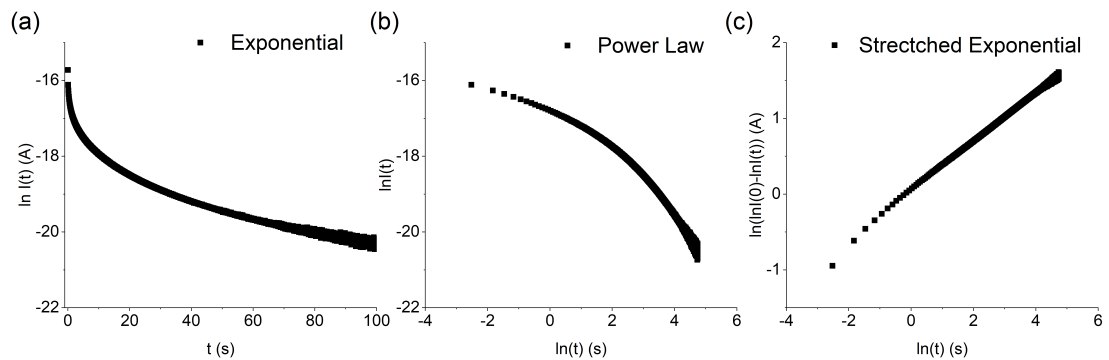


Figure 2.27: Transient decay modelled by (a) Exponential Decay (b) Power-law decay (c) Stretched Exponential

First, we examine the exponential decay. A single exponential is given by 2.10.

$$I(t) = I(0)\exp(-t/\tau_0) \quad (2.10)$$

In terms of n-type materials, this would represent a decay of electrons from the conduction band to the valence band, without intermediate reinteraction of the electrons and the traps. Figure 2.27 (a) shows the logarithmic photocurrent versus time, where we clearly do not observe a linear plot, which means that the single exponential decay is not a valid model for the decay mechanism.

An extension of the single exponential is the double exponential, which appears to be the fitting equation most commonly used by the majority of the Ga<sub>2</sub>O<sub>3</sub>, where the two decay processes are typically attributed to a fast and slow decay process. In the literature, fast decay has been attributed to recombination of free carriers and STH, whereas the slow process is related to defect-mediated recombination. The double exponential decay is expressed as

$$I(t) = I(0)\exp(-t/\tau_{01}) + I(0)\exp(-t/\tau_{02}) \quad (2.11)$$

Similarly to the reasoning for disregarding the single exponential decay, if the double exponential could describe the decay process, two distinct linear regions would be observed in Figure 2.27

*Power Law* Due to the shortcomings of the exponential decay model, we explore the use of a power-law decay to model the photocurrent decay. So far, to my knowledge, there has been no modelling of photocurrent decay in Ga<sub>2</sub>O<sub>3</sub> using a power function given by

$$I_t = t^\beta \quad (2.12)$$

Previous reports suggest that a power-law decay may be attributed to the case of multiple retrapping, where electrons in the conduction band will undergo a series of trapping/detrapping before recombination [146, 147] and have been observed in short-term decay measurements (ms regime) for materials such as ZnO by transient photocur-

rent measurements [148] where the power-law decay mechanism in short timescales was attributed to the multiple retrapping mechanism.

Figure 2.27(b) shows the linearised Power-law decay taken over a time range of 100 s where we can conclude that the power-law model does not describe the long-term decay of the photocurrent. However, it can be argued that in the initial regime of the decay appears somewhat linear. Therefore, a power-law model using multiple retrapping may explain the initial decay process in  $\alpha$ -Ga<sub>2</sub>O<sub>3</sub>.

*Stretched Exponential*

The stretched exponential function has been used to describe a decay mechanism involving an exponential distribution of traps within the bandgap [149].

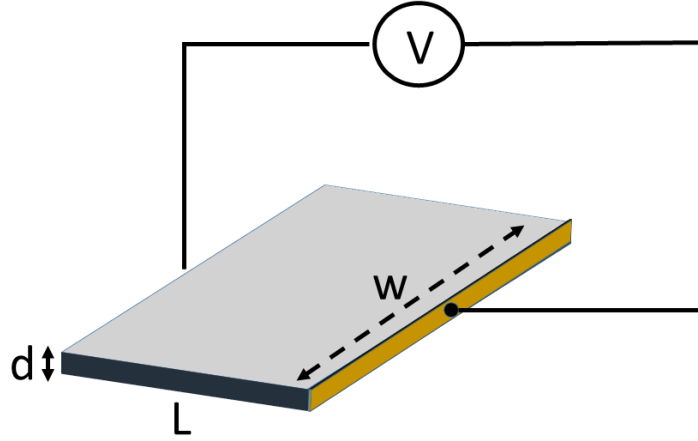
This fitting method is often used by prominent electrical characterisation group led by Polyakov in the Ga<sub>2</sub>O<sub>3</sub> community [106].

$$I = I_0 \exp\left(\frac{t}{\tau}\right)^\beta \quad (2.13)$$

where  $t$  is the time,  $\tau$  is the time constant and  $\beta$  is the stretching exponent. It can be seen when  $\beta=1$ , 2.13 reduces to a simple exponential. When  $0 < \beta < 1$ , there is a trap distribution where a larger  $\beta$  represents a narrower trap distribution, whereas a smaller  $\beta$  represents a broader distribution.

The stretched exponential model is represented in Figure 2.27(c) where we observe a strong linear relationship that reflects that the stretched exponential being the best model for describing the photocurrent decay. It can be observed that there is a slight variation in the linear plot in the short time regime. Due to the linear relationship in the short-time regime of the power-law model, this may reflect the photocurrent follows a power-law decay in the short time regime, dictated by the strong retrapping mechanism transitioning into a decay mechanism described by a distribution of states modelled by a stretched exponential function.

## 2.2.8 Unit conversions for photoconductivity measurements

Figure 2.28: Schematic of contact of contact architecture on 130 nm  $\alpha$ -Ga<sub>2</sub>O<sub>3</sub>

As expanded in further detail in Chapter 4, measuring the conductivity of a sample will serve as a better tool for comparison with detector performance from other research groups, as photocurrent can be influenced by a number of factors including excitation wavelength, illumination power, applied bias, and device architecture. Converting to units of conductivity ( $\text{S}\cdot\text{cm}^{-1}$ ) will account for the applied bias and the device architecture. Developing an equation for conductivity in terms of the device structure, we start with  $\mathbf{J}_{drf}$  can be written as

$$\mathbf{J}_{drf} = q(\mu n)\mathbf{E} = \sigma\mathbf{E} \quad (2.14)$$

Now consider the interdigitated nature of the device in Figure 2.28 consisting of 4 fingers, for simplicity at this stage, we will consider a single finger.

$\mathbf{J}$  is a measure of the current per unit area given by

$$\mathbf{J} = \frac{I}{A} \quad (2.15)$$

## Chapter 2. Experimental Methods

where  $I$  is the current and  $A$  is the conduction cross section. The conduction cross section area will be given as the space between 2 contact fingers *ca*  $100 \mu\text{m}$  ( $0.01 \text{ cm}$ ) and the depth of the material which is  $130 \text{ nm}$  ( $1.3 \times 10^{-5}$ ). The electric field, measured in  $\text{V/cm}$  is given by

$$E = \frac{V}{L} \quad (2.16)$$

where  $V$  is the applied voltage and  $L$  is the length of the contact. In figure 2.28 the length of the contact is  $500 \mu\text{m}$  ( $0.05 \text{ cm}$ ). Substituting 2.15 and 2.16 into 2.14 and rearranging for  $\sigma$  we obtain the following.

$$\sigma = \frac{IL}{VA} \quad (2.17)$$

Finally, using Ohms law  $R=V/I$ , we obtain

$$\sigma = \frac{L}{RA} \quad (2.18)$$

Equation 2.18 represents the conductivity measured between 2 fingers. However, this equation can be applied to any coplanar device, where the final conductivity value is multiplied by the number of fingers.

## 2.3 UV-VIS

### 2.3.1 Background

Optical absorption spectroscopy is a commonly used approach to obtain the optical bandgap of semiconductors from the variation of optical absorption as a function of wavelength. The absorption coefficient at a specific photon energy, of an electron being excited from the valence band to the conduction band, is governed by a transition rate given by [150]

$$W_{vb \rightarrow cb} = \frac{2\pi}{\hbar} |M|^2 g(E) \quad (2.19)$$

where  $M$  is the transition matrix element and  $g(E)$  is the density of states. First let us consider the case of direct optical absorption, where the electron is excited directly from the valence band to the conduction band, expressed as

$$\alpha_{dir}(E \geq E_{gap}) \propto (E - E_{gap})^{\frac{1}{2}} \quad (2.20)$$

For indirect optical absorption, a phonon is required for the conservation of momentum. Here, the relationship between the absorption coefficient and photon energy is given by

$$\alpha_{dir}(E \geq E_{gap}) \propto (E - E_{gap})^2 \quad (2.21)$$

From equations 2.20 and 2.21, a simple estimate of the band gap can be obtained by plotting  $\alpha^2$  (or  $\alpha^{\frac{1}{2}}$ ) for the direct (or indirect) bandgaps.

### 2.3.2 Experimental set up

Optical transmittance measurements were obtained using a Shimadzu UV-2600 UV-vis transmittance spectrometer installed with an integrating sphere, Illustrated in Figure 2.29

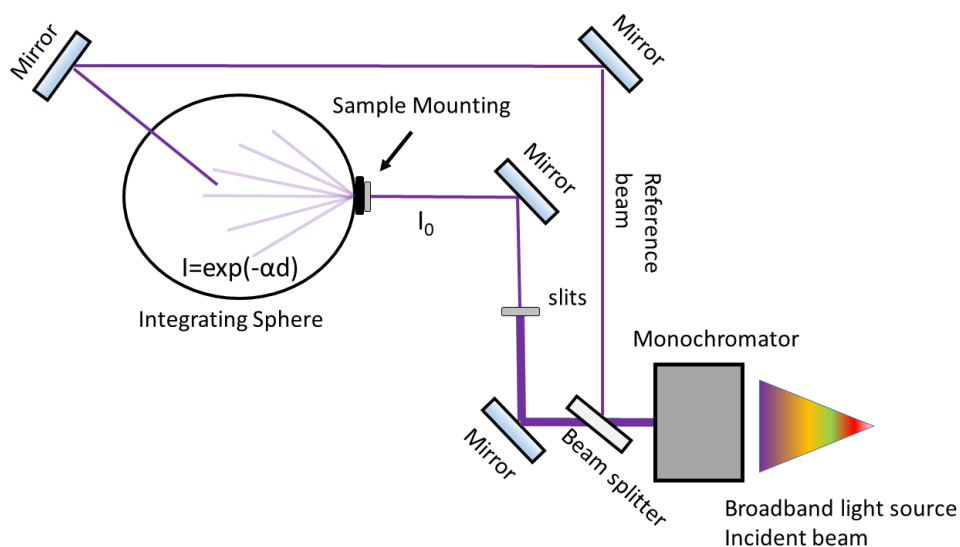


Figure 2.29: UV-VIS spectrophotometry setup. A broadband light source is spectrally resolved and illuminates the sample. The light source is spectrally resolved between 200-700 nm. Transmitted light is collected in an integrating sphere.

in this setup, 2 broadband light sources were used to cover the full spectral range from 200- 1100 nm. During the acquisition, the transition wavelength between the two light sources can be selected to avoid any distinguishing features on the spectrum.

The broadband light is spectrally resolved using a monochromator and the resolved light is directed to the sample via 2 mirrors while passing through a slit control the size of the incident beam. As the incident light ( $I_0$ ) interacts with the sample, the incident light is absorbed, reflected, or transmitted, depending on the wavelength-dependent absorption coefficient. The light that has been transmitted through the sample is dispersed into the integrating sphere where the intensity ( $I$ ) decays exponentially as a product of the absorption coefficient and the thickness of the sample given by the Beer-Lambert law

$$\frac{I(d)}{I(0)} = \exp(-\alpha d) \quad (2.22)$$

where  $I(0)$  is the light intensity at the sample surface,  $I(d)$  is the light intensity at a given sample depth,  $d$  is the sample thickness, and  $\alpha$  is the absorption coefficient.

A reference beam is used to compare the transmitted light through the sample to

the incident intensity.

### 2.3.3 The Transmission Spectrum

For the purposes of this thesis, transmittance measurements were used to view the optical absorption edge, where the steepness of the edge can be used as an indication of crystal quality and indicate the bandgap of the material.

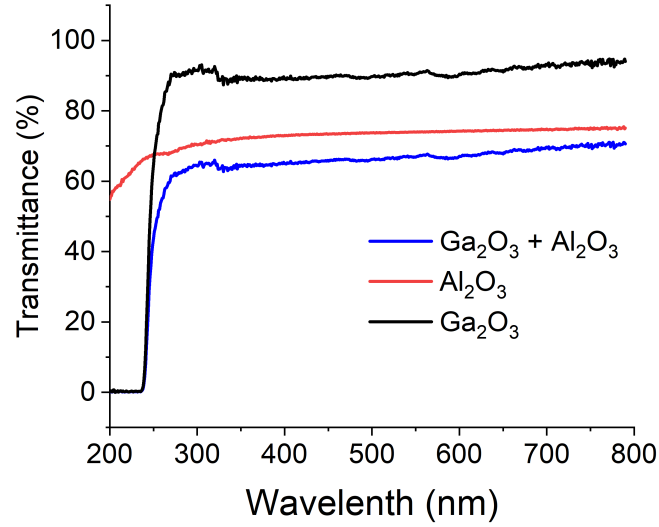


Figure 2.30: Optical Transmittance spectrum of  $> \mu\text{m}$  thick sample  $\alpha$  Ga<sub>2</sub>O<sub>3</sub> used in chapters 3

Figure 2.30 shows a typical transmittance measurement of the HVPE grown samples used in Chapter 3. Due to the heteroepitaxial nature of the samples, a transmittance measurement of the sample and an isolated Al<sub>2</sub>O<sub>3</sub> substrate was obtained. The overall transmittance of the Ga<sub>2</sub>O<sub>3</sub> film was obtained by taking a ratio of the two measurements.

Obtaining the bandgap from transmission measurements first requires a conversion from transmittance to absorbance (A).

$$\frac{I(0)}{I(d)} = \exp(-\alpha d) \quad (2.23)$$

Neglecting reflections, light that is not absorbed by the sample is transmitted

$(1=A+T)$  can be considered as the transmittance,  $T$ , expressed as

$$\alpha = \frac{1}{d} \ln\left(\frac{1}{T}\right) \quad (2.24)$$

using equation 2.24, we can transform the transmittance spectrum in Figure 2.30 into the absorption coefficient spectrum to use equation 2.20 to obtain the band gap.

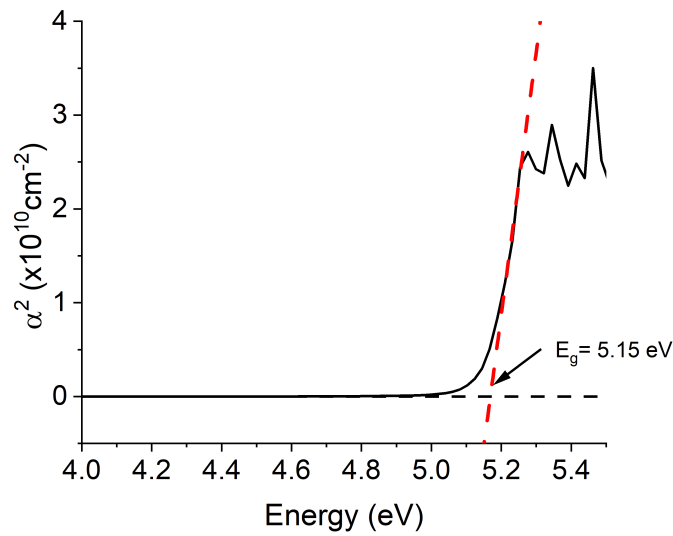


Figure 2.31: Optical Transmission Measurements of 250 nm thick samples  $\alpha\text{-Ga}_2\text{O}_3$  used in chapters 4,5 and 6

Figure 2.31 shows the absorption coefficient data and equation 2.20 to show  $\alpha^2$  as function of photon energy where the bandgap is obtained by taking the intersection of the linear regression from the steepest region of the absorption edge and the baseline. Here we obtain an estimated bandgap value of 5.15 eV, in line with the current literature for  $\alpha\text{-Ga}_2\text{O}_3$  [27, 70].

## Chapter 3

# Hydrogen Related Luminescence in $\alpha$ -Ga<sub>2</sub>O<sub>3</sub>

### 3.1 Background

Given the emergence of Ga<sub>2</sub>O<sub>3</sub> for applications ranging from power electronics to ultraviolet photodetectors, understanding the role of defects in the material is a crucial step to improve the efficiency and reliability of future devices. In the literature, many complementary techniques exist, such as DLTS [62], electron spin resonance [151], and luminescence measurements offer a non-invasive approach to defect characterisation.

Despite the advantages of  $\alpha$ -Ga<sub>2</sub>O<sub>3</sub>, much of the luminescence studies have focused on the more thermodynamically stable  $\beta$  phase. This is perhaps not too surprising given that the study of metastable phases has focused on material growth. Despite the different crystal structure, the limited luminescence measurements on  $\alpha$ -Ga<sub>2</sub>O<sub>3</sub> exhibit a similarity to that of the literature  $\beta$  with luminescence in the UV (3.2-3.6 eV), blue (2.8 - 3.0 eV) and green (2.5 eV) [68, 152, 153]. Our initial luminescence studies on the emission spectrum of  $\alpha$ -Ga<sub>2</sub>O<sub>3</sub> showed the expected broad luminescence features in agreement with the literature. However, at low-temperatures, we observed a new luminescence band centered around 3.8 eV. Here we employ temperature-dependent PL measurements on  $\alpha$ -Ga<sub>2</sub>O<sub>3</sub> grown by PEALD and HVPE to characterise the new lumi-

nescence feature around 3.8 eV. We then used low-temperature CL HSI measurements to correlate the surface morphology to the observed luminescence line.

## 3.2 Experimental method

### 3.2.1 Sample Details

The  $\alpha$ -Ga<sub>2</sub>O<sub>3</sub> films were grown on *c*-plane sapphire HVPE in a lab-made quartz reactor at 520°C under atmospheric pressure. O<sub>2</sub> (> 99.99995 % pure) and GaCl were used as the precursors. The GaCl was synthesized by a chemical reaction of metal Ga (> 99.99999 % pure) and HCl gas (> 99.999 % pure) upstream in the reactor at 570 °C. Additional HCl gas was also supplied to enable rapid growth [118] N<sub>2</sub> (dew point < -110°C) was used as the carrier gas. The growth conditions are summarized in Table 3.1, with P<sub>0</sub>(X) being the supply partial pressure of gas X. Here four samples were grown, labelled sample A, B, C, and D. The films were grown in two steps except for sample A. Samples B-D were grown relatively slowly at the first step, and the growth rate was increased at the second step by increasing the partial pressure of GaCl<sub>x</sub>, where *x* represents the stoichiometry of the GaCl compound and H<sub>2</sub> where H<sub>2</sub> was produced by the chemical reaction of Ga and HCl in the reactor yielding different concentrations of H and Cl, as measured by secondary ion mass spectrometry (SIMS) as reported in Table 3.1. Here we note that C, N, Si, and S levels were measured but the concentrations were below the SIMS detection limit. All films had a thickness in the range of 3.5-3.8  $\mu$  m.

The initial samples studied during the PL study were grown by PEALD system where 250 nm thick  $\alpha$ -Ga<sub>2</sub>O<sub>3</sub> was grown on *c*-plane sapphire substrate. The growth was carried out by our colleagues at the University of Liverpool with further details of the growth process found in [29].

PL measurements were obtained using a Photon Systems 224 nm HeAg pulsed laser with luminescence collected by a McPherson 207 monochromator with a grating of 300 lines mm<sup>-1</sup>. PL measurements were recorded between 9 - 290 K. A 280 nm low pass filter was positioned at the entrance slit of the spectrometer to remove laser lines from

Sample	A	B	C	D
P0(GaCl) (kPa)	0.125	0.125/0.25	0.125/0.5	0.125/1.0
P0(H2)(kPa)	0.063	0.063/0.125	0.063/0.25	0.063/0.5
P0 (O2) (kPa)	1.25		1.25/3.125	
P0 (HCl) (kPa)	0.125		0.125/1.25	
Growth rate ( $\mu\text{m}/\text{h}$ )	11.9	11.9/34.1	11.9/73.4	11.9/116
Thickness ( $\mu\text{m}$ )	3.8	0.4/3.4	0.4/3.2	0.4/3.1
H ( $\text{cm}^{-3}$ )	$< 6 \times 10^{16}$	$1.1 \times 10^{17}$	$1.5 \times 10^{17}$	$2.8 \times 10^{17}$
CL ( $\text{cm}^{-3}$ )	$1 \times 10^{16}$	$1.8 \times 10^{17}$	$4.1 \times 10^{17}$	$1.4 \times 10^{18}$
Tilt 0006 (arcsec)	-	135	359	103
Twist 10-12 (arcsec)	-	1820	1442	1361

Table 3.1: Summary of the growth conditions for H series of HVPE grown samples

the measured emission spectrum. A full description of the experimental setup can be found in Chapter 2, section 2.1.1

CL measurements were obtained on a FEI Quanta 250 electron microscope with 400 lines  $\text{mm}^{-1}$  gratings. Due to the required maintenance on the tip in the SEM, the images were obtained at a high operating voltage of 15 kV in an attempt to increase image resolution. However, we note here that this will decrease the CL resolution. At operating voltages as high as 15 kV, sample charging was significant. To reduce charging effects that will cause drift in the HSI map, silver paste was used to create a conductive path from the sample surface to the grounded sample stage.

### 3.3 PL Results

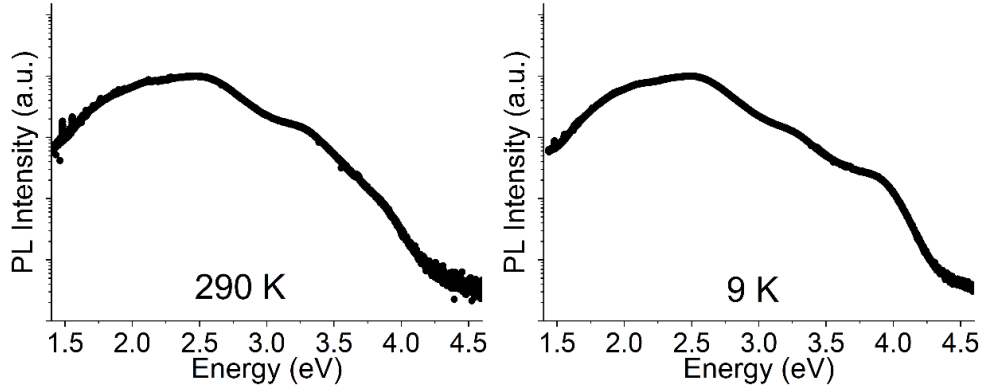


Figure 3.1: PL measurements on 250 nm thick PEALD samples obtained at (left) 290 K (right) 9 K. The Intensity axis is plotted in log scale due to the relative low intensity peak centered around 3.8 eV

The initial luminescence investigation was concentrated on samples with a thickness of 250 nm grown using PEALD, as described in the sample details section. As reported in the literature, the emission spectrum observed is extremely broad, ranging from 1.5 eV to 4.5 eV. It should be noted that the spectra presented in Figure 3.1 has not been corrected for system response. However, in the measurement taken at 9 K, we observe an intriguing feature centred around 3.8 eV. Interpreting this small peak is challenging, since the Al<sub>2</sub>O<sub>3</sub> substrate exhibits an emission feature at roughly 3.8 eV [154], and considering the sample thickness, potential emission from the substrate cannot be ruled out. Given that the absorption coefficient of  $\alpha$ -Ga<sub>2</sub>O<sub>3</sub> is in the order of  $\times 10^5 \text{ cm}^{-1}$  [155], which results in high surface absorption, only about 0.1 percent of light reaches the substrate. Furthermore, any light emitted from the substrate would be re-absorbed by the Ga<sub>2</sub>O<sub>3</sub> before being emitted from the surface, making it unlikely that the emission observed around 3.8 eV originated from the substrate. DLTS is a well-established method for detecting energy levels within the bandgap and appeared to be the most promising approach to identify potential defect levels that could facilitate the observed transition [99, 156]. The literature suggests that there was a consistent

### Chapter 3. Hydrogen Related Luminescence in $\alpha$ -Ga<sub>2</sub>O<sub>3</sub>

association with H-related defects located roughly 1.3 eV above the valence band in  $\beta$ -Ga<sub>2</sub>O<sub>3</sub>, suggesting the potential of H-related optical emission due to H incorporation in various growth processes. The above discussion led to the collaboration with Dr Yuichi Oshima to grow thick  $\alpha$ -Ga<sub>2</sub>O<sub>3</sub> samples grown by HVPE containing varying levels of H, as detailed in table 3.1.

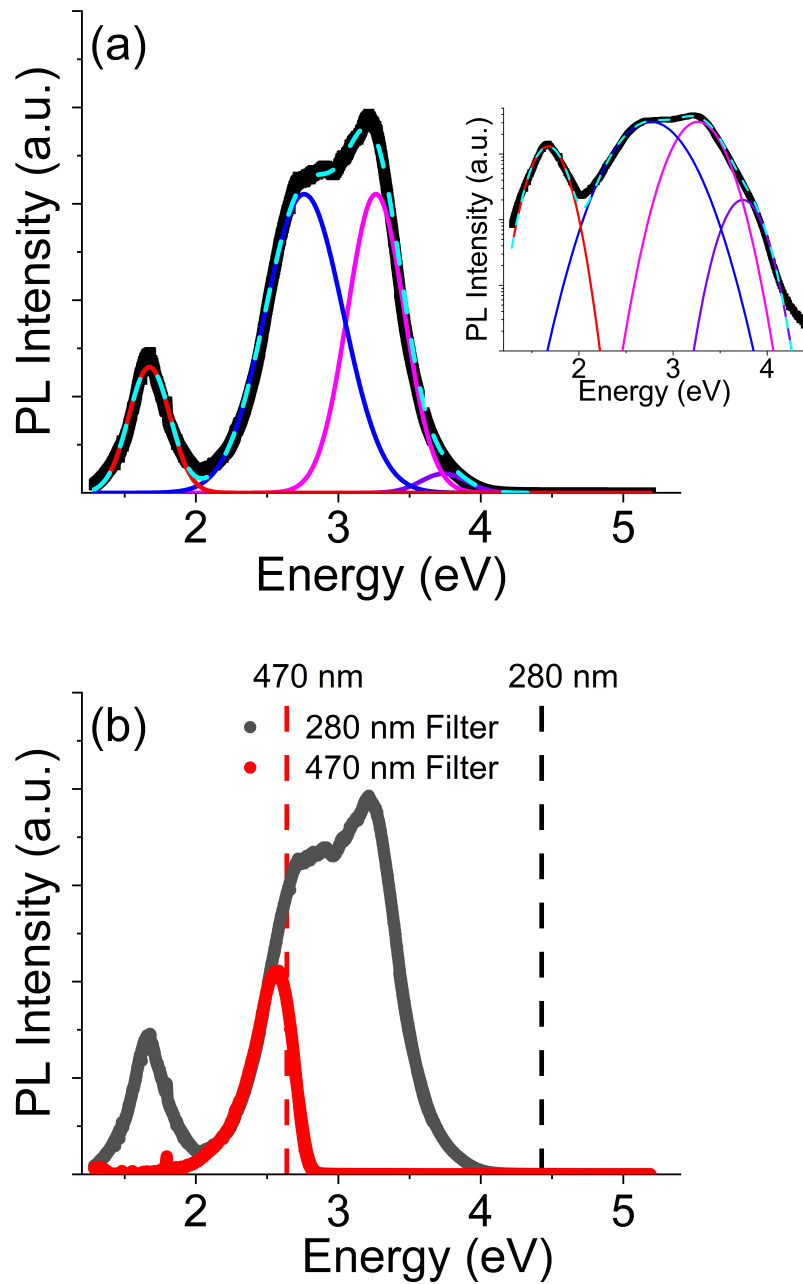


Figure 3.2: 290 K PL spectrum of sample C where the H concentration ( $[\text{H}] = 1.5 \times 10^{17} \text{ cm}^{-3}$ ). Inset shows the PL spectrum of sample C measured at 290 K in log scale highlighting the presence of the 3.8 eV peak (b) 290 K PL spectrum of sample C ( $[\text{H}] = 1.5 \times 10^{17} \text{ cm}^{-3}$ ) with 280 nm filter (black) and 470 nm filter (red)

Figure 3.2(a) shows the typical 290 K spectrum of sample C. The PL spectra exhibit broad emission bands centered at 3.3 eV (UV), 2.7 eV (blue) and 1.6 eV (red) in close agreement with the literature [78, 80, 85]. The emission in the blue spectral region is typically associated with DAP recombination involving a host of intrinsic defects with  $V_O$ ,  $V_O-V_{Ga}$ ,  $Mg_{Ga}$ , and  $Ga_i$  suggested as possible donors and acceptors [157, 158]. What we again observed was the small, barely distinguishable luminescence band around 3.8 eV demonstrated by the log scale plot in the inset of Figure 3.2(a), similar to what we saw from the PEALD grown samples in 3.1. Here we remind the reader that neither of the PL spectra in Figure 3.2 or Figure 3.1. The luminescence line has rarely been observed in the literature [67, 70, 153] and so far no assignment of its origin in  $\alpha$ -Ga<sub>2</sub>O<sub>3</sub>. The temperature effects on the luminescence line will be investigated later in this work in order to try and assign an origin. At this stage, we turn our attention to the luminescence feature in the red spectral region situated around 1.6 eV. Comparing the emission spectrum from the PEALD and HVPE grown samples, we see that the red luminescence is much more dominant for the HVPE sample series. Given that the literature suggests that the red luminescence line has origins associated with H or N impurities [70, 84], close attention was paid to the red luminescence line at 1.6 eV. At first instance, the increased red luminescence at 1.6 eV of the HVPE samples could be attributed to the increase in H concentration. Due to the high intensity and position of the 3.3 eV UV line, the possibility of second order diffraction having an impact on the emission spectra must be considered. To address this, we used a 470 nm long pass filter to remove the UV luminescence, which resulted in the removal of the red luminescence from the spectra, shown in Figure 3.2(b). Therefore, for the samples analysed in this chapter, the red emission is determined to be that of second order diffraction of the UV and will not be shown in the luminescence spectra in the later figures.

By analogy to  $\beta$ -Ga<sub>2</sub>O<sub>3</sub>, UV emission is typically attributed to the recombination of free electrons with STH. As a reminder of the discussion from Chapter 1, the main reason for the generation of these STH lies in the composition of the valence band for which the upper state is mainly made up of O 2p orbitals which have characteristics such as small dispersion and large effective masses [41]. The associated holes, with

large effective mass, become localized at O sites in the crystal lattice, resulting in lattice distortion generating a potential that actively lowers the mobility of holes. The self trapped In  $\beta$ -Ga<sub>2</sub>O<sub>3</sub> there are three non-equivalent O sites, two of which have trigonal coordination and one with tetrahedral coordination [159]. According to first-principles calculations, the holes tend to localize on the trigonally coordinated sites meaning there are two possible sites for the STHs in  $\beta$ -Ga<sub>2</sub>O<sub>3</sub> [159], which is reflected in PL with two bands resolved in the UV region [83]. However,  $\alpha$ -Ga<sub>2</sub>O<sub>3</sub> has only one type of O site [159]. Therefore, it may be expected that only one luminescence band in the UV region may be attributed to recombination of free electrons and STH, ruling out the assignment of the 3.8 eV line as STH-related.

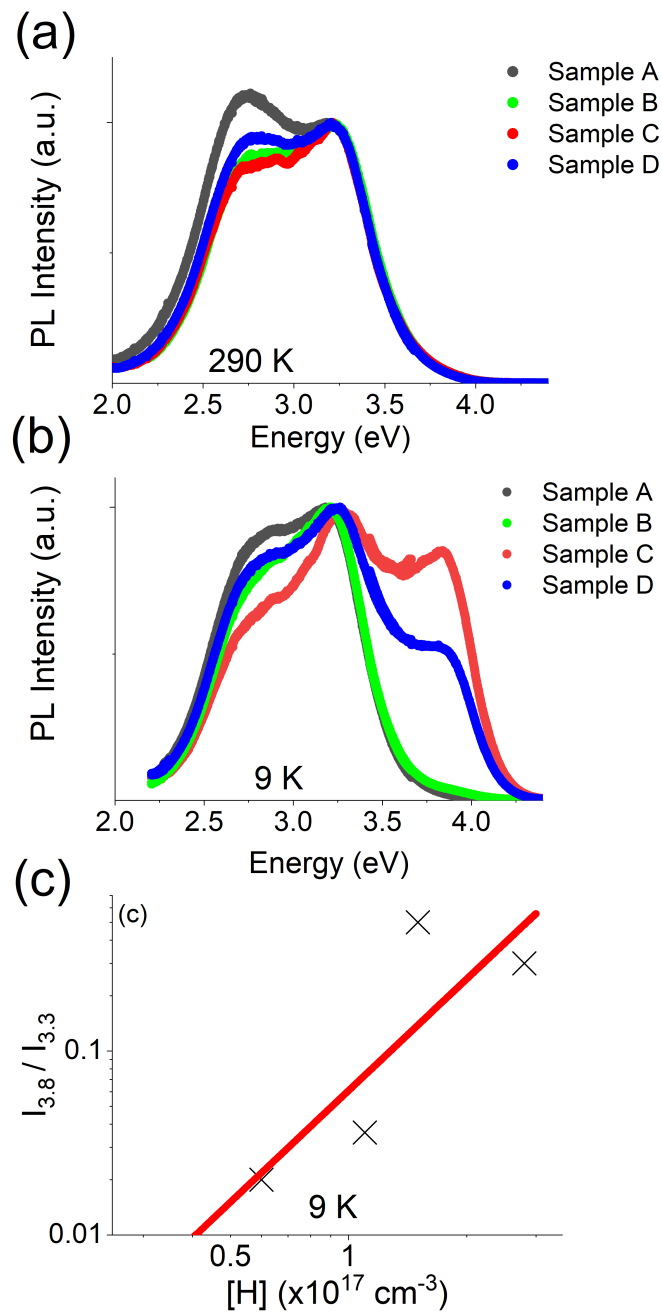


Figure 3.3: PL spectra of samples A, B, C and D measured at (a) 290 K (b) 9 K. (c) Illustrates the correlation between the integrated intensity of the 3.8 eV luminescence line and H concentrations of the samples

Figure 3.3(a) shows the PL spectra of the HVPE grown samples measured at 290 K. Other than the small variation in the blue line intensity, all 290 K PL spectra were

identical. A strong variation in the luminescence spectrum of the samples appeared when the temperature decreased to 9 K, as shown in Figure 3.3(b). Figure 3.3(b) shows a clear enhancement of the 3.8 eV luminescence line with respect to the 290 K measurements, particularly for samples C and D. To assess the impact of temperature on the luminescence lines, we looked at the ratio of the integrated intensities of each line measured at 9 K and 290 K. We observe a disproportionate enhancement of the integrated intensity of the 3.8 eV luminescence line of samples C and D, which increases by a factor of 18 and 15 respectively compared to samples A and B where for sample A there is no enhancement of the 3.8 eV luminescence line at 9 K and for B only increases by a factor of 2. Here we point out that using relative peak intensity should be treated tentatively due to the the PL system not being corrected for system response and can't be compared directly with the results from other groups. However, as the 4 samples in this work were measured using the same PL system a comparison between sample sets was deemed reasonable.

From the SIMS measurements shown in Table 3.1, it can be seen that samples C and D have a higher concentration of H and Cl. These impurities are incorporated into the films during the growth process where HCl was used, however  $P_0(\text{HCl})$  is the same for samples B-D. Therefore, additional HCl should not be the dominant cause of variation in [H] and [Cl]. Rather, we expect GaCl<sub>x</sub> and H<sub>2</sub> were the impurity sources because their partial pressures increased to increase the growth rate. Note that H<sub>2</sub> was produced by the chemical reaction at the Ga container upstream in the reactor ( $\text{Ga} + \text{HCl} = \text{GaCl} + 1/2\text{H}_2$ ). H<sub>2</sub> was also produced by the following reaction  $\text{GaCl} + 2\text{HCl} = \text{GaCl}_3 + \text{H}_2$ . More details can be found in [118]. The variation of the 3.8 eV integrated emission at 9 K with impurity concentration is a strong indicator that this luminescence line is not associated with STH emission, as STH luminescence is assumed to be impurity independent [83]. From theoretical calculations, it is predicted that both H and Cl can act as shallow donors in Ga<sub>2</sub>O<sub>3</sub> [41], which would explain the strong correlation of the integrated intensity with temperature. At high temperatures, electrons from shallow donors are thermally excited to the conduction band where they are free to recombine with a hole. At low-temperatures, there is less thermal energy

in the lattice resulting in the electron being effectively frozen at the donor state, thus reducing the number of available recombination pathways.

To distinguish whether H or Cl is responsible, we turn our attention to samples grown by PEALD [111]. The PEALD growth process involves the use of triethylgallium [Ga(C<sub>2</sub>H<sub>5</sub>)<sub>3</sub>] as Ga precursor, Ar as the purge gas and O<sub>2</sub> as the plasma source. No Cl is involved in the process, and to our knowledge in the design of the reactor. The PL spectra of the PEALD samples were measured at 9 K, shown in Figure 3.1(b). In this sample, we observe similar emission properties of the 3.8 eV luminescence line in that we observe low, barely distinguishable emission at 290 K and then a strong increase in intensity at 9 K, which leads us to believe that the 3.8 eV lines relates to H, and not Cl.

Therefore, we now turn our attention to the role of H in the samples. We observe a strong correlation between the integrated intensity ratio at 9 K of the luminescence lines centered at 3.3 eV and 3.8 eV where the integrated intensity ratio tends to increase with H concentration as shown in Figure 3.3. Atomic force microscopy (AFM) and X-ray diffraction (XRD) were used to assess whether this variation in luminescence could be due to sample quality. AFM data of the HVPE grown samples is shown in Figure 3.4 where the surface morphology of samples C and D is very similar, in terms of topography and roughness, shown in panel (c,d) respectively.

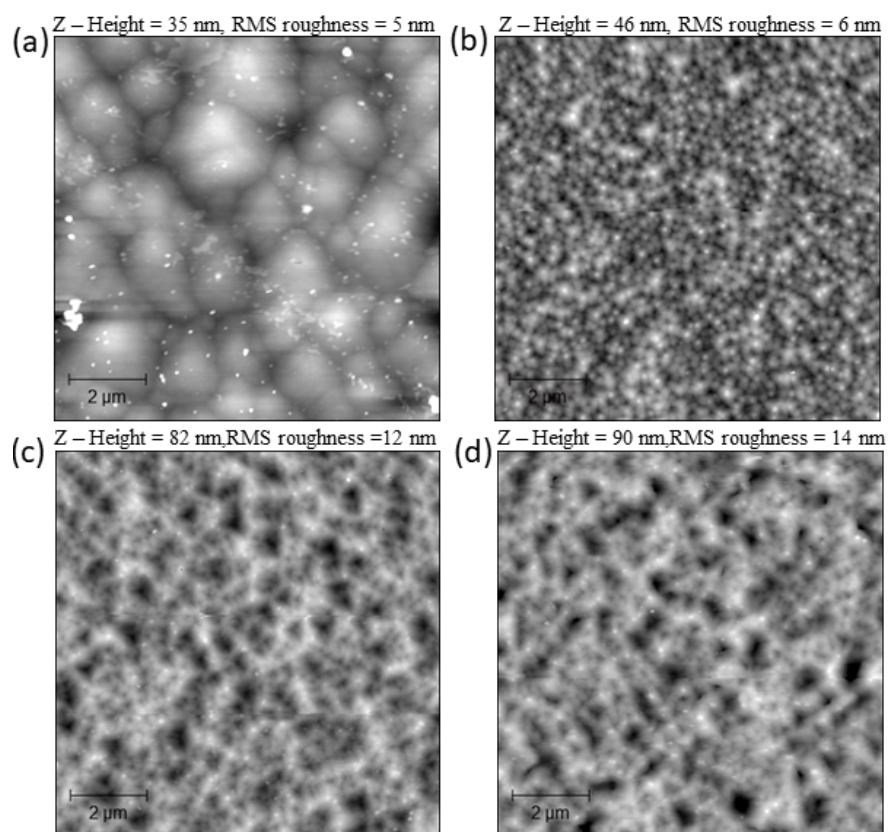


Figure 3.4: Topography maps obtained from AFM of (a) sample A, (b) sample B, (c) Sample C, and (d) sample D

XRD analysis shown in Figure 3.5 shows that the XRD diffractograms of samples B, C, and D showing a sharp characteristic  $\alpha$ -Ga<sub>2</sub>O<sub>3</sub> reflection around 40.25°

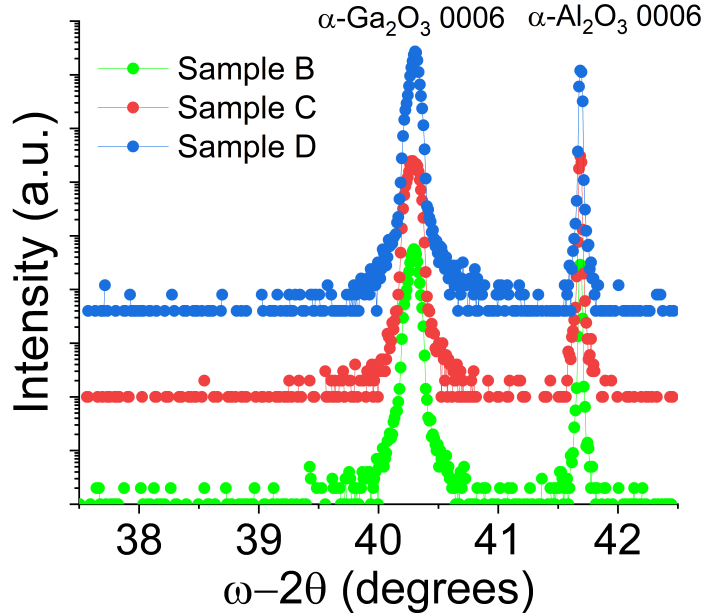


Figure 3.5: XRD diffractograms of samples B,C, and D showing a sharp characteristic  $\alpha$ -Ga<sub>2</sub>O<sub>3</sub> reflection around  $40.25^\circ$

We note that the main difference between samples C and D is that sample C exhibits a greater tilt (359 arcsecs) compared to sample D (103 arcsecs), detailed in table 3.1 While these values are still low, the increased tilt indicates a slightly greater misorientation of the grains, leading to a greater density of grain boundaries and dislocations in sample C which could have an (still not fully understood) effect on the luminescence. The 3.3 eV emission has already been attributed to STH which will be invariant of impurities. H incorporates into Ga<sub>2</sub>O<sub>3</sub> either on interstitial (H<sub>i</sub>) or substitutional (H<sub>O</sub>) sites, with both exhibiting low formation energies [54]. Therefore, both are likely to exist as shallow donors in Ga<sub>2</sub>O<sub>3</sub>. Previous work on muonium, which has similar characteristics to H, suggested that H is a shallow donor with a donor depth of  $15 < E_d < 30$  meV [160].

### Temperature-Dependent Measurements

We investigated the temperature dependence of the 3.8 eV line, shown in Figure 3.6. We can see that the intensity of the line increases dramatically as the temperature

decreases below 100 K, while the 3.3 eV line is comparatively less affected by the temperature.

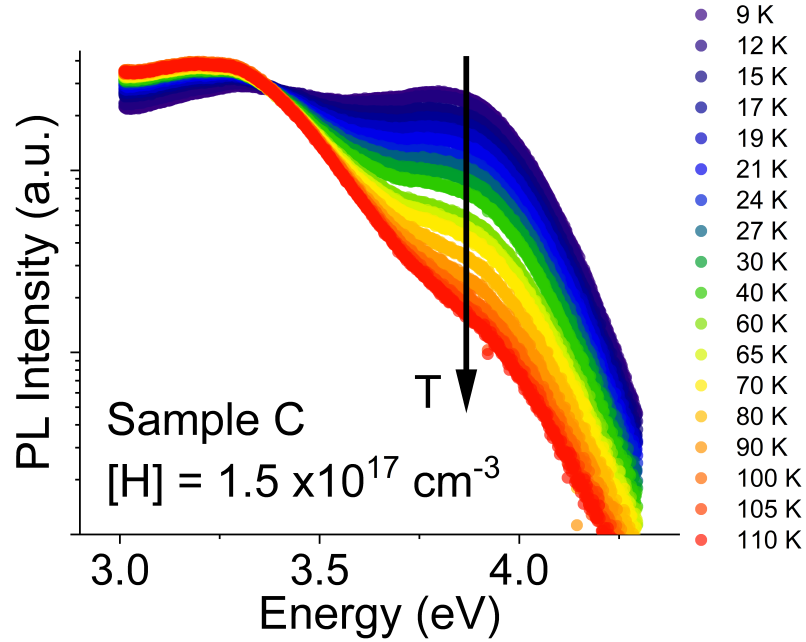


Figure 3.6: Temperature-dependent luminescence of sample C measured between 9 K and 110 K

*A quantitative approach*

Temperature-dependent PL typically offers an avenue for obtaining activation energies of the defects that are contributing to the emission peak. This is typically achieved by obtaining the integrated intensity of the peak as a function of temperature. Given here we obtain such a low activation energy of 3 meV, we must consider the accuracy of the measurement process, and whether this approach to activation energy is reliable in this instance.

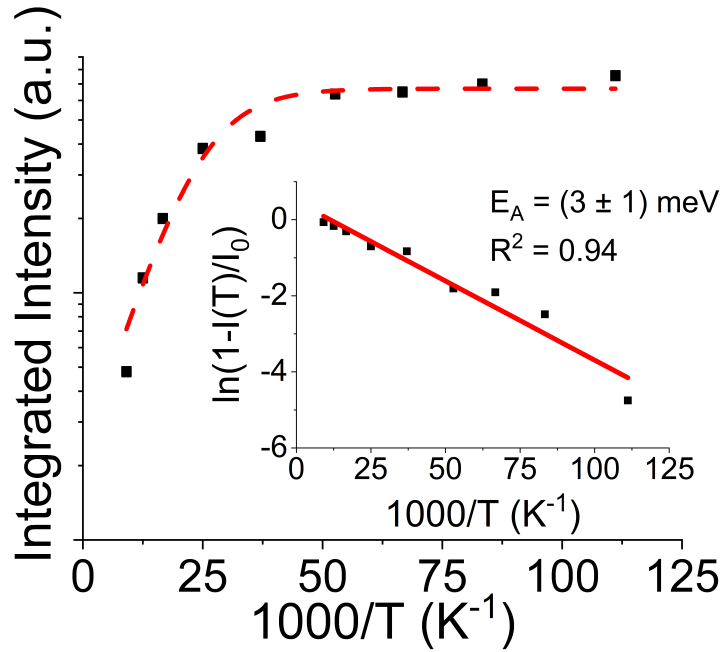


Figure 3.7: Arrhenius plot to obtain the activation energy of the 3.8 eV luminescence line

First, consider the position of the heater, the temperature sensor, and the sample itself. The heater is wrapped around the aluminium sample holder with the temperature sensor on the aluminium sample stub, and not the sample surface itself. Therefore, there may be a discrepancy between the sample temperature and the sample stub temperature. Furthermore, with Ga<sub>2</sub>O<sub>3</sub> and the Al<sub>2</sub>O<sub>3</sub> substrate both exhibiting such low thermal conductivities of 10 and 40 Wcm<sup>-2</sup> at room-temperature, respectively [161,162], this will result in a larger degree of uncertainty of the sample temperature. To try and alleviate the problem, the temperature was allowed to settle for roughly 5 minutes before each acquisition. In terms of light emission from the sample, Figure 3.6 shows a large degree of overlap in the peak centered at 3.3 and 3.8 eV. Due to the strong overlap between the lines, it would be inaccurate to attempt to extract an activation energy for this line.

*A qualitative approach*

However, such a temperature dependence is in line with an origin involving a shallow donor with  $E_d$  in the order of 10s meV given that shallow donors are characterised

by states that are close to the conduction band, therefore thermal excitation can be achieved at low temperature. Let us consider the available thermal energy at 100 K is around 9 meV using ( $E=kT$ ), at temperatures below 100 K the donor electron remains bound to the shallow state. At temperatures exceeding 100K the shallow state becomes ionised and the donor electron subsequently becomes a free electron free to move in the conduction band, and as a consequence no recombination occurs from the donor state. The low ionisation energy indicates the involvement of a shallow donor.

To address the energy emission of 3.8 eV, we require a deep level acceptor to facilitate the recombination from the aforementioned H related donor. It is well-established that it is difficult to identify with absolute certainty the defect involved in the recombination process via PL measurements, even more so in the case where broad, overlapping luminescence lines are involved such as those shown in Ga<sub>2</sub>O<sub>3</sub>. However, what we can establish is that there is a strong correlation between the H concentration of the thick films and the integrated intensity of the 3.8 eV luminescence line. Therefore, it is reasonable to suggest that H plays a significant role in the recombination process. As previously mentioned, the interaction of H and V<sub>Ga</sub> leads to the formation of H-decorated V<sub>Ga</sub> complexes (V<sub>Ga</sub>-nH), where n is the number of H atoms involved in the complex defect. Polyakov *et al.* identified a defect energy level positioned 1.3 eV above the valence band maximum [99]. We can tentatively improve on the precision of the number of H atoms involved in the complex vacancy by revisiting the work by Islam *et al.* which showed that the complex vacancy will be in the acceptor state when 1, 2, or 3 H atoms are bound to the V<sub>Ga</sub> [65]. To assess the suitability of the (V<sub>Ga</sub>-nH) related complex as the acceptor in our DAP recombination model, we use a dipole approximation expressed in equation 3.1 to calculate the emission energy [90].

$$hv(DAP) = E_g - (E_a - E_d) + \frac{e^2}{4\pi\epsilon r} \quad (3.1)$$

Where  $E_g$  is the band gap energy,  $E_a$  is the acceptor ionisation energy,  $E_d$  is the donor ionisation energy, the final term to the right represents the energy associated with the with the coulomb interaction where  $e$  is the charge of an electron,  $\epsilon$  is the

low-frequency dielectric constant and  $r$  is the separation of the donor and acceptor. As a first approximation, the distance  $r$  can be given as a function of donor concentration,  $N_D$ , given by equation 3.2

$$r = \sqrt[3]{\frac{3}{4\pi N_D}} \quad (3.2)$$

Calculating  $r$  yields a donor-acceptor pair separation of 11 nm assuming that the donor concentration is of the order of magnitude of the H concentration detected by the SIMS measurements shown in Table 3.1. Using 10 as the relative permittivity of  $\alpha$ -Ga<sub>2</sub>O<sub>3</sub> [99],  $E_d = 15$ -30 meV as the shallow donor ionization energy obtained from King *et al.* [160] (in line with our observation of Figure 3.6),  $E_a$  as 1.3 eV as obtained from Polyakov *et al.* [99] and finally  $E_g = 5.2$  eV from the transmittance measurements shown in Figure 2.31, we find a DAP emission energy of 3.9 eV which is in excellent agreement with our emission energy obtained experimentally. While  $E_d$  is small relative to  $E_g$  and  $E_a$ , it is essential to include both contributions for completeness, neglecting the  $E_d$  would omit an important component of the energy balance resulting in an incomplete characterisation of the emission energy

A schematic of the proposed DAP recombination process is shown in Figure 3.8.

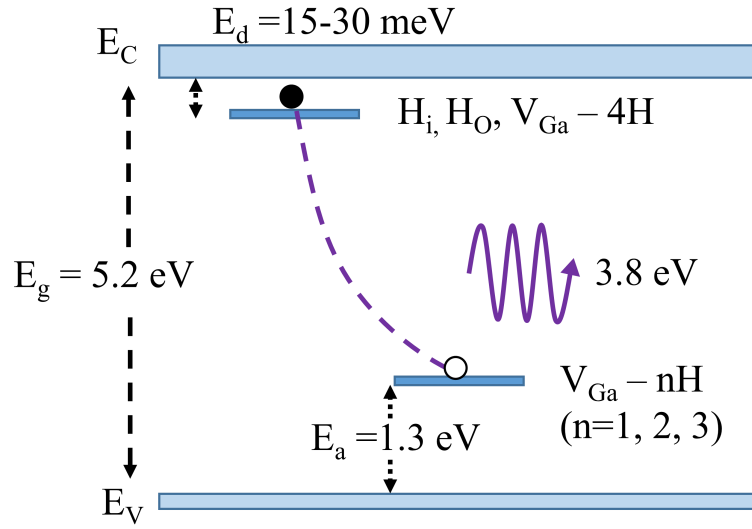


Figure 3.8: Model for the 3.8 eV luminescence recombination mechanism. The purple dashed line represents donor acceptor pair recombination when  $T < 110 \text{ K}$ .

The variation of the integrated intensity of the 3.8 eV line with H concentration, along with the identification of the  $V_{Ga}$  related complex 1.3 eV above the valence band by Polyakov *et al.* leads us to believe that there is strong evidence of H decorated  $V_{Ga}$  complex acts as an acceptor in our recombination model [99]. The low formation energy of H related donors, along with the low activation energy, strongly favours the incorporation of H as a donor in either the  $H_i, H_O, V_{Ga}-nH$  configuration [54, 65, 160]. However, due to the shallow donor depth, we cannot unequivocally rule out the role of a bound exciton.

Recombination involving free electrons in the conduction band was considered, however, the strong trend of the emission line with hydrogen supports DAP recombination. Furthermore, according to the Varshni equation, the band gap of  $\text{Ga}_2\text{O}_3$  increases as the temperature decreases [163]. Therefore, if the recombination were associated with free electrons in the conduction band, we would expect to observe a blue shift in the emission energy.

Further power-dependent and time resolved luminescence studies will offer further

insight into mechanisms involved in the 3.8 eV emission

### 3.4 CL Results

#### Room-temperature Measurements

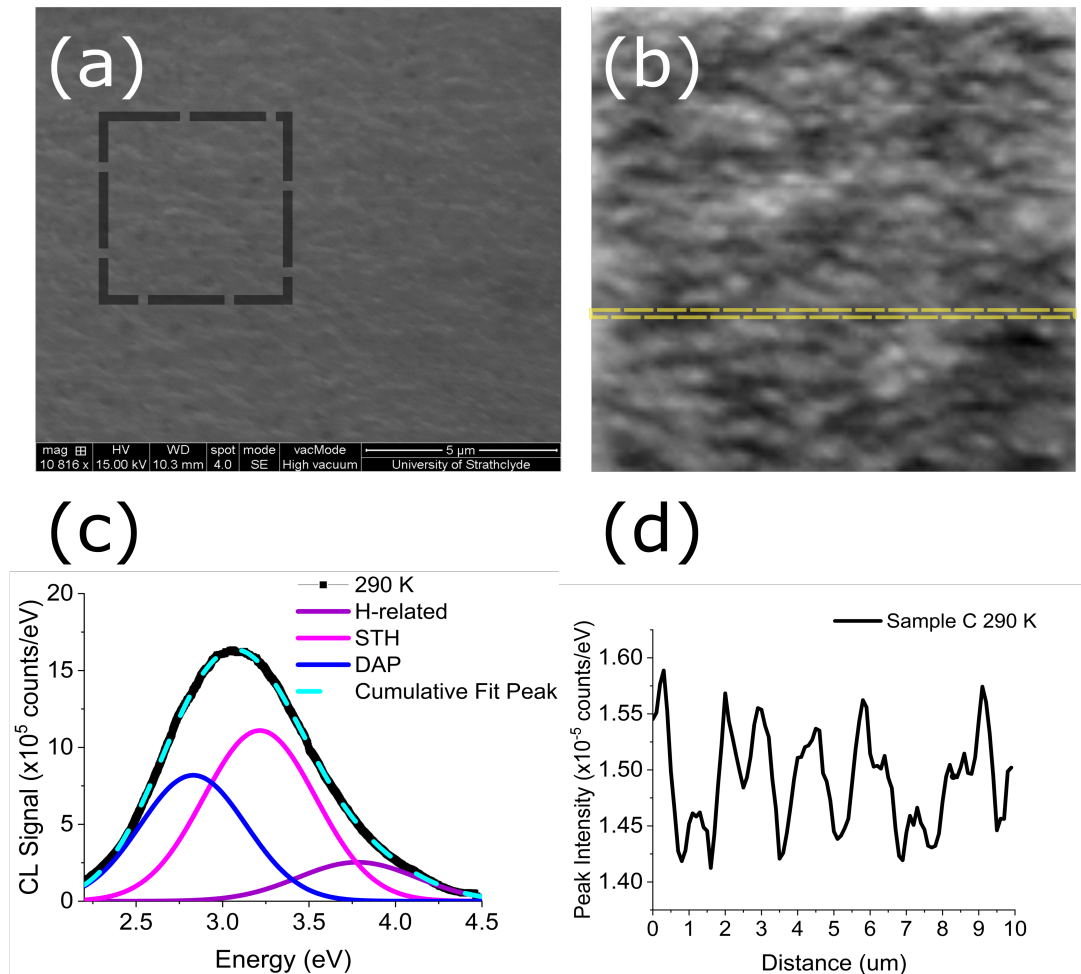


Figure 3.9: SEM information obtained from sample C with  $[H]=1.5 \times 10^{17} \text{ cm}^{-3}$  (a) SEM image (b) panchromatic CL image (c) System corrected CL spectra measured at 290 K (d) Horizontal line scan showing variations in CL peak intensity

Figure 3.9(a) shows an SEM SE image, indicating excellent resolution with granular grain structure comparable to that obtained by the AFM image shown in Figure 3.4. To

obtain spatially dependent luminescence information, a large hyperspectral image was obtained over a  $10\mu\text{m} \times 10\mu\text{m}$  region marked by the dashed line in the SEM image shown in Figure 3.9(a). To observe a system corrected response, a mean spectra was obtained from the hyperspectral map, resulting in the spectrum shown in Figure 3.9(c), where 3 peaks are observed around 3.8 eV, 3.3 eV and 2.7 eV. However, what appears to be more evident here is the prominence of the H-related peak at 3.8 eV at room temperature compared to the uncorrected PL spectrum, which is still largely dominated by STH and DAP emission. Figure 3.9 shows a line spectrum obtained from the hyperspectral image indicating some clear variation of the peak intensity, where the peak is the overall cumulative peak rather than the H-related, STH or DAP peaks. Interestingly, we see a close correlation with the trend of the peak intensity across the sample surface and the grain size observed by AFM measurements.

## Temperature-Dependent Measurements

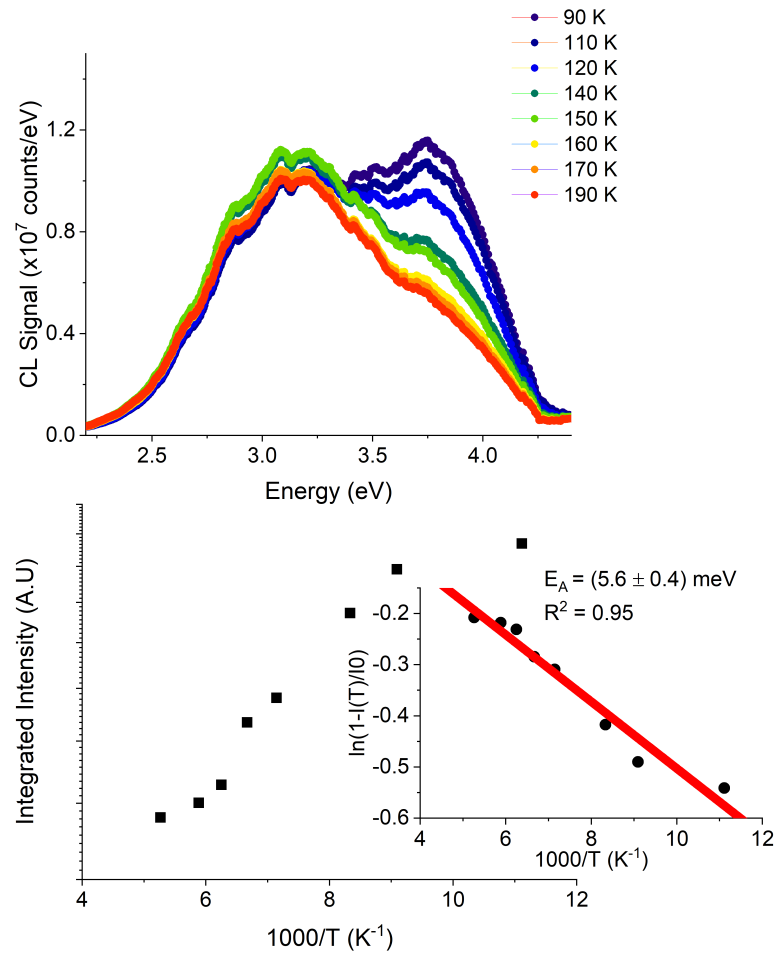


Figure 3.10: (top) CL temperature dependence measured between 90 K and 190 K (bottom) Activation energy obtained via Arrhenius equation revealing an activation energy of 5.6 meV

Figure 3.10 (top) shows the temperature-dependent CL spectra obtained by obtaining a mean spectrum obtained from the panchromatic CL image shown in Figure 3.11. The measurements were obtained between 90 K and 190 K, with the 90 K lower limit due to the liquid nitrogen cooling system. First of all, here we observe a confirmation of the uncorrected PL spectra where we see a strong emergence of the H-related luminescence peak centred at 3.8 eV. A clear difference between the CL and PL spectra is that the temperature effect on the 3.8 eV peak is dominant at higher temperatures relative to the

PL measurements. However, direct comparisons of PL and CL measurements must be caveated to the effect that the excitation source is different, with the effect of excitation power on the 3.8 eV unknown. Like the PL temperature-dependent measurements, an activation energy was obtained by the use of an Arrhenius equation with a value of 5.6 meV extracted, which is of the same order as the PL activation energy. However, this method remains questionable with the effect of overlapping peaks making interpretation difficult.

### **Spatial Information at 90 K**

Figure 3.11(a,b,c) shows the SEM images obtained by accelerating the 10 kV voltage and setting the spot size at 4. Figures 3.11(d,e,f) show the corresponding mean spectra recorded for sample C. The shaded region in the SEM images indicates the mapped region. Here we note the spectra have been corrected for the system response as detailed in Section 2.

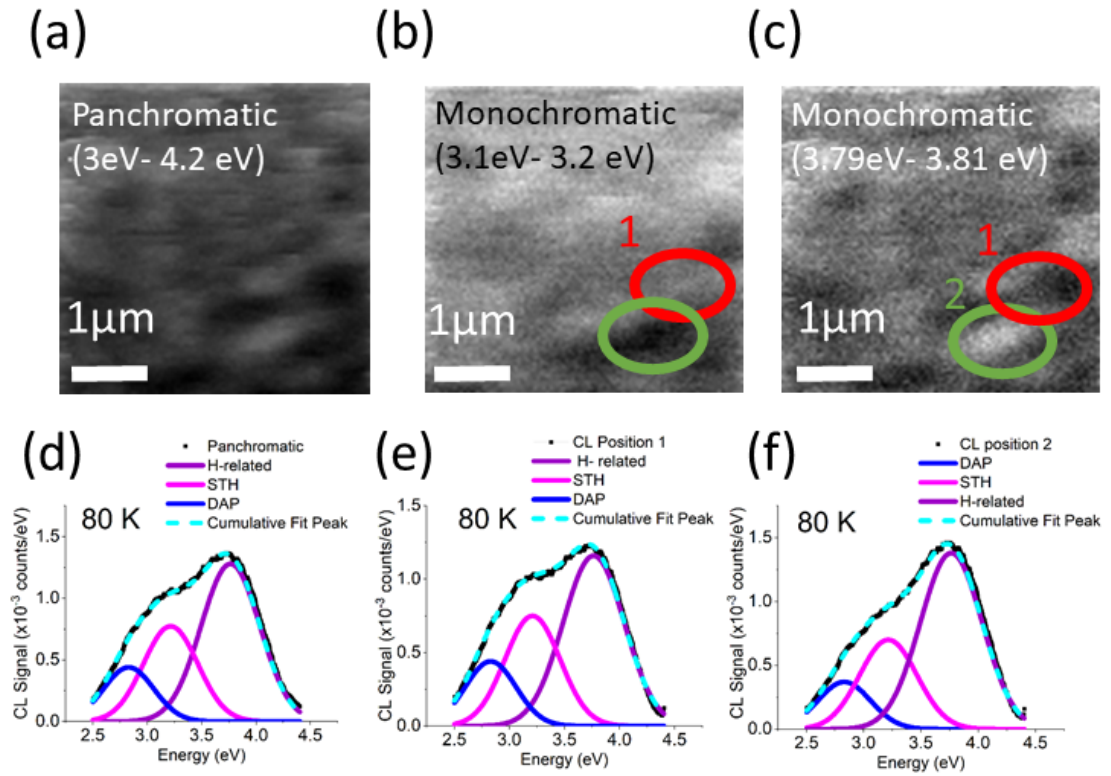


Figure 3.11: CL measurements obtained from sample C at 80 K. HSI measurements are shown in (a) Panchromatic between 3- 4.2 eV (b) Monochromatic 3.1 - 3.2 eV (c) Monochromatic (3.79-3.81 eV). Mean CL spectra measured (d) entire HSI region (e) mean spectra over region 1 marked by the red circle in image b (c) mean spectra over region 2 marked by the green circle shown in images b and c

In Figure 3.11, there is clear evidence of some spatial variations in the luminescence spectra measured at 90 K. The monochromatic CL images shown in (b) and (c) were generated by integrating the emission intensity over the spectral windows of 3.1 - 3.2 eV and 3.79-3.81 eV, respectively. Here we observe a degree of anticorrelation between the images. In the circles region, the mean spectra were recorded to make a comparison of the CL emission and to observe a variation in the relative intensities of the STH and H-related emission lines. The possibility of a non-uniform H distribution during the growth process is speculation here. This finding may be of particular interest for device design. As H<sub>i</sub> in Ga<sub>2</sub>O<sub>3</sub> is thought to be a shallow donor and speculated to increase the

conductivity of the material, an inhomogenous distribution of H concentrations may result in non-uniformity in the sample conduction properties at the surface.

### 3.5 Conclusions and future work

In conclusion, we investigated the optical properties of  $\alpha$ -Ga<sub>2</sub>O<sub>3</sub> thick films with measurable variations of H and Cl concentrations by means of temperature-dependent PL. The study shows a significant enhancement of the UV luminescence band at 3.8 eV at low temperatures, with a strong correlation with the H concentration of the samples. Sample A ( $[H] < 6 \times 10^{16} \text{ cm}^{-3}$ ) exhibits barely distinguishable luminescence at 3.8 eV even at temperatures as low as 9 K. On the other hand, Samples C ( $[H] = 1.5 \times 10^{17} \text{ cm}^{-3}$ ) and D ( $[H] = 2.8 \times 10^{17} \text{ cm}^{-3}$ ) showed an enhancement in integrated intensity by a factor of 15 and 20, respectively. The strong temperature dependence of the 3.8 eV luminescence line, indicates the role of a shallow donor. Here, we tentatively ascribe the luminescence to DAP recombination where the donor is H related to possible candidates H<sub>i</sub>, H<sub>O</sub> or V<sub>Ga</sub> - 4H, and the acceptor as V<sub>Ga</sub>-nH where n =1,2,3. This study indicates that even small changes in H content of less than 1 order of magnitude can have a significant effect on the UV luminescence properties.

Although this work has presented a good contribution to the field with the first identification of H-related luminescence in the deep UV region, there remain many opportunities for future experiments on this H series sample set. Firstly, a power-dependent luminescence experiment should be performed to gain further insight into the recombination mechanisms involved. DAP emission typically exhibits a power-dependent response, where the central peak wavelength would shift with power. This would further corroborate the assignment of the 3.8 eV luminescence line to DAP emission. At the time of the experiment, this was not possible on either the PL and CL system, with the 224 nm laser not able to provide a high enough power that could be degraded by the order of magnitude required for a reliable study.

Time-resolved luminescence measurements again may elude to the recombination process involved, where DAP and STH emission will exhibit differing decay times;

therefore, this experiment may provide more conclusive evidence of the STH emission assigned to the peak around 3.1 eV.

Due to the inhomogeneous nature of the 3.8 eV luminescence line, electron-beam-induced current experiments may provide useful information regarding the conductivity across the sample surface.

## Chapter 4

# Impact of Experimental Conditions on the Behavior of $\alpha$ -Ga<sub>2</sub>O<sub>3</sub> Photodetectors

### 4.1 Background

The development of the photoelectric characterisation setup marked a significant achievement in the PhD research, using the signatone probe station coupled to the source measurement unit, thus facilitating the characterisation of photodetectors with microscale device architectures. With an ultrawide-bandgap ranging from 5.1 to 5.3 eV [27, 70],  $\alpha$ -Ga<sub>2</sub>O<sub>3</sub> exhibits excellent solar-blind UV detection capabilities [69, 164, 165]. This capability of measuring UV light independently of the solar spectrum is crucial for addressing new practical challenges. As the impact of global warming becomes more apparent and the protection from the ozone layer decreases, solar-blind photodetectors have become essential in monitoring the increased levels of UV radiation [166, 167]. Furthermore, the increase in forest fires requires reliable flame detection methods to help mitigate their rapid spread [168].

A common parameter for describing photodetector performance is the so-called responsivity [13], defined as the photocurrent generated per unit of incident optical

Chapter 4. Impact of Experimental Conditions on the Behavior of  $\alpha$ -Ga<sub>2</sub>O<sub>3</sub> Photodetectors

power, given by the expression

$$R_{\lambda} = \left( \frac{I_{PH} - I_{dark}}{P_{\lambda}} \right) \quad (4.1)$$

where  $I_{PH}$  is the photocurrent,  $I_{dark}$  is the dark current, and  $P_{\lambda}$  is the incident optical power.

A second parameter that is a crucial metric in characterising photodetectors is the response speed, typically measured by the rise and decay times. A typical technique used within the Ga<sub>2</sub>O<sub>3</sub> community involves the use of a bi-exponential equation to model the photocurrent decay, where each exponential is related to rapid and slow time constants associated with band-band and defect-related transitions [169,170]. Traditionally, the rise time is defined by the time taken for the photocurrent to rise from 10% to 90% of its maximum value and vice versa for the decay time [13].

Literature on  $\alpha$ -Ga<sub>2</sub>O<sub>3</sub> detectors shows considerable variation in the values of responsivity and response time, highlighted in Table 4.1. The studies discussed also show significant variation in the experimental parameters, such as applied bias, illumination intensity, and excitation wavelength. Certain experimental parameters such as excitation wavelength have an obvious effect on the measured responsivity. However, Wang *et al.* studied the impact of illumination intensity on the responsivity and response speed, where the responsivity ranged from 0.4 to 0.7 AW<sup>-1</sup>, while response time exhibited a power-law relationship with illumination intensity [114].

Illumination Intensity ( $\mu$ Wcm <sup>2</sup> )	Applied Bias (V)	Responsivity (AW <sup>-1</sup> )	Rise/Decay (s)	Ref
130	20	0.015	not defined, sub 1s	[139]
70.5	10	70.26	0.41/0.04	[115]
Not mentioned	10	0.19	19/90 x10 <sup>-6</sup>	[171]
700	20	0.76	540/89 x10 <sup>-9</sup>	[172]
46	10	1.2	Several seconds	[70]
Not mentioned	20	500	5.47/0.44	[69]
100	5	4200	10s of seconds	[140]
Not mentioned	5	3.36	Not mentioned	[173]
Not mentioned	5	0.5	No mention	[174]

Table 4.1: Comparison of photodetector performance parameters of several Ga<sub>2</sub>O<sub>3</sub> based devices

This effect raises the question: How relevant and reflective is responsivity as a metric when assessing photodetector performance? Furthermore, it is possible to compare

photodetectors in the literature where experimental conditions such as applied voltage and illumination intensity vary significantly, if mentioned at all. Later in the chapter, we will also discuss the impact of the device architecture on the reported values. The primary aim of this chapter is to test the suitability of an experimental setup for photodetector characterisation purposes, leading to an investigation of how photodetector performance is reported in the literature, and to suggest an approach that may remove the impact of some experimental variables and act as a standardised approach to photodetector characterisation.

## 4.2 Method

For this study, we used a 130 nm thick *c*-plane  $\alpha$ -Ga<sub>2</sub>O<sub>3</sub> using a Keithley 6487 picoammeter coupled to a signatone probe station. Electrical contacts (Ti/Au) were deposited on the sample in an interdigitated finger configuration. Further details of the growth of the samples can be found in [29].

A deuterium light source and 250 nm LED were used as a source of optical excitation, with a Thorlabs SBH shutter used for transient photocurrent measurements. The data collection process was automated through a custom-built labVIEW program. More information on the experimental setup is available in Chapter 2. Power-dependent photocurrent measurements were performed using a combination of natural density filters. Optical power measurements were obtained using a Thorlabs photodiode. In practice, transient measurement constraints were due to the acquisition rate and the settling time of the photocurrent. The accuracy of the measurements is determined by the number of power line cycles (PLC) set in the Keithely, which describes the integration time to obtain a measurement. Low integration time provides faster measurements at the expense of reduced accuracy, and vice versa for longer integration times. At a low acquisition rate of 0.1 PLC, noise levels were prominent, affecting the transition between dark- and steady-state photocurrents. A longer sampling rate of 6 PLC led to missed measurements of the rise/decay times. As discussed later, rise and decay times occur within sub-second timescales, necessitating rapid acquisition rates

to balance between data readability and precise timing of rise/decay times.

## 4.3 Results and Discussion

### 4.3.1 Effect of illumination intensity

To explore optoelectronic characteristics, transient photocurrent experiments were performed using a spectrally resolved deuterium light source at 250 nm and a Thorlabs 250 nm LED, with illumination intensities of  $3 \mu\text{Wcm}^2$  and  $563 \mu\text{Wcm}^2$ , respectively, shown in Figure 4.1.

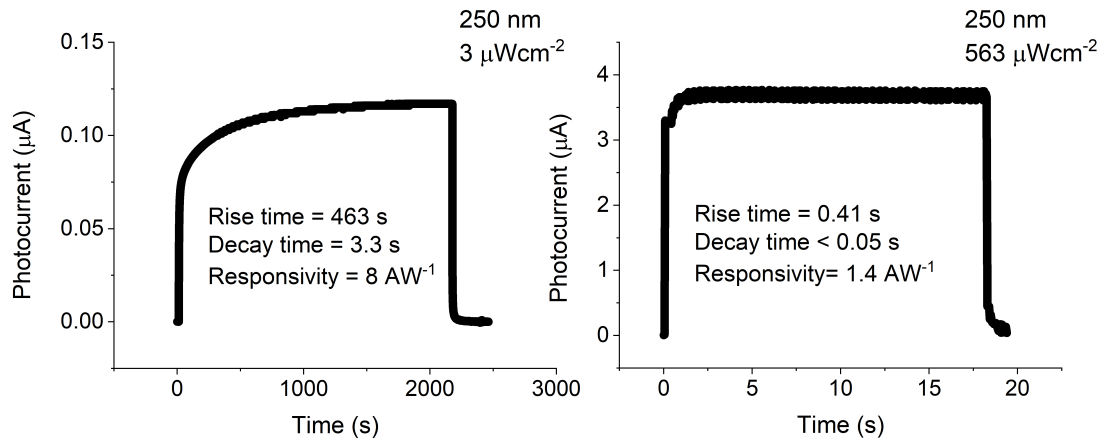


Figure 4.1: photocurrent transient using (left) deuterium light source (right) 250 nm LED, where the led is around 2 orders of magnitude higher in light intensity

Figure 4.1 shows the illumination intensity significantly influences key parameters used to evaluate photodetectors, such as responsivity and response speed, determined by their rise and decay times. When the low illumination power is used from the deuterium light source monochromated at 250 nm, we observe a slow rise time of 463 s from 10 % to 90 %, which is considered an underestimate, as the photocurrent fails to reach the steady-state photocurrent. At a higher illumination intensity of  $560 \mu\text{Wcm}^{-2}$ , we observe a 2 and 3 order of magnitude decrease in the decay and rise times, respectively. Furthermore, we see a significant decrease in responsivity from  $8 \text{AW}^{-1}$  to

$\approx 1.4 \text{ AW}^{-1}$ . Due to the impact of the optical power on the responsivity and response time, we pose a critical question regarding the comparison of photodetectors in the literature and, more crucially, how the performance of the photodetector correlates with the quality of the materials used. For example, Figure 4.1 illustrates that a fast detector can be described under high illumination conditions, or alternatively, a device can be described as being 5-6 times more responsive under significantly lower illumination levels. From a material perspective, this is of the utmost importance in order to identify the best material basis for using the material as a platform for photodetectors. Due to the evident illumination intensity dependent responsivity, a more rigorous intensity dependent study was conducted between between  $1\mu\text{Wcm}^{-2}$  to *ca*  $1000 \mu\text{Wcm}^{-2}$ . In various models proposed by Bube, the relationship can be approximately described by a power-law  $I_{ph} = P^\gamma$ , where  $I_{ph}$  is the photocurrent,  $P$  is the optical power, and  $\gamma$  is the power exponent relating the two. Plotting a log of the photocurrent versus log illumination intensity reveals a change  $\gamma$  with illumination intensity.

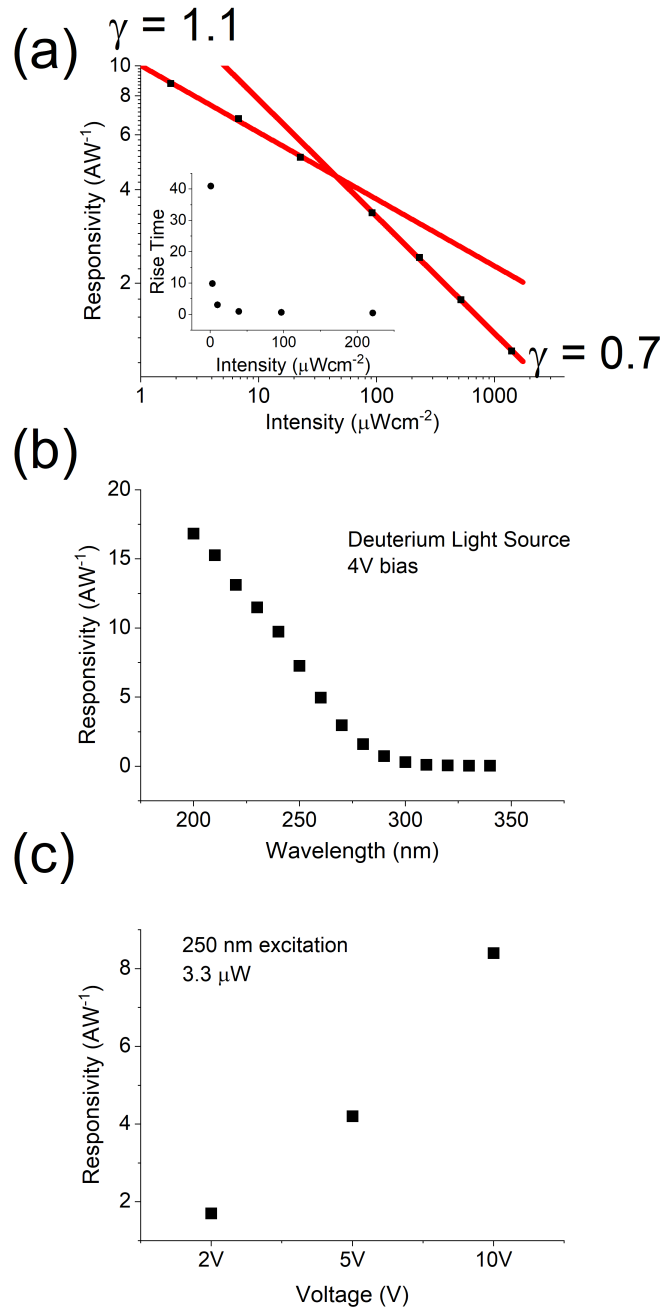


Figure 4.2: (a) Responsivity measured as a function of illumination intensity using 250 nm Thorlabs LED. Inset shows the response speed as a function of illumination intensity measured under a 10 V applied bias (b) Responsivity versus wavelength under 250 nm excitation (c) Responsivity as a function of excitation wavelength under a 4 V bias

Figure 4.2(a) shows a log-log plot of the photocurrent versus optical power, re-

vealing a non-unity relationship. A  $\gamma$  value of 1 would describe a situation in which increasing the illumination intensity by a factor of 2 would result in a doubling of the measured photocurrent. Therefore, the responsivity, according to Equation 4.1, would be independent of the illumination intensity. Fundamentally, this reveals insights into the carrier dynamics within the material. In the literature, when  $\gamma = 1$  reveals that the lifetime of the free electron is independent of the illumination intensity. Figure 4.2(a) exhibits a behaviour in which  $\gamma$  decreases as the illumination power increases. Here we can define this into two distinct regions, where region one is characterised by  $\gamma > 1$ , referred to in the literature as superlinear photoconductivity. Region two is characterised by  $\gamma < 1$ , defined as the sublinear region.

Although rare, Nakagomi *et al.* observed a similar trend in  $\beta$  Ga<sub>2</sub>O<sub>3</sub> heterojunctions, where a superlinear region ( $\gamma=1.5$ ) was observed from  $20\mu\text{Wcm}^{-2}$  to  $2\text{mWcm}^{-2}$  followed by a transition to sublinear behaviour ( $\gamma = 0.85$ ) [175]. However, no mechanism was described in the study. High photocurrent gain has been reported in Ga<sub>2</sub>O<sub>3</sub> where the mechanism by Armstrong *et al.* [50] could explain superlinear behaviour. The high gain in Ga<sub>2</sub>O<sub>3</sub> is tentatively attributed to the STH mechanism [50]. Here we suggest that at low illumination intensities, electrons are excited to the conduction band, and holes become trapped. In the conduction band, the electron can make many transits in the device before eventually recombining with the trapped hole, leading to a high gain i.e responsivity. At low carrier densities, the electron has a higher probability of interacting with an empty trap, thus reducing the effective time that the electron is in the conduction band. Rather than single trapping, multiple retrapping and strong interaction with the traps lead to a slow photocurrent rise time [101]. This process of long photocurrent rise times at low illumination intensity is reflected in the inset of Figure 4.2(a). Here we have the case where the generation rate  $\gg$  is the recombination rate, essentially stating that carriers are generated at a much faster rate than they can recombine, resulting in superlinear behaviour.

As the illumination intensity increases (and hence the generation rate),  $\gamma$  decreases, meaning the free carrier lifetime decreases with illumination intensity [100]. This effect could perhaps be attributed to the impact of the varying quasi-Fermi level with illumi-

nation intensity.  $\alpha$ -Ga<sub>2</sub>O<sub>3</sub> has a large distribution of donor states within 1 eV of the conduction band [99,176]. As the illumination intensity increases, the quasi-Fermi level shifts closer to the conduction band, populating the donor states during the transition. Hence, reducing the density of available traps results in an increased likelihood of the electron to be in the conduction band, thus increasing the likelihood of recombination. Here we see a process of the free carrier lifetime decreasing with increasing illumination intensity. As a consequence of the increased probability that the electron is in the conduction band rather than in a trap, the results in a faster rate of photocurrent rise time and response speed, as evident in the inset of Figure 4.2(a). Bube proposed that the distribution of traps will have a significant effect on  $\gamma$  [100]. Using a one-centre recombination model, it was shown that  $\gamma$  could only be either 0.5 or 1, irrespective of the Fermi level position. However, if the density of traps varies with depth, a case arises where  $0.5 \leq \gamma \leq 1$ .

Another aspect to consider is the dependence of electron mobility ( $\mu$ ) on carrier density. Sasaki *et al.* showed  $\mu$  reduced by a factor of 3 when the electron density increased from  $10^{17}$  to  $10^{19}$  in  $\beta$ -Ga<sub>2</sub>O<sub>3</sub> [177]. The electron concentration in the work presented in this chapter will be significantly lower than the values reported by Sasaki *et al.* However, a reduced mobility would correspond to a reduction in the measured photocurrent, hence the responsivity of the device. The decrease in mobility could be attributed to an increased rate of ionised impurity scattering at increased illumination intensities. However, we must point out that there is a general consensus that Polar-Optical phonon scattering is the dominant mechanism, particularly at room-temperature [178,179].

### 4.3.2 Effect of illumination wavelength

Figure 4.2(b) shows the effect of the excitation wavelength on the responsivity of the device. When  $\hbar\omega \geq E_g$ , electrons are excited to the conduction band from all filled states below the Fermi level to the valence band. When  $\hbar\omega \leq E_g$ , electrons don't have enough energy to be excited from the valence band, and only excitation from

sub-bandgap states contributes to conductivity. As the photon energy decreases, fewer states are sufficiently close to the conduction band to generate a photocurrent.

Figure 4.2(c) illustrates a near linear behaviour relationship between responsivity and applied bias. Assuming the drift current ( $J=\sigma E$ ) is the dominant transport mechanism, there is a linear relationship between the current density and the electric field. Furthermore, a linear relationship between photocurrent and electric field is indicative of Ohmic formation at the metal-semiconductor interface [111, 180, 181]. A general rule of thumb for the formation of ohmic contact in a semiconductor is determined by the semiconductors electron affinity relative to the work function of the metal. Subsequently, this process has been shown to be far more complex where interfacial reactions at the metal-semiconductor interface make a significant contribution [111, 182, 183].

### 4.3.3 Effect of applied voltage

The impact of illumination power on responsivity and response speed has been discussed in this work. However, we must now address the impact of the applied voltage, which will closely correlate with photodetector architecture. Commonly, the applied bias voltage is often stated, however, let us consider a more fundamental aspect to what the voltage does. The voltage here generates an electric field that will move the carriers, hence contributing to the photocurrent. The electric field is defined as the voltage per unit distance, where the distance is the distance between electrodes. Given that the electrode distance in our work is 100  $\mu\text{m}$ , this gives an electric field of  $1 \times 10^5$  V/cm,  $0.5 \times 10^5$  V/cm and  $0.2 \times 10^5$  V/cm for applied bias voltages of 10, 5 and 2 V, respectively. Here lies the fact that, simply by changing the electrode spacing and maintaining the same voltage, we could manipulate the electric field and thus the corresponding photocurrent and responsivity. Therefore, it seems clear that when comparing photodetectors, not only the measurement conditions but also the device architecture must be taken into account.

Figure 4.2 illustrates the impact of experimental conditions on the much reported responsivity. In turn, we could utilise these conditions to achieve a highly responsive detector by using low-intensity 200 nm excitation under a high electric field. Illuminat-

ing with high intensity light would, on the other hand, result in an increased response speed.

#### 4.3.4 Photocurrent overshoot

In Figure 4.1, we pay close attention to the power dependence on the transient photocurrent measurements. Specifically, the effect on the time taken for the photocurrent to reach a steady-state.

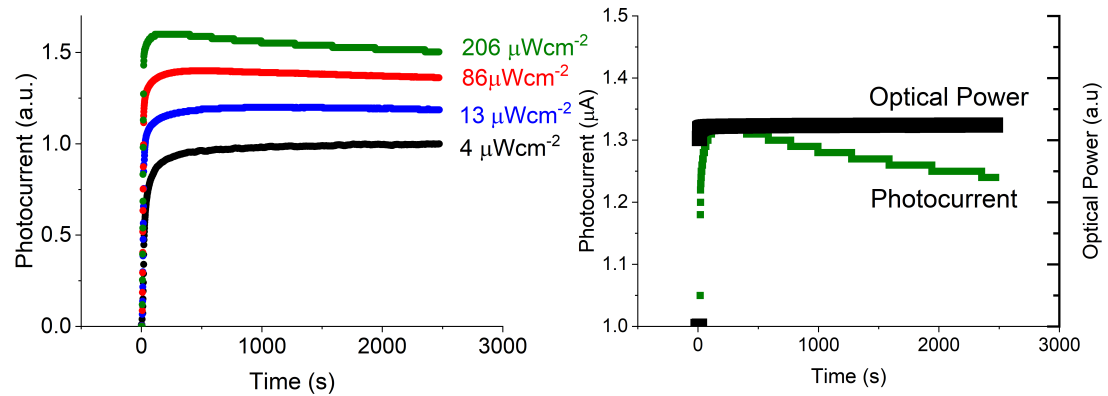


Figure 4.3: (left) Photocurrent rise after illumination with light measured at 4 different illumination intensities (right) Photocurrent decreasing as a function of time after initial saturation while the optical power remains constant

In Figure 4.2 we focussed on steady state current and the time taken to reach it, but we never described how it is reached. Figure 4.3(left) illustrates the general trend that after the light is switched on, there is a rapid increase in photocurrent. After some time, the photocurrent reaches a steady-state value at illumination intensities of 4 and 13  $\mu\text{Wcm}^{-2}$ . At larger illumination intensities of 86  $\mu\text{Wcm}^{-2}$  and 206  $\mu\text{Wcm}^{-2}$ , we observe a change in the transient behaviour, where the photocurrent reaches a maximum, followed by slow photocurrent decay while the illumination was maintained over the sample. As the illumination intensity increases from 86  $\mu\text{Wcm}^{-2}$  to 206  $\mu\text{Wcm}^{-2}$ , we observe an acceleration in the rate of decay of photocurrent, indicating the influence of carrier density on the mechanism responsible for the photocurrent decay. In correlation with the results in Figure 4.2, the overshoot is observed at illumination intensities at which the value of  $\gamma < 1$ , and the decay rate increases as  $\gamma$  tends toward 0.

The initial consideration here was perhaps that the LED optical power was decaying over time at higher driving currents. However, with the LED being driven at a maximum of 10 mA this effect was unlikely. The optical power was measured as a function of time and remained constant throughout the duration of the experiment, as shown in Figure 4.3(right)

Polyakov *et al.* observed a similar phenomenon in undoped  $\alpha$ -Ga<sub>2</sub>O<sub>3</sub> when illuminated by 259 (4.8 eV) and 530 (2.3 eV) LED's and referred to the process as "photocurrent overshoot" [106]. In this work, the samples were exposed to 3x 1000s illumination cycles, and the rate of photocurrent decay appears to be more significant when the sample is illuminated by the 259 nm compared to the 530 nm LED. For below-bandgap excitation, the photocurrent maximum was reduced after each successive illumination cycle, and the overshoot effect diminishes. Each of the decay processes was well described by a stretched exponential model which the group claims is indicative of current flow with a barrier for recombination or suggests the presence of potential fluctuations.

Girolami *et al.* observed the overshoot phenomenon in undoped  $\kappa$  Ga<sub>2</sub>O<sub>3</sub> xray photodetectors and assigned the the mechanism of the overshoot to trap mediated space charge effects [184]. They propose that carrier (electrons) become trapped at the metal-semiconductor interface, resulting in the formation of a space-charge region where the internal electrical field of the space-charge region opposes the applied electric field, resulting in a decrease in photocurrent.

## 4.4 Proposing a new metric

### 4.4.1 Photoconductance

Device characterisation will also be slightly ambiguous due to the large variance in responsivity with optical power. However, because the photocurrent will be affected by many other conditions, such as applied voltage and device architecture, an alternative measurement of photoconductance may provide a more unbiased metric for comparison

of the photodetector. The conductivity equations are simple and alleviate the effect of applied bias and device architecture and therefore the overall electric field strength. The conversion between photocurrent and conductivity can be found in Chapter 2.

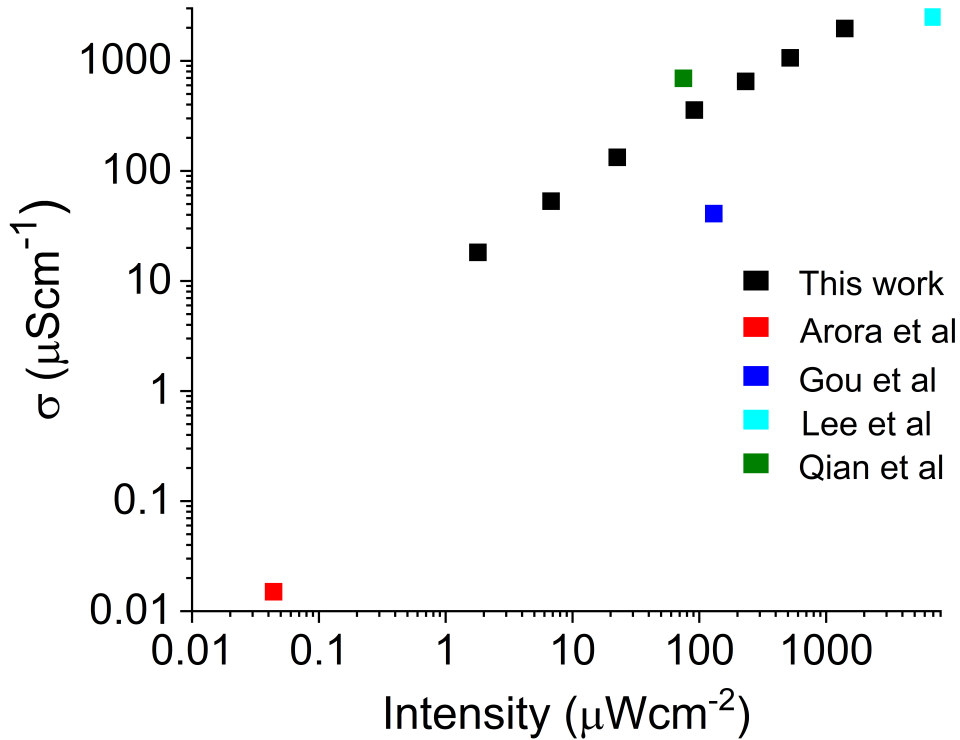


Figure 4.4: Photoconductance measured as a function of light intensity. Here we compare our detector performance with others in the field, converted to a standard parameter of photoconductance. Here we use an excitation wavelength 250 nm

Here we make a comparison between other reported Ga<sub>2</sub>O<sub>3</sub> photodetector devices in the field. Using our work as a reference, the device architecture gives a contact spacing of 100  $\mu\text{m}$  and an applied bias of 10 V, corresponding to an electric field of  $1 \times 10^5$  V/cm. The device in this work consisted of 4 pairs of electrodes, enhancing the effective length of the contact by a factor of 4. In the conversion between conductivity, this enhanced the conduction cross section by a factor of 4. The measured photocurrents as a function of illumination intensity were converted to photoconductance ( $\sigma$ ) using the procedure

Photocurrent ( $\mu$ A)	Illumination Intensity ( $\mu$ Wcm <sup>-2</sup> )	Photoconductance ( $\mu$ Scm <sup>-1</sup> )
0.04	1.79	18.23
0.13	6.77	53.09
0.32	22.57	132.93
0.87	91.40	356.81
1.58	232.03	650.23
2.59	520.31	1065.89
4.78	1401.56	1967.15

Table 4.2: Measured photocurrents and corresponding photoconductance transformations with 4 pairs of electrodes with a length  $\approx 500 \mu\text{m}$  spaced  $100\mu\text{m}$  apart.

detailed in Chapter 2.

#### 4.4.2 Comparing to the literature

Now, we compare our work with detectors under similar illumination intensities. Gou *et al.* (marked blue in Figure 4.4) measured the photocurrent response of  $\alpha$ -Ga<sub>2</sub>O<sub>3</sub> photodetectors under  $130 \mu\text{Wcm}^{-2}$  illumination intensity and reported a responsivity of  $1000 \text{ AW}^{-1}$  [139]. Given an applied bias of 20 V and a contact spacing of  $200 \mu\text{m}$ , this consequently equalled the same electric field as in our work.

Using the photocurrent reported in Table 4.2, our responsivity in the region of illumination intensity corresponds to a responsivity of  $3 \text{ AW}^{-1}$ . Given that the sample in our work is considered more conductive, as per Figure 4.4, it again probes further discussion on how reliable responsivity is as a gauge on the performance of a detector.

We turn our attention to the work of Qian *et al.* who reported a responsivity of  $70 \text{ AW}^{-1}$  under a 10V applied bias with an excitation wavelength of 254 nm [115]. With a contact spacing of  $5 \mu\text{m}$ , a resulting electric field of  $2 \times 10^5 \text{ V/cm}$ . At the reported illumination intensity of  $70 \mu\text{Wcm}^{-1}$ , our work reports a responsivity of around  $4 \text{ AW}^{-1}$  which in turn may be due to an increased electric field value. Converting Figure 4.4 into V/cm and extrapolating the field to match that of Qian *et al.* work, we would, in theory, achieve a responsivity of around  $1600 \text{ AW}^{-1}$ . To achieve this, this would require setting our applied bias at a value of 16 V, which exceeds the voltage limit of our source.

In light of the findings of this work, the reporting of photodetector performance may benefit from a standardised approach to characterisation. Here we propose that "responsivity" varies greatly with illumination intensity, and a power-dependent photocurrent measurement would certainly be beneficial for a reliable comparison with the literature. Secondly, many reports show photocurrent measurements with a range of illumination intensities. As the photocurrent can be significantly impacted by the device architecture (electrode spacing), we suggest the photoconductivity parameter to be effective for device comparison. Furthermore, emphasis should be placed on quoting the applied electric field rather than the applied voltage.

A final consideration must be applied to using responsivity as a suitable metric for assessing material quality for photodetector applications, given the dependence on several experimental parameters. In the end, what is important for photodetector testing is that the device is suitable for technological applications. In this chapter, we illustrate that by changing the device architecture and excitation conditions, the photodetector can be tailored to suit the requirements of the technology in which the device is employed.

## 4.5 Conclusion

In this study, we carried out a comprehensive photoconductive study of  $\alpha$ -Ga<sub>2</sub>O<sub>3</sub> thin films focussing on the impact of illumination intensity, voltage, and excitation wavelength on the photocurrent response in the material. In what is not new to the field, we found that the illumination intensity will have a significant impact on the reported responsivity and response times of the device. This was tentatively explained by the use of a power-law model in which we observed a non-unity relationship transitioning from a superlinear to a sublinear relationship indicating a significant change in carrier dynamics over the illumination range. Furthermore, we observed that excitation wavelength and applied bias will have a significant impact on responsivity and response time, coupled with the variation of device architecture, on the electric field, highlighting the complexity of comparing detectors with others in the literature. Here, we propose the necessity of reporting values of photoconductivity, rather than photocurrent, to make

a fairer comparison with those in the literature, paving the way for a more informed and reliable method for assessing photodetector performance.

A new metric, photoconductance, is proposed as an alternative to responsivity for photodetector characterisation. Unlike responsivity which has been shown to be influenced by factors such as illumination intensity and wavelength, applied voltage and device architecture, photoconductance will normalise for electric field due to applied bias and the geometry of the detector. Assessment of photodetector performance in terms of photoconductance will lead to a more intrinsic comparison among the field. We note that while photoconductance it has advantages in terms of normalisation, further work is required to account for variations in illumination intensity and wavelength dependencies.

The phenomena of photocurrent overshoot requires further investigation. It would be of interest to see what other experimental variables may influence the overshoot effect. The interest here would be whether this effect happens at sub-bandgap values, if the effect is inherently linked to carrier density in the mobility band. It could be postulated here that, at sufficiently high carrier density, what we observed is linked to scattering effects or perhaps even to an activation of a different recombination mechanism. Scattering can be further investigated by varying the electric field or temperature range of the measurements.

## Chapter 5

# Advanced Photoconduction Techniques to Probe Defect states in $\alpha$ -Ga<sub>2</sub>O<sub>3</sub> Thin Films

### 5.1 Background

In Chapter 4, we tested the functionality of the home-built photoconduction setup by measuring the photocurrent as a function of excitation wavelength, optical power and applied voltage. Power-dependent photocurrent measurements in Chapter 4 revealed a transition between superlinear and sublinear behaviour evidenced by a  $\gamma$  value transitioning between 1 and 0.7, indicating the significance of trapping in the material. Furthermore, although considered to be solar-blind, we observed a photo response at below-bandgap energies indicating the capability of the system to measure photocurrents generated from sub-bandgap states that can be measured by our system. Sub-bandgap absorption has been observed both experimentally and computationally [185] [186]. Transient capacitance measurements such as DLTS and ODLTS is considered the standard for probing electrically active defects in semiconductors, and studies of  $\alpha$  and  $\beta$  Ga<sub>2</sub>O<sub>3</sub> reveal a rich distribution of defect states across the bandgap [60, 61, 99, 176, 187, 188].

Given that the presence of defect states will influence how the light is absorbed by a material, measuring the sub-bandgap absorption coefficient as a function of photon energy may allow for a spectroscopic study of energetic states within the material. The optical absorption coefficient governs the absorption of light by a material and is typically measured using the optical transmission method, described in Chapter 2. The optical transmission method is well suited to measuring the absorption coefficient at photon energies at the bandgap. However, the accuracy quickly diminishes in the sub-bandgap region as transmission is high and the Si-based detector in the optical transmission measuring system cannot detect slight variations in transmittance. Photothermal deflection spectroscopy (PDS) is a widely accepted method for measuring the absorption coefficient at sub-bandgap energies [74]. Hao *et al.* measured the absorption coefficient in  $\beta$ -Ga<sub>2</sub>O<sub>3</sub> using PDS, revealing a pronounced Urbach tail measuring between 120-150 meV and showed defect related absorption was significantly impacted by the annealing conditions of the samples [6]. An alternative technique for measuring the absorption coefficient is the constant photocurrent method (CPM). CPM is a photoconduction technique that involves making continuous adjustments to the incident photon flux to maintain a constant photocurrent throughout the spectrum [75]. The CPM method has been widely used in materials such as Si [76, 141, 189], CdSe [190], and AlGa<sub>N</sub> / Ga<sub>N</sub> heterostructures [104]. Given the mechanism of how conductivity is stimulated by CPM, the measured energy-dependent absorption coefficient provides information regarding filled states below the dark Fermi level. In a material such as Ga<sub>2</sub>O<sub>3</sub> where p-type conductivity is prevented by the formation of STH [42], the CPM technique will only probe electron filled states meaning the technique has limitations when it comes to probing defect states across the full bandgap range. Therefore, an additional characterisation technique is required to supplement CPM. Through our collaboration with Dr. Stephen Reynolds at the University of Dundee, we were able to use a photoconduction setup, described in Chapter 2 that allowed for measurements of defects in the upper half of the bandgap using a technique known as TSC. As the name suggests, TSC is a thermal process in which a cooled sample is illuminated by above-bandgap light and the temperature is ramped at a constant rate with the added

thermal energy ionising defect states resulting in an increase of the conductivity of the material.

TSC is a well-established technique used for probing defect states, with some reports existing in the literature for Ga<sub>2</sub>O<sub>3</sub>. Wang *et al.* used TSC to probe defect states in Ti doped Ga<sub>2</sub>O<sub>3</sub>, revealing a dominant TSC signal around 250 K, which the group suggests is a convolution of three trap states with activation energies between 0.48 - 0.53 eV depending on Ti concentration in the films [113]. Tak *et al.* used TSC to investigate trap states in  $\beta$ -Ga<sub>2</sub>O<sub>3</sub> using a combination of various heating cycles and revealed nine trap states with activation energies from 0.16 - 1 eV [191], and to our knowledge is the shallowest defect state in Ga<sub>2</sub>O<sub>3</sub> probed via TSC owing to the onset of the temperature measurements beginning at 80 K. Thus far, Polyakov *et al.* is the only group to apply the TSC method to  $\alpha$ -Ga<sub>2</sub>O<sub>3</sub> films and reported five defect states with activation energies of 0.25, 0.35, 0.5, 0.6 and 0.8 eV [106]. Given that TSC is an effective tool for identifying defect states above the dark Fermi level, and CPM provides a measurement of absorption coefficient owing to absorption from filled states below the Fermi level, we combine TSC and CPM to map defect states across the bandgap. This process is illustrated in Figure 5.1

## 5.2 Theoretical Background

### Constant Photocurrent Method

The theoretical background in this chapter is adapted from our published work [192]. Photoconduction is the process by which the conductivity  $\sigma$  of a material increases under photon illumination. Under light illumination, photoconductivity  $\Delta\sigma$  can be expressed as

$$\Delta\sigma = q(\Delta n\mu_n) \tag{5.1}$$

where  $q$  is the charge of the carrier,  $\Delta n$  is the excess free electron density generated by the incident photons, and  $\mu_n$  mobility [97].

Since  $\Delta n$  is intrinsically a product of the generation rate,  $G$ , and the electron

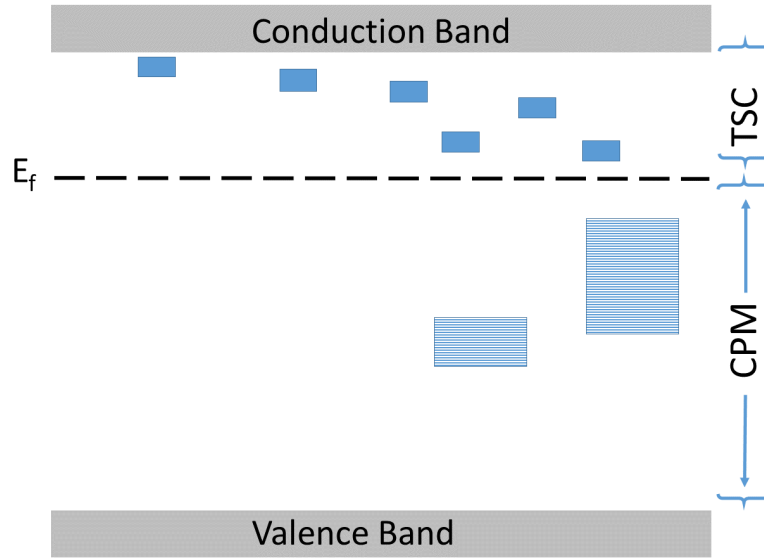


Figure 5.1: Schematic of accessible states available from CPM and TSC measurements. CPM works as a tool for probing defect states below the dark Fermi level (black dashed line) whilst TSC serves as a tool for probing defect states above the dark Fermi level.

lifetime  $\tau_n$

$$\Delta n = G\tau_n \quad (5.2)$$

Substituting equation 5.1 into 5.2 gives

$$\Delta\sigma = Gq\tau_n\mu_n \quad (5.3)$$

The average photocarrier generation rate  $G$  is defined as [97]

$$G = \eta\phi(1 - R)\frac{1 - \exp(-\alpha d)}{d} \quad (5.4)$$

Where  $\eta$  is the quantum efficiency,  $\phi$  is the incident photon flux,  $R$  is the film reflectance,  $\alpha$  is the absorption coefficient of the film, and  $d$  is the film thickness.

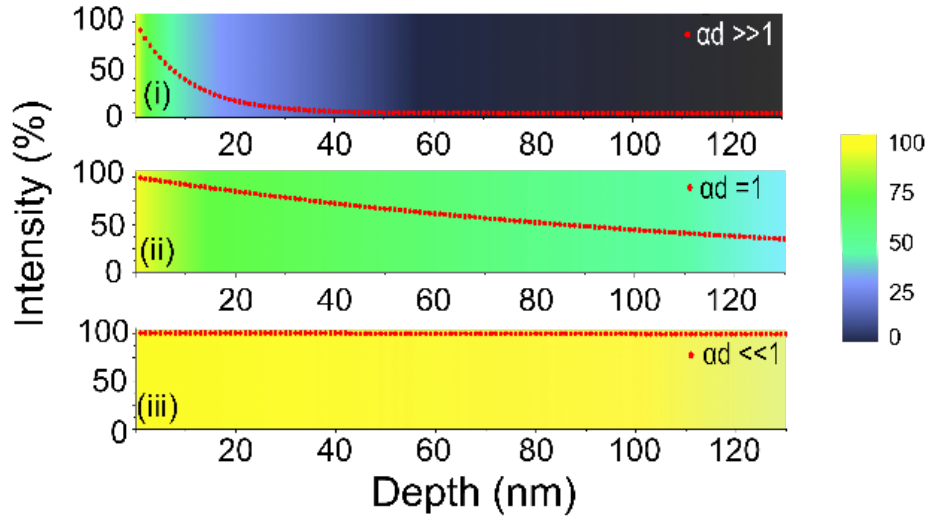


Figure 5.2: Transmitted light intensity (incident from the left) versus depth in a 130 nm thick film, described by the Beer-Lambert law: i)  $\alpha d \gg 1$ : incident light is strongly absorbed at the surface of the film; ii)  $\alpha d = 1$ . 67 % of the light is absorbed non-uniformly within the film; and iii)  $\alpha d \ll 1$ : light absorption is small and uniform throughout the film, giving a constant generation rate and carrier lifetime

Figure 5.2 illustrates the effect of various  $\alpha d$  products in the cases where (top) the absorption coefficient is much greater than the depth of the sample (middle) The absorption coefficient is the same order of magnitude of as the depth of the sample (bottom) the absorption coefficient is much less than the depth of the sample. From Figure 5.2 we can see the situation that when  $\alpha d \ll 1$ , the transmission of light, hence the absorption, is approximately uniform throughout the thickness of the material resulting in a uniform generation rate. In this case, equation 5.4 can be approximated as

$$G \approx \eta\phi(1 - R)\alpha \quad (5.5)$$

Here we can see that as we expect the G to be independent of film thickness. Therefore, the range for which CPM is applicable is heavily influenced by material thickness. Substituting equation 5.5 into 5.3

$$\Delta\sigma = \eta\phi(1 - R)\alpha q\tau_n\mu n \quad (5.6)$$

Under the reasonable assumption that  $\eta$ ,  $\mu_n$  and  $R$  do not vary significantly with incident photon energy, as is typically the case of sub-bandgap excitation, Equation 5.6 indicates that the absorption coefficient is a function of the  $\Delta\sigma$ ,  $\phi$  and  $\tau_n$ . If we actively maintain a constant photocurrent by adjusting  $\phi$  at each photon energy, the quasi-Fermi levels are fixed, which in turn maintains a constant  $\tau_n$ . The requirement for the CPM approach itself lies in the requirement for a condition of constant  $\tau_n$  with photon energy. Identifying how the  $\tau_n$  behaves as a function of photon energy can be illustrated by the use of a power-dependent photocurrent measurement. Bube showed that there is a power-law relationship between the photocurrent and the illumination intensity, where  $I_{ph} = \phi^\gamma$  [100], where  $\phi$  is the illumination intensity and  $\gamma$  is the power law exponent. The case of a constant  $\tau_n$  with  $E_p$  is observed when  $\gamma=1$ . Our earlier work in Chapter 4 highlights that  $\gamma$  varies between 1.1 and 0.7, showing the  $\tau_n$  is heavily dependent on the illumination intensity. Under the constant photocurrent condition, equation 5.6 reduces to

$$\alpha(E_p) = \frac{Constant}{\phi(E_p)} \quad (5.7)$$

Equation 5.7 shows that if we measure the photon flux required to keep the photocurrent constant, we can obtain a relative measurement of the absorption coefficient as a function of the photon energy, in effect a spectroscopic measurement. The relative aspect of the measurement lies with the requirement of calibrating the CPM spectrum with a known absorption measurement process. Here, we use the high accuracy of the optical transmission measurement at near-bandgap values to calibrate our spectrum by overlapping the CPM spectrum with the optical transmission spectrum at near-bandgap values where both methods are approximately valid ( $\alpha d \simeq 1$ ).

The absorption coefficient is determined by the sum of all allowed transitions between occupied and empty electron states. It follows that the absorption coefficient and the DOS, defined as the number of states per unit volume per unit energy, are related. During the CPM experiment, the sweep from lower to higher  $E_p$  induces transitions from deeper filled states in the bandgap, which continue to accrue with increasing photon energy as additional filled states are brought into play. Therefore, CPM can be

used as a DOS spectroscopy technique of localised states, provided that (i) the states are filled, i.e. below the Fermi level, (ii) the conduction band edge is sharp relative to the distribution of the localised states in the bandgap, and (iii) thermally assisted transitions are ignored [141]. The DOS  $g(E)$ , where  $E=E_c-E_P$ , is then proportional to  $(d\alpha(E))/(dE_P)$  [193].

### Thermally Stimulated Current Spectroscopy

To describe the origins of TSC in Ga<sub>2</sub>O<sub>3</sub>, we need to consider an electron trap within the bandgap. Given that the emission of electrons from trap states is thermally stimulated, the emission rate of the electrons can be expressed as

$$e_n = \sigma_n N_c V_{th} \exp\left(\frac{-E_T}{K_b T}\right) \quad (5.8)$$

where  $\sigma_n$  is the capture cross section of the trap state,  $N_c$  is the DOS in the conduction band,  $V_{th}$  is the thermal velocity of the electron,  $K_b$  is the Boltzmann constant,  $T$  is the temperature, and  $E_T$  is the trap depth with respect to the conduction band. The corresponding thermally generated current ( $I_{TSC}$ ) as the quasi electron Fermi level unveils a trap is given by

$$I_{TSC} = C V_b e \mu_n \tau_n N_T e_n \exp\left(-\int e_n / \beta dT\right) \quad (5.9)$$

where  $e$  the charge of an electron,  $\mu_n$  is the electron mobility,  $\tau_n$  is the lifetime of the free electron,  $N_T$  is the trap density,  $V_b$  is the applied voltage and  $C$  is a constant that quantifies the geometry of the sample, and  $\beta$  is the temperature ramp rate applied during the measurement.

From equation 5.9, it can be seen that by ramping the temperature, changes in the obtained TSC signal as a function of temperature will reveal information relating to trapping levels within the bandgap where the density of traps can be estimated by integrating over the TSC signal. This approach is referred to as the Bube approach.

Bube postulated that the energy level of the trap can be obtained by the following

equation [100].

$$E_T = K_b T_m \ln \left( \frac{\sigma_n N_c V_{th} T_m^2}{\beta E_T} \right) \quad (5.10)$$

where  $T_m$  is the maximum temperature of the peak in the TSC spectrum. From equation 5.10, two main methods can be used to approximate the energy level of the traps in the bandgap relative to the conduction band. Equation 5.10 can be rearranged as

$$\frac{\ln T_m^2}{\beta} = \frac{E_T}{K_b T_m} - \ln \frac{\sigma_n N_c V_{th} K_b}{E_T} \quad (5.11)$$

From equation 5.11 plotting  $\ln T_m^2$  vs  $1/T_m$  should produce a straight line with gradient equal to  $E_T$  with the intercept capable of revealing information regarding the capture cross section and thermal velocity.

An alternative approach to calculating the  $E_T$  uses some approximations of the temperature dependence on the DOS  $N_c$  and the thermal velocity  $V_{th}$ . Given the temperature dependence on  $N_c$  is approximated by

$$N_c = 2 \left( \frac{K_b T m^*}{2\pi h^2} \right)^{\frac{3}{2}} \quad (5.12)$$

where  $h$  is Planck's constant, and  $m^*$  is the effective mass of the electron. we can see that  $N_c$  scales with  $T^{\frac{3}{2}}$

for the thermal velocity, we can see that the  $V_{th}$  scales as  $T^{\frac{1}{2}}$  from

$$V_{th} = \sqrt{\frac{3K_b T}{m^*}} \quad (5.13)$$

Substituting equations 5.12 and 5.13 into 5.11 gives an approximation of the trap depth as

$$E_T = K_b T_m \ln \frac{T_m^4}{\beta} + \ln \frac{K_b N_0 S V_0}{E_T} \quad (5.14)$$

where  $N_0$  is the DOS at room-temperature and  $V_0$  is the thermal velocity at room-temperature. Given that the term on the left dominates the term on the right, the trap depth can be approximated by

$$E_T \approx K_b T_m \ln \frac{T_m^4}{\beta} \quad (5.15)$$

The mathematical derivation was obtained from the work of Khan *et al.* [194]. Throughout this chapter, this method will be referred to as the T<sup>4</sup> approach

## 5.3 Method

### 5.3.1 Constant Photocurrent Method

Details of the experimental setup can be found in Chapter 2 section 2.2.3 The processes for the measurements were conducted as follows.

The first step of the approach was to choose a value of photocurrent to be kept constant throughout the experiment, referred to as the CPM reference value. This value must be sufficiently high to give a good signal-to-noise ratio but remain low so that the photocurrent must not greatly exceed the sample dark current; otherwise, the occupancy of states in the gap close to the Fermi level would be modified which in turn would yield an inaccurate value of the absorption coefficient. The dark current in our device was typically 1 pA at room-temperature, and a CPM reference value of 7.8 pA was chosen. The validity of the CPM reference was demonstrated over a range of 7.8–117 pA. Due to the limited power of the LEDs in the low absorption region, it was not possible to maintain a high CPM reference current in that region. Therefore, a CPM reference value of 7.8 pA was selected to probe deeper into the bandgap of the material. Furthermore, as Ga<sub>2</sub>O<sub>3</sub> was reported to have a low conduction band DOS, the possibility of excitation to a second transport band in the conduction band was considered. Peelaers *et al.* demonstrated theoretically that when the carrier density

exceeds  $ca\ 10^{19}\text{cm}^{-3}$ , carriers are excited to additional conduction bands [186]. In this work, our sample is un-intentionally doped (UID), and the low photocurrent used results in a carrier density orders of magnitude lower than predicted by Peelaers. Therefore, this effect is considered to be unlikely. The longest wavelength, 465 nm LED, was first selected and scanned spectrally from 470 to 450 nm in 3 nm steps using the monochromator. The initial setting of the CPM reference value was carried out at 470 nm. The optical flux was then measured using the power meter. The wavelength-selection in the monochromator was then decreased by 3 nm and the LED driving current was adjusted so that the sample photocurrent remained matched to the CPM reference value within 5%, with the optical flux measured at each wavelength increment. This process was repeated with the same LED until the CPM reference value could not be reached (i.e. when the chosen wavelength was too far from the LED peak wavelength to generate sufficient photocurrent). The light source was then switched to the LED next inline, here a 450 nm LED, and the process repeated. At the cross-over wavelength between LEDs, spectral overlap was required to generate a continuous spectrum. The final two measurements of the 465 nm LED and the first two measurements with the 450 nm LED were matched and the spectra overlapped. This process was repeated with the complete series of LEDs until reaching bandgap excitation, here 240 nm. As presented in the theoretical background section, plotting the reciprocal of the optical flux versus photon energy results in a value proportional to the absorption coefficient shown in Figure 5.7—the proportionality lies with the constants outlined in equation 5.6. To remove the proportionality factor, the CPM spectrum is normalized to the absorption coefficient in the high absorption region (i.e. near-bandgap energy) obtained from the optical transmission method spectrum. This was achieved by overlapping the CPM and the optical transmission spectrum where both were approximately valid at  $\alpha d \leq 1$ . This process is illustrated by a flow diagram in figure 5.3

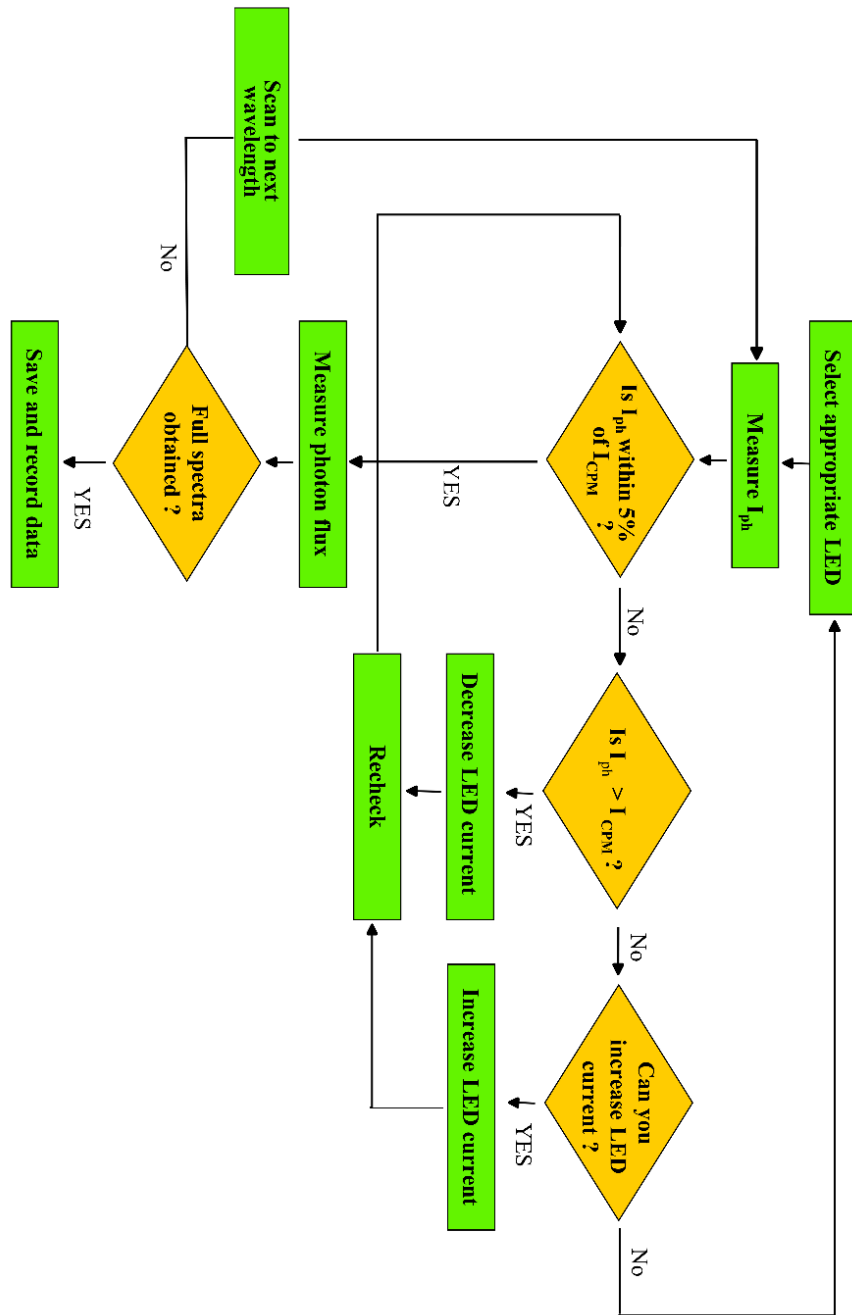


Figure 5.3: Workflow diagram for obtaining CPM spectrum. Green box represents an action where the gold diamond shows a decision

### 5.3.2 Thermally Stimulated Current Spectroscopy

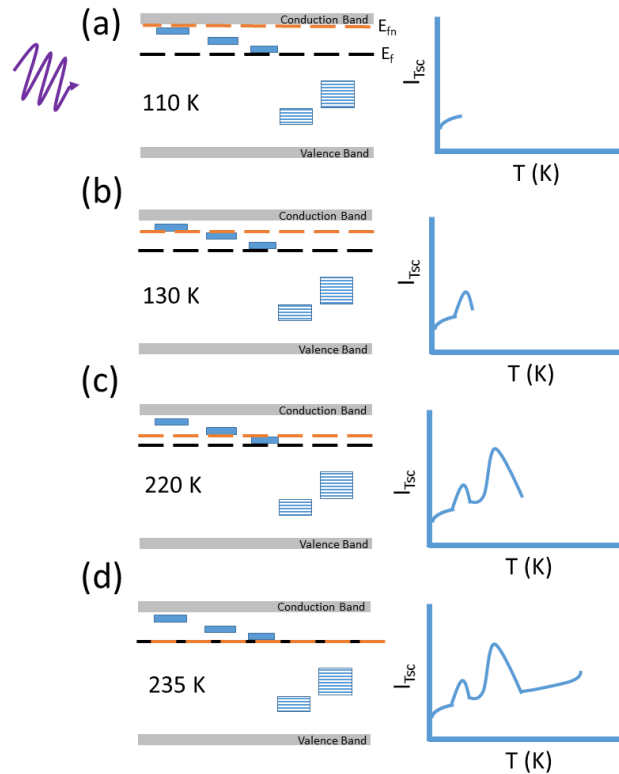


Figure 5.4: TSC band diagram schematic showing experimental process (a) sample cooled to low-temperature illuminated with light and allowed to reach steady-state (b) temperature increases and the quasi-Fermi level drops below trap level, resulting in an increase in the measured TSC signal. The TSC signal decreases due to trap depopulation (c) Temperature increased again and a second trap becomes thermally activated resulting in a second peak in the observed TSC spectrum (d) Temperature increased further to reveal 3rd trap and quasi-Fermi level brought back down to the dark Fermi level observed after thermal annealing

Details of the experimental setup can be found in Chapter 2 section 2.2.6

#### Optical filling - Process (a)

The sample was placed in the vacuum chamber and the 250 nm LED was aligned to illuminate the sample from a distance of *ca* 5 cm. The vacuum was then applied

and the sample temperature was increased to 400 K to provide enough thermal energy for electrons to escape deeper lying traps that become thermally activated at higher temperatures from those that are readily available at lower temperatures. Liquid nitrogen was introduced into the chamber to bring the chamber temperature down to 110 K. A Keithley 617 electrometer applied a 10 V bias. Once the temperature stabilised, the 250 nm LED was operated at nominal LED settings, and the sample was left under illumination for a period of 1 hour to fill all trap levels in the bandgap indicated by the observed saturation of the photocurrent. This stage of the process is represented by panel (a) in 5.4. At this stage, because of the low thermal energy at 110 K (around 13 meV), carriers will remain trapped.

#### **Applying the temperature ramp- process (b,c)**

After traps have been filled and current allowed to stabilise, the illumination is terminated with carriers effectively frozen at the defect levels in the bandgap. A temperature ramp of 2 K per minute was applied to the sample to allow a constant heating rate. The heating rate plays an important role in the TSC process, and obtaining spectra at various heating rates will allow an approximation of the trap depth according to equation 5.13. Unfortunately, the data acquired during this experiment were obtained at a single ramping rate due to time constraints at the end of the PhD, and additional measurements at various ramping rates is strongly suggested to make a comparison between the 2 methods proposed in Section 5.2. Although no direct comparison has been made in the Ga<sub>2</sub>O<sub>3</sub> literature regarding the accuracy of the methods, Schafferhans *et al.* showed similar activation energy ( $E_a$ ) of TSC traps for both methods above 100 K, however, this work was carried out on Methnofullerenes [195]. We note here that the kinetics may differ in comparison to that of wide-bandgap crystalline semiconductors.

As the available thermal energy increases, the Fermi level decreases, and at a given trap depth (in eV) the trapped electron will have enough thermal energy escape the trap and be excited to the conduction band, hence contribute to the conductivity. This will appear as an increase in the measured TSC signal as represented by (b) in 5.4. At a given temperature,  $T_m$ , the trap occupancy will be reduced to zero and the

electrons in the conduction band will recombine and reduce the TSC level. This process is detailed in figure 5.4(c). Here, the temperature was increased to 400 K, where there was a temperature limitation due to the electrical contact in the vacuum chamber and sample.

The process was repeated without light excitation. This allowed a dark current to be subtracted from the TSC measurements. The increase in dark current with temperature is shown in Figure 5.4(d).

## 5.4 Results

### 5.4.1 TSC for above Fermi level measurements

#### Establishing the Fermi level Position

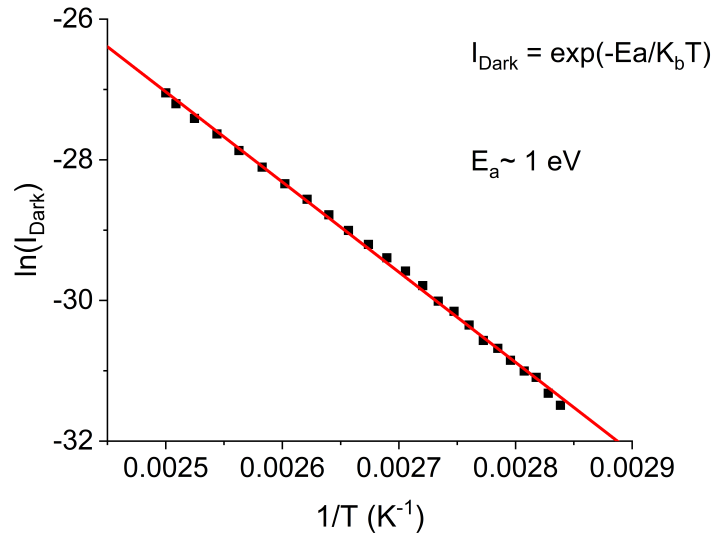


Figure 5.5: Dark current activation energy of PEALD grown  $\alpha$  Ga<sub>2</sub>O<sub>3</sub> measured between 350 - 400 K, revealing an activation energy of around 1 eV

Figure 5.5 illustrates the measurement of the dark current  $E_a$  within the temperature range of 350 to 400 K. At temperatures  $< 350$  K, the dark current levels are below the detection limits of the Keithley 617. The  $E_a$  was determined using an Arrhenius plot, which yields a value of 1 eV, indicating that the Fermi level of our samples is approximately 1 eV below the conduction band edge. Polyakov *et al.* identified the trap

state at 1 eV to be  $V_O$  related [98]. Therefore, we tentatively assign the dark current in our samples is generated from  $V_O$  in the lattice. The dark current  $E_a$  identified in this work aligns with the findings of Tak *et al* , who reported a dark current  $E_a$  of 1.01 eV for UID  $\beta$ -Ga<sub>2</sub>O<sub>3</sub> [191]. Determining the position of the dark Fermi level is essential for further analysis in this chapter, as it defines the range where TSC and CPM are applicable. This results suggest that CPM can be utilized to investigate defect states from the valence band up to  $Ev + 4$  eV (i.e.  $E_C - 1$ eV), provided the material's absorption is sufficiently strong.

### Probing defect states using TSC

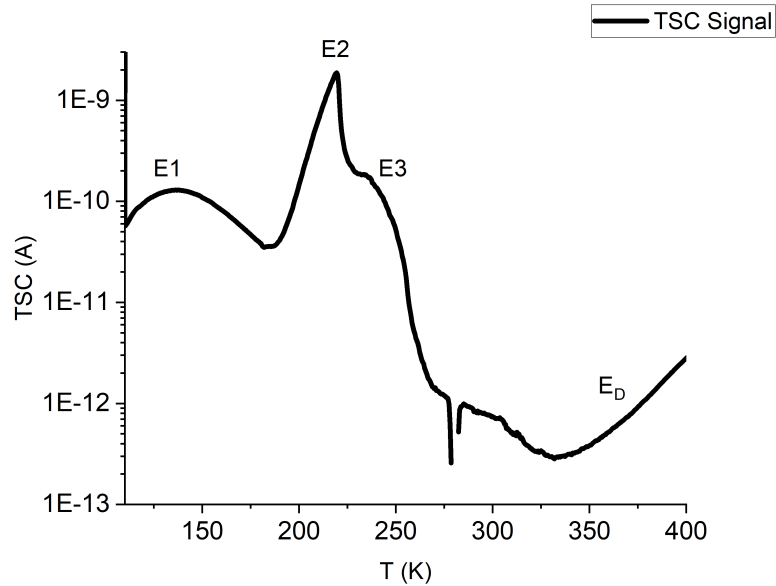


Figure 5.6: TSC spectrum obtained from TSC measurements between 110 - 400 K revealing 3 distinct peaks labelled E1-E3. E4 appears at a discontinuity therefore disregarded. Onset of the dark current is observed from around 350 K

Figure 5.6 shows the TSC results of  $\alpha$ -Ga<sub>2</sub>O<sub>3</sub> measured between 110-400 K. Here the results were obtained at the University of Dundee with experimental details of the setup detailed in chapter 2. The measurements were taken under the supervision of Dr Stephen Reynolds. In Figure 5.6 we observe three distinct peaks, labelled E1-E3. E2 is the dominant peak in the spectra located around 220 K, which also has a shoulder around 235 K, labelled peak E3. A broader peak (E1) is observed around 138 K.

Trap	T (K)	(E <sub>a</sub> ) (eV)
E1	138	0.28
E2	220	0.47
E3	235	0.51

Table 5.1: Trap activation energies obtained from TSC measurement using the T4 approximation

Interestingly, there appears to be a contrast in the line shape of the peaks, indicating variations in trap densities, capture coefficients, and attempt-to-escape frequencies. Furthermore, there is a clear asymmetry in the TSC peaks shown in Figure 5.6 that most likely arises from the convoluted effect of various overlapping peaks. Retrapping will also have an effect on the lineshape, with electrons undergoing multiple retrapping processes extending the effective lifetime of the electron, resulting in a slower decay of the TSC signal.

Identification of the presence of defects by electrical characterisation was a key objective of this study and extracting useful information about the trap in terms of trap depth and concentration would be beneficial for characterisation purposes.

As discussed in section 5.2, two main methods are used in the literature of Ga<sub>2</sub>O<sub>3</sub> for extracting the E<sub>T</sub> from a TSC spectrum. The "Bube" method uses an Arrhenius plot with several heating rates, while the T<sup>4</sup> method relies on assumptions of the thermal velocity and shape of the conduction band being parabolic. [195] showed similar results using the T4 and Bube method for temperatures above 100 K.

A precise measurement of trap energy and trap densities would therefore require further theoretical and computational modelling. Therefore, at this stage is considered outside the scope of this work. Here we will use the T4 method as an approximation of trap E<sub>T</sub> as a means of comparing with the current Ga<sub>2</sub>O<sub>3</sub> literature.

Using Equation 5.13, the trap energies are approximated and listed in Table 5.1.

### **E1 at 138 K**

Consider peak 1, denoted as E1 in Figure 5.6. Here we observe a broad feature in the TSC spectrum relative to peaks E2 and E3. Using equation 5.15, the peak has an

approximate  $E_T$  *ca* 0.28 eV. The broad nature of E1 may be the result of a convolution of trap states with overlapping activation energies. To our knowledge, Polyakov *et al.* is the only published work on  $\alpha$ -Ga<sub>2</sub>O<sub>3</sub> an observed trap level at 0.25 eV [106], which is in close agreement with E1 in Figure 5.6, with the variation in trap  $E_a$  coming from approximations and assumptions made in the derivation of equation 5.9 itself. Further work from the Polyakov group investigated the influence of Sn doping on deep traps in  $\alpha$ -Ga<sub>2</sub>O<sub>3</sub> and identified the emergence of a trap with an  $E_a$  of around 0.23 eV when significant Sn doping generated carrier densities of the order of  $\times 10^{19} \text{cm}^{-3}$  [196]. However, questions arise here as to whether Sn doping was directly responsible for the TSC peak or whether the TSC peak was more related to the high carrier density, prompting the question whether other "shallow"-type impurities such as Si or H, which would likely also generate a similar level of carrier density, also result in an increased TSC emission.

Using the same reasoning used in Chapter 3 that  $\alpha$  and  $\beta$  Ga<sub>2</sub>O<sub>3</sub> exhibit a similar trap distribution, we turn our attention to the TSC literature of  $\beta$ -Ga<sub>2</sub>O<sub>3</sub> as a comparison tool. Tak *et al.* reported a broad feature in the TSC spectrum between *ca* 110-200 K. The broad feature was resolved by a method known as the fractional emptying method. Here, the broad feature was resolved to a series of five peaks with activation energies of 0.16, 0.23, 0.28, 0.33 and 0.45 eV with the 0.28 eV trap in close agreement with our work [191]. However, no origin of the 0.28 eV trap was discussed. Luchechko *et al* conducted TSC investigations on  $\beta$ -Ga<sub>2</sub>O<sub>3</sub> crystals and identified a series of traps with characteristic maximum temperatures of 116, 145 and 165 K [197]. The group used a different method to estimate the  $E_a$  of the peaks compared to this study, by calculating the  $E_T$  from the slope of the TSC peak. As a result, it is deemed inappropriate to compare the activation energies directly. To explore the origin of the TSC peaks, samples were annealed in an oxygen atmosphere for 10 and 100 hours, noting a significant impact on the relative intensities of the deconvoluted peaks. Specifically, a reduction in the relative intensity of the peak at 116 K was observed after 100 hours of annealing, suggesting the involvement of  $V_O$  in the trap.

We turn our attention to an alternative method of trap identification in Ga<sub>2</sub>O<sub>3</sub>.

Polyakov *et al.* conducted a DLTS investigation on a series of Sn doped  $\alpha$ -Ga<sub>2</sub>O<sub>3</sub> with Sn concentrations of  $1.1 \times 10^{17}$ ,  $5 \times 10^{17}$  and  $4.8 \times 10^{19}$  cm<sup>-3</sup>. A peak in the DLTS spectrum emerged at 0.23 eV at the highest doping concentration. Indicating the role of Sn in the generation of shallow traps in the material [196]. Polyakov *et al.* observed a peak in the DLTS spectrum of Si doped  $\beta$ -Ga<sub>2</sub>O<sub>3</sub> after  $\alpha$  particle irradiation, where no assignment was given to the origin of the trap.

Huang *et al.* [198] used first principal calculations and experimental DLTS literature to assign trap distributions from a theoretical perspective. Calculations indicated transition energies of  $O_{Ga} - V_{Gal}$  are predicted to form donor levels in Ga<sub>2</sub>O<sub>3</sub> and favourable to form in O-rich conditions. This work overlaps nicely with the oxygen annealed study of  $\beta$ -Ga<sub>2</sub>O<sub>3</sub> by Luchechko *et al.* [197] where the peak at 116 K increased in intensity after annealing in O for 100 hours. Here we tentatively assign trap E1 to be related to O related di-vacancies such as  $O_{Ga} - V_{Ga}$

### **E2 and E3 between 200-250 K**

In the TSC spectra shown in Figure 5.6, we observe the dominant peak situated at 220 K with a shoulder at 235 K, corresponding to trapping energies of 0.47 and 0.51 eV, respectively. Polyakov *et al.* observed a similar peak with an  $E_a$  of 0.5 eV on HVPE  $\alpha$ -Ga<sub>2</sub>O<sub>3</sub> grown samples. However, no discussion of the origin of the peak was discussed. Tak *et al.* observe a strong dominant peak around 250 K with an  $E_a$  of 0.51 eV [191]. Given that the dominant peak with a smaller shoulder is observed by various groups, we are confident in the validity of the double peak, resulting from traps within a small energy range of each other.

To assign an origin of the TSC peak, we again turn our attention to the DLTS literature. Reports on this trap remain scarce with the first identification by Ghadi *et al.* in 2020 where no specific origin was suggested, just an overall suggestion that due to the fast emission rates the source was most likely related to a simple point defect [156]. Later in the work, a comparison between Ge-doped, UID-doped, and Si-doped samples revealed the trap is only observed in the Si-doped samples and may indicate the trap has a Si-based origin. However, each sample was produced by different

growth methods, with Si-doped samples grown by MOCVD. Therefore, the influence of the growth method and trap states need to be considered further. A later review in 2023 by *Labad et al.* identifies a series of traps ranging from 0.4-0.6 eV, known as the E1 trap [199]. Here, it was reminded that Polyakov *et al.* suggested the trap in this range may be related to Si-based complexes with H, notably Si<sub>Ga</sub>-H, which is divacancy between substitutional Si on the Ga site and H. In Chapter 3, it was shown that H has a dramatic impact on the luminescence properties of  $\alpha$ -Ga<sub>2</sub>O<sub>3</sub>.

The role of Si in defect formation in  $\alpha$ -Ga<sub>2</sub>O<sub>3</sub> was studied computationally by Jewel *et al.* and found that substitutional Si in Ga sites (Si<sub>Ga</sub>) exhibits an E<sub>a</sub> around 0.5 eV below the conduction band, supporting Polyakovs conclusions [4]. Other groups speculated on the incorporation of Cr<sup>3+</sup> as a possible candidate for E2. However, Naresh-Kumar et al reported the origin of red luminescence because of the incorporation of Cr ions [85]. However, the red luminescence signature of Cr<sup>3+</sup> was not observed in the luminescence measurements of our samples in this work, therefore the assignment of Cr seems unlikely.

Here we conclude from the evidence of the observed TSC spectrum, supporting evidence from the DLTS literature and computational studies from Polyakov et al and Jewel et al, respectively, we assign the origin of trap E2 to be related to Si<sub>Ga</sub>-H complexes

### 5.4.2 CPM for below Fermi level measurements

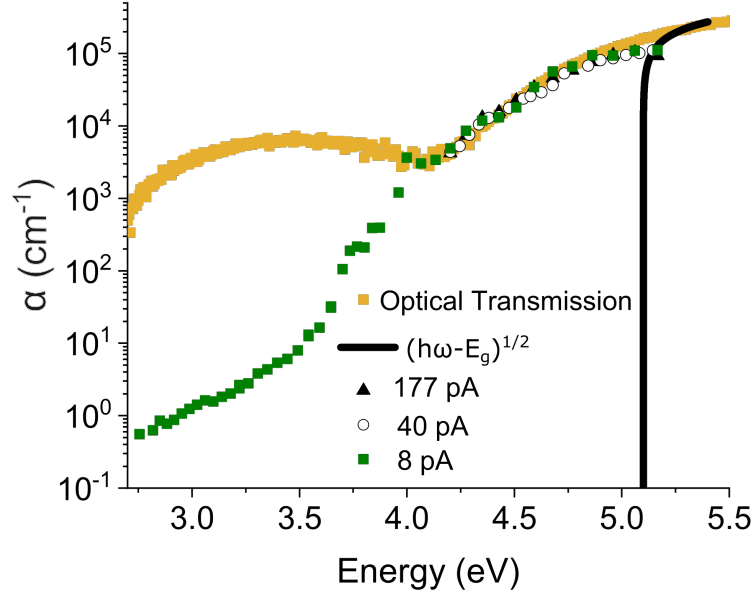


Figure 5.7: Absorption coefficient spectra of  $\alpha$ -Ga<sub>2</sub>O<sub>3</sub> obtained via CPM using different CPM reference currents (8 pA [green squares], 40 pA [white circles], and 177 pA [black triangles]) and optical transmission methods [gold]. The black line indicates how the absorption coefficient should scale in a direct bandgap semiconductor for a perfect crystal [8]

This work in this section is taken directly from published work [192], where I was the first author of the paper. Figure 5.7 compares the experimental absorption coefficient versus the photon energy obtained by CPM and the optical transmission spectrum for our  $\alpha$ -Ga<sub>2</sub>O<sub>3</sub> sample. As explained in the experimental section, the CPM spectrum is overlapped with the high-absorption region in the optical transmission spectrum at ca. 4.7 eV (corresponding to  $\alpha d=1$  condition). The requirement for scaling the CPM spectrum using the absolute values of the absorption coefficient from the optical absorption spectrum is rooted in equation 5.7, which shows that plotting the reciprocal of the photon flux versus the photon energy yields a value proportional to the absorption coefficient. In this spectral region, it becomes increasingly difficult to measure the absorbance using conventional optical spectrophotometry, and this is evident in the

gold spectrum figure 5.7, the source of the slight increase in the absorbance spectrum is currently unknown. In principle, reflections could excite additional carriers into the conduction band which would show as a series of fringes in the obtained CPM absorption spectrum. Typically, this is taken into account by simultaneously measuring the light transmitted through the sample, often referred to as “absolute CPM” [141]. However, here we observed no sign of interference fringes in the measured CPM absorption spectra shown in Figure 5.7, therefore, the absolute CPM technique was deemed unnecessary. In principle, carrier transitions yielding either a free electron or free hole can give rise to an increase in carrier photocurrent, leading to a potentially complex situation. Fortunately, the hole mobility is low in Ga<sub>2</sub>O<sub>3</sub>. Calculations of the band structure indicate that the valence band is composed of oxygen (O) 2p orbitals, giving a flat E-k relationship and a low effective mass. Furthermore, because of strong electron-hole coupling, holes tend to self-trap at O sites due to local lattice distortions [8]. We therefore believe that it is reasonable to suppose that electron transport dominates the measured photocurrent, due to transitions from filled states below the Fermi level to the conduction band. The CPM spectrum exhibits a number of features and is divided into 4 regions for the purpose of discussion. These are highlighted in Figure 5.8(a) and the corresponding electronic transitions are schematised in 5.8(b). It should be noted here that we have measured the dark current  $E_a$  for our samples, which lie in the range of 0.6 to 1.0 eV, placing the dark Fermi level at a similar energy level below the conduction band edge. This indicates that under CPM conditions, states from the valence band to above the midgap are fully occupied and, therefore, are accessible.

Region (i) spans the energy range greater than 5.1 eV and represents the high absorption region of the film. Given that  $\alpha$ -Ga<sub>2</sub>O<sub>3</sub> exhibits a bandgap energy of 5.1 eV, as determined here from the optical transmission and in line with previous reports [27–29], in that region we expect carriers to be excited to the conduction band from all filled states below the Fermi level including excitation from valence band to conduction band. If the material were a perfect direct bandgap semiconductor, with no states in the bandgap, the energy-dependent absorption coefficient should scale with the square root of the photon energy above the bandgap [200]. We would then expect

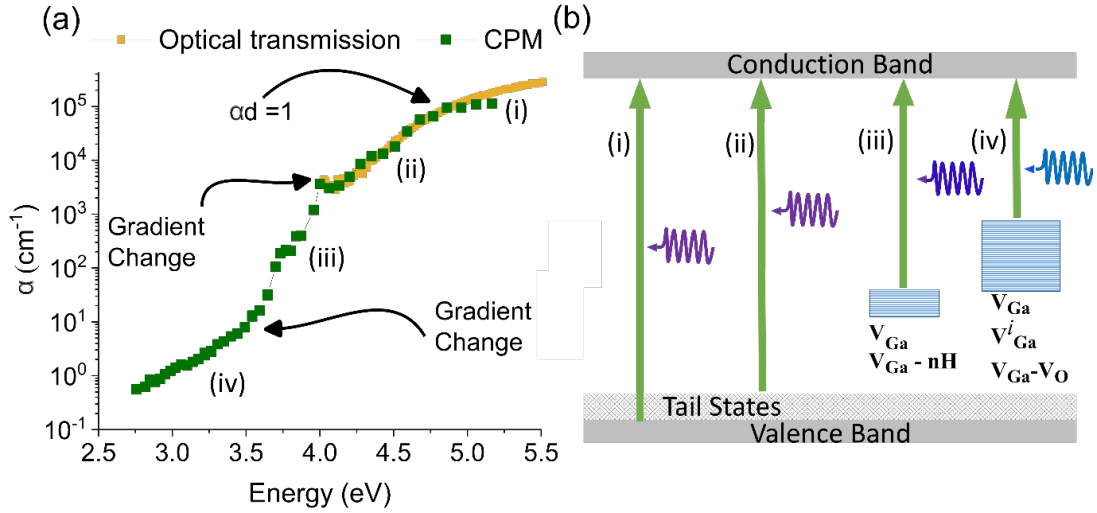


Figure 5.8: (a) Absorption coefficient obtained using CPM (b) Band diagram illustrating electron transitions from deep lying states below the Fermi Level

the absorption coefficient to fall rapidly to zero at energies below the bandgap energy – as illustrated by the black line in Figure 5.7. If states extending from the valence band edge into the bandgap are present, the absorption coefficient will fall less rapidly as the photon energy is gradually reduced below the bandgap energy. This is observed in region (ii), spanning energies between 4 eV and 5.1 eV. Here we see a pronounced broadening of the absorption edge. In bulk single crystal  $\beta$ -Ga<sub>2</sub>O<sub>3</sub>, the extension of the band edge into the sub-bandgap region has been measured by Hao *et al.* using photothermal deflection spectroscopy, in which their results were characterised by a characteristic slope energy of 100-200 meV [6]. In our work, we obtain a value of 430 meV which is significantly wider, attributed to structural disorder, defect incorporation and phase inclusions which we know are present in this film [29,70]. An important element in interpreting absorption coefficient versus photon energy curve is to deduce which set of states (empty, filled, or both) determines its ‘shape’ in each region. Generally, the broader (or less steeply varying) of the two will be the dominant process in the convolution. In the case of Ga<sub>2</sub>O<sub>3</sub>, it seems likely that the conduction band edge is a relatively sharp energy probe, with a narrow, low density of tail states. If significant tail states were present, they would reduce electron mobility by multiple

trapping – repeatedly immobilising carriers in shallow states until they are re-emitted to the conduction band. Since mobilities in the range of  $100 \text{ cm}^2\text{V}^{-1}\text{s}^{-1}$  have been measured in Ga<sub>2</sub>O<sub>3</sub> at room-temperature [201], and values of  $200\text{-}300 \text{ cm}^2\text{V}^{-1}\text{s}^{-1}$  are predicted [1,45,178], and controlled n-type doping with shallow donors is possible, there is no support for conduction band tail states being responsible for the transitions in region (ii). We therefore believe this broad absorption in Ga<sub>2</sub>O<sub>3</sub>, extending between 4.0 and 5.1 eV, is associated with filled states adjacent to the valence band. Region (iii), which covers energies from 3.6 eV to 4 eV, highlights the effectiveness of the CPM approach for obtaining values of the absorption coefficient in the sub-bandgap region. As previously discussed, the accuracy of the optical transmission measurement diminishes as the transmitted light is maximised and the detector cannot accurately measure relatively small intensity variations against a large transmitted background. On the other hand, CPM reveals 2 orders of magnitude of the absorption coefficient, from  $3 \times 10^3 \text{ cm}^{-1}$  at 4 eV to  $16 \text{ cm}^{-1}$  at 3.6 eV. Furthermore, we observe that the slope differs from that of region (ii) in terms of steepness, which could imply that electrons are being excited from states with different absorption characteristics than region (ii). Given that the photon energy is here much lower than the bandgap energy, it seems reasonable to infer that absorption in region (iii) corresponds to transitions of electrons from filled states below the Fermi level to the conduction band. Here we refer to the literature as a reference to defect states in the bandgap of  $\alpha$ -Ga<sub>2</sub>O<sub>3</sub> [62]. Due to the energy range, we are looking at defect levels which would reside between 3.6 eV and 4.0 eV below the conduction band. Theoretical calculations suggest that isolated gallium vacancies ( $V_{Ga}$ ) reside around 3.5 eV below the conduction band edge in  $\alpha$ -Ga<sub>2</sub>O<sub>3</sub> [4]. Gallium interstitials ( $Ga_i$ ) and substitutional gallium ( $Ga_O$ ) are predicted to have activation energies in the same energy region, however, both defects exhibit high formation energies, therefore, are not expected to be the responsible defect [4,55]. This was supported experimentally by deep level optical spectroscopy revealing  $V_{Ga}$  related defect states located ca 3.5 eV below the conduction band [60,98]. Further work from Polyakov *et al.* suggested H-decorated complexes exhibit defect levels situated 3.8-3.9 eV below the conduction band edge [99], and luminescence studies in chapter

3 of this work has associated 3.8 eV luminescence with H-decorated  $V_{Ga}$  [103]. The low formation energy of the H-decorated  $V_{Ga}$  compared to isolated  $V_{Ga}$  suggests it is the most probable form of the defect [202]. Here we must note that if a discrete set of traps were responsible for the transition, this would be reflected as a series of steps in the absorption spectrum, with each step associated with the  $E_a$  of that discrete level. Figure 5.7 is more reflective of an exponentially distributed set of states within the bandgap. In chapter 4, it was proposed that an exponentially distributed set of traps could explain the sublinear relationship observed from our power-dependent photocurrent measurements. We therefore tentatively ascribe an exponential distribution of  $V_{Ga}$ -nH complexes as the origin of the absorption in region (iii). We finally point out that the transitions in region (iii) will be a convolution of transitions from filled states in regions (iii) and (iv). Lastly, region (iv) that the decrease in the absorption coefficient extends further, from  $16 \text{ cm}^{-1}$  at 3.6 eV to  $0.8 \text{ cm}^{-1}$  at 2.7 eV, with a different slope compared to region (ii)-(iii). Again, this region is masked on the optical transmission measurements. Following a similar reasoning as for region (iii), we interpret absorption in that region as resulting from transitions from filled states below the Fermi level to the conduction band. To interpret the origin of this region in absorption, we should look for defect states residing between 2.7-3.6 eV below the conduction band. As previously mentioned, isolated  $V_{Ga}$  reside around 3.5 eV below the conduction band edge, however, it is observed in the ODLTS literature that di-vacancies of  $V_{Ga}$  and  $V_O$  ( $V_{Ga}$ - $V_O$ ) add additional energetic states distributed between ca 2.0-3.5 eV below the conduction band, depending on the charge state of each isolated defect [55, 62]. From a theoretical perspective, Varley *et al.* revealed the possibility of isolated  $V_{Ga}$  which have relaxed to occupy interstitial sites, with energetic levels calculated to be in the range of 2.1-3.3 eV below the conduction band, with the energy level determined by the charge state of the defect [202]. Therefore, we tentatively interpret region (iv) as arising from an exponentially distributed set of states related to  $V_{Ga}$ -related defects involving  $V_{Ga}$ - $V_O$  complexes, isolated  $V_{Ga}$  or relaxed  $V_{Ga}$  occupying interstitial sites.

## 5.5 Summary and Future work

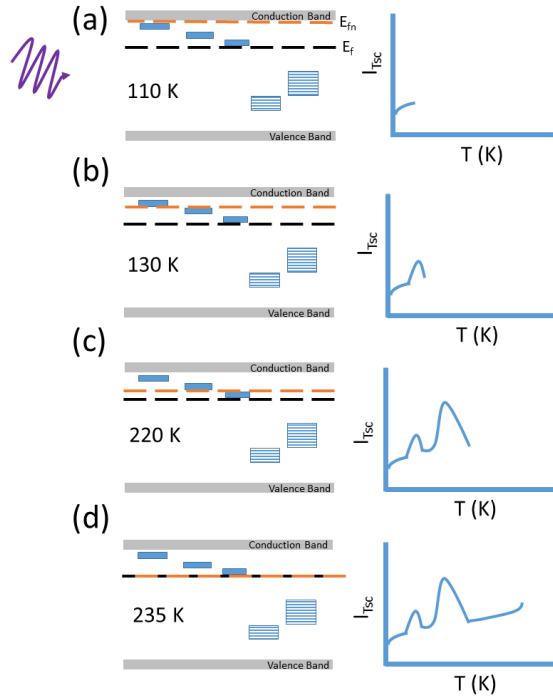


Figure 5.9: Schematic of defect states identified using a combination of TSC and CPM

In this chapter, we concentrate on using photoconduction techniques to examine defect states within the bandgap of  $\alpha$ -Ga<sub>2</sub>O<sub>3</sub> using the CPM for states below the Fermi level and TSC for states above the Fermi level. We used a novel technique to reintroduce the CPM as a means to determine the absorption coefficient at sub-bandgap energies in wide-bandgap semiconductor films, demonstrating its application on  $\alpha$ -Ga<sub>2</sub>O<sub>3</sub>. This study combines the optical transmission measurement with CPM to obtain values of the absorption coefficient ranging from  $0.8 \text{ cm}^{-1}$  to  $10^5 \text{ cm}^{-1}$  across an energy range of 2.7 to 5.3 eV above the valence band edge. The absorption spectrum is divided into four distinct regions, each highlighting different electronic transitions that contribute to photocurrent generation in the material. These regions include contributions from band-to-band transitions (region (i)), band tails (region (ii)), and defect-mediated transitions tentatively attributed to an exponentially distributed set of states associated

with isolated  $V_{Ga}$  and  $V_{Ga-nH}$  complexes (region (iii)), as well as  $V_{Ga-V_O}$  divacancies and relaxed  $V_{Ga}$  in interstitial sites (region (iv)). The study confirms that CPM is an effective technique for measuring the absorption coefficient in the sub-bandgap region, and for investigating deep trap states in thin films. Given the work here served as a proof of concept of the approach of the CPM technique to  $\alpha$ -Ga<sub>2</sub>O<sub>3</sub>, the next work should be a comparative study on the same sample using CPM and PDS via a collaborative study with the group led by Martin Stutzmann. Next, given our work aims to correlate changes in the absorption coefficient due to defects, further studies should examine the effects of annealing conditions and doping species on the measured CPM spectrum.

TSC measurements were conducted over a temperature range of 110 to 400 K. The emission spectrum identified three traps at approximately 138 K, 220 K, and 235 K, which correspond to trap activation energies of 0.28 eV, 0.47 eV, and 0.51 eV, respectively, as determined by the T4 approximation. The UID nature of the samples resulting in a heavy reliance the literature to establish an origin of the traps. Tentatively, we assign trap E1 (0.28 eV) to be related to O related divacancies such as  $O_{Ga}-V_{Ga}$ , where the Sn related complexes also demand attention. Theoretical calculations predict that isolated  $V_O$  reside around 1 eV below the conduction band, therefore unlikely to be the origin of the trap. Trap E2(0.47 eV) and E3 (0.51 eV) were tentatively assigned to  $Si_{Ga}-H$ . Although 2 traps were resolved by TSC, the ambiguity in obtaining accurate trap activation energies of two peaks in close proximity in terms of energy makes trap assignment difficult. Here we propose future experimental work with a range of samples with different doping species to observe the emergence/quenching of TSC peaks. Extensive theoretical and computational studies are required to fully understand the kinetics in gallium oxide to better interpret the TSC spectrum to establish the correct method in obtaining trap activation energies. In the short term, a calibration spectrum could be used to estimate the best technique for obtaining the  $E_a$ . A comparative study of a sample studied by DLTS with well-defined trapping energies could be used to compare with the TSC spectrum measured at different ramping rates to use both the the Bube method and T4 approximation.

## Chapter 6

# A Novel Approach to Water Quality Monitoring using $\alpha$ -Ga<sub>2</sub>O<sub>3</sub> photodetectors

### 6.1 Background

Ensuring access to clean water is of paramount humanitarian and ecological importance. It is estimated that around 1 billion people worldwide lack access to clean water, resulting in over 2 million deaths per year [203]. With population rapidly expanding, and industrial applications reducing the availability of water which is safe for human consumption, there is a growing need to effectively monitor the quality of water [204, 205]. The importance of water quality has been recognised at an international level, with the United Nations listing clean water and sanitation as a Sustainable Development Goal, with the target of establishing clean water for all by 2030 [206]. A first step to reduce harmful contaminants in water sources is to develop effective methods to monitor their concentrations. The concentration of certain compounds in water can suit as an excellent metric to define water quality. Three common impurities are nitrates, dissolved organic carbon (DOC) and suspended solid concentration (SSC). Nitrates are compounds that are formed in the natural nitrogen cycle, and used in many

applications ranging from fertilizers to explosives. Nitrates are the most common contaminant in water and can have a detrimental effect on human health by enhancing pathogenesis of some gastric cancers [207, 208]. Furthermore, elevated nitrate levels will have adverse effects on aquatic animals causing histopathological alterations in the gills, oesophagus, and the brain [209]. Nitrate incorporation in aquatic life will inevitably trickle down to human consumption via the food chain. DOC can come from a variety of sources, but usually from the decomposition of dead organic matter, including plants and wildlife. It can have staggering effects on water quality due to its ability to form complexes to alter the mobility heavy metals, and challenges the efficiency of water treatment processes [210]. Finally, SSC is a measure of the suspended solids residing in water. Suspended solids in large concentrations reduce light penetration and can act as an absorber, and alter the physical, chemical and biological properties of water. Increased water temperatures and reduced dissolved oxygen levels through a reduction in the photosynthesis process are linked to high SSC levels absorbing light [211–213]. To deliver the United Nations’ access to clean water for all target, it will be critical to develop solutions to effectively monitor nitrate, DOC and SSC levels in water in a convenient way that can be widespread, energy-efficient and simple to use. Recently UV-vis spectrophotometry has been gaining attention as an effective water monitoring method able to trace impurity concentrations over wide spectral range [214]. The aforementioned contaminants exhibit different absorption characteristics. While nitrates strongly absorb light in the 200-250 nm spectral region, DOC exhibit characteristic absorbance in the 250-350 nm range, and SSC dominantly affects absorption in the 350-700 nm range [215, 216]. However, a number of system requirements limit practical usage of UV-vis spectrophotometry to conduct water quality monitoring in-situ in water streams. These systems are typically classified by two measurement methods: spectrophotometers and spectrometers, which differ in their design and operation. On the other hand, a spectrometer employs a fixed diffraction grating to spatially separate incoming light onto a detector array, typically composed of Si photodiodes, as described in Chapter 2 section 2.1.1. However, Si-based detector arrays exhibit poor responsivity in the deep UV region (below 300 nm) due to their

narrow bandgap (1.1 eV), limiting their effectiveness in detecting contaminants such as nitrates and DOC, which absorb in the 200–350 nm range. Additionally, prolonged UV exposure can accelerate ageing and degradation of Si photodetectors. To monitor the water sample absorbance over a wide spectral range, UV-vis systems employ light sources, often a combination of xenon and halogen bulbs, which are inefficient, bulky, fragile and with limited lifetime. The requirement to spectrally resolve the broad light sources means that an extra monochromator is necessary. Overall, this presents a current challenge in the field to be able to monitor nitrate, DOC, and SSC levels simultaneously whilst ensuring the detection device is cost effective and compact. The recent emergence of ultrawide-bandgap semiconductors such as Ga<sub>2</sub>O<sub>3</sub> with bandgap energies nearing 5 eV (*ca.* 250 nm) is opening new opportunities for deep UV sensing with greater efficiency and lower size and power consumption requirements over Si-based detectors [217]. Earlier in the thesis it was discussed that Ga<sub>2</sub>O<sub>3</sub> is typically referred to as a solar-blind photodetector, such that the material is insensitive to light in the visible wavelength range (400-700 nm) but responds well to illumination of light less than 280 nm. However, in Chapters 4 and 5 it was demonstrated that defect states within the bandgap stimulate absorption of sub-bandgap energy light. In Chapter 5, we used CPM to quantify the absorption coefficient at sub-bandgap energies [192]. In this study, we demonstrate that we can take advantage of the different electronic transition pathways (band-to-band, defect-to-band) in  $\alpha$ -Ga<sub>2</sub>O<sub>3</sub> to realise a simplified setup allowing simultaneous monitoring of nitrate, DOC and SSC levels in waters.

## 6.2 Methods

A 250 nm thick film of  $\alpha$ -Ga<sub>2</sub>O<sub>3</sub> was deposited on c-plane sapphire substrate using PEALD following the detailed growth procedure [111] described in Chapter 1. The samples were processed into a planar photodetector device using Cr/Au contacts with a material thickness of (3/30) nm deposited in an interdigitated finger configuration.

Optical excitation was performed under two different regimes. To test for nitrate absorption, a Thorlabs deuterium light source coupled to a SolarLS ML44 monochro-

mator was used to illuminate the sample with 225 nm light. For below-band excitation, a range of LEDs with different peak wavelengths (250, 260, 275, 375, 405, and 465 nm) were used, with the details of the LED listed in table 2.1. The generated light was focused onto a quartz cuvette before illuminating the sample. Photocurrent was measured using a Signatone probe station coupled with a Keithley 6487 piccoammeter for voltage source and photocurrent reading. Due to the highly resistive nature of undoped Ga<sub>2</sub>O<sub>3</sub>, the measurements were obtained under 10 V. A schematic of the experimental setup is illustrated in Chapter 2 Figure 2.24. The photocurrent was first allowed to reach a steady-state with an empty cuvette, and the cuvette was subsequently filled with water containing various concentrations of Nitrates, DOC and SSC following which the new steady-state photocurrent was recorded.

Water samples were prepared with nitrate concentrations ranging from 1.69 mg/L to 677 mg/L, DOC concentrations ranging from 1.99 mg / L to 6.7 mg / L and SSC from 22.4 mg/L to 1247 mg/L. The water samples were acidified for preservation and analysed using a Torch combustion total organic carbon analyser (Teledyne-Tekmar, USA). Water samples with nitrate concentrations ranging from 1.69mg/L to 677 mg/L were prepared using a 1000 mg/L nitrate standard for IC (Sigma-Aldrich, St. Louis, MO, USA). Water samples with SSC ranging from 22.4 mg/L to 1247 mg/L were prepared using fine particles (  $30 \mu\text{m}$ )

### 6.3 Results and Discussion

XRD diffratograms carried out by our collaborators reveal a dominant reflection centred near  $2\theta = 40.25^\circ$ , which is associated with the 0006 reflection from  $\alpha$ -Ga<sub>2</sub>O<sub>3</sub>, and a peak at  $2\theta = 38.20^\circ$  associated with the 111 reflection from the Au electrode. The XRD results are presented in Figure 6.1(c) Transmission electron microscopy measurements supported the XRD conclusion that the material was dominantly  $\alpha$ -Ga<sub>2</sub>O<sub>3</sub>, and Figure 6.1(d) further reveals that the film consisted of  $\alpha$ -Ga<sub>2</sub>O<sub>3</sub> columns (lighter contrast in Figure 6.1(d)) with inclusions of amorphous and  $\kappa$ -Ga<sub>2</sub>O<sub>3</sub> between the columns (darker contrast in Figure 6.1(d)) [218].  $\alpha$  and  $\kappa$  Ga<sub>2</sub>O<sub>3</sub> exhibit bandgaps of 5.1–5.3 eV and

Chapter 6. A Novel Approach to Water Quality Monitoring using  $\alpha$ -Ga<sub>2</sub>O<sub>3</sub> photodetectors

4.7–5.0 eV, respectively. Therefore, incorporating both phases broadens the absorption edge toward longer wavelengths compared to phase-pure  $\alpha$ -Ga<sub>2</sub>O<sub>3</sub>, thereby extending the device’s spectral sensitivity in the UV region.

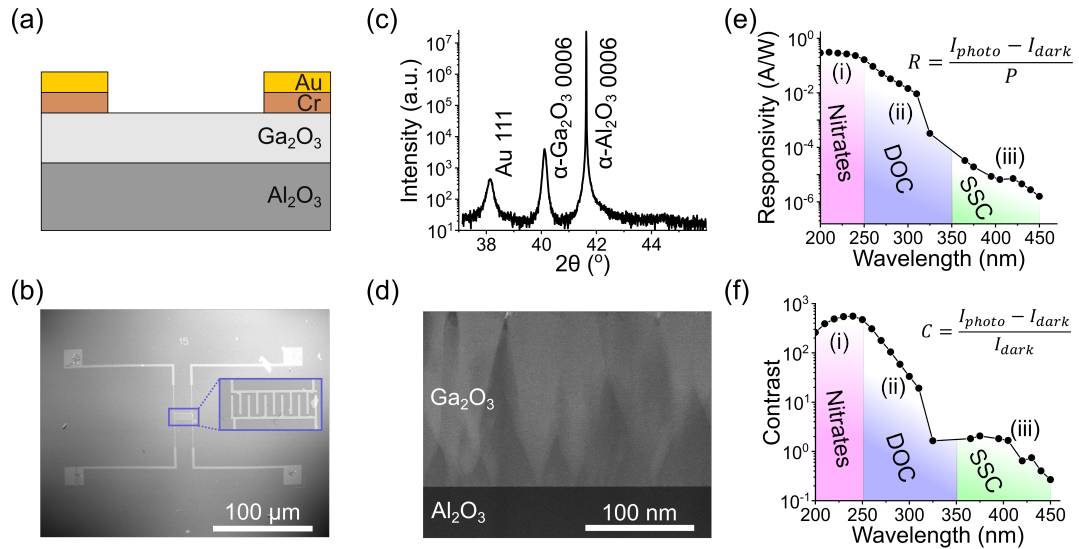


Figure 6.1: (a) Schematic of the cross section of the Ga<sub>2</sub>O<sub>3</sub>-based photodetector. (b) SEM image of the contact structure, with inset showing a magnified image of the interdigitated finger area. (c) XRD diffractogram revealing reflections from Al<sub>2</sub>O<sub>3</sub>, Ga<sub>2</sub>O<sub>3</sub>, and Au. (d) Transmission electron microscope image of device cross section (e) Photodetector responsivity and (f) contrast versus wavelength

The important characteristics of the Ga<sub>2</sub>O<sub>3</sub> photodetector against the illumination wavelength are shown in Figure 6.1(e,f). Here we note the spectra shown in Figure 6.1 is measured directly on the material, i.e. no light is passing through the water sample prior to illuminating the sample. As discussed in Chapter 3, responsivity describes the photogenerated current per incident optical power, providing useful information on the fundamental properties of the photodetector. Here we can see that the photogenerated current is at a maximum in the deep UV region corresponding to the bandgap of the material (*ca.* 230 nm). At longer incident wavelengths, the responsivity exponentially decays from *ca.* 250 nm to 350 nm, the extent and steepness of which are indications of disorder and defect incorporation in the material. The contrast, shown in Figure 6.1(f), is a related metric that describes the photogenerated current compared to the dark current, without normalisation of incident power. This metric holds greater sig-

nificance in technological applications because it allows for the consideration that over a broad spectral range, the available output power of illumination sources will vary significantly. Figure 6.1(e) serves as a reminder of the work in Chapter 4 showing broad optical absorption. Here, while Figures 6.1 (e,f) show similar trends, we see that the exponential decrease in contrast in the 250-350 nm range is less pronounced than for the responsivity, spanning 2 orders of magnitude instead of 3, and is due to the availability of more powerful LEDs in that region (typical power of 5- 20 mW) compared to deep UV LEDs ( *around* 0.5-1 mW) or a spectrally resolved deuterium source (approx 10-60 nW).

Looking at the curves in more detail, we can distinguish three regions relating to the electronic band structure of the material. As mentioned above, given the bandgap of 5.1-5.3 eV for  $\alpha$ -Ga<sub>2</sub>O<sub>3</sub> [27–29], the response in region (i) (200-250 nm) is attributed to intrinsic photogeneration of free carriers in the conduction band excited from the valence band. In that region, the photocurrent is ca. 300 times greater than the dark current, demonstrating the excellent deep-UV sensing capabilities of Ga<sub>2</sub>O<sub>3</sub>. The UV sensing capabilities in region (i) align perfectly with the characteristic absorption of nitrates. Region (ii) extends from 250 nm to 350 nm and is related to the photocurrent arising from carriers generated through transitions between the band tail states and the conduction band identified in Chapter 5. In a direct semiconductor with no states in the bandgap, the absorption coefficient will rapidly fall to zero at photon energies lower than the bandgap scaling such as  $(E_{\text{ph}}-E_{\text{g}})^{\frac{1}{2}}$  with the slope of the decrease of the absorption coefficient with energy referred to as the absorption edge. However, as material quality degrades, attributed to a number of factors such as point defect incorporation, extended defects, and phase purity, the absorption edge broadens into the bandgap near the optical band edges, referred to as a band tail. This effect is illustrated in Figure 6.2.

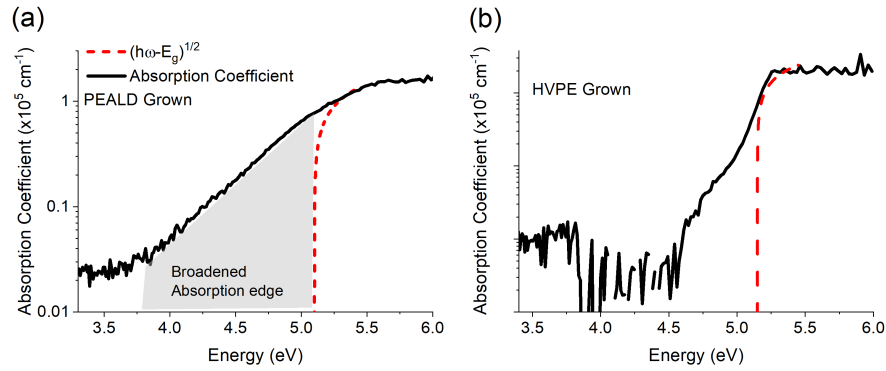


Figure 6.2: Absorption Coefficient measured between 3.4 and 6 eV for (a) PEALD grown sample 250 nm (b) HVPE grown sample. The red dashed line represents how the absorption coefficient scales with in energy in perfect direct bandgap semiconductor

Figure 6.2(a) illustrates the absorption coefficient as a function of photon energy where we see a broad absorption edge compared to a high-quality HVPE grown sample shown in Figure 6.2(b).

As a reminder of the discussion in chapter 5, the absorption edge of single crystal material would be in the order of 10s of meV for materials such as ZnO and GaN and of the order of 100-400 meV for Ga<sub>2</sub>O<sub>3</sub> measured in Chapter 5. In this study, thin film  $\alpha$ -Ga<sub>2</sub>O<sub>3</sub> was used as the detector material and X-ray diffratograms Figure 6.1(c) shows a single narrow peak for  $\alpha$ -Ga<sub>2</sub>O<sub>3</sub> at 40.25°, but previous analysis by transmission electron microscope revealed that small inclusions of amorphous and  $\kappa$  phase were present between the  $\alpha$ -phase columns (Figure 6.1 with more details found in [218]). The results of XRD diffratograms and transmission electron microscope measurements indicate a degradation in structural quality resulting in a broadening of the absorption edge beyond what is expected for single crystal Ga<sub>2</sub>O<sub>3</sub>. The broad exponential tail in semiconductors may be considered a negative aspect in terms of structural quality. However, here it is beneficial in the context of water quality testing, as a measurable photocurrent can be extracted at wavelengths that are below the bandgap energy of the material. The photocurrent measurements and absorption characteristics shown in Figure 6.1 indicate that region (ii) aligns well with the absorption characteristics of DOC. If the high-quality HVPE grown sample shown in Figure 6.2(b), the absorption coefficient is dominated by noise from around 4.5 eV, compared to 4 eV for the PEALD

grown sample, and in terms of detection capabilities, this would limit absorption wavelengths we could probe with our detector.

Finally, region (iii) extends from 350 nm to the visible wavelength region and relates to defect-assisted transitions to the conduction band. Ga<sub>2</sub>O<sub>3</sub> is a relatively new material, incorporating a large number of defects resulting in a large DOS distributed through the bandgap reflected in the luminescence measurements in Chapter 3 and photoconduction measurements in Chapters 4 and 5. Although the photocurrent generated through these transitions is 4-5 orders of magnitude lower than for band edge transitions, the availability of powerful LEDs (typically in the order of mWs) in this wavelength range makes it a practical region to probe SSC contamination for the purposes of water quality testing. Therefore, Figures 6.1(e,f) show that in principle, we can take advantage of the different electronic transition pathways in  $\alpha$ -Ga<sub>2</sub>O<sub>3</sub> to monitor nitrate, DOC and SSC levels in water, illustrated in Figure 6.3

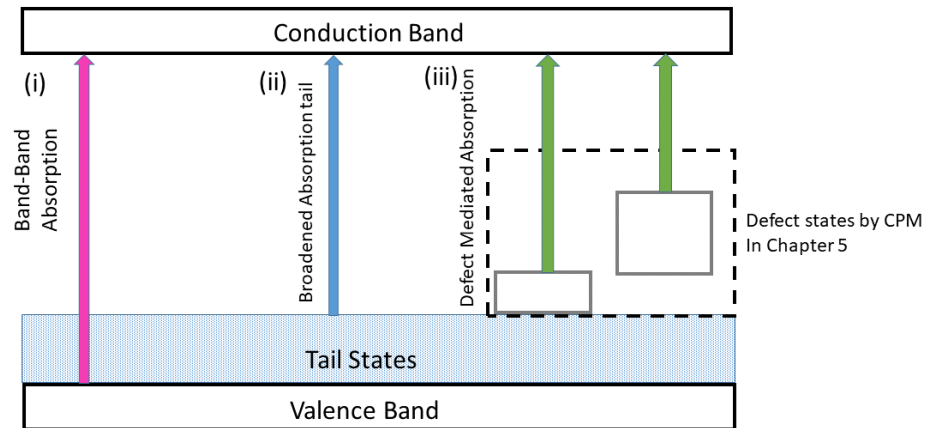


Figure 6.3: Defect diagram indicating the various electronic pathways to the conduction band to enable water quality monitoring for (i) Nitrates (ii) DOC (iii) SSC

We now turn our attention to assessing the sensitivity of the detector to sense variations in concentration of these contaminants. Figure 6.4(a) shows the effect of nitrate concentration on the measured photocurrent using above-bandgap 225 nm illumina-

tion. Here, the excitation was generated from a deuterium light source due to the low availability of LEDs in the suitable wavelength range of 220-230 nm. However, recent advances in LED technology indicate that these will soon be commercially available with optical power in the  $\mu$ W-mW range, offering a significant improvement in terms of optical power, lifetime, system size and power consumption compared to the deuterium source.

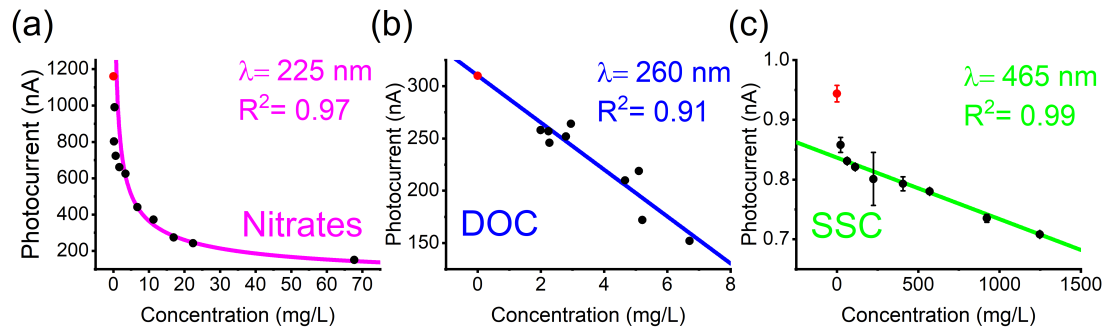


Figure 6.4: Photocurrent measurements versus concentration of (a) nitrates using 225 nm optical excitation (b) DOC using 260 nm optical excitation (c) SSC using 465 nm optical excitation. The data point marked in red signifies the photocurrent response to the cuvette filled with deionised water.

Here we observe a strong power-law decay in the measured photocurrent as the nitrate concentration increases, reflected in a high goodness of fit with an  $R^2$  of 0.97. When illuminating the nitrate-containing water sample with 225 nm light, nitrates absorb the incident light, thus reducing the intensity of the light reaching the detector. The high absorption in this spectral region, which is characteristic of ultrawide-bandgap semiconductors like Ga<sub>2</sub>O<sub>3</sub>, suggests a high sensitivity to variations in nitrate concentrations and therefore small changes in concentration should yield substantial changes in photocurrent. Here, the high sensitivity to nitrate concentration is advantageous for Ga<sub>2</sub>O<sub>3</sub>, and presents a substantial technological improvement compared to the Si-based detector system, which exhibits a substantial decrease in responsivity in the deep UV range. The fitting of the data presents a method of calibration that can be used to estimate concentration levels in untested water samples. With the greater of the  $R^2$  values presenting a more accurate concentration estimation. As a reminder to the reader, it was shown that the responsivity and hence the sensitivity of the detector can

be varied by reducing the illuminating power. Given that the photocurrent is of the order of  $\mu\text{A}$ , improvements could be made to the sensitivity of the detector by reducing the illumination intensity.

Figure 6.4 shows the effect of the concentration of DOC on the measured photocurrents. Using a 260 nm LED as illumination source, we observe a linear relationship between the concentration of DOC and the photocurrent with the goodness of fit  $R^2$  of 0.91, which demonstrates the excellent capabilities for Ga<sub>2</sub>O<sub>3</sub> for DOC detection in water. Here, the trend is linear and not exponential as in Figure 6.4(a) due to the inherently lower absorbance of water in that spectral range, which means that the Beer-Lambert law can be reasonably approximated as a linear relationship. This variation of the power-law behaviour of the nitrates to the linear behaviour of the DOC can be explained by analysing the Beer-Lambert law and the absorption coefficient measured by UV-Vis spectrophotometry.

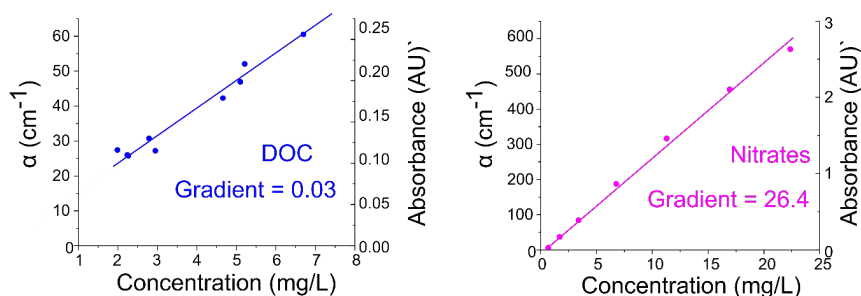


Figure 6.5: Absorbance measurements of (left) DOC (right) Nitrates

Figure 6.5 shows the absorbance measurements obtained by UV-vis spectrophotometry. We note a significant difference in the trend in relation to the photocurrent response to nitrate concentration compared to DOC. This may be explained in terms of the absorption characteristics of the contaminants at the selected excitation wavelength. As discussed in Chapter 2, the Beer-Lambert law states that the transmitted light is proportional to  $\exp(-\alpha d)$  where  $\alpha$  is the absorption coefficient and thickness  $d$  of the medium through which the light transmits. Figure 6.5 shows a comparison of absorbance versus concentration for both nitrates and DOC, with the gradient of the line taken to compare the effects. In both cases, we see a linear relationship between

absorbance and concentration. However, in the case of DOC there is a multiple orders of magnitude decrease in the gradient coefficient. Here lies the explanation of the behaviour of the photocurrent decay. In Figure 6.4, we see a strong power decay of the photocurrent as the nitrate concentration increases. This would be expected because of the exponential term in the Beer-Lambert law. However, Figure 6.4(b) reveals a linear behaviour between photocurrent and DOC concentrations. This can be explained in terms of the gradient shown in Figure 6.5, where the slope gradient is shown to be orders of magnitude smaller than that for nitrates. If we consider a Taylor expansion series such that when  $\exp(x) = 1 - x$  when  $x$  is  $\ll 1$ . Therefore, we expect an approximate linear relationship between the photocurrent and the concentration of DOC, as shown in Figure 6.5.

Lastly, Figure 6.4(c) shows the impact of SSC concentration on the measured photocurrents. Here we use a 465 nm LED for illumination to reveal a linear relationship between SSC concentration and photocurrent when SSC levels exceed approximately 60 mg / L, with an excellent goodness of fit  $R^2$  of 0.99. Similarly to the case for DOC, the relationship is linear rather than exponential because of the low absorption of light by water at that wavelength. The nonlinear region at low concentrations may present a limit to the calibration curves used to estimate SSC levels at low concentrations. This could be attributed to the relatively low absorption profile of the SSC and the low absorption material parameters. Therefore a large concentrations required to make a noticeable change in the photocurrent. Figure 6.4 (c) illustrates the ability to advantageously use the presence of disorder and defects in Ga<sub>2</sub>O<sub>3</sub> for detecting SSC in water.

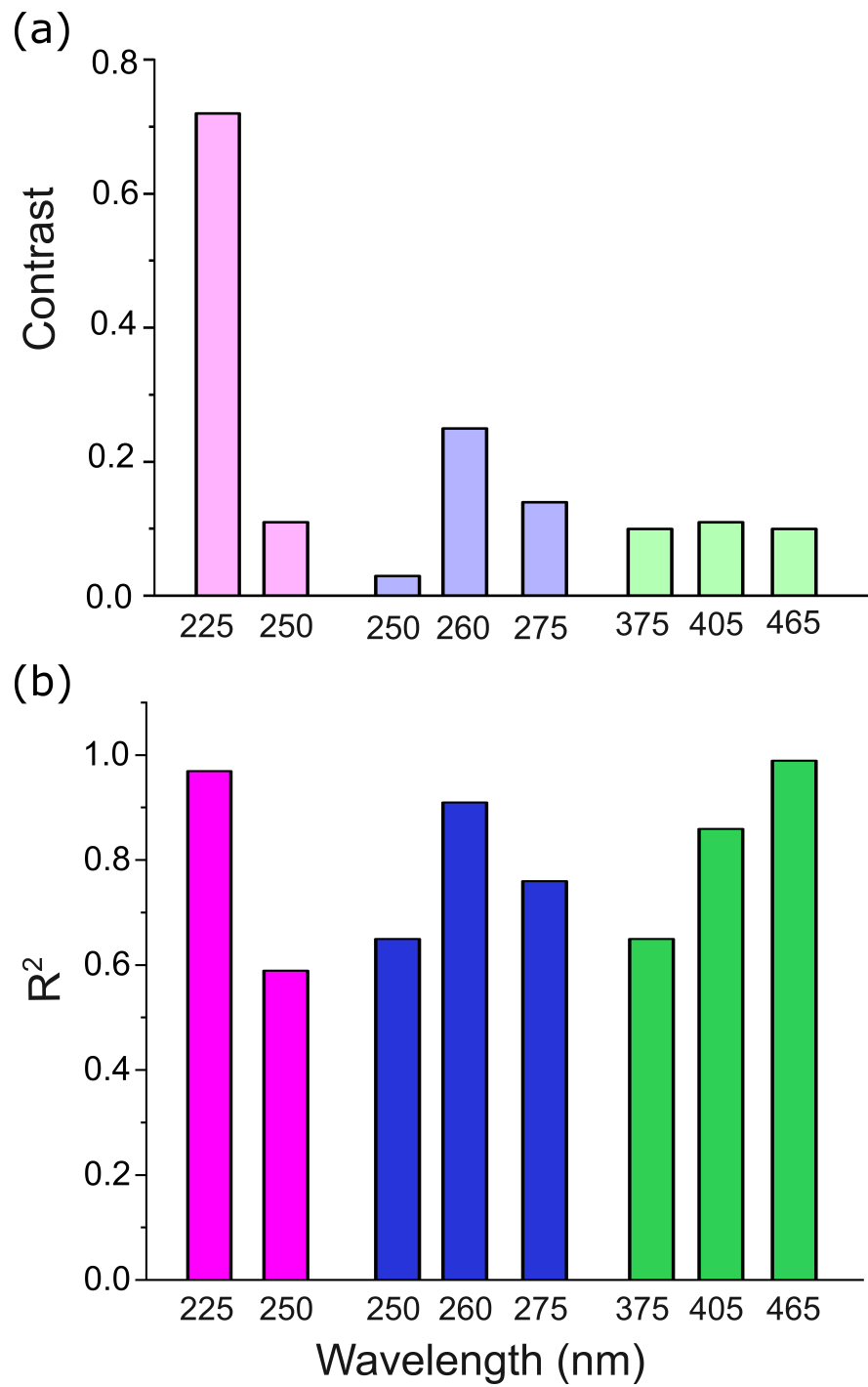


Figure 6.6: Effect of excitation wavelength on (a) contrast (b) goodness of fit values for water quality monitoring

The photocurrent measured as an output of the water monitoring process is a convo-

lution of the light source emission power, the absorbance spectrum of the contaminant, and the spectral response of the detector. Therefore, it is expected that there will be an optimal wavelength to use in order to obtain a maximal detector sensitivity for a given contaminant. Figure 6.6 shows that changing the illumination wavelength from 225 nm to 250 nm for nitrate detection results in a 7-fold decrease in contrast (from 0.79 to 0.11) and a marked decrease in goodness of fit from 0.97 to 0.59, with the variation in contrast and goodness of fit dominated by the absorption properties of nitrates which have a significantly higher absorption profile at 225 nm compared to 250 nm [219]. Similarly for DOC, Figure 6.6 shows the significant dependence of the excitation wavelength on both contrast and goodness of fit, with the 260 nm excitation yielding superior detection performance compared to the 250 and 275 nm excitation. Finally, Figure 6.6 shows a clear dependence on the excitation wavelength for SSC contamination detection, with the 475 nm excitation showing an excellent goodness of fit of 0.99 compared to 0.83 and 0.62 for the 405 nm and 375 nm excitation, respectively. Here we note that there is not much variation in the contrast values; this may be explained by the low response of the detector in the sub-bandgap region. Further work is required to define the detection limits for Ga<sub>2</sub>O<sub>3</sub> based detectors for water quality monitoring and to define the wavelength detection range that can be used. The logical parameter which will define the detector sensitivity is of course the dark current and responsivity of the detector, which will be heavily influenced by growth and doping methods and a trade-off of the effects will have to be considered. In this work, excitation with wavelengths greater than 465 nm resulted in a photocurrent response comparable to the dark current.

## 6.4 Summary and Future Work

In conclusion we present  $\alpha$ -Ga<sub>2</sub>O<sub>3</sub> as an alternative material that shows great promise for monitoring water quality with greater sensitivity, system size, and power consumption requirements compared to Si-based technology. Ga<sub>2</sub>O<sub>3</sub> exhibits a broad photoresponse spanning the UV and visible spectral range, which is a key component in

detecting contaminants that absorb in different spectral regions. Using advantageously different carrier excitation pathways in the material, photocurrent measurements reveal 3 distinct regions that match key water contaminant absorption characteristics. Region (i) (200-250 nm) corresponds to band-to-band transitions and is ideal for nitrate detection, region (ii) (250-350 nm) is related to band tail transitions and fits the absorption peak of DOC, and finally, region (iii) (350-470 nm) addresses SSC detection using defect-mediated transitions. For the wavelengths selected for the contamination test, strong correlations ( $R^2 > 90$ ) were observed between the concentration of the contaminant and the photocurrent. The  $R^2$  correlations strongly depended on the selected illumination wavelength, which demonstrates good selectivity of the photodetectors. This work opens the door to a more sensitive, compact, and energy-efficient system to monitor water quality.

## Chapter 7

# Conclusions and Further Work

### 7.1 Conclusions

In this thesis, we present optical and electrical characterisation of  $\alpha$ -Ga<sub>2</sub>O<sub>3</sub> thin films, with a particular focus on understanding the influence of defects on the material properties. Here we employ various experimental techniques ranging from luminescence spectroscopy to photoelectrical techniques such as CPM, to identify defect related behaviour in the material and demonstrate the capabilities of  $\alpha$ -Ga<sub>2</sub>O<sub>3</sub> for future optoelectronic devices.

A central finding was the pronounced sensitivity of the optical emission to we used luminescence techniques to investigate the role of H in the material and observed a new luminescence line centred at 3.8 eV that exhibited a strong temperature dependence attributed to DAP recombination between H donor and H decorated V<sub>Ga</sub>. Here we observed a remarkable sensitivity to H concentration in the films, where we observed a significant increase in the relative intensity of the H-related luminescence line with H concentration, which may be used as a quick tool for H detection in  $\alpha$ -Ga<sub>2</sub>O<sub>3</sub>. In this work, the first low-temperature HSI was conducted on  $\alpha$ -Ga<sub>2</sub>O<sub>3</sub> and revealed that the 3.8 eV line not only exhibited a significant temperature dependence, but also a spatial dependence where the peak intensity was non-uniform across the sample surface.

On the photoelectrical characterisation side. Here we tested the functionality of the home-built photoelectrical characterisation set-up and observed the significant impact

of experimental conditions (illumination power and device architecture, and applied bias) on the reporting of relevant photodetector parameters such as responsivity and response time. The key point from Chapter 4 was that, when comparing photodetectors from the literature, claims of a "super fast" or "High response" must be taken with a pinch of salt, as these parameters are highly dependent on experimental conditions. This work highlights the need for standardised reporting metrics when reporting photodetector performance to make fair comparison between devices in the field-an issue of increasing importance as we approach commercialisation of  $\alpha$ -Ga<sub>2</sub>O<sub>3</sub> devices.

Knowing the impact defects can have on devices, we demonstrated the use a combination of CPM and TSC as a proof-of-concept approach to mapping defect states across the bandgap. Here, we present a revival of CPM to measure sub-bandgap absorption in  $\alpha$ -Ga<sub>2</sub>O<sub>3</sub> from 0.8 cm<sup>-1</sup> at the sub-bandgap energy level to 1x10<sup>5</sup> at 5.3 eV, where changes in the steepness of the absorption curve in the sub-bandgap region are in excellent agreement with defect energy states identified by robust defect characterisation techniques such as DLTS. Although CPM acts as a tool for probing filled defect states below the Fermi level, TSC spectroscopy can supplement the shortfall of CPM to probe shallow states near the conduction band. TSC measurements revealed 3 distinct peaks around 0.28, 0.47, and 0.51 eV. Although DLTS and ODLTS remains the most robust electrical characterisation technique for probing defect states in semiconductors, the technique requires Schottky contacts, whereas the technique proposed offers a characterisation approach independent of contact type.

The discovery of broad photoconductive response identified through CPM paves the way for novel sensing applications, as demonstrated here with a proof-of-concept water quality monitoring system. Here we were able to show the sensitivity of the material to contaminants such as Nitrates, DOC, and SSC and targeted absorption regions by using a series of LEDs as a light source. With continued progress in controlling growth conditions, refining defect analysis methods, and standardising characterisation practices,  $\alpha$ -Ga<sub>2</sub>O<sub>3</sub> could become a key material in next-generation optoelectronic and power devices.

## 7.2 Further Work

To expand on the work in this thesis, a number of additional experiments would aid in understanding the impact of defects on the optical and electrical properties of  $\alpha$ -Ga<sub>2</sub>O<sub>3</sub>.

Given that the 3.8 eV luminescence line identified in Chapter 3 was attributed to a DAP recombination mechanism, a series of power-dependent and time-resolved luminescence measurements will offer more evidence to support the assignment of and DAP recombination mechanism to the 3.8 eV line. It has been observed in other literature, notably from M. Reschikov from the GaN community reported that the luminescence intensity follows a power-law dependence on the excitation power with  $I_L = P^\gamma$ , where  $\gamma = 1$  is typical of a recombination mechanism involving STH or excitons, and  $1 \leq \gamma < 2$  is representative of a DAP transition [220]. Furthermore, a shift in the peak position would be observed in the luminescence spectrum for a DAP-related transition. Time-resolved luminescence measures the decay rate of the luminescence spectrum. The decay rate can be indicative of the recombination mechanism in which exciton or STH luminescence decays at a much faster rate relative to DAP transitions [89]. It is unclear at this stage how the overlapping luminescence bands in the spectrum of  $\alpha$ -Ga<sub>2</sub>O<sub>3</sub> will influence the interpretation of the power-dependent and time-resolved measurements. However, because of the different power dependencies on the STH and DAP luminescence, a relative measurement of the UV and H-related line at 3.8 eV will be enough to indicate a different recombination mechanism, where we would expect the H-related luminescence to have a stronger power dependence than the STH UV line. Furthermore, an additional study with samples that contain a greater variance in H concentration would be beneficial.

In Chapters 4,5, and 6 we introduced some photoconduction concepts to probe defect states in  $\alpha$ -Ga<sub>2</sub>O<sub>3</sub>. However, an exciting aspect is the room for further photoconduction studies. A further suggestion here would be the implementation of a temperature-controlled stage to study the temperature-dependent processes in the material, similar to what is used at the University of Dundee. There is currently a gap in the literature for in-depth analysis of the photocurrent transient behaviour. At a mini-

mum, this would formalise the transient decay behaviour in terms of being modelled appropriately, but an experimental approach called Transient Photocurrent Spectroscopy can be used to study shallow level defects in a material by monitoring the decay following short pulses of light. Establishing the first CPM measurement of  $\alpha\text{-Ga}_2\text{O}_3$  was a major success of the work in this thesis. However, there is room for improvement on the acquisition process. At this stage, manual adjustments of the LED driving current are required to match the CPM reference current. A control feedback system should be used to regulate the driving current to reduce the duration of the experiment. If LED's were used, an system would have to be designed to switch over LED's. An alternative approach would be to use a more intense broadband emitter, but using a double monochromator to reduce the second-order diffraction effects. In terms of experimental data, series of samples of varying degrees of doping concentration should be studied.

For TSC measurements in this study provided an initial study of shallow defects in  $\alpha\text{-Ga}_2\text{O}_3$ . However, it is obvious that there is some ambiguity in the analysis methods used to extract the activation energy of the defects. More work is required to determine the correct analysis approach and determine the error amongst each of the different approaches. Using a sample with well-known shallow defects measured by DLTS could be used as a reference measurement to compare with each of the TSC analysis methods. Further measurements should be carried out on a number of sample sets. A set of samples should contain various Si concentrations that range from below the detection limits and are increased by several orders of magnitude. This process should be repeated with samples containing other known shallow defects in  $\alpha\text{-Ga}_2\text{O}_3$  such as Si, Sn, Cl, and Ge.

# Bibliography

- [1] M. Higashiwaki, K. Sasaki, A. Kuramata, T. Masui, and S. Yamakoshi, “Gallium oxide (ga2o3) metal-semiconductor field-effect transistors on single-crystal  $\beta$ -ga2o3 (010) substrates,” *Applied Physics Letters*, vol. 100, no. 1, 2012.
- [2] T. Kobayashi, T. Gake, Y. Kumagai, F. Oba, and Y.-i. Matsushita, “Energetics and electronic structure of native point defects in  $\alpha$ -ga2o3,” *Applied Physics Express*, vol. 12, no. 9, p. 091001, 2019.
- [3] A. Mock, R. Korlacki, C. Briley, V. Darakchieva, B. Monemar, Y. Kumagai, K. Goto, M. Higashiwaki, and M. Schubert, “Band-to-band transitions, selection rules, effective mass, and excitonic contributions in monoclinic  $\beta$ -ga 2 o 3,” *Physical Review B*, vol. 96, no. 24, p. 245205, 2017.
- [4] M. U. Jewel, S. Hasan, and I. Ahmad, “A comprehensive study of defects in gallium oxide by density functional theory,” *Computational Materials Science*, vol. 218, p. 111950, 2023.
- [5] H. Okumura and J. B. Varley, “Mocvd growth of si-doped  $\alpha$ -(alga) 2o3 on m-plane  $\alpha$ -al2o3 substrates,” *Japanese Journal of Applied Physics*, 2024.
- [6] S. Hao, M. Hetzl, V. F. Kunzelmann, S. Matich, Q. Sai, C. Xia, I. D. Sharp, and M. Stutzmann, “Sub-bandgap optical spectroscopy of epitaxial  $\beta$ -ga2o3 thin films,” *Applied Physics Letters*, vol. 116, no. 9, 2020.
- [7] M. Ezzahmouly, A. Elmoutaouakkil, M. Ed-Dhahraouy, H. Khallok, A. Elouahli, A. Mazurier, A. ElAlbani, and Z. Hatim, “Micro-computed tomographic and sem

## Bibliography

- study of porous bioceramics using an adaptive method based on the mathematical morphological operations,” *Heliyon*, vol. 5, no. 12, 2019.
- [8] J. I. Pankove, *Optical processes in semiconductors*. Courier Corporation, 1975.
- [9] F. Laeri, F. Schüth, U. Simon, and M. Wark, *Host-Guest-Systems Based on Nanoporous Crystals*. John Wiley & Sons, 2006.
- [10] W. Smith, *The action of light on selenium*. 1876.
- [11] W. Bludau, A. Onton, and W. Heinke, “Temperature dependence of the band gap of silicon,” *Journal of Applied Physics*, vol. 45, no. 4, pp. 1846–1848, 1974.
- [12] Z. Han, H. Zhu, Y. Zou, J. Lu, F. Zhu, and Q. Ning, “Band gap regulation and a selective preparation method for single-walled silicon carbide nanotubes,” *Results in Physics*, vol. 38, p. 105658, 2022.
- [13] E. Monroy, F. Omnès, and F. Calle, “Wide-bandgap semiconductor ultraviolet photodetectors,” *Semiconductor science and technology*, vol. 18, no. 4, p. R33, 2003.
- [14] R. Aiba, K. Matsui, M. Baba, S. Harada, H. Yano, and N. Iwamuro, “Demonstration of superior electrical characteristics for 1.2 kv sic schottky barrier diode-wall integrated trench mosfet with higher schottky barrier height metal,” *IEEE Electron Device Letters*, vol. 41, no. 12, pp. 1810–1813, 2020.
- [15] Q. Wahab, T. Kimoto, A. Ellison, C. Hallin, M. Tuominen, R. Yakimova, A. Henry, J. Bergman, and E. Janzen, “A 3 kv schottky barrier diode in 4h-sic,” *Applied physics letters*, vol. 72, no. 4, pp. 445–447, 1998.
- [16] J. Wang and X. Jiang, “Review and analysis of sic mosfets’ ruggedness and reliability,” *IET Power Electronics*, vol. 13, no. 3, pp. 445–455, 2020.
- [17] U. K. Mishra, L. Shen, T. E. Kazior, and Y.-F. Wu, “Gan-based rf power devices and amplifiers,” *Proceedings of the IEEE*, vol. 96, no. 2, pp. 287–305, 2008.

## Bibliography

- [18] J. L. Hudgins, G. S. Simin, E. Santi, and M. A. Khan, “An assessment of wide bandgap semiconductors for power devices,” *IEEE Transactions on power electronics*, vol. 18, no. 3, pp. 907–914, 2003.
- [19] N. Kaminski and O. Hilt, “Sic and gan devices—wide bandgap is not all the same,” *IET Circuits, Devices & Systems*, vol. 8, no. 3, pp. 227–236, 2014.
- [20] T. Oshima, T. Okuno, N. Arai, N. Suzuki, H. Hino, and S. Fujita, “Flame detection by a  $\beta$ -ga<sub>2</sub>o<sub>3</sub>-based sensor,” *Japanese Journal of Applied Physics*, vol. 48, no. 1R, p. 011605, 2009.
- [21] Y. Sui, H. Liang, Q. Chen, W. Huo, X. Du, and Z. Mei, “Room-temperature ozone sensing capability of igzo-decorated amorphous ga<sub>2</sub>o<sub>3</sub> films,” *ACS applied materials & interfaces*, vol. 12, no. 7, pp. 8929–8934, 2020.
- [22] T. Rahman, T. Masui, and T. Ichiki, “Single-crystal gallium oxide-based biomolecular modified diode for nucleic acid sensing,” *Japanese Journal of Applied Physics*, vol. 54, no. 4S, p. 04DL08, 2015.
- [23] S. Pearton, J. Yang, P. H. Cary, F. Ren, J. Kim, M. J. Tadjer, and M. A. Mastro, “A review of ga<sub>2</sub>o<sub>3</sub> materials, processing, and devices,” *Applied Physics Reviews*, vol. 5, no. 1, 2018.
- [24] J. Furthmüller and F. Bechstedt, “Quasiparticle bands and spectra of ga<sub>2</sub>o<sub>3</sub> polymorphs,” *Physical Review B*, vol. 93, no. 11, p. 115204, 2016.
- [25] S. Yoshioka, H. Hayashi, A. Kuwabara, F. Oba, K. Matsunaga, and I. Tanaka, “Structures and energetics of ga<sub>2</sub>o<sub>3</sub> polymorphs,” *Journal of Physics: Condensed Matter*, vol. 19, no. 34, p. 346211, 2007.
- [26] R. Roy, V. Hill, and E. Osborn, “Polymorphism of ga<sub>2</sub>o<sub>3</sub> and the system ga<sub>2</sub>o<sub>3</sub>—h<sub>2</sub>o,” *Journal of the American Chemical Society*, vol. 74, no. 3, pp. 719–722, 1952.

## Bibliography

- [27] D. Shinohara and S. Fujita, “Heteroepitaxy of corundum-structured  $\alpha$ -ga<sub>2</sub>o<sub>3</sub> thin films on  $\alpha$ -al<sub>2</sub>o<sub>3</sub> substrates by ultrasonic mist chemical vapor deposition,” *Japanese Journal of Applied Physics*, vol. 47, no. 9R, p. 7311, 2008.
- [28] H. Sun, K.-H. Li, C. T. Castanedo, S. Okur, G. S. Tompa, T. Salagaj, S. Lopatin, A. Genovese, and X. Li, “Hcl flow-induced phase change of  $\alpha$ -,  $\beta$ -, and  $\varepsilon$ -ga<sub>2</sub>o<sub>3</sub> films grown by mocvd,” *Crystal Growth & Design*, vol. 18, no. 4, pp. 2370–2376, 2018.
- [29] J. Roberts, P. Chalker, B. Ding, R. Oliver, J. Gibbon, L. Jones, V. Dhanak, L. Phillips, J. Major, and F.-P. Massabuau, “Low temperature growth and optical properties of  $\alpha$ -ga<sub>2</sub>o<sub>3</sub> deposited on sapphire by plasma enhanced atomic layer deposition,” *Journal of Crystal Growth*, vol. 528, p. 125254, 2019.
- [30] V. D. Wheeler, N. Nepal, D. R. Boris, S. B. Qadri, L. O. Nyakiti, A. Lang, A. Koehler, G. Foster, S. G. Walton, C. R. Eddy Jr, *et al.*, “Phase control of crystalline ga<sub>2</sub>o<sub>3</sub> films by plasma-enhanced atomic layer deposition,” *Chemistry of Materials*, vol. 32, no. 3, pp. 1140–1152, 2020.
- [31] E. Ahmadi, O. S. Koksaldi, S. W. Kaun, Y. Oshima, D. B. Short, U. K. Mishra, and J. S. Speck, “Ge doping of  $\beta$ -ga<sub>2</sub>o<sub>3</sub> films grown by plasma-assisted molecular beam epitaxy,” *Applied Physics Express*, vol. 10, no. 4, p. 041102, 2017.
- [32] A. J. Green, J. Speck, G. Xing, P. Moens, F. Allerstam, K. Gumaelius, T. Neyer, A. Arias-Purdue, V. Mehrotra, A. Kuramata, *et al.*, “ $\beta$ -gallium oxide power electronics,” *Apl Materials*, vol. 10, no. 2, 2022.
- [33] R. Jinno, C. S. Chang, T. Onuma, Y. Cho, S.-T. Ho, D. Rowe, M. C. Cao, K. Lee, V. Protasenko, D. G. Schlom, *et al.*, “Crystal orientation dictated epitaxy of ultrawide-bandgap 5.4-to 8.6-ev  $\alpha$ -(alga) <sub>2</sub>o<sub>3</sub> on m-plane sapphire,” *Science Advances*, vol. 7, no. 2, p. eabd5891, 2021.
- [34] K. Kaneko, K. Uno, R. Jinno, and S. Fujita, “Prospects for phase engineering of semi-stable ga<sub>2</sub>o<sub>3</sub> semiconductor thin films using mist chemical vapor deposition,” *Journal of Applied Physics*, vol. 131, no. 9, 2022.

## Bibliography

- [35] S. Fujita and K. Kaneko, “Epitaxial growth of corundum-structured wide band gap iii-oxide semiconductor thin films,” *Journal of crystal growth*, vol. 401, pp. 588–592, 2014.
- [36] A. Barthel, J. Roberts, M. Napari, M. Frentrup, T. Huq, A. Kovács, R. Oliver, P. Chalker, T. Sajavaara, and F. Massabuau, “Ti alloyed  $\alpha$ -ga<sub>2</sub>o<sub>3</sub>: Route towards wide band gap engineering,” *Micromachines*, vol. 11, no. 12, p. 1128, 2020.
- [37] J. Zhang, J. Shi, D.-C. Qi, L. Chen, and K. H. Zhang, “Recent progress on the electronic structure, defect, and doping properties of ga<sub>2</sub>o<sub>3</sub>,” *APL Materials*, vol. 8, no. 2, 2020.
- [38] A. K. Mondal, M. A. Mohamed, L. K. Ping, M. F. Mohamad Taib, M. H. Samat, M. A. S. Mohammad Haniff, and R. Bahru, “First-principles studies for electronic structure and optical properties of p-type calcium doped  $\alpha$ -ga<sub>2</sub>o<sub>3</sub>,” *Materials*, vol. 14, no. 3, p. 604, 2021.
- [39] M. Marezio and J. Remeika, “Bond lengths in the  $\alpha$ -ga<sub>2</sub>o<sub>3</sub> structure and the high-pressure phase of ga<sub>2-x</sub>fe<sub>x</sub>o<sub>3</sub>,” *Journal of Chemical Physics*, vol. 46, no. 5, pp. 1862–1865, 1967.
- [40] H. Xue, Q. He, G. Jian, S. Long, T. Pang, and M. Liu, “An overview of the ultrawide bandgap ga<sub>2</sub>o<sub>3</sub> semiconductor-based schottky barrier diode for power electronics application,” *Nanoscale research letters*, vol. 13, pp. 1–13, 2018.
- [41] J. B. Varley, J. R. Weber, A. Janotti, and C. G. Van de Walle, “Oxygen vacancies and donor impurities in  $\beta$ -ga<sub>2</sub>o<sub>3</sub>,” *Applied physics letters*, vol. 97, no. 14, 2010.
- [42] J. B. Varley, A. Janotti, C. Franchini, and C. G. Van de Walle, “Role of self-trapping in luminescence and p-type conductivity of wide-band-gap oxides,” *Physical Review B*, vol. 85, no. 8, p. 081109, 2012.
- [43] F. Ricci, F. Boschi, A. Baraldi, A. Filippetti, M. Higashiwaki, A. Kuramata, V. Fiorentini, and R. Fornari, “Theoretical and experimental investigation of

## Bibliography

- optical absorption anisotropy in  $\beta$ -ga2o3,” *Journal of Physics: Condensed Matter*, vol. 28, no. 22, p. 224005, 2016.
- [44] C. Sturm, J. Furthmüller, F. Bechstedt, R. Schmidt-Grund, and M. Grundmann, “Dielectric tensor of monoclinic ga2o3 single crystals in the spectral range 0.5–8.5 eV,” *APL Materials*, vol. 3, no. 10, 2015.
- [45] A. Sharma and U. Singiseti, “Low field electron transport in  $\alpha$ - ga2o3: An ab initio approach,” *Applied Physics Letters*, vol. 118, no. 3, 2021.
- [46] M. Hilfiker, R. Korlacki, R. Jinno, Y. Cho, H. G. Xing, D. Jena, U. Kilic, M. Stokey, and M. Schubert, “Anisotropic dielectric functions, band-to-band transitions, and critical points in  $\alpha$ -ga2o3,” *Applied Physics Letters*, vol. 118, no. 6, 2021.
- [47] J. Ding, Y. Liu, X. Gu, L. Zhang, X. Zhang, X. Chen, W. Liu, Y. Cai, S. Guo, and C. Sun, “Electronic transport and optical properties of five different phases ( $\alpha$ ,  $\beta$ ,  $\epsilon$ ,  $\delta$  and  $\gamma$ ) of ga2o3: A first-principles study,” *Physica B: Condensed Matter*, vol. 682, p. 415888, 2024.
- [48] J. L. Lyons, “Electronic properties of ga2o3 polymorphs,” *ECS Journal of Solid State Science and Technology*, vol. 8, no. 7, p. Q3226, 2019.
- [49] B. E. Kananen, N. C. Giles, L. E. Halliburton, G. Foundos, K. Chang, and K. Stevens, “Self-trapped holes in  $\beta$ -ga2o3 crystals,” *Journal of Applied Physics*, vol. 122, no. 21, 2017.
- [50] A. M. Armstrong, M. H. Crawford, A. Jayawardena, A. Ahyi, and S. Dhar, “Role of self-trapped holes in the photoconductive gain of  $\beta$ -gallium oxide schottky diodes,” *Journal of Applied Physics*, vol. 119, no. 10, 2016.
- [51] V. Lordi, P. Erhart, and D. Åberg, “Charge carrier scattering by defects in semiconductors,” *Physical Review B—Condensed Matter and Materials Physics*, vol. 81, no. 23, p. 235204, 2010.

## Bibliography

- [52] A. Navarro-Quezada, S. Alamé, N. Esser, J. Furthmüller, F. Bechstedt, Z. Galazka, D. Skuridina, and P. Vogt, “Near valence-band electronic properties of semiconducting  $\beta$ -Ga<sub>2</sub>O<sub>3</sub> (100) single crystals,” *Physical Review B*, vol. 92, no. 19, p. 195306, 2015.
- [53] P. Mazzolini, J. Varley, A. Parisini, A. Sacchi, M. Pavesi, A. Bosio, M. Bosi, L. Seravalli, B. Janzen, M. Marggraf, *et al.*, “Engineering shallow and deep level defects in  $\kappa$ -Ga<sub>2</sub>O<sub>3</sub> thin films: comparing metal-organic vapour phase epitaxy to molecular beam epitaxy and the effect of annealing treatments,” *Materials Today Physics*, vol. 45, p. 101463, 2024.
- [54] J. B. Varley, “First-principles calculations 2: Doping and defects in Ga<sub>2</sub>O<sub>3</sub>,” in *Gallium Oxide: Materials Properties, Crystal Growth, and Devices*, pp. 329–348, Springer, 2020.
- [55] M. E. Ingebrigtsen, A. Y. Kuznetsov, B. G. Svensson, G. Alfieri, A. Mihaila, U. Badstübner, A. Perron, L. Vines, and J. B. Varley, “Impact of proton irradiation on conductivity and deep level defects in  $\beta$ -Ga<sub>2</sub>O<sub>3</sub>,” *Appl Materials*, vol. 7, no. 2, 2019.
- [56] M. A. Blanco, M. B. Sahariah, H. Jiang, A. Costales, and R. Pandey, “Energetics and migration of point defects in Ga<sub>2</sub>O<sub>3</sub>,” *Physical Review B—Condensed Matter and Materials Physics*, vol. 72, no. 18, p. 184103, 2005.
- [57] D. A. Neamen and D. Biswas, *Semiconductor physics and devices*. McGraw-Hill higher education New York, 2011.
- [58] H. Grimmeiss, “Deep level impurities in semiconductors,” *Annual Review of Materials Science*, vol. 7, no. 1, pp. 341–376, 1977.
- [59] B. Liu, M. Gu, and X. Liu, “Lattice dynamical, dielectric, and thermodynamic properties of  $\beta$ -Ga<sub>2</sub>O<sub>3</sub> from first principles,” *Applied Physics Letters*, vol. 91, no. 17, 2007.

## Bibliography

- [60] E. Farzana, E. Ahmadi, J. S. Speck, A. R. Arehart, and S. A. Ringel, “Deep level defects in ge-doped (010)  $\beta$ -ga<sub>2</sub>o<sub>3</sub> layers grown by plasma-assisted molecular beam epitaxy,” *Journal of Applied Physics*, vol. 123, no. 16, 2018.
- [61] Z. Zhang, E. Farzana, A. Arehart, and S. Ringel, “Deep level defects throughout the bandgap of (010)  $\beta$ -ga<sub>2</sub>o<sub>3</sub> detected by optically and thermally stimulated defect spectroscopy,” *Applied Physics Letters*, vol. 108, no. 5, 2016.
- [62] Z. Wang, X. Chen, F.-F. Ren, S. Gu, and J. Ye, “Deep-level defects in gallium oxide,” *Journal of Physics D: Applied Physics*, vol. 54, no. 4, p. 043002, 2020.
- [63] T. Oishi, K. Harada, Y. Koga, and M. Kasu, “Conduction mechanism in highly doped  $\beta$ -ga<sub>2</sub>o<sub>3</sub> single crystals grown by edge-defined film-fed growth method and their schottky barrier diodes,” *Japanese Journal of Applied Physics*, vol. 55, no. 3, p. 030305, 2016.
- [64] M. Higashiwaki, A. Kuramata, H. Murakami, and Y. Kumagai, “State-of-the-art technologies of gallium oxide power devices,” *Journal of Physics D: Applied Physics*, vol. 50, no. 33, p. 333002, 2017.
- [65] M. M. Islam, M. O. Liedke, D. Winarski, M. Butterling, A. Wagner, P. Hosemann, Y. Wang, B. Uberuaga, and F. A. Selim, “Chemical manipulation of hydrogen induced high p-type and n-type conductivity in ga<sub>2</sub>o<sub>3</sub>,” *Scientific reports*, vol. 10, no. 1, p. 6134, 2020.
- [66] M. J. Tadjer, J. L. Lyons, N. Nepal, J. A. Freitas, A. D. Koehler, and G. M. Foster, “Review—theory and characterization of doping and defects in  $\beta$ -ga<sub>2</sub>o<sub>3</sub>,” *ECS Journal of Solid State Science and Technology*, vol. 8, no. 7, pp. Q3187–Q3194, 2019.
- [67] Y. Wei, X. Li, J. Yang, C. Liu, J. Zhao, Y. Liu, and S. Dong, “Interaction between hydrogen and gallium vacancies in  $\beta$ -ga<sub>2</sub>o<sub>3</sub>,” *Scientific Reports*, vol. 8, no. 1, p. 10142, 2018.

## Bibliography

- [68] L. Ghadbeigi, J. Cooke, G. T. Dang, T. Kawaharamura, T. Yasuoka, R. Sun, P. Ranga, S. Krishnamoorthy, M. A. Scarpulla, and B. Sensale-Rodriguez, “Optical characterization of gallium oxide  $\alpha$  and  $\beta$  polymorph thin-films grown on c-plane sapphire,” *Journal of Electronic Materials*, vol. 50, pp. 2990–2998, 2021.
- [69] S. Kim, Y. Yoon, D. Seo, J.-H. Park, D.-W. Jeon, W. S. Hwang, and M. Shin, “Alpha-phase gallium oxide-based uvc photodetector with high sensitivity and visible blindness,” *APL Materials*, vol. 11, no. 6, 2023.
- [70] J. Moloney, O. Tesh, M. Singh, J. Roberts, J. Jarman, L. Lee, T. Huq, J. Brister, S. Karboyan, M. Kuball, *et al.*, “Atomic layer deposited  $\alpha$ -ga<sub>2</sub>o<sub>3</sub> solar-blind photodetectors,” *Journal of Physics D: Applied Physics*, vol. 52, no. 47, p. 475101, 2019.
- [71] X. Hou, H. Sun, S. Long, G. S. Tompa, T. Salagaj, Y. Qin, Z. Zhang, P. Tan, S. Yu, and M. Liu, “Ultrahigh-performance solar-blind photodetector based on  $\alpha$  -phase- dominated ga<sub>2</sub>o<sub>3</sub> film with record low dark current of 81 fa,” *IEEE Electron Device Letters*, vol. 40, no. 9, pp. 1483–1486, 2019.
- [72] J. Tauc, “Optical properties and electronic structure of amorphous ge and si,” *Materials research bulletin*, vol. 3, no. 1, pp. 37–46, 1968.
- [73] N. Ghobadi, “Band gap determination using absorption spectrum fitting procedure,” *International Nano Letters*, vol. 3, no. 1, p. 2, 2013.
- [74] W. B. Jackson, N. M. Amer, A. Boccaro, and D. Fournier, “Photothermal deflection spectroscopy and detection,” *Applied optics*, vol. 20, no. 8, pp. 1333–1344, 1981.
- [75] S. Kasap and P. Capper, *Springer handbook of electronic and photonic materials*. Springer, 2017.
- [76] M. Vaněček, J. Kočka, J. Stuchlik, and A. Tríska, “Direct measurement of the gap states and band tail absorption by constant photocurrent method in amorphous silicon,” *Solid State Communications*, vol. 39, no. 11, pp. 1199–1202, 1981.

## Bibliography

- [77] K. Pierz, H. Mell, and J. Terukov, “Subbandgap absorption in a-si: H from photoconductivity spectra,” *Journal of Non-Crystalline Solids*, vol. 77, pp. 547–550, 1985.
- [78] T. Onuma, S. Fujioka, T. Yamaguchi, M. Higashiwaki, K. Sasaki, T. Masui, and T. Honda, “Correlation between blue luminescence intensity and resistivity in  $\beta$ -ga<sub>2</sub>o<sub>3</sub> single crystals,” *Applied Physics Letters*, vol. 103, no. 4, 2013.
- [79] Y. Wang, P. T. Dickens, J. B. Varley, X. Ni, E. Lotubai, S. Sprawls, F. Liu, V. Lordi, S. Krishnamoorthy, S. Blair, *et al.*, “Incident wavelength and polarization dependence of spectral shifts in  $\beta$ -ga<sub>2</sub>o<sub>3</sub> uv photoluminescence,” *Scientific reports*, vol. 8, no. 1, p. 18075, 2018.
- [80] Y. Berencén, Y. Xie, M. Wang, S. Prucnal, L. Rebohle, and S. Zhou, “Structural and optical properties of pulsed-laser deposited crystalline  $\beta$ -ga<sub>2</sub>o<sub>3</sub> thin films on silicon,” *Semiconductor Science and Technology*, vol. 34, no. 3, p. 035001, 2019.
- [81] O. Bordun, B. Bordun, I. Y. Kukharsky, and I. Medvid, “Photoluminescence properties of  $\beta$ -ga<sub>2</sub>o<sub>3</sub> thin films produced by ion-plasma sputtering,” *Journal of Applied Spectroscopy*, vol. 84, pp. 46–51, 2017.
- [82] E. G. Vllora, M. Yamaga, T. Inoue, S. Yabasi, Y. Masui, T. Sugawara, and T. Fukuda, “Optical spectroscopy study on  $\beta$ -ga<sub>2</sub>o<sub>3</sub>,” *Japanese journal of applied physics*, vol. 41, no. 6A, p. L622, 2002.
- [83] Q. D. Ho, T. Frauenheim, and P. Deák, “Origin of photoluminescence in  $\beta$ -g a<sub>2</sub> o<sub>3</sub>,” *Physical Review B*, vol. 97, no. 11, p. 115163, 2018.
- [84] T. T. Huynh, E. Chikoidze, C. P. Irvine, M. Zakria, Y. Dumont, F. H. Teherani, E. V. Sandana, P. Bove, D. J. Rogers, M. R. Phillips, *et al.*, “Red luminescence in h-doped  $\beta$ -g a<sub>2</sub> o<sub>3</sub>,” *Physical Review Materials*, vol. 4, no. 8, p. 085201, 2020.
- [85] G. Naresh-Kumar, H. MacIntyre, S. Subashchandran, P. R. Edwards, R. W. Martin, K. Daivasigamani, K. Sasaki, and A. Kuramata, “Origin of red emission in

## Bibliography

- $\beta$ -ga<sub>2</sub>o<sub>3</sub> analyzed by cathodoluminescence and photoluminescence spectroscopy,” *physica status solidi (b)*, vol. 258, no. 2, p. 2000465, 2021.
- [86] N. Mott and A. Stoneham, “The lifetime of electrons, holes and excitons before self-trapping,” *Journal of Physics C: Solid State Physics*, vol. 10, no. 17, p. 3391, 1977.
- [87] J. Heyd, G. E. Scuseria, and M. Ernzerhof, “Hybrid functionals based on a screened coulomb potential,” *The Journal of chemical physics*, vol. 118, no. 18, pp. 8207–8215, 2003.
- [88] T. O. A. Fattah, J. Jacobs, V. P. Markevich, N. V. Abrosimov, M. P. Halsall, I. F. Crowe, and A. R. Peaker, “High-resolution photoluminescence study on donor-acceptor pair (dap) recombination in silicon crystals co-doped with phosphorous and gallium,” *Journal of Science: Advanced Materials and Devices*, vol. 8, no. 4, p. 100629, 2023.
- [89] M. A. Reshchikov, “Luminescence from point defects in widebandgap, direct-gap semiconductors,” in *Characterisation and Control of Defects in Semiconductors*, pp. 45–96, 2019.
- [90] I. Pelant and J. Valenta, *Luminescence spectroscopy of semiconductors*. OUP Oxford, 2012.
- [91] K. Shimamura, E. G. Villora, T. Ujiie, and K. Aoki, “Excitation and photoluminescence of pure and si-doped  $\beta$ -ga<sub>2</sub>o<sub>3</sub> single crystals,” *Applied Physics Letters*, vol. 92, no. 20, 2008.
- [92] H. Wakai, Y. Sinya, and A. Yamanaka, “Effect of cr<sup>3+</sup> ions on optical properties in  $\beta$ -ga<sub>2</sub>o<sub>3</sub> semiconductor,” *physica status solidi c*, vol. 8, no. 2, pp. 537–539, 2011.
- [93] T. Huynh, L. Lem, A. Kuramata, M. Phillips, and C. Ton-That, “Kinetics of charge carrier recombination in  $\beta$ -ga<sub>2</sub>o<sub>3</sub> crystals,” *Physical Review Materials*, vol. 2, no. 10, p. 105203, 2018.

## Bibliography

- [94] C. Liu, Y. Berencén, J. Yang, Y. Wei, M. Wang, Y. Yuan, C. Xu, Y. Xie, X. Li, and S. Zhou, “Irradiation effects on the structural and optical properties of single crystal  $\beta$ -ga2o3,” *Semiconductor Science and Technology*, vol. 33, no. 9, p. 095022, 2018.
- [95] I. Hany, G. Yang, C. E. Zhou, C. Sun, K. Gundogdu, D. Seyitliyev, E. O. Danilov, F. N. Castellano, D. Sun, and E. Vetter, “Low temperature cathodoluminescence study of fe-doped  $\beta$ -ga2o3,” *Materials Letters*, vol. 257, p. 126744, 2019.
- [96] G. Pozina, M. Forsberg, M. Kaliteevski, and C. Hemmingsson, “Emission properties of ga2o3 nano-flakes: effect of excitation density,” *Scientific Reports*, vol. 7, no. 1, p. 42132, 2017.
- [97] A. Meeder, D. F. Marrón, A. Rumberg, M. C. Lux-Steiner, V. Chu, and J. Conde, “Direct measurement of urbach tail and gap state absorption in cugase 2 thin films by photothermal deflection spectroscopy and the constant photocurrent method,” *Journal of applied physics*, vol. 92, no. 6, pp. 3016–3020, 2002.
- [98] A. Polyakov, N. Smirnov, I. Shchemerov, E. Yakimov, S. Pearton, C. Fares, J. Yang, F. Ren, J. Kim, P. Lagov, *et al.*, “Defects responsible for charge carrier removal and correlation with deep level introduction in irradiated  $\beta$ -ga2o3,” *Applied Physics Letters*, vol. 113, no. 9, 2018.
- [99] A. Y. Polyakov, V. I. Nikolaev, E. B. Yakimov, F. Ren, S. J. Pearton, and J. Kim, “Deep level defect states in  $\beta$ -,  $\alpha$ -, and -ga2o3 crystals and films: Impact on device performance,” *Journal of Vacuum Science & Technology A*, vol. 40, no. 2, 2022.
- [100] R. H. Bube, *Photoelectronic properties of semiconductors*. Cambridge University Press, 1992.
- [101] Q. Zhao, W. Wang, F. Carrascoso-Plana, W. Jie, T. Wang, A. Castellanos-Gomez, and R. Frisenda, “The role of traps in the photocurrent generation mechanism in thin inse photodetectors,” *Materials horizons*, vol. 7, no. 1, pp. 252–262, 2020.

## Bibliography

- [102] A. Musiienko, J. Pipek, P. Praus, M. Brynza, E. Belas, B. Dryzhakov, M.-H. Du, M. Ahmadi, and R. Grill, “Deciphering the effect of traps on electronic charge transport properties of methylammonium lead tribromide perovskite,” *Science advances*, vol. 6, no. 37, p. eabb6393, 2020.
- [103] D. Nicol, Y. Oshima, J. Roberts, L. Penman, D. Cameron, P. Chalker, R. Martin, and F.-P. Massabuau, “Hydrogen-related 3.8 eV uv luminescence in  $\alpha$ -Ga<sub>2</sub>O<sub>3</sub>,” *Applied Physics Letters*, vol. 122, no. 6, 2023.
- [104] M. Niehus, R. Schwarz, S. Koynov, M. Heuken, D. Meister, and B. Meyer, “Sub-bandgap absorption from photocurrent spectra in Al<sub>0.18</sub>Ga<sub>0.82</sub>N/GaN heterostructures,” *Diamond and related materials*, vol. 10, no. 3-7, pp. 1331–1334, 2001.
- [105] I.-H. Ahn, J. Kyhm, J. Lee, S. Cho, Y. Jo, D. Y. Kim, S. H. Choi, and W. Yang, “An alternative method for measurement of charge carrier mobility in semiconductors using photocurrent transient response,” *Current Applied Physics*, vol. 19, no. 4, pp. 498–502, 2019.
- [106] A. Polyakov, A. Almaev, V. Nikolaev, A. Pechnikov, V. Shchemerov, A. Vasilev, E. Yakimov, A. Kochkova, V. Kopyev, B. Kushnarev, *et al.*, “Mechanism for long photocurrent time constants in  $\alpha$ -Ga<sub>2</sub>O<sub>3</sub> UV photodetectors,” *ECS Journal of Solid State Science and Technology*, vol. 12, no. 4, p. 045002, 2023.
- [107] J. Zhang, P. Dong, K. Dang, Y. Zhang, Q. Yan, H. Xiang, J. Su, Z. Liu, M. Si, J. Gao, *et al.*, “Ultra-wide bandgap semiconductor Ga<sub>2</sub>O<sub>3</sub> power diodes,” *Nature communications*, vol. 13, no. 1, p. 3900, 2022.
- [108] B. Peng, L. Yuan, H. Zhang, H. Cheng, S. Zhang, Y. Zhang, Y. Zhang, and R. Jia, “Fast-response self-powered solar-blind photodetector based on Pt/ $\beta$ -Ga<sub>2</sub>O<sub>3</sub> Schottky barrier diodes,” *Optik*, vol. 245, p. 167715, 2021.
- [109] P. S. Y. J. Cary IV, “Ph ren f. kim j. tadjer mj mastro ma appl,” *Phys. Rev.*, vol. 5, p. 011301, 2018.

## Bibliography

- [110] Y. Yao, R. F. Davis, and L. M. Porter, “Investigation of different metals as ohmic contacts to  $\beta$ -ga<sub>2</sub>o<sub>3</sub>: comparison and analysis of electrical behavior, morphology, and other physical properties,” *Journal of Electronic Materials*, vol. 46, no. 4, pp. 2053–2060, 2017.
- [111] F. Massabuau, D. Nicol, F. Adams, J. Jarman, J. Roberts, A. Kovács, P. Chalker, and R. Oliver, “Study of ti contacts to corundum  $\alpha$ -ga<sub>2</sub>o<sub>3</sub>,” *Journal of Physics D: Applied Physics*, vol. 54, no. 38, p. 384001, 2021.
- [112] J. Xu, W. Zheng, and F. Huang, “Gallium oxide solar-blind ultraviolet photodetectors: a review,” *Journal of Materials Chemistry C*, vol. 7, no. 29, pp. 8753–8770, 2019.
- [113] B. Wang, D. Look, and G. Farlow, “Optical and electrical properties of ti-doped  $\beta$ -ga<sub>2</sub>o<sub>3</sub> (ti<sup>3+</sup>:  $\beta$ -ga<sub>2</sub>o<sub>3</sub>) bulk crystals grown by floating zone method,” *Journal of Physics D: Applied Physics*, vol. 53, no. 44, p. 444001, 2020.
- [114] Y. Wang, S. Li, J. Cao, Y. Jiang, Y. Zhang, W. Tang, and Z. Wu, “Improved response speed of  $\beta$ -ga<sub>2</sub>o<sub>3</sub> solar-blind photodetectors by optimizing illumination and bias,” *Materials & Design*, vol. 221, p. 110917, 2022.
- [115] L.-X. Qian, Z.-H. Wu, Y.-Y. Zhang, P. Lai, X.-Z. Liu, and Y.-R. Li, “Ultra-high-responsivity, rapid-recovery, solar-blind photodetector based on highly nonstoichiometric amorphous gallium oxide,” *Acs Photonics*, vol. 4, no. 9, pp. 2203–2211, 2017.
- [116] G. Shen, Z. Liu, K. Tang, S. Sha, L. Li, C.-K. Tan, Y. Guo, and W. Tang, “High responsivity and fast response  $8 \times 8$   $\beta$ -ga<sub>2</sub>o<sub>3</sub> solar-blind ultraviolet imaging photodetector array,” *Science China Technological Sciences*, vol. 66, no. 11, pp. 3259–3266, 2023.
- [117] X. Xiu, L. Zhang, Y. Li, Z. Xiong, R. Zhang, and Y. Zheng, “Application of halide vapor phase epitaxy for the growth of ultra-wide band gap ga<sub>2</sub>o<sub>3</sub>,” *Journal of Semiconductors*, vol. 40, no. 1, p. 011805, 2019.

## Bibliography

- [118] Y. Oshima, K. Kawara, T. Oshima, M. Okigawa, and T. Shinohe, “Rapid growth of  $\alpha$ -ga<sub>2</sub>o<sub>3</sub> by hcl-boosted halide vapor phase epitaxy and effect of precursor supply conditions on crystal properties,” *Semiconductor Science and Technology*, vol. 35, no. 5, p. 055022, 2020.
- [119] D. Hu, S. Zhuang, Z. Ma, X. Dong, G. Du, B. Zhang, Y. Zhang, and J. Yin, “Study on the optical properties of  $\beta$ -ga<sub>2</sub>o<sub>3</sub> films grown by mocvd,” *Journal of Materials Science: Materials in Electronics*, vol. 28, pp. 10997–11001, 2017.
- [120] I. E. Paulauskas, G. E. Jellison Jr, L. A. Boatner, and G. M. Brown, “Photoelectrochemical stability and alteration products of n-type single-crystal zno photoanodes,” *International Journal of Electrochemistry*, vol. 2011, no. 1, p. 563427, 2011.
- [121] J. Mooney and P. Kambhampati, “Get the basics right: Jacobian conversion of wavelength and energy scales for quantitative analysis of emission spectra,” 2013.
- [122] K. Kanaya and S. Okayama, “Penetration and energy-loss theory of electrons in solid targets,” *Journal of Physics D: Applied Physics*, vol. 5, no. 1, p. 43, 1972.
- [123] D. Drouin, A. Coutre, R. Gauvin, P. Hovington, P. Horny, and H. Demers, “Montecarlo simulation of electron trajectories in solids (casino), university of sherbrooke, quebec, canada.”
- [124] N. Balcon, D. Payan, M. Belhaj, T. Tondu, and V. Inguibert, “Secondary electron emission on space materials: Evaluation of the total secondary electron yield from surface potential measurements,” *IEEE Transactions on Plasma Science*, vol. 40, no. 2, pp. 282–290, 2011.
- [125] A. Howie, “Recent developments in secondary electron imaging,” *Journal of Microscopy*, vol. 180, no. 3, pp. 192–203, 1995.
- [126] J. I. Goldstein, D. E. Newbury, P. Echlin, D. C. Joy, C. E. Lyman, E. Lifshin, L. Sawyer, J. R. Michael, J. I. Goldstein, D. E. Newbury, *et al.*, “Specimen

## Bibliography

- preparation of polymer materials,” *Scanning Electron Microscopy and X-ray Microanalysis: Third Edition*, pp. 565–590, 2003.
- [127] D. B. Holt and D. C. Joy, *SEM microcharacterization of semiconductors*. Academic Press, 2013.
- [128] J. Christen, M. Grundmann, and D. Bimberg, “Scanning cathodoluminescence microscopy: A unique approach to atomic-scale characterization of heterointerfaces and imaging of semiconductor inhomogeneities,” *Journal of Vacuum Science & Technology B: Microelectronics and Nanometer Structures Processing, Measurement, and Phenomena*, vol. 9, no. 4, pp. 2358–2368, 1991.
- [129] R. Martin, P. Edwards, K. O’Donnell, M. Dawson, C.-W. Jeon, C. Liu, G. Rice, and I. Watson, “Cathodoluminescence spectral mapping of iii-nitride structures,” *Physica status solidi (a)*, vol. 201, no. 4, pp. 665–672, 2004.
- [130] P. R. Edwards and R. W. Martin, “Cathodoluminescence nano-characterization of semiconductors,” *Semiconductor Science and Technology*, vol. 26, no. 6, p. 064005, 2011.
- [131] J. Cazaux, “About the mechanisms of charging in epma, sem, and esem with their time evolution,” *Microscopy and Microanalysis*, vol. 10, no. 6, pp. 670–684, 2004.
- [132] D. Lawson, “A closer look at planck’s blackbody equation,” *Physics Education*, vol. 32, no. 5, p. 321, 1997.
- [133] I. González de Arrieta, “Wien’s displacement law and blackbody radiation quartiles,” *The Physics Teacher*, vol. 59, no. 6, pp. 464–466, 2021.
- [134] B. Brenny, T. Coenen, and A. Polman, “Quantifying coherent and incoherent cathodoluminescence in semiconductors and metals,” *Journal of Applied Physics*, vol. 115, no. 24, 2014.
- [135] C. Wu, C. He, D. Guo, F. Zhang, P. Li, S. Wang, A. Liu, F. Wu, and W. Tang, “Vertical  $\alpha/\beta$ -ga<sub>2</sub>o<sub>3</sub> phase junction nanorods array with graphene-silver nanowire

## Bibliography

hybrid conductive electrode for high-performance self-powered solar-blind photodetectors,” *Materials Today Physics*, vol. 12, p. 100193, 2020.

- [136] X. Hou, H. Sun, S. Long, G. S. Tompa, T. Salagaj, Y. Qin, Z. Zhang, P. Tan, S. Yu, and M. Liu, “Ultrahigh-performance solar-blind photodetector based on

$\alpha$ -phase-dominated  $\text{Ga}_2\text{O}_3$  film with record low dark current of  $81 \text{ fA}$ ,” *IEEE Electron Devices Letters*, vol. 40, pp. 1486–1486, 2019.

- [137] K. Arora, N. Goel, M. Kumar, and M. Kumar, “Ultrahigh performance of self-powered  $\beta$ - $\text{Ga}_2\text{O}_3$  thin film solar-blind photodetector grown on cost-effective Si substrate using high-temperature seed layer,” *Acs Photonics*, vol. 5, no. 6, pp. 2391–2401, 2018.

- [138] Y. Qin, H. Sun, S. Long, G. S. Tompa, T. Salagaj, H. Dong, Q. He, G. Jian, Q. Liu, H. Lv, *et al.*, “High-performance metal-organic chemical vapor deposition grown

$\epsilon$ - $\text{Ga}_2\text{O}_3$  solar-blind photodetector with asymmetric Schottky electrodes,” *IEEE Electron Devices Letters*, vol. 40, pp. 1478–1478, 2019.

- [139] D. Guo, X. Zhao, Y. Zhi, W. Cui, Y. Huang, Y. An, P. Li, Z. Wu, and W. Tang, “Epitaxial growth and solar-blind photoelectric properties of corundum-structured  $\alpha$ - $\text{Ga}_2\text{O}_3$  thin films,” *Materials Letters*, vol. 164, pp. 364–367, 2016.

- [140] J. Bae, D.-W. Jeon, J.-H. Park, and J. Kim, “High responsivity solar-blind metal-semiconductor-metal photodetector based on  $\alpha$ - $\text{Ga}_2\text{O}_3$ ,” *Journal of Vacuum Science & Technology A*, vol. 39, no. 3, 2021.

- [141] M. Vaněček, J. Kočka, A. Poruba, and A. Fejfar, “Direct measurement of the deep defect density in thin amorphous silicon films with the “absolute” constant photocurrent method,” *Journal of applied physics*, vol. 78, no. 10, pp. 6203–6210, 1995.

## Bibliography

- [142] N. M. Gabor, Z. Zhong, K. Bosnick, J. Park, and P. L. McEuen, “Extremely efficient multiple electron-hole pair generation in carbon nanotube photodiodes,” *Science*, vol. 325, no. 5946, pp. 1367–1371, 2009.
- [143] B. Y. Zhang, T. Liu, B. Meng, X. Li, G. Liang, X. Hu, and Q. J. Wang, “Broadband high photoresponse from pure monolayer graphene photodetector,” *Nature communications*, vol. 4, no. 1, p. 1811, 2013.
- [144] R. H. Bube, “Analysis of photoconductivity applied to cadmium-sulfide-type photoconductors,” *Journal of Physics and Chemistry of Solids*, vol. 1, no. 4, pp. 234–248, 1957.
- [145] R. R. Haering and E. N. Adams, “Theory and application of thermally stimulated currents in photoconductors,” *Physical Review*, vol. 117, no. 2, p. 451, 1960.
- [146] T. Tiedje and A. Rose, “A physical interpretation of dispersive transport in disordered semiconductors,” *Solid State Communications*, vol. 37, no. 1, pp. 49–52, 1981.
- [147] J. Orenstein and M. Kastner, “Photocurrent transient spectroscopy: measurement of the density of localized states in a-as 2 se 3,” *Physical Review Letters*, vol. 46, no. 21, p. 1421, 1981.
- [148] M. Niehus and R. Schwarz, “Correlation between transient decays in wide gap semiconductors: Photoluminescence vs. photocurrent,” *Superlattices and Microstructures*, vol. 42, no. 1-6, pp. 299–305, 2007.
- [149] J. Luo, A. U. Adler, T. O. Mason, D. Bruce Buchholz, R. Chang, and M. Grayson, “Transient photoresponse in amorphous in-ga-zn-o thin films under stretched exponential analysis,” *Journal of Applied Physics*, vol. 113, no. 15, 2013.
- [150] A. R. Zanatta, “Revisiting the optical bandgap of semiconductors and the proposal of a unified methodology to its determination,” *Scientific reports*, vol. 9, no. 1, p. 11225, 2019.

## Bibliography

- [151] N. T. Son, Q. D. Ho, K. Goto, H. Abe, T. Ohshima, B. Monemar, Y. Kumagai, T. Frauenheim, and P. Deák, “Electron paramagnetic resonance and theoretical study of gallium vacancy in  $\beta$ -ga2o3,” *Applied Physics Letters*, vol. 117, no. 3, 2020.
- [152] R. Moriya, J. Kikawa, S. Mouri, T. Shinohe, S. Xiao, H. Miyake, and T. Araki, “Cathodoluminescence study of m-plane  $\alpha$ -ga2o3 grown by mist chemical vapor deposition,” *physica status solidi (b)*, vol. 259, no. 4, p. 2100598, 2022.
- [153] S. Shapenkov, O. Vyvenko, E. Ubyivovk, O. Medvedev, G. Varygin, A. Chikiryaka, A. Pechnikov, M. Scheglov, S. Stepanov, and V. Nikolaev, “Halide vapor phase epitaxy  $\alpha$ -and  $\varepsilon$ -ga2o3 epitaxial films grown on patterned sapphire substrates,” *physica status solidi (a)*, vol. 217, no. 14, p. 1900892, 2020.
- [154] H. H. Kusuma, B. Astuti, and Z. Ibrahim, “Absorption and emission properties of ruby (cr: Al2o3) single crystal,” in *Journal of Physics: Conference Series*, vol. 1170, p. 012054, IOP Publishing, 2019.
- [155] A. Segura, L. Artús, R. Cuscó, R. Goldhahn, and M. Feneberg, “Band gap of corundum-like  $\alpha$ - ga 2 o 3 determined by absorption and ellipsometry,” *Physical Review Materials*, vol. 1, no. 2, p. 024604, 2017.
- [156] H. Ghadi, J. F. McGlone, C. M. Jackson, E. Farzana, Z. Feng, A. Bhuiyan, H. Zhao, A. R. Arehart, and S. A. Ringel, “Full bandgap defect state characterization of  $\beta$ -ga2o3 grown by metal organic chemical vapor deposition,” *APL Materials*, vol. 8, no. 2, 2020.
- [157] L. Binet and D. Gourier, “Origin of the blue luminescence of  $\beta$ -ga2o3,” *Journal of Physics and Chemistry of Solids*, vol. 59, no. 8, pp. 1241–1249, 1998.
- [158] Y. Nie, S. Jiao, S. Li, H. Lu, S. Liu, S. Yang, D. Wang, S. Gao, J. Wang, and Y. Li, “Modulating the blue and green luminescence in the  $\beta$ -ga2o3 films,” *Journal of Alloys and Compounds*, vol. 900, p. 163431, 2022.
- [159] T. Gake, Y. Kumagai, and F. Oba, “First-principles study of self-trapped holes and acceptor impurities in ga 2 o 3 polymorphs,” *Physical Review Materials*, vol. 3, no. 4, p. 044603, 2019.

## Bibliography

- [160] P. King, I. McKenzie, and T. D. Veal, “Observation of shallow-donor muonium in  $\text{Ga}_2\text{O}_3$ : Evidence for hydrogen-induced conductivity,” *Applied Physics Letters*, vol. 96, no. 6, 2010.
- [161] B. Dongre, J. Carrete, N. Mingo, and G. K. Madsen, “Ab initio lattice thermal conductivity of bulk and thin-film  $\alpha\text{-Al}_2\text{O}_3$ ,” *MRS Communications*, vol. 8, no. 3, pp. 1119–1123, 2018.
- [162] G. Yang, P. R. Romeo, A. Apostoluk, and B. Vilquin, “First principles study on the lattice thermal conductivity of  $\alpha$ -phase  $\text{Ga}_2\text{O}_3$ ,” *Journal of Vacuum Science & Technology A*, vol. 40, no. 5, 2022.
- [163] C. Lee, N. D. Rock, A. Islam, M. A. Scarpulla, and E. Ertekin, “Electron–phonon effects and temperature-dependence of the electronic structure of monoclinic  $\beta\text{-Ga}_2\text{O}_3$ ,” *APL Materials*, vol. 11, no. 1, 2023.
- [164] X. Zhang, L. Wang, X. Wang, Y. Chen, Q. Shao, G. Wu, X. Wang, T. Lin, H. Shen, J. Wang, *et al.*, “High-performance  $\beta\text{-Ga}_2\text{O}_3$  thickness dependent solar blind photodetector,” *Optics Express*, vol. 28, no. 3, pp. 4169–4177, 2020.
- [165] K. Shimazoe, H. Nishinaka, Y. Taniguchi, T. Kato, K. Kanegae, and M. Yoshimoto, “Vertical self-powered ultraviolet photodetector using  $\alpha\text{-Ga}_2\text{O}_3$  thin films on corundum structured rh-ITO electrodes,” *Materials Letters*, vol. 341, p. 134282, 2023.
- [166] X. Chen, F. Ren, S. Gu, and J. Ye, “Review of gallium-oxide-based solar-blind ultraviolet photodetectors,” *Photonics Research*, vol. 7, no. 4, pp. 381–415, 2019.
- [167] E. Monroy, F. Calle, C. Angulo, P. Vila, A. Sanz, J. A. Garrido, E. Calleja, E. Muñoz, S. Haffouz, B. Beaumont, *et al.*, “GaN-based solar-ultraviolet detection instrument,” *Applied Optics*, vol. 37, no. 22, pp. 5058–5062, 1998.
- [168] A. Hirano, C. Pernot, M. Iwaya, T. Detchprohm, H. Amano, and I. Akasaki, “Demonstration of flame detection in room light background by solar-blind AlGaN pin photodiode,” *physica status solidi (a)*, vol. 188, no. 1, pp. 293–296, 2001.

## Bibliography

- [169] W.-J. Chen, H.-P. Ma, L. Gu, Y. Shen, R.-Y. Yang, X.-Y. Cao, M. Yang, and Q.-C. Zhang, "Influence of annealing pretreatment in different atmospheres on crystallization quality and uv photosensitivity of gallium oxide films," *RSC advances*, vol. 14, no. 7, pp. 4543–4555, 2024.
- [170] A. A. A. Mohammed and W. F. Lim, "High photosensitivity performance vertical structured metal-semiconductor based ultraviolet photodetector using ga<sub>2</sub>o<sub>3</sub> thin film sputtered on n-type si (100)," *Materials Science and Engineering: B*, vol. 308, p. 117613, 2024.
- [171] S. Cui, Z. Mei, Y. Zhang, H. Liang, and X. Du, "Room-temperature fabricated amorphous ga<sub>2</sub>o<sub>3</sub> high-response-speed solar-blind photodetector on rigid and flexible substrates," *Advanced Optical Materials*, vol. 5, no. 19, p. 1700454, 2017.
- [172] S. H. Lee, K. M. Lee, Y.-B. Kim, Y.-J. Moon, S. B. Kim, D. Bae, T. J. Kim, Y. D. Kim, S.-K. Kim, and S. W. Lee, "Sub-microsecond response time deep-ultraviolet photodetectors using  $\alpha$ -ga<sub>2</sub>o<sub>3</sub> thin films grown via low-temperature atomic layer deposition," *Journal of Alloys and Compounds*, vol. 780, pp. 400–407, 2019.
- [173] G. Qiao, Q. Cai, T. Ma, J. Wang, X. Chen, Y. Xu, Z. Shao, J. Ye, and D. Chen, "Nanoplasmonically enhanced high-performance metastable phase  $\alpha$ -ga<sub>2</sub>o<sub>3</sub> solar-blind photodetectors," *ACS applied materials & interfaces*, vol. 11, no. 43, pp. 40283–40289, 2019.
- [174] U. U. Muazzam, P. Chavan, S. Raghavan, R. Muralidharan, and D. N. Nath, "Optical properties of mist cvd grown  $\alpha$ -ga<sub>2</sub>o<sub>3</sub>," *IEEE Photonics Technology Letters*, vol. 32, no. 7, pp. 422–425, 2020.
- [175] S. Nakagomi, "Ultraviolet photodetector based on a beta-gallium oxide/nickel oxide/beta-gallium oxide heterojunction structure," *Sensors*, vol. 23, no. 19, p. 8332, 2023.
- [176] D.-W. Jeon, H. Son, J. Hwang, A. Polyakov, N. Smirnov, I. Shchemerov, A. Chernykh, A. Kochkova, S. Pearton, and I.-H. Lee, "Electrical properties, structural properties,

## Bibliography

and deep trap spectra of thin  $\alpha$ -ga<sub>2</sub>o<sub>3</sub> films grown by halide vapor phase epitaxy on basal plane sapphire substrates,” *APL Materials*, vol. 6, no. 12, 2018.

- [177] K. Sasaki, A. Kuramata, T. Masui, E. G. Villora, K. Shimamura, and S. Yamakoshi, “Device-quality  $\beta$ -ga<sub>2</sub>o<sub>3</sub> epitaxial films fabricated by ozone molecular beam epitaxy,” *Applied Physics Express*, vol. 5, no. 3, p. 035502, 2012.
- [178] Y. Kang, K. Krishnaswamy, H. Peelaers, and C. G. Van de Walle, “Fundamental limits on the electron mobility of  $\beta$ -ga<sub>2</sub>o<sub>3</sub>,” *Journal of Physics: Condensed Matter*, vol. 29, no. 23, p. 234001, 2017.
- [179] N. Ma, N. Tanen, A. Verma, Z. Guo, T. Luo, H. G. Xing, and D. Jena, “Intrinsic electron mobility limits in  $\beta$ -ga<sub>2</sub>o<sub>3</sub>,” *Applied Physics Letters*, vol. 109, no. 21, 2016.
- [180] L. A. Lyle, “Critical review of ohmic and schottky contacts to  $\beta$ -ga<sub>2</sub>o<sub>3</sub>,” *Journal of Vacuum Science & Technology A*, vol. 40, no. 6, 2022.
- [181] H. Sheoran, V. Kumar, and R. Singh, “A comprehensive review on recent developments in ohmic and schottky contacts on ga<sub>2</sub>o<sub>3</sub> for device applications,” *ACS Applied Electronic Materials*, vol. 4, no. 6, pp. 2589–2628, 2022.
- [182] M.-H. Lee and R. L. Peterson, “Interfacial reactions of titanium/gold ohmic contacts with sn-doped  $\beta$ -ga<sub>2</sub>o<sub>3</sub>,” *APL Materials*, vol. 7, no. 2, 2019.
- [183] H. T. Aller, X. Yu, A. Wise, R. S. Howell, A. J. Gellman, A. J. McGaughey, and J. A. Malen, “Chemical reactions impede thermal transport across metal/ $\beta$ -ga<sub>2</sub>o<sub>3</sub> interfaces,” *Nano letters*, vol. 19, no. 12, pp. 8533–8538, 2019.
- [184] M. Girolami, M. Bosi, V. Serpente, M. Mastellone, L. Seravalli, S. Pettinato, S. Salvatore, D. M. Trucchi, and R. Fornari, “Orthorhombic undoped  $\kappa$ -ga<sub>2</sub>o<sub>3</sub> epitaxial thin films for sensitive, fast, and stable direct x-ray detectors,” *Journal of Materials Chemistry C*, vol. 11, no. 11, pp. 3759–3769, 2023.
- [185] Y. Bao, X. Wang, and S. Xu, “Sub-bandgap refractive indexes and optical properties of si-doped  $\beta$ -ga<sub>2</sub>o<sub>3</sub> semiconductor thin films,” *Journal of Semiconductors*, vol. 43, no. 6, p. 062802, 2022.

## Bibliography

- [186] H. Peelaers and C. G. Van de Walle, “Sub-band-gap absorption in  $\text{ga}_2\text{o}_3$ ,” *Applied Physics Letters*, vol. 111, no. 18, 2017.
- [187] M. E. Ingebrigtsen, J. Varley, A. Y. Kuznetsov, B. G. Svensson, G. Alfieri, A. Mihaila, U. Badstübner, and L. Vines, “Iron and intrinsic deep level states in  $\text{ga}_2\text{o}_3$ ,” *Applied Physics Letters*, vol. 112, no. 4, 2018.
- [188] K. Irmscher, Z. Galazka, M. Pietsch, R. Uecker, and R. Fornari, “Electrical properties of  $\beta$ - $\text{ga}_2\text{o}_3$  single crystals grown by the czochralski method,” *Journal of Applied Physics*, vol. 110, no. 6, 2011.
- [189] C. Main, S. Reynolds, I. Zrinščak, and A. Merazga, “Comparison of ac and dc constant photocurrent methods for determination of defect densities,” *Journal of non-crystalline solids*, vol. 338, pp. 228–231, 2004.
- [190] J. Kaur and S. Tripathi, “Determination of density of states using constant photocurrent method in nc-cdse: Sn thin films,” in *AIP Conference Proceedings*, vol. 1512, pp. 224–225, American Institute of Physics, 2013.
- [191] B. R. Tak, M.-M. Yang, M. Alexe, and R. Singh, “Deep-level traps responsible for persistent photocurrent in pulsed-laser-deposited  $\beta$ - $\text{ga}_2\text{o}_3$  thin films,” *Crystals*, vol. 11, no. 9, p. 1046, 2021.
- [192] D. Nicol, S. Reynolds, K. Barr, J. W. Roberts, J. J. Jarman, P. R. Chalker, and F. C.-P. Massabuau, “Constant photocurrent method to probe the sub-bandgap absorption in wide bandgap semiconductor films: The case of  $\alpha$ - $\text{ga}_2\text{o}_3$ ,” *physica status solidi (b)*, p. 2300470, 2024.
- [193] E. Akar, I. Dimkou, A. Ajay, E. Robin, M. I. den Hertog, and E. Monroy, “Gan and algan/aln nanowire ensembles for ultraviolet photodetectors: effects of planarization with hydrogen silsesquioxane and nanowire architecture,” *ACS Applied Nano Materials*, vol. 6, no. 14, pp. 12792–12804, 2023.
- [194] M. R. Khan, J. A. Schwenzer, J. Lehr, U. W. Paetzold, and U. Lemmer, “Emergence of deep traps in long-term thermally stressed  $\text{ch}_3\text{nh}_3\text{pb}_3$  perovskite revealed by thermally

## Bibliography

- stimulated currents,” *The Journal of Physical Chemistry Letters*, vol. 13, no. 2, pp. 552–558, 2022.
- [195] J. Schafferhans, C. Deibel, and V. Dyakonov, “Electronic trap states in methanofullerenes,” *Advanced Energy Materials*, vol. 1, no. 4, pp. 655–660, 2011.
- [196] A. Polyakov, N. Smirnov, I. Shchemerov, E. Yakimov, V. Nikolaev, S. Stepanov, A. Pechnikov, A. Chernykh, K. Shcherbachev, A. Shikoh, *et al.*, “Deep trap spectra of sn-doped  $\alpha$ -ga<sub>2</sub>o<sub>3</sub> grown by halide vapor phase epitaxy on sapphire,” *APL Materials*, vol. 7, no. 5, 2019.
- [197] A. Luchechko, V. Vasylytsiv, L. Kostyk, O. Tsvetkova, and B. Pavlyk, “Thermally stimulated luminescence and conductivity of  $\beta$ -ga<sub>2</sub>o<sub>3</sub> crystals,” *Journal of nano-and electronic physics*, no. 11, no. 3, pp. 03035–1, 2019.
- [198] Y. Huang, X. Xu, J. Yang, X. Yu, Y. Wei, T. Ying, Z. Liu, Y. Jing, W. Li, and X. Li, “Library of intrinsic defects in  $\beta$ -ga<sub>2</sub>o<sub>3</sub>: First-principles studies,” *Materials Today Communications*, vol. 35, p. 105898, 2023.
- [199] L. Madani, S. Nouredine, C. V. Prasad, H. Mohamed, and Y. S. Rim, “On the nature of majority and minority traps in  $\beta$ -ga<sub>2</sub>o<sub>3</sub>: A review,” *Materials Today Physics*, p. 101155, 2023.
- [200] A. Fejfar, A. Poruba, M. Vaněček, and J. Kočka, “Precise measurement of the deep defects and surface states in a-si: H films by absolute cpm,” *Journal of non-crystalline solids*, vol. 198, pp. 304–308, 1996.
- [201] Z. Feng, A. Anhar Uddin Bhuiyan, M. R. Karim, and H. Zhao, “Mocvd homoepitaxy of si-doped (010)  $\beta$ -ga<sub>2</sub>o<sub>3</sub> thin films with superior transport properties,” *Applied Physics Letters*, vol. 114, no. 25, 2019.
- [202] M. Higashiwaki and S. Fujita, *Gallium Oxide: Materials Properties, Crystal Growth, and Devices*, vol. 293. Springer Nature, 2020.
- [203] W. H. Organisation., “Drinking water,” November 2023.

## Bibliography

- [204] J. A. Foley, N. Ramankutty, K. A. Brauman, E. S. Cassidy, J. S. Gerber, M. Johnston, N. D. Mueller, C. O’Connell, D. K. Ray, P. C. West, *et al.*, “Solutions for a cultivated planet,” *Nature*, vol. 478, no. 7369, pp. 337–342, 2011.
- [205] M. H. Ward, R. R. Jones, J. D. Brender, T. M. De Kok, P. J. Weyer, B. T. Nolan, C. M. Villanueva, and S. G. Van Breda, “Drinking water nitrate and human health: an updated review,” *International journal of environmental research and public health*, vol. 15, no. 7, p. 1557, 2018.
- [206] W. H. Organisation., “Goal 6: Clean water and sanitation, sustainable development goals, united nations development programme,” August 2023.
- [207] R. F. Spalding and M. E. Exner, “Occurrence of nitrate in groundwater—a review,” *Journal of environmental quality*, vol. 22, no. 3, pp. 392–402, 1993.
- [208] J. O. Lundberg, E. Weitzberg, J. A. Cole, and N. Benjamin, “Nitrate, bacteria and human health,” *Nature Reviews Microbiology*, vol. 2, no. 7, pp. 593–602, 2004.
- [209] P. Banerjee, P. Garai, N. C. Saha, S. Saha, P. Sharma, and A. K. Maiti, “A critical review on the effect of nitrate pollution in aquatic invertebrates and fish,” *Water, Air, & Soil Pollution*, vol. 234, no. 6, p. 333, 2023.
- [210] E. S. Kritzberg, E. M. Hasselquist, M. Škerlep, S. Löfgren, O. Olsson, J. Stadmark, S. Valinia, L.-A. Hansson, and H. Laudon, “Browning of freshwaters: Consequences to ecosystem services, underlying drivers, and potential mitigation measures,” *Ambio*, vol. 49, pp. 375–390, 2020.
- [211] G. S. Bilotta and R. E. Brazier, “Understanding the influence of suspended solids on water quality and aquatic biota,” *Water research*, vol. 42, no. 12, pp. 2849–2861, 2008.
- [212] E. M. Systems, “Turbidity, total suspended solids and water clarity,” September 2023.
- [213] U. EPA, “Water data and tools,” September 2023.
- [214] Y. Guo, C. Liu, R. Ye, and Q. Duan, “Advances on water quality detection by uv-vis spectroscopy,” *Applied Sciences*, vol. 10, no. 19, p. 6874, 2020.

## Bibliography

- [215] J. Causse, O. Thomas, A.-V. Jung, and M.-F. Thomas, “Direct doc and nitrate determination in water using dual pathlength and second derivative uv spectrophotometry,” *Water research*, vol. 108, pp. 312–319, 2017.
- [216] O. Thomas and M. Brogat, “Organic constituents [chapter 4],” *UV-Visible Spectrophotometry of Water and Wastewater (3rd ed.)*, pp. 95–160, 2022.
- [217] C. Xie, X.-T. Lu, X.-W. Tong, Z.-X. Zhang, F.-X. Liang, L. Liang, L.-B. Luo, and Y.-C. Wu, “Recent progress in solar-blind deep-ultraviolet photodetectors based on inorganic ultrawide bandgap semiconductors,” *Advanced Functional Materials*, vol. 29, no. 9, p. 1806006, 2019.
- [218] F.-P. Massabuau, J. Roberts, D. Nicol, P. Edwards, M. McLelland, G. Dallas, D. Hunter, E. Nicolson, J. Jarman, A. Kovács, *et al.*, “Progress in atomic layer deposited [alpha]-ga<sub>2</sub>o<sub>3</sub> materials and solar-blind detectors,” in *Oxide-based Materials and Devices XII*, vol. 11687, pp. 23–30, SPIE, 2021.
- [219] H. Zhang, Q. Wu, Y. Li, and S. Xiong, “Simultaneous detection of nitrate and nitrite based on uv absorption spectroscopy and machine learning,” 2021.
- [220] M. A. Reshchikov, “Measurement and analysis of photoluminescence in gan,” *Journal of applied physics*, vol. 129, no. 12, 2021.